UNIVERSITÀ DEGLI STUDI DI TORINO

DIPARTIMENTO DI SCIENZE DELLA TERRA

DOCTORAL SCHOOL OF SCIENCE AND INNOVATIVE TECHNOLOGIES

PhD PROGRAMME IN EARTH SCIENCES

PhD CYCLE: XXXV

Tectono-metamorphic evolution of the Nappe Zone of the Sardinian Variscan belt, Italy

Constraining the architecture of the hinterland-foreland transition zone in collisional environment

PhD CANDIDATE: PETROCCIA Alessandro[1]

SUPERVISOR: *Prof.* CAROSI Rodolfo[1]

CO-SUPERVISORS: *Prof. ssa* MONTOMOLI Chiara[1,2]

Dr. IACCARINO Salvatore[1]

CONTRIBUTOR: *Prof.* VITALE BROVARONE Alberto[2,3,4]

PhD PROGRAMME CO-ORDINATOR: *Prof.* DELA PIERRE Francesco[1]

[1]Dipartimento di Scienze della Terra, Università di Torino, Via Valperga Caluso 35, 10125, Torino, Italy

[2]Institute of Geosciences and Earth Resources, National Research Council of Italy, Pisa, Italy

[3]Dipartimento di Scienze Biologiche, Geologiche e Ambientali, Alma Mater Studiorum Università di Bologna, Piazza di Porta San Donato 1, 40126, Bologna, Italy

[4]Sorbonne Université, Muséum National d'Histoire Naturelle, UMR CNRS 7590, IRD, Institut de Minéralogie, de Physique des Materiaux et de Cosmochimie, IMPMC, 4 Place Jussieu, 75005, Paris, France

ACADEMIC YEARS: 2019/2020, 2020/2021, 2021/2022

SCIENTIFIC DISCIPLINARY SECTOR: GEO/03

“It’s a long way to the top if you wanna rock’n’roll”

AC/DC

The research reported in this Thesis was carried out at:

Dipartimento di Scienze della Terra, Università di Torino

Via Valperga Caluso, 35

10125 Torino

Italy

Institute of Geological Sciences, University of Bern

Baltzerstrasse, 3

3012 Bern

Switzerland

Reading committee:

Prof. Pierre Lanari (University of Bern)

Dr. Fabrizio Cocco (University of Cagliari)

Prof. Marco Gattiglio (University of Turin)

On the cover: field and micro photograph of a refolded fold from the Baunei area

ABSTRACT

The anatomy of collisional belts is highly diverse, partly due to differences in size, shape and mechanical strength among colliding plates and to the effects of various pre-, syn- and post-collisional tectonic histories. The convergence direction can vary from highly oblique to nearly orthogonal. These differences influence the mechanisms of collisional orogenesis. Structural investigations at different scales, flow kinematics, and finite strain analyses are fundamental tools to determine how deformation is accommodated and partitioned, but spatial temperature variations can be responsible for the crust's dynamic weakening and strain localization. By integrating field observations, meso- and microstructural analyses, kinematic vorticity estimations, and finite strain data with a quantitative thermometric analysis by Raman Spectroscopy on Carbonaceous Material (RSCM), the structural and thermal architecture across the Nappe Zone of the Sardinian Variscan belt (i.e., the Internal and External nappes) and the ductile tectonic boundary in between (i.e., the Barbagia Thrust) has been investigated. The obtained T_{RSCM} highlighted a temperature difference, from ~470-440 °C down to ~440-380 °C, for the Internal and External nappes, respectively. Along the Barbagia Thrust, an increase in both simple shear and temperature (~50 °C) toward the core has been recognized. Using the multi-equilibrium approach on chlorite and K-white mica, compared with forward modeling, and integrated with RSCM, the *P-T*-peak conditions of 0.6-0.8 GPa and 420-450 °C and 0.4-0.5 GPa and 370-400 °C from the Internal and External nappes have been obtained. The retrograde path indicates a decompression with no relevant temperature changes, with values of 0.4-0.5 and 0.2 GPa for the Internal and External nappes, respectively. In addition, as an anomaly within the greenschist-facies rocks of the hinterland-foreland transition zone, the Monte Grighini dome and the associated shear zone have been investigated. It is associated with an H*T* pervasive non-coaxial deformation associated with sub-vertical mylonitic foliation and subhorizontal object lineation. *In-situ* U-(Th)-Pb monazite geochronology reveals that the shear deformation initiated at ~315 Ma in a time span of ~15 My. Obtained results point out that both Internal and External nappes experienced syn-nappe emplacement greenschist-facies metamorphism with different *P-T* conditions, further heating localized along the Barbagia Thrust, and finally, post-nappe stacking regional-scale folding that deformed the thermo-structural spatial distribution and drove the present-day architecture. The hinterland-foreland transition zone in Sardinia is ascribable to a spatial and temporal strain partitioning at the belt scale developed from syn-collisional shear zones orthogonal to the displacement direction of the belt to orogen-parallel transpressive shear zones, resulting in an oblique tectonic setting.

ACKNOWLEDGEMENT

First of all, I want to thank my supervisor and co-supervisors Prof. Rodolfo Carosi, Prof. ssa Chiara Montomoli and Dr. Salvatore Iaccarino, for giving me the possibility to do my PhD journey under their insightful and supportive supervision. They taught me the importance of consistency and the scientific process's thoroughness, which is something that cannot be learned by reading. I want to express my deep gratitude, and it is impossible to thank them here properly for all the effort, encouragement, advice and financial support they have given me during these years. They always helped me through instructive discussions and supported me during my entire PhD with funny anecdotes and life lessons. Joining this group, I learned how to conduct my scientific activity. They are not only my supervisors but the "scientific family". In this group, I also want to include and thank Dr. Matteo Simonetti, a mentor and a friend.

Then I am indebted to Prof. Alberto Vitale Brovarone: he showed me, for the first time, the wonders of Raman Spectroscopy on Carbonaceous Material, one of the main methods and aims of my Thesis.

I also want to thank Prof. Pierre Lanari and Dr. Jacob Forshaw for showing me the "magic" of petrology and thermodynamic modeling and grooming me into the petrologist that I could try to be. They initiated me into the discipline of *P-T* studies and the beauty and the beast of phase thermodynamics "Lanari et al., 2022, IEC". They helped me with their insightful comments and observations during my growth and my understanding (that still has a long way to go) of thermodynamics and also the quirks of Theriak-Domino. Without their help, this Thesis would not have been the same. Also, I'm very proud to have been part of the Computational Petrology and Geochemistry (CPaG) hosted at the Institute of Geological Sciences, University of Bern.

Furthermore, I thank all the members of the University of Bern for their amazing efficiency and friendliness. The Institut für Geologie has been an ideal place to conduct part of my research. A special thank is dedicated to all the friends in Bern, with whom I enjoyed my free time and I discovered the fantastic outdoors in Switzerland. Thanks for all the brainstorming during lunchtime and coffee breaks! I also want to thank one by one, Thorsten Markmann, Jiahui Liu, Qian W.L. Zhang, Ferdinando Musso Piantelli, Hugo Dominguez, Mona Lueder, Florence Frund, Hoda Moradi, Natalia Nevskaya, Renée Jade Tamblyn, Michelle Ulrich, Coralie Vesin and Nils Gies. I want to thank Prof. Jörg Hermann, Prof. Daniela Rubatto and Dr. Francesca Piccoli for all the discussions, suggestions, and scientific cues.

Many thanks to Maurizio Petrelli for providing me the opportunity to carry out LA-ICP-MS analysis in Perugia and for all the invaluable advice and support to my research.

Also, thanks to the BeGeoScientists community, all the people and friends I met during my career, and to my special “guest” friends Costantino Zuccari, Alessandro Todrani, Lorenzo Dulcetta, Stefania Corvò and Aboubaker Farah.

My entire journey could not have been possible without my family (*Mamma* Simonetta, *Papà* Michele, *Sorella* Francesca and my three dogs, Jack, Pluto and Gaira). They supported me during these years, and even though they could not fully understand what the hell I was doing all these years, they still put in a lot of effort in trying to understand me and my passion: I’m already happy that they now know what Sardinia Island is (maybe without deformation)!

And finally, but not least, I thank the “Paper lovers”, “Gang del Bosco”, and “Drunken pistolero group”, made by my *best* friends, for showing the fun of doing research and geology! It is impossible to count the many times, beers, memories and scientific discussions we performed together. I want to thank Mauro Bonasera, Fabiola Caso, Alberto Corno, Davide Dana, Andrea Maffeis, Sara Nerone and Davide Vianello.

This Thesis is also dedicated to my dog “*Gaira*”, that has been found during my fieldwork in Sardinia and is still with me in the overall PhD.

THESIS CONTENT

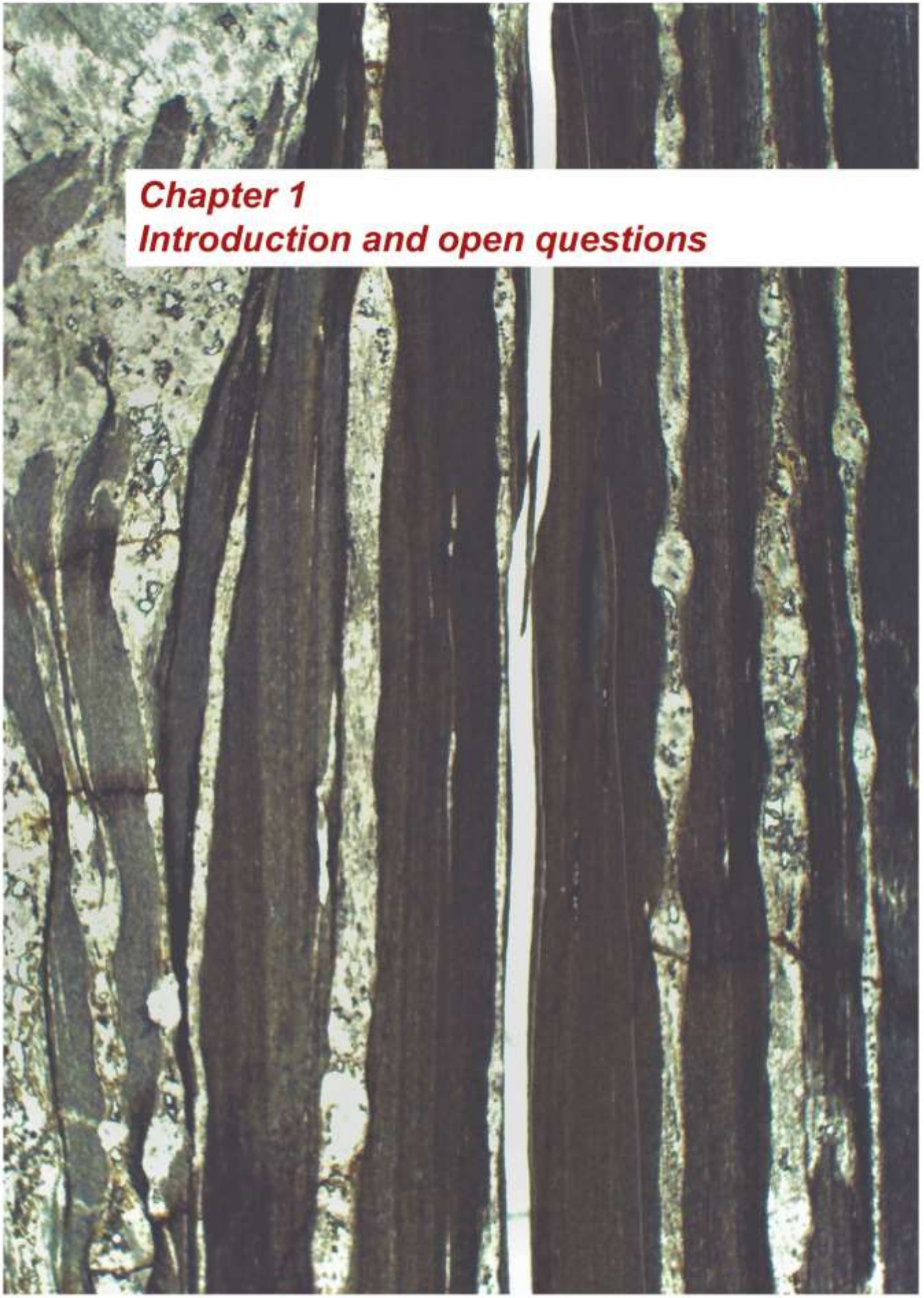

Chapter 1
Introduction and open questions

Orogenic processes that operate from the lithospheric- to the micro-scale are inexorably linked. Over the last two decades, numerical and theoretical models of collisional systems have become increasingly complex, allowing explicit coupling of fundamental processes such as kinematics, mechanics, and thermal/metamorphic evolution at the orogen scale (Konstantinovskaia & Malavieille, 2005, 2011; Thigpen et al., 2010, 2021). At the same time, significant advancements have been made in the comparative analysis of orogens worldwide through large multi-disciplinary and field-derived datasets. Structural geology, petrology and petrochronology, giving insights into regional geology and tectono-metamorphic architecture, are the basis of the geodynamic interpretation of orogens.

When two major continents collide, the resulting collisional orogen will be very complex and articulate (Fig. 1.1a). It may contain several sutures or tectonic contacts separating different blocks, each with its unique geologic history. In several cases, collisional orogens involve the accretion of exotic terranes before the collision of the larger continents and the final closure of the intervening ocean, so such complexity is the norm rather than the exception (Lister et al., 2001; Rogers & Santosh, 2004; Condie et al., 2007; Domeier & Torsvik, 2014). Meanwhile, the crust thickens considerably in the internal part of the orogen, or its hinterland, where intense folding, ductile shearing, and regional metamorphism occur. With the ongoing collision, the metamorphism and deformation move toward the foreland, and often large-scale nappes and recumbent folds develop. Thus, the geodynamic evolution of collisional orogens has been classically described using an orogenic wedge model, where different rock packages experience different finite tectono-metamorphic histories (e.g., Davis et al., 1983; Platt, 1993; Jaquet et al., 2018; Malavieille et al., 2019; Fig. 1.1b). Metamorphic rocks of the hinterland and the hinterland-foreland transition zone are eventually exhumed due to a combination of different tectonic processes. Despite the importance of the horizontal shortening that takes place in the crust during collisional tectonics, the thickening of the crust cannot continue infinitely because, as the crust thickens, rocks at depth become weaker (e.g., Buck, 1991; Avouac & Burov, 1996). Consequently, the differential stress linked to the weight of the overlying rocks exceeds the yield strength of those at depth, and rocks begin to flow, classically called extensional collapse or orogenic collapse (Henk, 1997; Van der Pluijm & Marshak, 2003).

The hinterland-foreland transition zone is defined as a zone where the progressive transition from tectonic units occurring in the metamorphic core of the belt to the ones deformed at shallower crustal levels and steadily included in the orogenic wedge occurs (Larson et al., 2010; Thigpen et al., 2010, 2017; Schneider et al., 2014; Montomoli et al., 2018; Figs. 1.1b, c).

Geologists have struggled to understand the nature of fold-thrust belts since the 1820s, but most of the crucial data come from the second half of the twentieth century with seismic-reflection profiling and oil-well drilling. Investigations from the 1960s to the 1980s refined the geometric and kinematic rules governing the shape and evolution of thrust-related folds (e.g. Butler et al., 2020 for a review). Studies continue in the twenty-first century as geologists work to characterize fold-thrust belts in three dimensions and try to predict the geometry of their component structures in the subsurface (see Hammerstein et al., 2020 for a critical review).

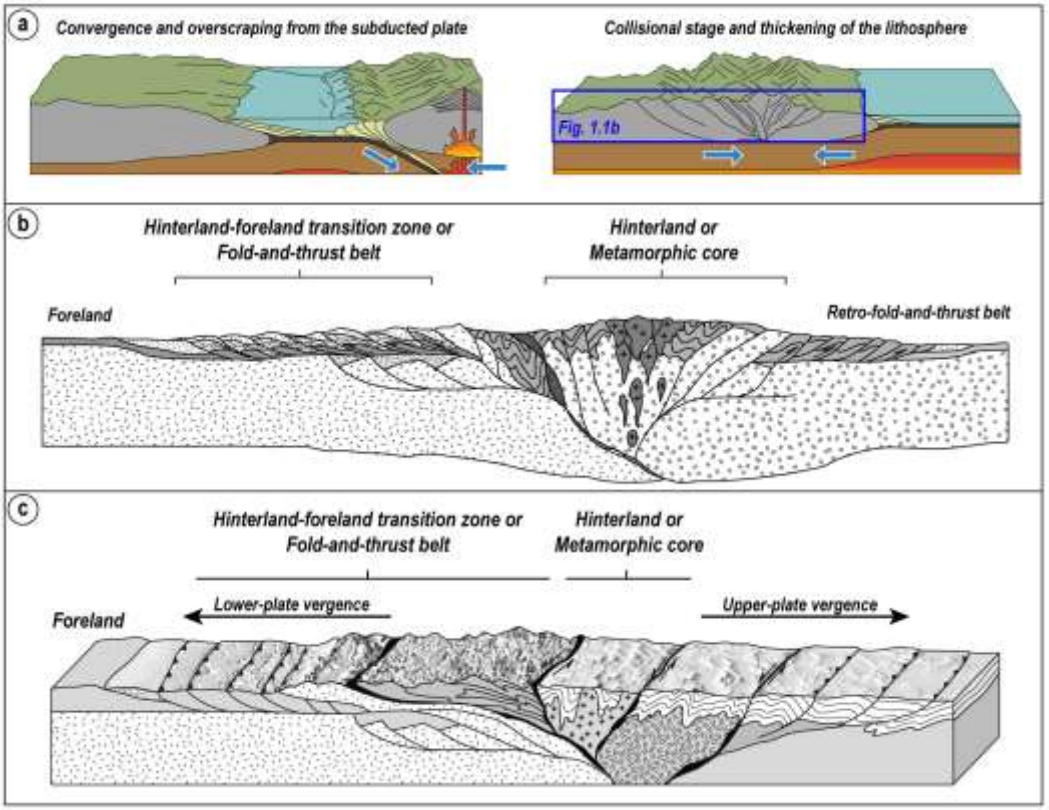

Figure 1.1 a) Idealized cross sections first during convergent-margin tectonism and then during continent-continent collision; b,c) in a mature collisional orogen, the subducting slab has broken off, a suture has formed, and metamorphic rocks are uplifted and exhumed in the core of the orogen. A fold-thrust belt or hinterland-foreland transition zone forms. The double vergence of the belt, related to the upper or lower plate, is recognizable. Modified from Van der Pluijm & Marshak (2003).

Different features control the tectonic architecture of orogenic wedges in collisional belts, such as the detachment zones, the efficiency of erosion and the temperature distribution (Jamieson et al., 1996, 1998, 2002; Jamieson & Beaumont, 1998, 2013; Avouac, 2003; Konstantinovskaia & Malavieille, 2005, 2011; Graveleau et al., 2012; Piccolo et al., 2018; Agard, 2021).

For this reason, quantitative constraints about the thermal and baric variation in space and time are necessary for understanding and modeling paleo-wedges (Jaquet et al., 2018; Girault et al., 2020; Thigpen et al., 2021). However, except along a few favorable crustal sections (e.g., Beyssac et al., 2007; Long et al., 2016; Grujic et al., 2020), quantitative estimations are often scattered and not continuously distributed across the chain, leaving large volumes of metasediments uninvestigated. Despite the significant occurrence of low-grade rocks, and in particular metasediments, and the impressive progress in modeling metamorphic rocks over the last two decades, relatively fewer methods, compared to those applied for metamorphism at higher pressure-temperature conditions, are appropriate and available for low-grade metapelites (Willner, 2020). Unraveling the architecture and evolution of orogenic wedges is also hampered by the presence of: (i) strongly deformed large-scale nappes made by apparently homogeneous low-grade metasedimentary rocks lacking index minerals; (ii) strong overprinting of post-nappe stacking deformation that modifies the original attitude of pre- and syn-nappe stacking elements (e.g., secondary foliations, tectonic contacts, folds vergence); and (iii) the presence of mylonitic rocks along km-scale ductile shear zones, which lead to the formation of thrust sheets or tectonic nappes. In addition, dome-shaped structures, characterized by a core of high-grade metamorphic or granitic rocks surrounded by low-grade ones, are important tectonic features in orogens that may also occur within the hinterland-foreland transition zone (Burg, 2004; Whitney et al., 2004, 2013; Platt et al., 2015; Cao et al., 2022). Domes origin and tectonic setting are still debated, and several mechanisms have been proposed for their formation, tectonic regime and exhumation (Coney, 1980; Whitney et al., 2004). The existence of pre- and syn-collisional planar anisotropies involved during the belt's exhumation may give rise to a strain partitioning of deformation observable from the orogenic macroscale to the mesoscopic and even microscopic scales. As far as deformation associated with mountain building processes is concerned, using overprinting criteria at the outcrop scale, different deformation (and/or metamorphic) phases are classically described in many natural examples (Ramsay 1967; Fossen et al., 2019 and references therein). However, quantitative constraints about the pressure (*P)* - temperature (*T)* - deformation (D) - time (*t)* variation are necessary for understanding paleo-wedges architecture and evolution in order to build tightly constrained models (e.g., Jaquet et al., 2018; Girault et al., 2020; Thigpen et al., 2021). Moreover, dense and systematic sampling is needed to identify eventual *P-T* variations linked to structural or thermal gradients.

The Variscan belt in Sardinia represents a continental crustal section, exposing a continuous metamorphic field gradient from greenschist- to granulite-facies rocks (Carmignani et al., 1994; Cruciani et al., 2015 for a review). The variety of metamorphic conditions registered within the Medium- and High-Grade Metamorphic complexes (e.g., Cruciani et al., 2015, 2022; Casini et al., 2022) makes the Variscan belt in Sardinia an ideal natural laboratory to understand processes and tectonic styles during the continental collision. Indeed, this area is important to investigate how crustal-scale thrust-sense shear zones (i.e., the Barbagia Thrust; Carosi & Pertusati, 1990; Carosi & Malfatti, 1995; Conti et al., 1998; Carosi et al., 2004; Montomoli et al., 2018) influence the thermal architecture of orogenic systems. This area is also fundamental when exploring the link between the thermal architecture and deformation along space and time of the orogenic wedge and unraveling the variation from thrust-sense perpendicular to orogen-parallel transpression at the belt scale. Despite their potential to help the tectono-metamorphic interpretation of the belt, due to the previously cited difficulties, few *P*-*T*-D-*t* constraints are available for low-grade rocks in the Nappe Zone or the hinterland-foreland transition zone.

The aim of this Thesis is thus to address some missing points:

i. The lack of a tectono-metamorphic evolution and thermo-structural architecture of the Nappe Zone exposed in Sardinia and of the ductile boundary in between (i.e., the Barbagia Thrust)
ii. The meaning of the Monte Grighini dome and related shear zone in the framework of the Variscan belt exposed in Sardinia and within the Southern European Variscan belt

In order to explore these topics, an approach with a broad perspective was chosen, combining fieldwork with different scales of structural analysis, quantitative *P*-*T* and geochronological constraints coupled with kinematic of the flow and finite strain estimations. This process was iterative, requiring hypotheses to be validated and refined. A major challenge was not to lose the links through these different scales, to be able to put information from microtextures into a regional context and to see if patterns established during fieldwork would find corresponding evidence in thin sections and throughout the metamorphism and timing obtained data.

This work is the outcome of a close collaboration with Computational Petrology and Geochemistry members of the University of Bern, Prof. Lanari P. and Dr. Forshaw J.B. The application of the empirical thermometer using the Raman Spectroscopy on Carbonaceous Material, the RSCM methodology, has been supervised by Prof. Vitale Brovarone A. (University of Bologna). Prof. Franceschelli M. and Prof. Cruciani G. (University of Cagliari) are also thanked for sharing their experience in the Mt. Grighini area (Sardinia, Italy). Many thanks to Maurizio Petrelli for allowing me to carry out LA-ICP-MS analysis in Perugia.

ORGANIZATION OF THE THESIS

The Thesis is structured in different chapters, with several ones reporting the basis of "ready-to-use" articles draft, submitted or nearly close to submission, to peer-reviewed international journals. The structure of the PhD Thesis is as follows:

Chapter 1: Introduction and open questions

Chapter 2: Geology of the Variscan belt in Sardinia

Chapter 3: Approach and methodologies

Chapter 4: Geology of the contact area between the Internal and External Nappe Zone of the Sardinian Variscan belt (Italy): new insights on the complex polyphase deformation occurring in the hinterland-foreland transition zone of collisional belts

This chapter aims to decipher the structural evolution of a sector of the hinterland-foreland transition zone in the Sardinian Variscan belt. Combining the geological survey with meso- and microstructural analysis, a 1:10.000 scale geological map of the Barbagia Thrust deformed zone has been provided. This sector represents the contact zone between the Meana Sardo Unit (belonging to the External Nappe Zone) in the footwall and the Barbagia Unit (belonging to the Internal Nappe Zone) in the hanging wall. Both units preserve (i) an early phase generally observed far from the tectonic contact and mainly in the Meana Sardo Unit (D_1), (ii) a syn-nappe ductile deformation with a top-to-the S-SW sense of shear linked to the Barbagia Thrust activity (D_2) and (iii) a large-scale nappe refolding (D_3). A late extensional stage (D_4), with the development of collapse folds, marks the end of the orogenic cycle. Data presented in this chapter were published in the Journal of Maps (Petroccia et al., 2022b);

Chapter 5: Deformation and temperature variation along thrust-sense shear zones in the hinterland-foreland transition zone of collisional settings: a case study from the Barbagia Thrust (Sardinia, Italy)

This chapter presents the results from the integration of field observations, meso- and microstructural analyses, kinematic vorticity estimations, and finite strain data with a quantitative thermometric analysis by Raman Spectroscopy on Carbonaceous Material along the Barbagia Thrust. These analyses, performed in two different parts of the shear zone, yield similar finite strain gradients, albeit with an increasing component of simple shear with increasing temperature, highlighting the feedback between temperature and vorticity. The obtained results are best by a tectonic scenario with shear heating, where higher magnitude gradients correspond to higher vorticity and finite strain values, indicating greater shear and heating values. The heating quantified along the Barbagia Thrust is compared favorably to numerical and mechanical models (~50 °C). Data presented in this chapter were published in the Journal of Structural Geology (Petroccia et al., 2022a);

Chapter 6: Thermal variation across collisional orogens: insights from the hinterland-foreland transition zone of the Sardinian Variscan belt

This chapter discusses the Raman Spectroscopy on Carbonaceous Material (RSCM) analysis carried out in the low-grade metamorphic rocks of the Sardinian hinterland-foreland transition zone. The obtained T_{RSCM} of the Sardinian Nappe Zone highlighted a temperature difference between Internal and External nappes. Obtained results highlighted that both nappes experienced syn-nappe greenschist-facies metamorphism with different T_{RSCM}, with further heating localized along the tectonic boundary in between, i.e., the Barbagia Thrust. Finally, post-nappe stacking regional-scale folding deformed the T_{RSCM} distribution and drove the present-day thermal architecture. Data presented in this chapter were published in the Terra Nova (Petroccia et al., 2022c);

Chapter 7: Infer the structural position of "nowadays isolated" crustal fragments in collisional belts with the aid of RSCM and structural investigations: a case from the Baunei area (Sardinia, Italy)

In this chapter, using thermometry based on the Raman Spectroscopy on Carbonaceous Material (RSCM) in different portions of the Internal Nappe Zone of the Variscan belt of Sardinia, and comparing obtained results with the existing dataset on the thermal architecture of the belt, an eastward, or strike-parallel, decrease in temperature within the same nappe has been recognized.

Structural investigations at different scales highlight a polyphasic deformation developing within a protracted orogenic history that resulted in a complex superposition of multiple generations of foliations and folds. The lack of mylonites, and the presence of folds with the same vergence of the basal tectonic contact (e.g., the Barbagia Thrust), coupled with lower T_{RSCM}, allow inferring the original structural position of the Baunei sector within the nappe pile. The reason for the present-day exposure of this septum could be explained by the presence of tertiary normal faults that dragged down the Baunei area from the nappe pile. This chapter forms the basis of a draft plan to be submitted soon to the International Journal of Earth Sciences;

Chapter 8: Pressure and temperature estimation in low-grade metapelites

This chapter discusses the metamorphic analysis of low-grade rocks from the Sardinian belt. The first aim is, yielding the *P-T* conditions of both the Internal and External nappes, understanding the evolution of the Sardinian orogenic wedge, and developing a tectonic interpretation and model.

The metamorphic conditions were estimated by integrating different inverse approaches, such as chlorites and K-white mica multi-equilibrium calculations, the latter combined with RSCM thermometry. The second aim is, taking this area as a case study of low-grade metamorphism, to examine how closely different databases and relative solution models predicted phase assemblages and mineral compositions observed in natural low-grade metapelites. This chapter critically evaluates the reliability, limitations and strengths of the phase diagram approach in low-grade metapelites. It also assesses the mutual consistency and the differences at which *P-T* conditions can be derived using the inverse method with RSCM and predictions inferred by the phase equilibrium diagrams. Data and results listed in this section are part of an in-progress draft to be submitted to the Journal of Metamorphic Geology;

Chapter 9: Transtension or Transpression? Tectono-metamorphic constraints on the formation of the Monte Grighini dome (Sardinia, Italy) and implications for the Southern European Variscan belt

This chapter discusses the structural, kinematic and petrochronological study of the Monte Grighini dome within the Sardinian Variscan hinterland-foreland transition zone. This area, representing an anomaly within the Sardinian Nappe Zone, has been characterized by high-temperature pervasive deformation associated with sub-vertical mylonitic foliation and sub-horizontal lineation marked by a prevalent component of pure shear.

In-situ U-(Th)-Pb monazite geochronology reveals that the shear deformation initiated at ~315 Ma in a time span of ~15 My. Although this area has been previously related to a transtensional deformation regime driven by the Monte Grighini shear zone, it shows striking similarities with dextral ductile transpressive shear zones in the Southern European Variscan belt. Obtained results demonstrate that the network of interconnected transpressive shear zones related to the East Variscan Shear Zone framework is not restricted only within migmatites or at the boundary between medium- and high-grade complexes but also deformed the nappe zone with a progressive renjuvement of the shear activity. A draft nearly ready for the submission on Tectonics is based on this chapter.

Chapter 10: Discussion and conclusion

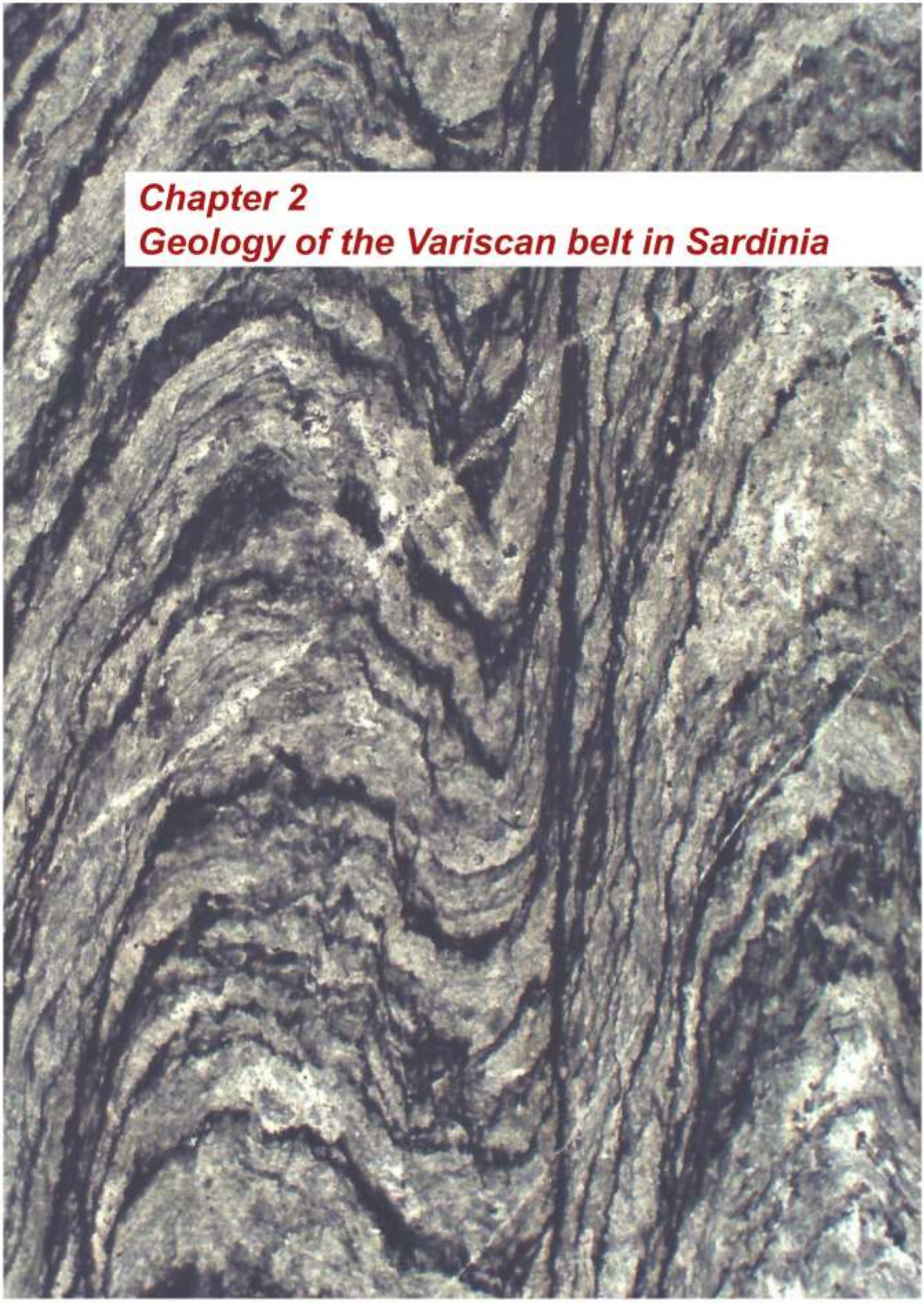

Chapter 2
Geology of the Variscan belt in Sardinia

The Variscan belt's shape in Europe results from a Devonian-Carboniferous continent-continent collision between Laurentia-Baltica and Gondwana (Matte, 1998, 2001). The metamorphic basement of the Sardinia island is a fragment of the southern European Variscan belt and, due to the lack of the Alpine age overprint, it represents a good locality to investigate the Paleozoic tectono-metamorphic evolution. It is made up of (Carmignani et al., 1994, 2001, 2016; see Cruciani et al., 2015 for a critical review):

(i) the External Zone or the foreland;

(ii) the Axial Zone or the hinterland;

(iii) the Nappe Zone or hinterland-foreland transition zone.

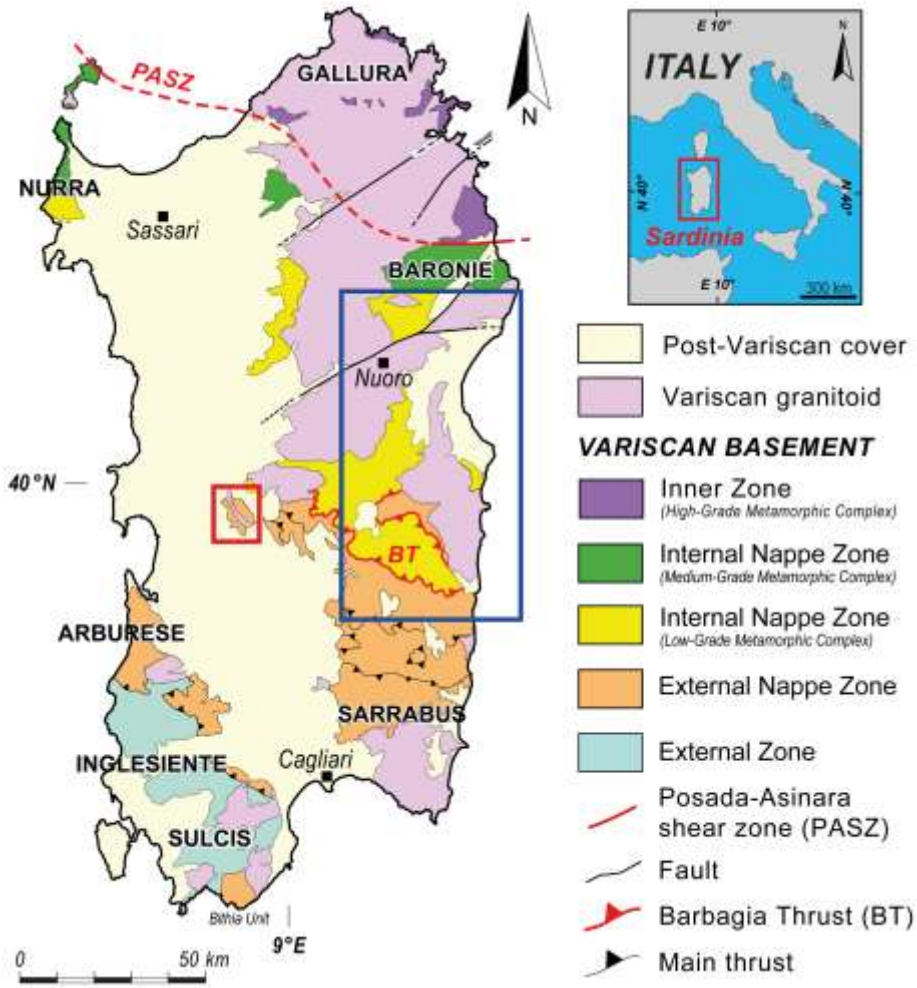

Figure 2.1: Tectonic map of Sardinia island (modified after Carosi et al., 2020). The geographic position of the island has been provided. The coloured squares indicate the investigated areas (red for the Monte Grighini dome and blue for the Barbagia and Meana Sardo units area) during the PhD work. The trace of the geological cross-section A-A' presented in figure 2.2 is also displayed.

The Sardinian Variscan basement is characterized by a northward increase in metamorphism from the External Zone or the foreland to the SW, to the Inner Zone or the hinterland, to the NE (Carmignani et al., 1994; Fig. 2.1). The investigated areas are located in the Nappe Zone, i.e., the hinterland-foreland transition zone. This Thesis discusses in detail only the lithostratigraphy and the tectono-metamorphic evolution knowledge of this sector of the Sardinian Variscan belt.

2.1. The Nappe Zone

The Nappe Zone of central and southern Sardinia (i.e., the hinterland-foreland transition zone; Fig. 2.1) has received considerable attention over the last 40 years (e.g., Carmignani & Pertusati, 1977; Carmignani et al., 1982, 1994, 2012, 2016; Carosi & Pertusati, 1990; Carosi et al., 1991, 2004; Conti et al., 1998, 1999, 2001; Franceschelli et al., 2005; Casini et al., 2010; Cocco & Funedda, 2011, 2017; Cocco et al., 2018, 2022; Montomoli et al., 2018). It has been divided into External (central to southern Sardinia) and Internal (northern to central Sardinia) Nappe Zone (Fig. 2.1). The boundary between them is marked by a regional-scale, top-to-the S-SW thrust-sense ductile to brittle shear zone, the Barbagia Thrust (BT; Carosi & Malfatti, 1995; Montomoli et al., 2018; Figs. 2.1 and 2.2). The lithostratigraphic succession is similar in both nappes: Lower Cambrian to Ordovician metasandstone, phyllite and quartzite (Carmignani et al., 1994; Pertusati et al., 2002; Cocco et al., 2018), Middle Ordovician metaconglomerate and metavolcanic rocks (Oggiano et al., 2010), Upper Ordovician meta-arkose and metasiltstone, Silurian-Lower Devonian black shale, phyllite, and marble, Middle-Upper Devonian marble, and Lower Carboniferous synorogenic flysch (Conti et al., 2001). The main difference between Internal and External nappes is the lack or the paucity of Ordovician metavolcanic rocks and Devonian limestones in the Internal Nappe Zone sequence (Carmignani et al., 1994, 2001).

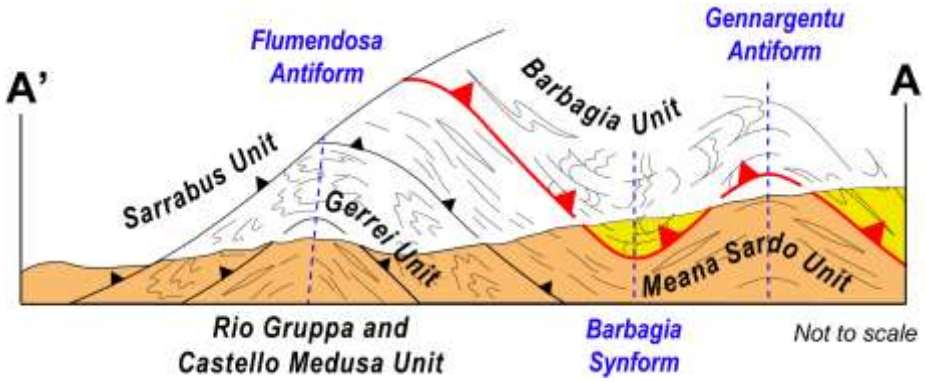

Figure 2.2: Schematic geological cross-section (A-A') along the Nappe Zone (modified after Carmignani et al., 1994; Conti et al., 1999, 2001).

2.1.1. The Internal Nappe Zone

The Internal Nappe Zone (Fig. 2.1) comprises: (i) the Low-Grade Metamorphic Complex (LGMC; Barbagia, Goceano, and southern Nurra units; Vai & Cocozza, 1974; Carmignani et al., 1994; Pertusati et al., 2002; Montomoli, 2003; Casini & Oggiano, 2008) which reached greenschist-facies metamorphic conditions, and (ii) the Medium-Grade Metamorphic Complex (MGMC; Baronie, Anglona, and northern Nurra units; Carmignani et al., 1994, 2001) which reached amphibolite-facies conditions (Cruciani et al., 2015, 2022; Carosi et al., 2020). The boundary zone between the Internal Nappe Zone and the High-Grade Metamorphic Complex (HGMC) is marked by the Posada-Asinara shear zone (PASZ; Elter et al., 1990; Carosi & Palmeri, 2002; Carosi et al., 2020, 2022 and references therein; Fig. 2.1), a dextral transpressive Late-Variscan shear zone, active from ~325 up to ~300 Ma (Di Vincenzo et al., 2004; Carosi et al., 2012; 2020).

In the Internal Nappe Zone, quartzitic and micaceous metasandstone alternating with metasiltstone and quartzite interbedded with grey phyllite crop out within the Monti del Gennargentu ("Postgotlandiano" Auct. and Correboi Unit; Vai & Cocozza, 1974; Dessau et al., 1982), Goceano and Nurra. This lithology is commonly called Filladi Grigie del Gennargentu Fm. The Internal Nappe Zone also includes acidic metavolcanic rocks ("Porfiroidi"), with related meta-arkose and microcline-bearing quartzite, as well as mafic and intermediate (andesite) metavolcanic rocks of probable Cambrian to Ordovician age (Carmignani et al., 1994; Pertusati et al., 2002). In particular, the Upper Ordovician succession in the Internal Nappe Zone is poorly defined. In the Gennargentu Massif, the metasediments attributed to the Upper Ordovician are mainly quartzite (Dessau et al., 1982), suggesting the erosion of an older, mature, crystalline basement, rather than a volcanic arc. As regards the Upper Ordovician to Lower Carboniferous sequences, the Internal Nappe Zone is characterized by Siluro-Devonian graphite-rich phyllite, marble and calcschist intercalations, and metadolerite and metagabbro attributed to the Lower Carboniferous (Carmignani et al., 1994).

2.1.2. The External Nappe Zone

In the External Nappe Zone, five main tectonic units have been identified, which are from the structurally lower to upper (Fig. 2.2): (i) Monte Grighini Unit, (ii) Riu Gruppa/Castello Medusa Unit, (iii) Gerrei Unit / Bithia Unit, (iv) Meana Sardo Unit and (v) Sarrabus Unit (Calvino, 1959; Minzoni, 1975; Barca & Jäger, 1989; Carosi & Pertusati, 1990; Carosi et al., 1991; Musumeci, 1992; Di Milia & Tongiorgi, 1993; Loi, 1993; Carmignani et al., 1994; Conti et al., 2001; Barca et al., 2003; Funedda et al., 2011, 2015; Pavanetto et al., 2012; Musumeci

et al., 2015; Meloni et al., 2017; Cocco et al., 2018, 2022). Tectonic units are emplaced with a main top-to-the S-SW transport direction, except for the Sarrabus Unit. Most of them are characterized by syn-tectonic regional greenschist-facies metamorphism (Carmignani et al., 1994; Carosi et al., 1991, 2010; Franceschelli et al., 1992; Montomoli et al., 2018). The deepest unit of the External Nappe Zone is the Monte Grighini Unit, representing an exception, reaching amphibolite-facies conditions (Musumeci, 1992; Cruciani et al., 2016), within the core of the greatest tectonic culmination, i.e., the Flumendosa Antiform (Fig. 2.2).

The External Nappe Zone can be organized into three main sequences, separated by two regional unconformities (Carmignani et al., 1994, 2001): (i) a Middle Cambrian to Lower Ordovician sequence, (ii) a Middle Ordovician volcano-sedimentary sequence and (iii) an Upper Ordovician to Lower Carboniferous sequence. The oldest unconformity separates the base of the volcano-sedimentary sequence from the pre-Middle Ordovician sequence, i.e., the Sarrabese unconformity (e.g., Loi et al., 2022 for a review). The sequence predating the Sarrabese unconformity is represented by a thick siliciclastic succession (Arenarie di Solanas-San Vito Fm.; Calvino, 1959; Barca et al., 1988) composed of alternating sandstone, siltstone and pelite. The base of the Arenarie di Solanas-San Vito Fm. is never exposed, whereas its top is always erosive, at least in the External Nappe Zone, where a thickness of 500-600 m can be inferred (Carmignani et al. 1982; Oggiano 1994). The age of this formation is Middle Cambrian-Lower Ordovician based on paleontological constraints (Barca et al., 1988; Di Milia & Tongiorgi, 1993; Gnoli & Pillola, 2002). A volcano-sedimentary sequence unconformably caps the Arenarie di Solanas-San Vito Fm. in the External Nappe Zone (see Cocco et al., 2018, 2022 for further details). The overlying volcanic pile consists of metaconglomerate, metavolcanoclastite, grey-green metarhyolite, green metabasalt and dacitic metaignimbrite belonging to the Monte Santa Vittoria Fm. (Conti et al., 2001; Carosi et al., 2004). The Monte Santa Vittoria Fm. includes three lithostratigraphic units that were previously informally defined by Minzoni (1975), including the Manixeddu, Monte Corte Cerbos, and Serra Tonnai formations (Carosi et al., 2004). The age of the protolith is ~460 Ma (Middle-Late Ordovician) based on radiometric analyses (Pavanetto et al., 2012) confirming the stratigraphic ages (Carmignani et al., 1994). The age of the volcanic activity is Middle Ordovician, as these volcanic rocks are sandwiched between the Lower Ordovician portion of the Arenarie di Solanas-San Vito Fm., and the transgressive fossiliferous deposits of Upper Ordovician age (Punta Serpeddì Fm.; Loi et al., 1992; Shale of Riu Cannoni; Naud, 1979). These deposits are thus typical for each tectonic unit and range from lithic sandstone, to greywacke, arkose and shale with rare crinoids-bearing limestone (Orroleddu Fm. in the Meana Sardo Unit; Bosellini & Ogniben, 1968; Loi, 1993; Loi & Dabard, 1997; Genna Mesa

Fm. in the Gerrei Unit; Carmignani et al., 2001; Punta Serpeddì Fm. in the Sarrabus Unit; Loi et al., 1992). Notably, the Upper Ordovician succession of the External Nappe Zone retains several bodies of metabasites in the form of pillow lavas (Gattiglio & Oggiano, 1990), bearing alkaline within-plate signature (Di Pisa et al., 1992; Gaggero et al., 2012). The overlain Silurian sediments are typical graptolite-bearing black shale (Barca & Jäger, 1989). The Silurian succession is followed by shelf carbonate deposits of the Devonian-Lower Carboniferous age (Gnoli, 1993; Corradini et al., 1998). The entire sequence is capped by a Lower Carboniferous culm-like formation consisting of alternating sandstone, conglomerate with distinctive black chert-derived pebbles, and epiclastite layers with turbiditic structures.

2.2. Tectono-metamorphic overview

A complex structural evolution has been detected and described in both Internal and External nappes by several authors (e.g., Carmignani & Pertusati, 1977; Carmignani et al., 1982, 1994; Carosi & Pertusati, 1990; Carosi et al., 1991; Conti & Patta, 1998; Conti et al., 1998; Carosi, 2004; Carosi et al., 2004; Montomoli et al., 2018). D_1 and D_2 deformation phases are related to continental collision and thrust-related shortening, responsible for nappe emplacement, followed by later D_3 and D_4 tectonic phases (Conti et al., 1998, 2001; Carosi et al., 2002, 2004). The latter is attributed to the chain's collapse in an extensional regime, resulting in overall vertical shortening accommodated by brittle-ductile extensional shear zones (Casini et al., 2010).

In this framework, D_1 collision-related phase is associated with a penetrative S_1 axial plane foliation of SW-facing folds, well and mainly detected in the External Nappe Zone (Carosi & Malfatti, 1995; Conti et al., 1998, 1999; Carosi et al., 2002, 2004; Carosi, 2004; Funedda, 2009). The D_1 phase was progressively obliterated by the D_2 event developed during the nappe emplacement stage and linked to the BT activity (Montomoli et al., 2018 and references therein). This tectonic structure is a regional-scale thrust-sense shear zone that marks the boundary between the Internal and the External nappes and is responsible for developing a pervasive high-strain mylonitic zone (Carosi & Malfatti, 1995; Carosi et al., 2002, 2004; Montomoli et al., 2018). The D_2 deformation prevails over large areas, and syn-tectonic asymmetric to isoclinal folds, formed during continuous shear deformation, are locally preserved (Carosi et al., 2004). The BT activity has been constrained in a ductile (Carosi et al., 2004; Montomoli et al., 2018) to brittle regime, highlighted by cataclastic deformation overprinting mylonite (Carosi et al., 1991; Carosi & Malfatti, 1995). The syn-tectonic recrystallization of muscovite, quartz, albite, and chlorite on the mylonitic foliation confirms the greenschist-facies condition.

Several authors (Conti et al., 1998, Carosi et al., 2004; Montomoli et al., 2018) deciphered a strain gradient approaching and across the BT, but no evidence of thermal gradient was detected along the contact.

After nappe-stacking deformation linked to D_1 and D_2 phases, the D_3 phase is responsible for the development of regional-scale antiforms and synforms (from south to north: Flumendosa Antiform, Barbagia Synform, and Gennargentu Antiform; Carmignani et al., 1994; Conti et al., 1999; Figs. 2.1 and 2.2). The entire nappe pile and the BT were refolded by these km-scale uprights to gently asymmetric folds with axes trending WNW-ESE or W-E. The metamorphic grade is lower than the D_2 phase, and pressure solution is the main mechanism of the D_3 event.

Very few detailed studies have been done thus far on the metamorphic evolution of the Nappe Zone during Variscan orogeny. Two metamorphic events, M_1 and M_2 (D_1 and D_2 phases), have been recognized (Carmignani et al., 1994). During the M_1 event, low-grade metamorphism was attained with blastesis of muscovite + chlorite + albite. Further data on M_1 events were supplied by illite and chlorite crystallinity investigations (Franceschelli et al., 1992; Carosi et al., 2010; Montomoli et al., 2018) reporting anchizonal-epizonal conditions (~200-350 °C; Frey & Robinson, 1999) for this sector of the belt. During the M_2 event, the metasediments show the persistence of low-grade conditions, with syn-S_2 blastesis of chlorite + muscovite + albite. Along the axis of the Flumendosa Antiform, prograde metamorphism was observed from SE (Riu Gruppa Unit) to NW (Castello Medusa Unit), applying the calcite-dolomite geothermometer to dolostone levels from Siluro-Devonian marble (Carosi et al., 1990). A higher metamorphic grade was attained only in the deepest units of Castello Medusa and Monte Grighini and in the metamorphic complexes of Sa Lilla, Mandas, Monte Trempu and Asuni (Carmignani et al., 1994; Funedda et al., 2015).

The onset of the collisional stage has been fixed at ~360-345 Ma on the basis of the conodonts-bearing Upper Devonian marble in the Internal Nappe Zone (Pili & Saba, 1975) and of Lower Carboniferous (Tournaisian) sediments in the External Nappe Zone, both involved in the Variscan tectono-metamorphic events (Carmignani et al., 1994; Cocco & Funedda, 2017). The stacked tectonic units and the interposed tectonic contact (Carmignani et al., 1994; Carosi and Malfatti, 1995; Conti et al., 1999) were deformed by the post-nappe folding event during the contractional regime (from south to north: Barbagia Synform, and Gennargentu Antiform; Fig. 2.2). Following the Variscan orogenesis (Carmignani et al., 1994), several basins developed unconformably over the Sardinian Variscan basement (Cassinis et al., 2003; Costamagna, 2019, 2022).

Basins were filled with clastic and minor carbonate deposits during Upper Pennsylvanian to Permian times (Carmignani et al., 1994; Costamagna, 2019), representing the consequence of the collapse of the thickened Variscan chain. Therefore, the emplacement of the Sardo-Corso batholith, constrained at ~320-280 Ma (Del Moro et al., 1975; Casini et al., 2012, 2015) and cross-cutting the deformed Variscan basement, coupled with the contemporaneous development of continental basins indicate the end of the orogenic shortening and the development of the post-collisional extensional phases (Cortesogno et al., 1998).

2.3. The Monte Grighini dome

The Monte Grighini dome (Musumeci, 1992; Musumeci et al., 2015; Fig. 2.1), consists of three tectonic units that, from the structurally bottom to the top, are (Fig. 2.3): (i) the Monte Grighini Unit (MGU), (ii) the Castello Medusa Unit, and (iii) the Gerrei Unit. The MGU comprises amphibolite-facies metavolcanite, metasediment, and intrusive granitic rocks (Musumeci et al., 2015). The Truzzulla Fm. is associated with Upper Ordovician (~447 ± 4.3 Ma) metavolcanite, meta-arkose, and arkosic metasandstone (Cruciani et al., 2013). The Toccori Fm. consists of metapelite (Cruciani et al., 2013, 2017) passing to hornfels in the most adjacent zones close to the intrusions forming the Intrusive Complex (IC; Cruciani et al., 2016). The IC is a NW-SE trending, sub-vertical intrusive body with ages of ~303 ± 18 Ma and ~305 ± 16 Ma (Rb/Sr isochron) for two-mica leucogranite and monzogranite, respectively (Carmignani et al., 1987). Furthermore, K/Ar, Ar/Ar, and Rb/Sr dating of igneous biotite and muscovite yielded cooling ages ranging between ~305-295 Ma (Del Moro et al., 1991; Musumeci, 1992).

The MGU underwent polyphase deformation (Musumeci, 1992; Cruciani et al., 2016). The D_1 and D_2 deformation phases are related to syn-collisional shortening and regional-scale southwestward nappe stacking (Cruciani et al., 2016). These phases are followed by late folding and transtensive tectonics (D_3 and D_4 phases), according to Musumeci (1992) and Cruciani et al. (2016). The main foliation (S_2) is a NW-SE striking continuous schistosity that dips at high-angle both to the NE and SW. The S_2 foliation is characterized by syn-metamorphic pervasive ductile shearing (Cruciani et al., 2016). According to Musumeci (1992) and Cruciani et al. (2016), the parallelism between F_2 fold axes and L_2 lineations, coupled with the asymmetry of F_1 folds is consistent with a top-to-the SW simple shear deformation coeval with nappe stacking. D_3 folds are represented by large-scale NW-SE trending upright antiforms and synforms, related to the development of a regional-scale late folding event.

D_3 is characterized by syn-kinematic minerals recrystallization, indicating deformation at lower metamorphic conditions (Cruciani et al., 2016). The D_4 phase corresponds to a kilometre-wide NW-SE trending dextral transtensional shear zone located in the western sector of the MGU (Musumeci, 1992; Columbu et al., 2015; Musumeci et al., 2015; Cruciani et al., 2016, 2017). This shear zone, i.e., the Monte Grighini Shear Zone (MGSZ; Elter et al., 1990), is associated with a steeply dipping foliation and subhorizontal to gently plunging object and mineral lineations (Musumeci et al., 2015). The MGSZ is marked by the syn-kinematic sub-vertical emplacement of the intrusive complex, with a top-to-the NW strike-slip displacement (Musumeci, 1992). Along the westernmost and the southwesternmost sector of the dome, a NW-trending fault characterized by a cataclasite zone marks the contact between the MGU and the overlying Gerrei Unit (Musumeci et al., 2015). A ductile-brittle thrust contact in the northeastern sector of the dome marks the boundary between the Monte Grighini dome and the Castello Medusa Unit.

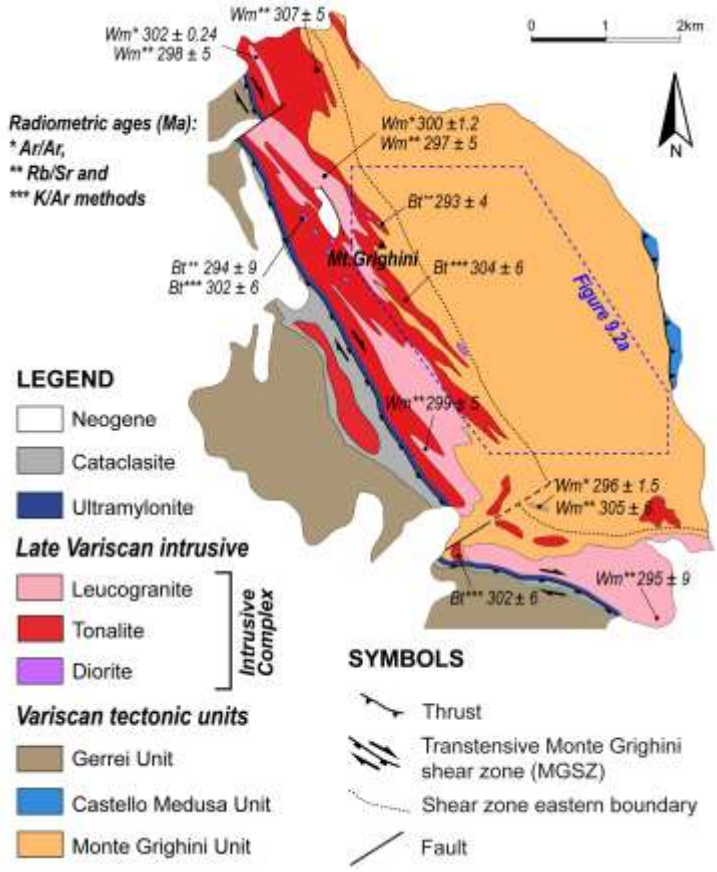

Figure 2.3: Simplified Monte Grighini dome geological map (modified after Musumeci et al., 2015; Cruciani et al., 2016). Previous radiometric ages, the method used for dating, and the studied mineralogical phase are shown in the inset. The dashed blue line indicates the perimeter of the investigated area (Fig. 9.2a).

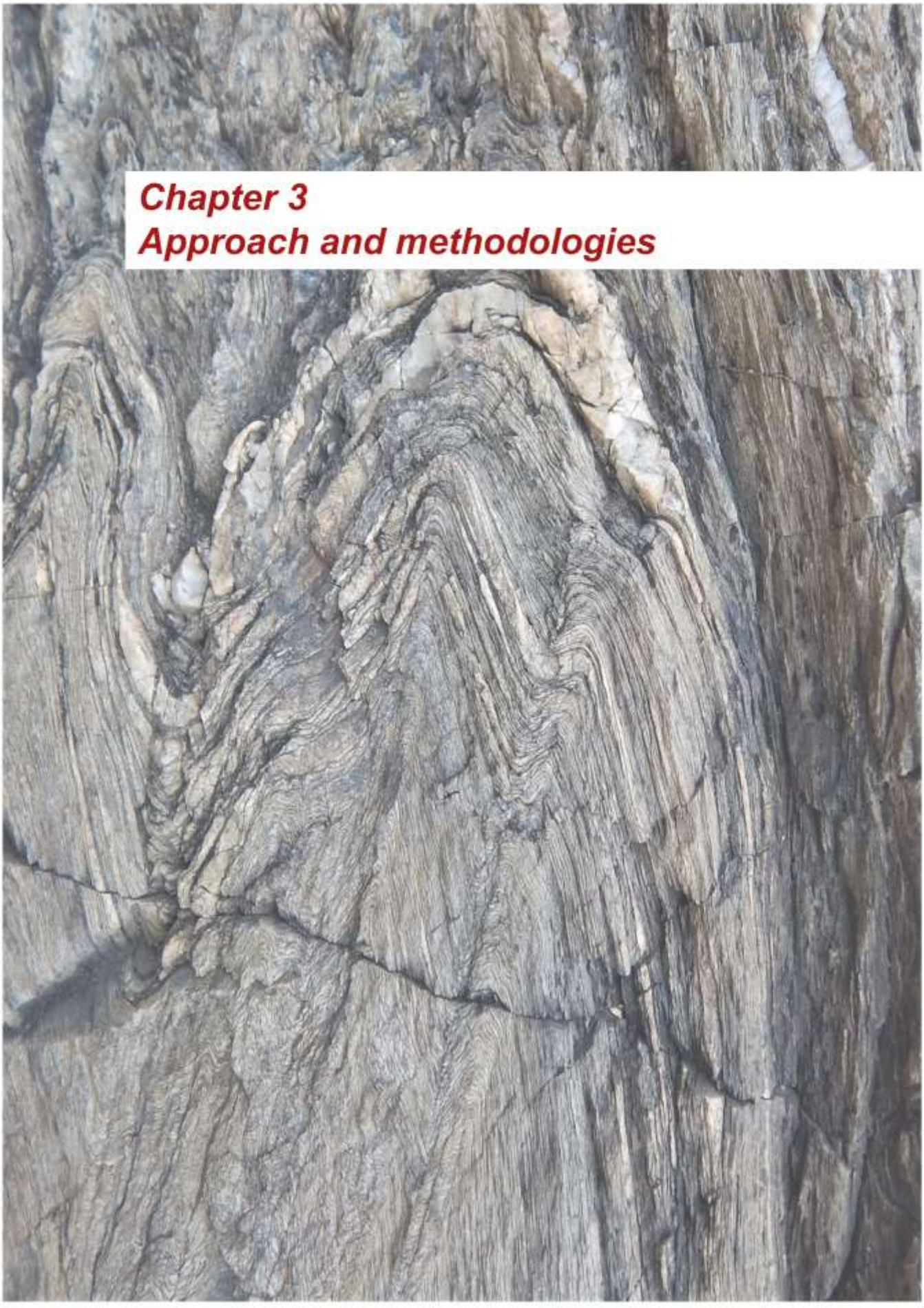

Chapter 3
Approach and methodologies

Shear zones and metamorphic basements contain valuable information that can be extracted by analysing small-scale structures with implications for larger-scale tectonics. In fact, field-based studies need to be supported by detailed microstructural work and high-resolution analytical techniques to constrain intrinsic and extrinsic factors, such as temperature, pressure, mineralogy, deformation mechanisms and timing. Detailed geological field mapping, integrated with meso- and microstructural investigations, kinematic of the flow and finite strain analyses, combined with metamorphic constraints and geochronology, are fundamental tools to unravel the *P*-*T*-D-*t* evolution. The Thesis outcome highlights the importance of a multidisciplinary approach to unveil the tectono-metamorphic evolution of the hinterland-foreland transition zone in Sardinia, starting from the geological mapping and going to different scales and types of approaches.

3.1. Vorticity and finite strain analysis

Structural geologists have long been interested in the kinematic reconstruction of the crustal-scale shear zones, which is thought to be one of the most effective ways to constrain key aspects of the exhumation processes of collision orogens. Deformation in shear zones is often approximated to simple shear, especially in high-strain zones (Xypolias, 2010). However, an important component of pure shear has been detected in many regional-scale shear zones developed in different tectono-metamorphic conditions. Thus, a quantitative assessment of the kinematic vorticity in natural shear zones is required. The non-coaxiality of the flow in shear zones is expressed by the kinematic vorticity parameter *Wk* (Xypolias, 2010), which several vorticity analysis techniques can estimate. Pure and simple shear components may be described through the dimensionless mean kinematic vorticity parameter (*Wm*). Since its introduction into the geological literature, vorticity analysis methodologies have become increasingly sophisticated (e.g., Tikoff & Fossen, 1995; Jessup et al., 2007; Xypolias, 2010; Fossen, 2016). In a ductile flow, the non-coaxial deformation can be normalized to the stretching along the strain axes to obtain a dimensionless number, i.e., the kinematic vorticity parameter. It could be derived through the relation proposed by Passchier (1987):

$$Wk = W/|d2 - d3|$$

where W represents the vorticity and d2–d3 represents the stretching difference along the intermediate and minimum principal strain axes. The mean kinematic vorticity number (*Wm*) could be assumed to be equal to *Wk* because it represents the average value over the deformation interval during which the structure or fabric formed (Xypolias, 2010; Fossen & Cavalcante, 2017).

Pure and simple shear is associated with *Wk* = 0 and *Wk* = 1, respectively. Simple and pure shear contribute equally during the deformation when *Wk* = 0.71 (Law et al., 2004; Passchier & Trouw, 2005; Xypolias, 2010).

In the present Thesis, the *C'* shear band method (Kurz & Northrup, 2008; Gillam et al., 2013) and two different porphyroclasts-based methods, the porphyroclast aspect ratio method (PAR; Passchier, 1987; Wallis et al., 1993) and the rigid grain net method (RGN; Jessup et al., 2007), have been applied to evaluate the percentage of pure and simple shear of the Barbagia Thrust and the Monte Grighini shear zone. To constrain the deformation regime (e.g., transpression/transtension; Fossen et al., 1994; Fossen & Tikoff, 1998), the angle

$$\theta = (\arcsin Wk)/2$$

(Xypolias, 2010), between the maximum Instantaneous Stretching Axis (ISA max) in the horizontal plane and the shear zone boundary has been calculated for the Monte Grighini shear zone. According to Fossen et al. (1994) θ angles larger than 45° are indicative of transtensive deformation, while θ angles smaller than 45° are indicative of transpressional deformation.

The nominal error for vorticity analysis is ± 0.1 (Tikoff & Fossen, 1995). A comparison of different possible systematic error sources indicates that for medium to low vorticity numbers (*Wm* < 0.8), the vorticity data minimum systematic error is ± 0.2 (Iacopini et al., 2011).

3.1.1. C' shear band method

In any type of flow, it is possible to recognize two lines representing the flow apophyses (A1 and A2), along which the particles do not undergo rotation. They are orthogonal in a pure shear dominated deformation and coincide with each other during a simple shear flow. The first method is based on the measurement of the orientation of *C'* planes with respect to the shear zone boundaries (*v* angle). Theoretically, *C'* planes nucleated as the bisector of the angle between the two flow apophyses (Platt & Vissers, 1980; Kurz & Northrup, 2008; Xypolias, 2010). This approach assumes that the *C'* planes nucleated as a bisector of the angle between the two apophyses and the *C* planes are parallel to the shear zone boundaries and the A2 apophyses, respectively. The kinematic vorticity, as proposed by Kurz & Northrup (2008), is derived from the relation

$$Wk = \cos 2v$$

where 2*v* represents the angle between the two flow apophyses (see Kurz & Northrup, 2008; Gillam et al., 2013 for methodological details; Fig. 3.1a).

Following the procedure proposed by Gillam et al. (2013), the *v* angle has been measured, since the mylonitic foliation has a constant trend, sub-parallel to both the *C* and the well-defined and mapped shear zone boundaries (Fig. 3.1b). As each element in a progressive flow tends to rotate, including *C'* planes, it is necessary to consider the largest value for v, among the measured ones, to estimate the initial amplitude of the angle during the formation of the *C'* planes.

Gillam et al. (2013) proposed to use an average value of the angle *v* for low-strain rocks or in cases where *C'* planes developed in a late stage of the deformation history and nucleated in a stable orientation, as in this case, they underwent little or no rotation after inception. For highly strained rocks deformed in long-lasting shear zones, the maximum value of *v* is preferable because, as demonstrated by Kurz & Northrup (2008), the average value is not representative of the original angle of nucleation of *C'* planes.

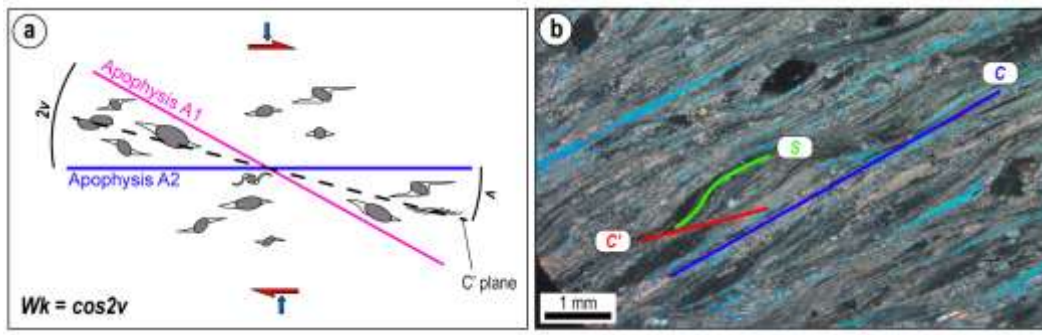

Figure 3.1: a) Schematic diagram of possible microstructures developed under general flow conditions in a mylonite with a dextral sense of shear is displayed. The flow apophyses A1 and A2 are indicated in red and blue, respectively. The angle 2v between the two apophyses is bisected by the C' shear plane (dotted line). The equation to calculate Wk is also shown (modified after Kurz & Northrup 2008); b) microphotograph (XPL: crossed-polarized light) showing C', C and S planes (red, yellow and green, respectively) in a mylonite of the Barbagia Thrust.

3.1.2. Porphyroclasts-based methods

In both porphyroclasts-based methods, the measurement and the best-fit ellipse shapes were determined using EllipseFit 3.8.0 software (Vollmer, 2015). Only samples with an adequate number of freely rotating clasts (>50) lacking internal deformation were chosen for vorticity estimates. Attempts were also made to avoid samples that show evidence of post-shearing deformation. The results were plotted on both the porphyroclast aspect ratio (PAR; Wallis et al., 1993) and rigid grain net (RGN; Jessup et al., 2007) graphs. In detail, the PAR method consists of measuring the axial ratio of porphyroclasts (R) and the angle (ϕ) between the long axis of the rigid grain and the mylonitic foliation (Passchier, 1987; Wallis et al., 1993).

These data are plotted on a graph to estimate a critical axial ratio, Rc (Wallis et al., 1993), which discriminates the field where porphyroclasts reach a stable position from a field where they continue to rotate. The Rc minimum and Rc maximum and average Rc have been calculated. The RGN method involves the measurement of both the axial ratio and the angle between the clast long axis and the foliation. The RGN plot of the rigid grain's shape factor (*B**) and the angle of the long axis with macroscopic foliation has been used to directly estimate the kinematic vorticity values (Passchier, 1987)

$$B = [(M_x)^2 - (M_n)^2] / [(M_x)^2 + (M_n)^2]$$

where M_x is the long axis of the clast and M_n is the short axis. The vertical parts of the positive and negative semi-hyperbolas of the RGN graph are used to determine the critical *B** value that is directly considered the *Wm* value.

3.1.3. Finite strain estimation

Finite strain analyses were performed using the centre-to-centre method (Fry, 1979) by the EllipseFit 3.8.0 software (Vollmer, 2015). Samples were cut and polished perpendicular to the foliation and both parallel and perpendicular to the mineral lineation (XZ and the YZ sections of finite strain ellipsoid). This method is based on the redistribution of the centres of the strain markers caused by deformation and is independent from the shape of the strain markers. Data have been plotted on the Flinn diagram (Flinn, 1962).

3.2. *P-T* estimation methods

3.2.1. *Raman Spectroscopy on Carbonaceous Material (RSCM) geothermometer*

The peak temperature was obtained using Raman Spectroscopy on Carbonaceous Material (RSCM) geothermometer. This method is based on the progressive transformation of Carbonaceous Material (CM) during the temperature increase, and it is not affected by the retrograde history (Beyssac et al., 2002; Beyssac & Lazzeri, 2012).

The Raman spectrum of perfect graphite is made by a single G band at ~1580 cm^{-1} and other bands D1 and D2 at ~1350 cm^{-1} and ~1620 cm^{-1}, respectively. The intensity of the D1 band is used to evaluate the degree of disorder in the CM. Beyssac et al. (2002) established a correlation between the temperature and Raman parameters of the CM called R2. The structural organization of the CM can be quantified through the R2 parameter defined as

$$R2 = D1/(G+D1+D2)$$

Temperatures by RSCM can be estimated over a very large range, from sub-greenschist to upper amphibolite-facies with different geothermometer calibrations (Beyssac et al., 2002; Bollinger et al., 2004; Rahl et al., 2005; Aoya et al., 2010; Lahfid et al., 2010; Kouketsu et al., 2014, 2019; Henry et al., 2019; Skrzypek, 2021). In detail, for ~330-650 °C temperature range, the Beyssac et al. (2002) calibration used samples affected by regional metamorphism, whereas Aoya et al. (2010) carried out the calibration independently from regional metamorphism. Beyssac et al. (2018) concluded that the two calibrations (Beyssac et al., 2002 and Aoya et al., 2010) are in excellent agreement below 600 °C. The applicability of RSCM thermometry was extended to a lower temperature (~150-400 °C) by Rahl et al. (2005), Lahfid et al. (2010), and Kouketsu et al. (2014).

The RSCM geothermometer has an absolute precision of ± 50 °C due to uncertainties of the petrological data used for the calibration. The relative uncertainties on temperature are ± 10-15 °C if the guidelines and recommendations of Beyssac et al. (2002, 2004) and Lündsorf et al. (2014, 2017) are followed, allowing accurate estimation of field thermal gradients (Bollinger et al., 2004). Also, the value of the standard deviation for each sample ($\sigma/\sqrt{n}$) which gives an insight on internal sample heterogeneity, following the procedures proposed by Beyssac et al. (2002, 2003), has been provided.

Because the orientation of CM could affect the Raman spectrum (Wopenka & Pasteris 1993), thin sections were cut perpendicular to the foliation and parallel to the stretching lineation (XZ plane of the finite strain ellipsoid), meaning perpendicular to the basal plane of the CM and perpendicular to the mean c-axis. Since the preparation of a thin section could induce damage during the polishing stage (Kouketsu et al., 2019), the measurements were done by focusing the laser beam a few microns beneath the CM. Due to the emplacement of km-scale intrusive granitic bodies and the possible re-heating of CM, sampling has been conducted, as far as possible, at a distance of approximately 100-200 m from its thermo-metamorphic aureola and from the associated pluri-m dykes, to exclude the occurrence of contact metamorphism overprinting. In addition to these considerations, no quartz annealing is present in the investigated samples to confirm the absence of re-heating. No occurrence of multiple R2 modes in individual samples implying the presence of detrital CM grains has been observed (Yamaoka et al., 2022).

Raman microspectroscopy has been performed with the Horiba Jobin Yvon LabRam HRVIS Raman System at the Centro “G. Scansetti”, Dipartimento di Scienze della Terra, Università degli Studi di Torino. Before each measurement session, the spectrometer was calibrated using the 520.5 cm^{-1} peak (r band) of a silicon standard.

Spectra were acquired by a beam spot of approximately one µm diameter with a green Nd 532.06 nm laser source at 80 mW, corresponding to 2-4 mW at the sample surface, with a 100x magnification. For each sample, a minimum of 10 spectra was recorded, except for samples containing very little CM amount, with acquisition times from 30 to 60 s (Beyssac et al., 2002). The peak position, band area, and bandwidth (FWHM) were determined using the computer program PeakFit 4.0, following the fitting procedure described by Beyssac et al. (2002). The fitting itself used the Voigt area, and the algorithm combined Gaussian and Lorentzian profiles. Beyssac et al. (2002) geothermometer is based on the R2 ratio, which is:

$$T(°C) = -445(R2)+641$$

This equation refers to the temperature range of ~330-650 °C and was obtained by using a 514.5 nm laser (Beyssac et al., 2002).

Because obtained spectra were acquired using a green Nd 532.06 nm laser, the RSCM temperature estimates discussed in the following sections were derived from the Aoya et al. (2010) calibration, which was established based on the same laser wavelength:

$$T(°C) = 221(R2)^2-637.1(R2)+672.3$$

3.2.2. Multi-equilibrium involving chlorite and white mica

The multi-equilibrium calculation is a semi-empirical approach based on the thermodynamic database proposed by Berman (1988) and implemented, for low-grade metapelite, by Vidal & Parra (2000), Vidal et al. (2001; 2006), Parra et al. (2002) and Dubacq et al. (2010). Inverse thermodynamic models aim to retrieve equilibrium conditions from local phase compositions of an assemblage of minerals (Berman, 1991; Powell & Holland, 1988, 1994; Vidal & Parra, 2000). This approach is based on the convergence of the equilibria involving chlorite and mica end-members in the presence of quartz and water (see Vidal et al., 2006 for details). The convergence of reactions in the *P-T* space indicates that the selected mineral compositions are consistent with chemical equilibrium. What it does not provide, in the absence of Gibbs energy minimization, is the unequivocal evidence that the considered phases were in chemical equilibrium for the reactive bulk composition and the expected abundance of phases (Lanari & Duesterhoeft, 2019). In other words, not all the phases used to calculate the metamorphic conditions in an inverse model might be stable for an appropriate bulk composition at the given *P-T* conditions. Support from compositional maps can assist the interpretations by providing detailed microstructural information (Lanari et al.,

2012, 2013; Scheffer et al., 2016), but *P-T* estimates obtained via an inverse model strongly rely on *a priori* assumptions of equilibrium relationships.

The chlorite-K-white mica-quartz-water approach of Vidal et al. (2005, 2006) was applied using the program ChlMicaEqui 1.5 (Lanari, 2012). The Dubacq et al. (2010) model allowed calculating the equilibrium of chlorite-white mica incorporating the hydrated pyrophyllite endmember (H_2O in A-site). It requires the knowledge of the composition of chlorite and K-white mica and the assumption that they formed close to chemical equilibrium conditions at a given stage of their metamorphic history.

Dubacq et al. (2010) proposed a relation that involves dehydrated micas and hydrated pyrophyllite-like thermodynamic end-members to model these compositional variations as a function of *T* and *P*. The equilibrium condition of K-white mica-quartz-water is represented by a divariant *P-T* line along which only the amount of water in the interlayer site content varies. Dubacq et al. (2010) showed that the K-white mica-quartz-water equilibrium could be used as a barometer at given temperature conditions (detailed procedure in Lanari et al., 2012).

3.2.3. Ti-in-Bt geothermometer

The Ti-in-Bt conventional geothermometry (Henry et al., 2005) has been applied. The Ti content has been demonstrated to increase at increasing *T*, while it decreases with increasing *P* (e.g., Robert, 1976; Patiño Douce, 1993). At the same time, Ti content increases with decreasing *XMg* (Arima & Edgar, 1981; Abrecht & Hewitt, 1988). The Ti-in-Bt geothermometer, calibrated combining these parameters (Henry et al., 2005), needs the presence of a Ti reservoir, such as rutile or ilmenite, and has been calibrated for a temperature range of 450-750 °C and for a narrow range of pressure conditions (0.4-0.8 GPa).

3.2.4. Forward thermodynamic modeling or phase diagram approach

A “pseudosection” is a phase diagram showing the stability fields of different mineral assemblages for a specific bulk-rock composition (e.g., Powell & Holland, 1988; Spear & Menard, 1989). Pseudosection modeling allows calculating points by coexisting phases, their modes and composition, with the possibility to constrain petrographic and microstructural observations and directly link the main assemblage in equilibrium observed to certain *P-T* conditions. An interesting tool of pseudosection modeling is the possibility to plot compositional isopleth for one or more phases in the *P-T* field, which can be compared with results from classical geothermobarometry.

The *P-T* conditions were estimated using the isochemical phase diagrams approach calculated using Theriak–Domino software (De Capitani & Brown, 1987; De Capitani & Petrakakis, 2010). Mineral compositions and quantitative micro-mapping (X-ray maps) were obtained with a JEOL JXA 8200 electron probe micro-analyzer (EPMA) located in the Institute of Geological Sciences at the University of Bern, Switzerland, following the procedure described by Lanari et al. (2017).

Bulk composition strongly influences the predicted phase diagram topology and phase proportions/compositions in an equilibrium assemblage (e.g., Stüwe & Powell, 1995). Different methods exist for determining a bulk composition. The bulk composition for modeling was determined using an X-ray map of a representative area of the thin section.

The program XMapTools 4 (Lanari et al., 2014) was used to process compositional maps, including (i) classification, (ii) analytical standardization, (iii) structural formulae calculation and (iv) distinction of compositional groups. Local bulk compositions were generated from the oxide weight-percentage maps by averaging pixels with a density correction (Lanari & Engi, 2017). The *P-T* condition has been inferred with compositional isopleths thermobarometry.

3.2.5. U-(Th)-Pb geochronology in-situ on monazite

Monazite is a light rare earth element (LREE)-bearing phosphate mineral and a reliable geochronometer (e.g., Parrish, 1990). It is nowadays well known how monazite can record the timing of metamorphic processes for a wide spectrum of metamorphic conditions (Williams et al., 2007). Several contributions have pointed out the impressive resolution and importance of *in-situ* U-(Th)-Pb monazite dating, integrated with its chemical and microstructural characterization (see Kohn et al., 2017 for a detailed review). Before isotopic monazite dating, grain locations, internal features (e.g., inclusions) and their textural position were investigated through a scanning electron microscope hosted at the Department of Earth Sciences of the University of Torino (Italy). The further step was to analyze the chemistry and the zoning of each monazite crystal using the JEOL 8200 Super Probe electron microprobe hosted at the Department of Earth Sciences “A. Desio” of the University of Milano (Italy). Monazite chemistry and X-ray compositional maps are necessary to define the compositional zoning required for correctly interpreting monazite grains and relative ages. Monazite crystals were analyzed *in-situ*, on 30 µm-thick thin sections, by the Laser Ablation Inductively Coupled Plasma-Mass Spectrometry (LA-ICP-MS) at the University of Perugia (Italy). The instrumentation consisted of a Teledyne/Photon Machine G2 LA device equipped with a HelEx2 two-volumes cell and coupled with a Thermo-Fisher Scientific

quadrupole-based iCAP-Q ICP-MS. Monazite crystals were analyzed using a circular laser beam of 8-10 µm diameter, a frequency of 10 Hz and a laser density on the sample surface of ~3.5 J/cm^2. Oxide formations were checked on the NIST SRM 612 by monitoring and maintaining the ThO/Th ratio below 0.005.

The Delaware standard (424.9 ± 0.8 Ma; Aleinikoff et al., 2006) was used as a calibrator. The Moacir (or Moacyr, 507.7 ± 1.3 Ma (207Pb/^{235}U) and 513.6 ± 1.2 Ma (^{206}Pb/^{238}U); Gonçalves et al., 2016) and Manangotry (555 ± 2 Ma, Horstwood et al., 2003; 537 ± 14 Ma, Montel et al., 2018) monazites were used as quality controls. Data reduction has been performed in Iolite4 (Paton et al., 2011) utilising the VizualAge_UcomPbine data reduction scheme (Chew et al., 2014). All subsequent data processing and plotting were done with the software ISOPLOT (Ludwig, 2003).

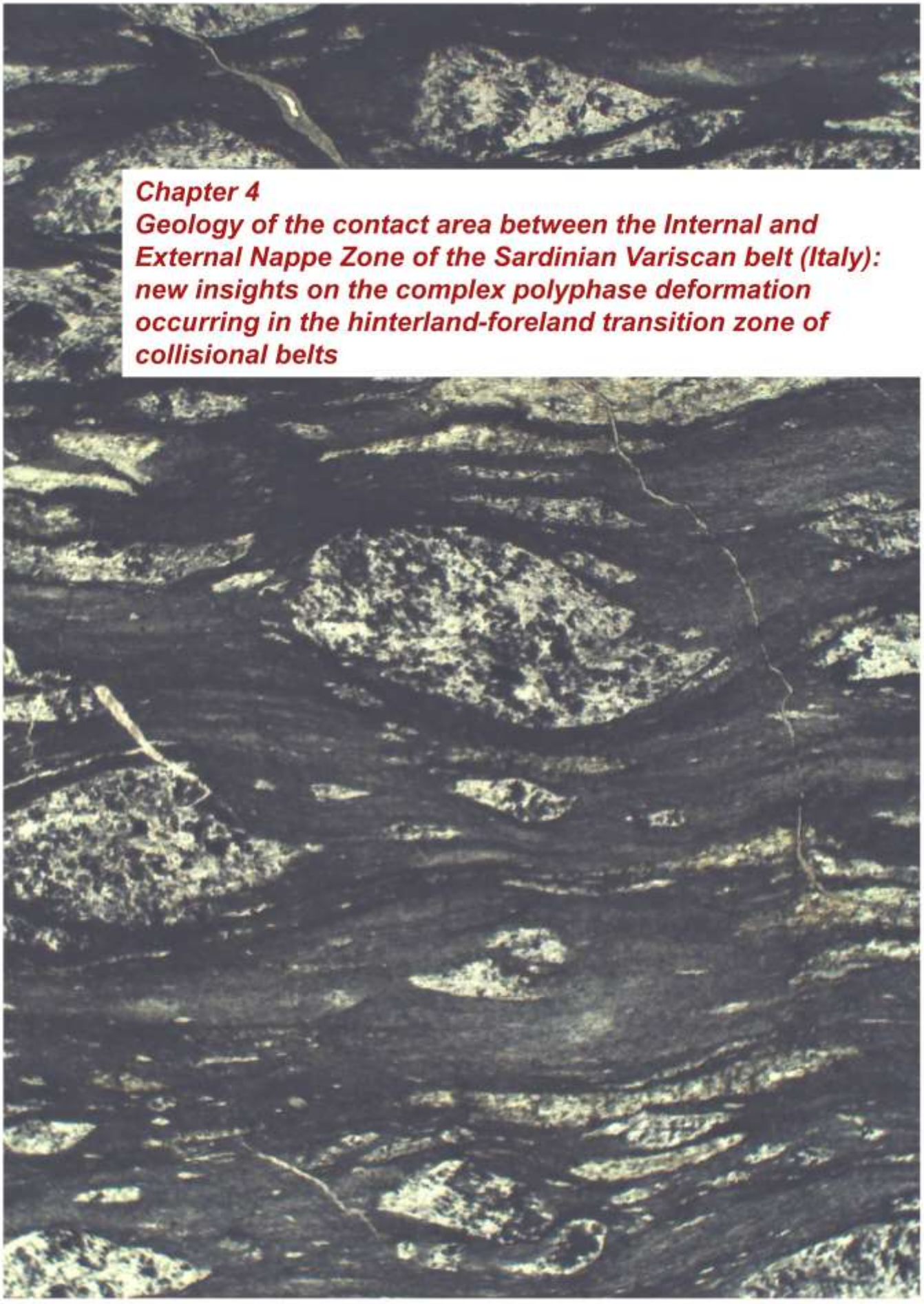

Chapter 4
Geology of the contact area between the Internal and External Nappe Zone of the Sardinian Variscan belt (Italy): new insights on the complex polyphase deformation occurring in the hinterland-foreland transition zone of collisional belts

4.1. Introduction

The hinterland-foreland transition zone, forming a fold-and-thrust belt, is generally characterized by large-scale nappe stacks with different generations of superimposed folds and cleavages that complicate understanding the structural architecture (Thigpen et al., 2010, 2013; Sarkarinejad & Ghanbarian, 2014; Montomoli et al., 2018; Ghosh et al., 2020). Nappe boundaries are often marked by the presence of regional-scale contractional (thrust-sense) ductile shear zones that accommodate large displacements and control the growth of orogenic wedges (Grasemann et al., 1999; Ring & Brandon, 1999; Thigpen et al., 2010; Ghosh et al., 2020). Several difficulties in unraveling the tectono-metamorphic evolution of the hinterland-foreland transition zone arise from the overprinting of post-nappe stacking deformation that modifies the original attitude of pre- and syn-nappe stacking elements (e.g., secondary foliations, tectonic contacts, folds vergence). Untangling the geological complexity derived from the geological survey and outcrop observation requires microstructural analysis (e.g., Carosi et al., 2016; Papeschi et al., 2020; Caso et al., 2021). Chapter 4 provides a new 1:10.000 scale geological map (Main Map published in Petroccia et al., 2022b) supported by meso- and microstructural data. The excellent exposures of both rocks and structures make this sector of the Sardinian belt a fundamental area to unravel the complex polyphasic history that occurred during the Variscan pre-, syn- and post-nappe stacking deformation.

4.2. Investigated area and methods

The study area (Fig. 4.1) is in the Barbagia region in the southwestern sector of the Lago Alto del Flumendosa in central Sardinia and covers an area of ~20 km^2. It is represented by the structurally upper Barbagia Unit (BU, Internal Nappe Zone) overthrust on the Meana Sardo Unit (MSU, External Nappe Zone). Here, a well-exposed mylonitic zone marking the contact between the Internal and External nappes; i.e., the Barbagia Thrust (BT), has been investigated and mapped. The BT and all previous structural elements (e.g., F_2 folds, S_2 foliation) were subsequently refolded by an upright kilometre-scale antiform, the Gennargentu Antiform (Fig. 4.1). The investigated sector is located in its southern limb (Fig. 4.1), where previous F_2 folds change their attitude and F_2 axial planes dip towards the S-SW and not to the hinterland or N-NE (Carosi et al., 2004; Montomoli et al., 2018). New 10 m contour lines have been obtained using the DTM TINITALY/01 (Tarquini et al., 2007) with 10 m-cell size m grid resolution, integrated into a WGS 84, UTM 32N GIS spatial database to derive a Hillshade map. The geological map has been realized at 1:10.000 scale.

To better document the distribution of the metamorphic basement, quaternary deposits have not been provided in the resulting map. The mapping workflow includes (i) mapping of both lithologies and structures; (ii) measurement of structural elements: (S) for syn-metamorphic surfaces or axial plane foliation; (A) for fold axes; (L) for object lineations; (F) for folds; and (D) for the deformation phases; and (iii) microstructural analysis on oriented thin sections, cut parallel to the object lineation and perpendicular to the main foliation (approximating the XZ plane of the finite strain ellipsoid). A numerical progression in the description of deformation phases, besides the primary bedding S_0, has been used (e.g., S_1, S_2). All the collected structural elements have been plotted in equal-area stereo diagrams in the lower hemisphere.

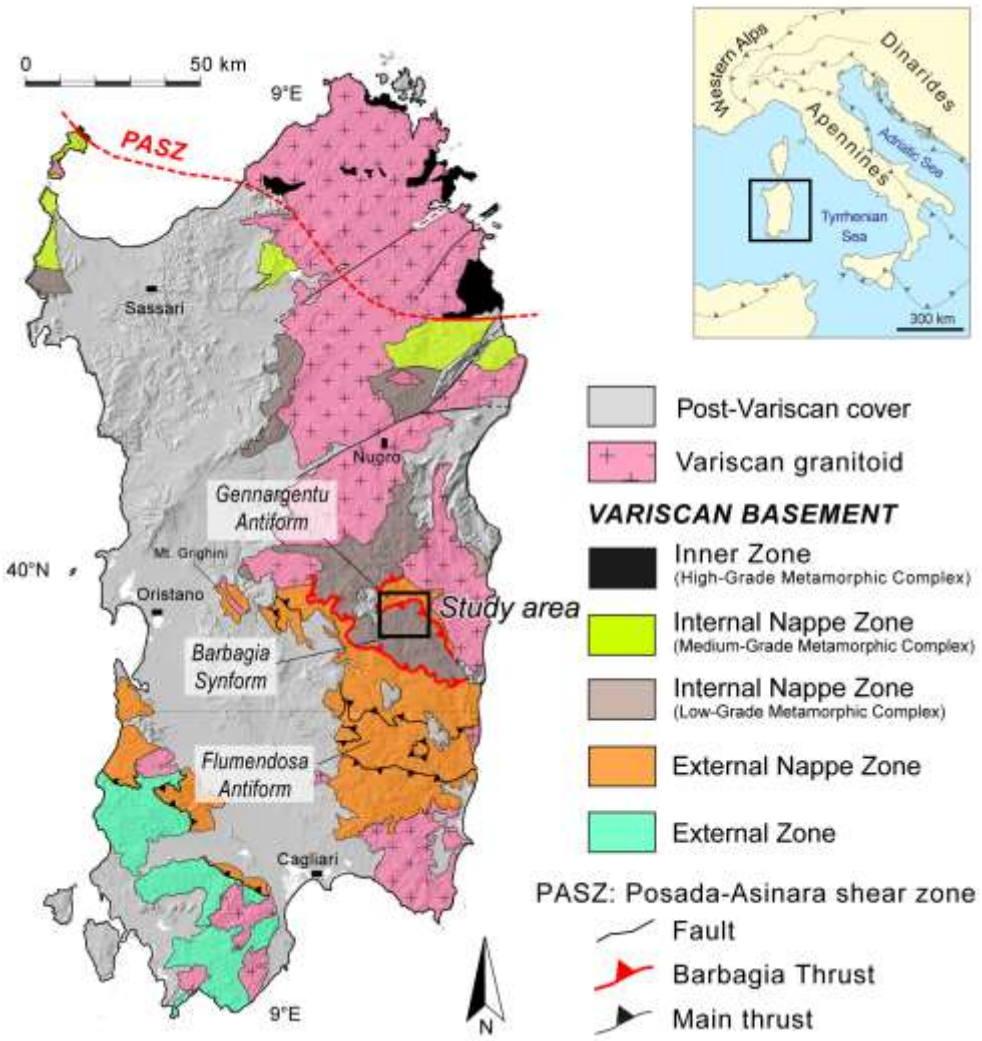

Figure 4.1: Tectonic sketch map of the Sardinia island (modified after Montomoli et al., 2018; Carosi et al., 2020).

4.3. Lithostratigraphy

The BU succession, belonging to the Internal Nappe Zone (Fig. 4.2; also known as 'Postgotlandiano'; Vai & Cocozza, 1974), has been mapped as a single metasedimentary formation (Filladi Grigie del Gennargentu Fm., Fg; see Main Map published in Petroccia et al., 2022b). It is constituted by quartzitic and micaceous metasandstone alternating with metasiltstone and quartzite interbedded with grey phyllite. Sometimes, close to the BT, a thin and not mappable layer of porphyroids has been recognized. The protolith age was referred from Cambrian to Ordovician (Carmignani et al., 1994; Pertusati et al., 2002). The MSU, belonging to the External Nappe Zone, begins with a basal silicoclastic succession (Fig. 4.2; Arenarie di Solanas-San Vito Fm., Sv; Calvino, 1959; Barca et al., 1988), dated from Middle Cambrian to Lower Ordovician (Di Milia & Tongiorgi, 1993). It is made by alternating fine- to coarse-grained metasandstone, grey-green metasiltstone, and meta-argillite, with thickness varying from cm- to m-scale. The succession continues with volcanic rocks belonging to the Monte Santa Vittoria Fm. (Ms; Carmignani et al., 2001). This formation includes three lithostratigraphic units that were previously informally defined by Minzoni (1975), including the Manixeddu, Monte Corte Cerbos, and Serra Tonnai formations (Carosi et al., 2004). It is mainly represented by metaconglomerate, metavolcanoclastite, grey-green metarhyolite, green metabasalt and dacitic metaignimbrite. The age of the protolith is ~460 Ma (Middle-Upper Ordovician) based on radiometric analyses (Pavanetto et al., 2012), confirming previous stratigraphic ages (Carmignani et al., 1994). A change from volcanic to siliciclastic rocks is testified by the presence of Upper Ordovician terrigenous formation (Orroeledu Fm., Or; Loi, 1993; Loi & Dabard, 1997). It consists of metarkose, metagraywacke and phyllite with quartz-sericite-chlorite matrix. These metasediments locally contain interbedded basic to intermediate metaepiclastite. The youngest lithological unit is made by black graphitic shale with interbedded metalimestone layers (Scisti a Graptoliti Fm., Sg) that are Silurian to Lower Devonian in age (Barca & Jäger, 1989; Gnoli, 1993; Corradini et al., 1998). The post-Variscan magmatic rocks are made by northwest-trending rhyolitic to rhyodacitic aplitic dykes (α; Upper Carboniferous-Permian; Carmignani et al., 2001). They contain phenocrysts of quartz, feldspar, and plagioclase, as well as aggregates of biotite crystals within a fine-grained groundmass. The Triassic-Jurassic rocks are recognizable in the Perda et Liana inselberg. They are characterized by dolostone, which is typically massive and structureless, alternating shale and dolomitic limestone, quartzitic sandstone and conglomerate (Triassic-Jurassic Genna Selole and Dorgali Fm., C; Costamagna & Barca, 2004).

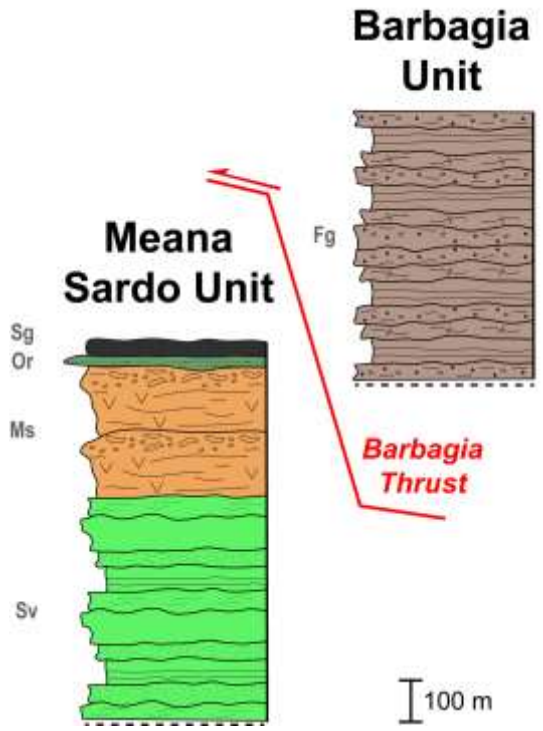

Figure 4.2: Lithostratigraphic column of the Meana Sardo Unit and the overlying Barbagia Unit.

4.4. Structural analysis

Based on overprinting criteria and structures observed from meso- to microscale, four ductile deformation phases heterogeneously distributed in both units have been defined. The original bedding (S_0; Fig. 4.3a) is only recognizable as a compositional alternation or dismembered lens-shaped fragments in sectors where a strong lithological contrast, e.g., quartz layers within a metasandstone matrix, is present. Due to the strong transposition related to the D_2 phase in the investigated area, it is nearly impossible to identify fold systems associated with the D_1 phase. The D_1 structural elements are well recognizable, mainly in the MSU, far from the BT. S_1 foliation can be identified in the hinge zone of the F_2 folds or as meso- and microscale microlithons (Figs. 4.3b, c). In thin section, the S_1 is marked by syn-kinematic recrystallization of white mica, chlorite, quartz, calcite, opaque minerals and rare albite (Fig. 4.3d). The intensity of strain increases toward the BT, as does the mylonitic foliation. It is worth noting that the frequency of the occurrence of the D_1 structures decreases approaching the BT, due to the D_2 overprinting. Structures related to the D_2 phase are tight to isoclinal, overturned to recumbent folds, and developed from micro- to map-scale.

The interlimb angles of F_2 folds range from 60° to ~2° (close to sub-isoclinal; Fig. 4.3e) and vary from gently inclined to recumbent. F_2 folds generally show rounded and thickened hinges with stretched limbs (class 2 of Ramsay, 1967), which can be classified as B5, according to Hudleston (1973). F_2 folds show an S_2 foliation parallel or sub-parallel to the relative fold axial planes, and it generally represents the main foliation at the outcrop-scale. The strike of the S_2 foliation is quite constant, ranging from E-W to NW-SE with scattered values (Fig. 4.3d). A_2 fold axes show a main E-W trend gently plunging toward both E and W, with quite scattered values (Fig. 4.3e). A N-S or NE-SW trend of the L_2 object lineation on the S_2 foliation is recognizable (Fig. 4.3d). The F_2 fold axes are nearly perpendicular to the L_2.

In the MSU metavolcanic rocks, the principal anisotropy is a continuous and pervasive S_2 foliation. In the metapelite and metasandstone, the S_2 can be generally classified as a gradational to discrete spaced crenulation cleavage. Far from the tectonic contact, the S_2 is mainly associated with pressure solution and reorientation of pre-existing tabular grains (Fig. 4.3c). Moving toward the BT, the S_2 becomes a mylonitic continuous foliation (Fig. 4.3d) associated with the blastesis of white mica + chlorite. The D_3 phase is characterized by meso- to macroscopic scale, E-W trending F_3 folds that overprint and refold all previous structural elements (Figs. 4.3f, g). A_3 fold axes (Fig. 4.3f) generally trend parallel to the A_2 ones and perpendicular to the L_2 object lineation. The F_3 structures are gentle to open S-SE verging upright to steeply inclined parallel or asymmetric folds with centimetric (Fig. 4.3f) to pluri-metric long wavelength. Locally, kink-type folds occur. In the F_3 hinge zones and only in less competent rocks, the S_3 axial-plane foliation is represented by a spaced, disjunctive cleavage. No metamorphic mineral assemblage related to this phase has been observed, whereas the main deformation mechanism is pressure solution and reorientation of pre-existing grains. D_3 folds affect all previous structural elements, determining the variation of the axial plane dipping of the F_2 folds. The studied sector is indeed located in the southern limb of one of these regional-scale folds (i.e., Gennargentu Antiform), where F_2 folds display S-SW dip of the axial plane and not toward the N-NE as well explained by previous knowledge (Carosi et al., 2004; Montomoli et al., 2018). Thus, all F_2 folds display a S-SW vergence, but they are anticlinal synforms and synclinal antiforms (see the Main Map published in Petroccia et al., 2022b). The last D_4 phase is associated with gentle to open folds, with sub-horizontal axes and axial planes (Fig. 4.3h). Locally, some minor-scale kink-folds occur. No axial plane and metamorphic mineral assemblage related to the D_4 phase has been observed. A late brittle deformation with N-S striking faults has been recognized.

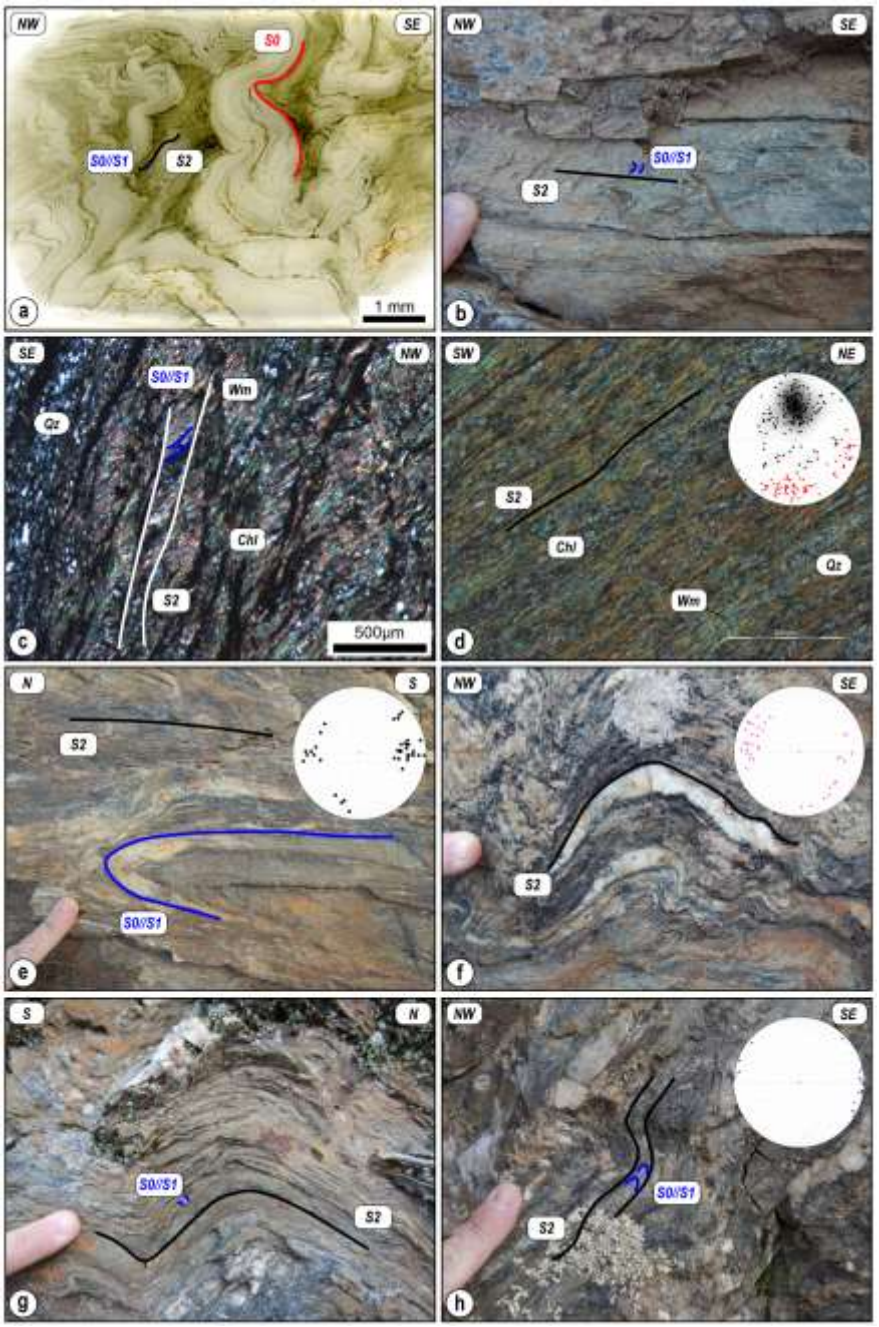

Figure 4.3: Outcrop and microscale view of the main structural features. The structural equal-areal projections (lower hemisphere) of the S_2 poles and L_2 (d), A_2 (e), A_3 (f) and A_4 (h) axes are shown. a) Microscopic evidence of S_2 gradational crenulation cleavage. S_0 bedding and S_1 foliation, parallel to S_0, are also present; b, c) S_2 spaced foliation at both meso- and microscale (XPL). In the thin section, S_1 is marked by Wm + Chl; d) fine continuous S_2 foliation is defined by Wm + Chl (XPL); e) F_2 fold, deforming the S_0//S_1 foliation in metasedimentary rocks belonging to the BU; f, g) F_3 folds, deforming the S_2 foliation in metasedimentary rocks belonging to the MSU. No clear S_3 axial-plane foliation in the F_3 hinge zone is recognizable; h) late open folds (F_4) with sub-horizontal axes and axial planes deforming S_2 spaced foliation.

4.4.1. The Barbagia Thrust

In the mapped area, the BT is characterized by a hm-thick mylonitic zone. The BT-related structures (D_2) overprint both metasedimentary and metavolcanic or metavolcanoclastic rocks of the MSU and metasandstone, metasiltstone, and metapsammite of the BU. In both units, a variation in structural style moving toward the BT across the deformation gradient is recognizable. The intensity of deformation increases toward the BT, where folds become tighter and lineation more pervasive; contemporaneously, the spacing between foliation domains decreases. Approaching the high-strain zone, the mylonitic foliation obliterates the previous D_1 structures, thus they are rarely detectable. Kinematic indicators, including *C*-*C'*-S fabric and asymmetric porphyroclasts of quartz or feldspar indicating a general top-to-the S-SW sense of shear with local variation to SE have been recognized (Fig. 4.4a).

Sheared metavolcanic rocks belonging to MSU are characterized by a progressive grain-size reduction and a transition from mylonite to ultramylonite along a deformation gradient towards the centre of the shear zone (Fig. 4.4b). The foliation wraps around rotated plagioclase and feldspar porphyroclasts. Feldspar shows undulose extinction and rare flame perthite. In ultramylonite, quartz recrystallization mechanism could not be detected due to its extremely small grain size and phase-mixing with mica.

In metasedimentary rocks from both nappes, the intensity of deformation increases going toward the BT. The spacing between foliation domains decreases, and at the same time, the foliation varies from a spaced/disjunctive cleavage to a continuous cleavage (Fig. 4.3c). Mylonitic foliation is defined by elongated quartz grains and phyllosilicate-rich levels. Phyllosilicate layers are dominated by chlorite + white mica. In the farthest samples from the BT, quartz shows a strong undulose extinction, deformation bands, small new grains and rare brittle deformation features. These structures indicate that bulging (BLG) is the main dynamic deformation mechanism (Stipp et al., 2002; Law, 2014). However, quartz often shows elongated sub-grains with new quartz grains of smaller size surrounding larger ones, generating a bimodal grain size, indicating the presence of subgrain rotation recrystallization (SGR) mechanism.

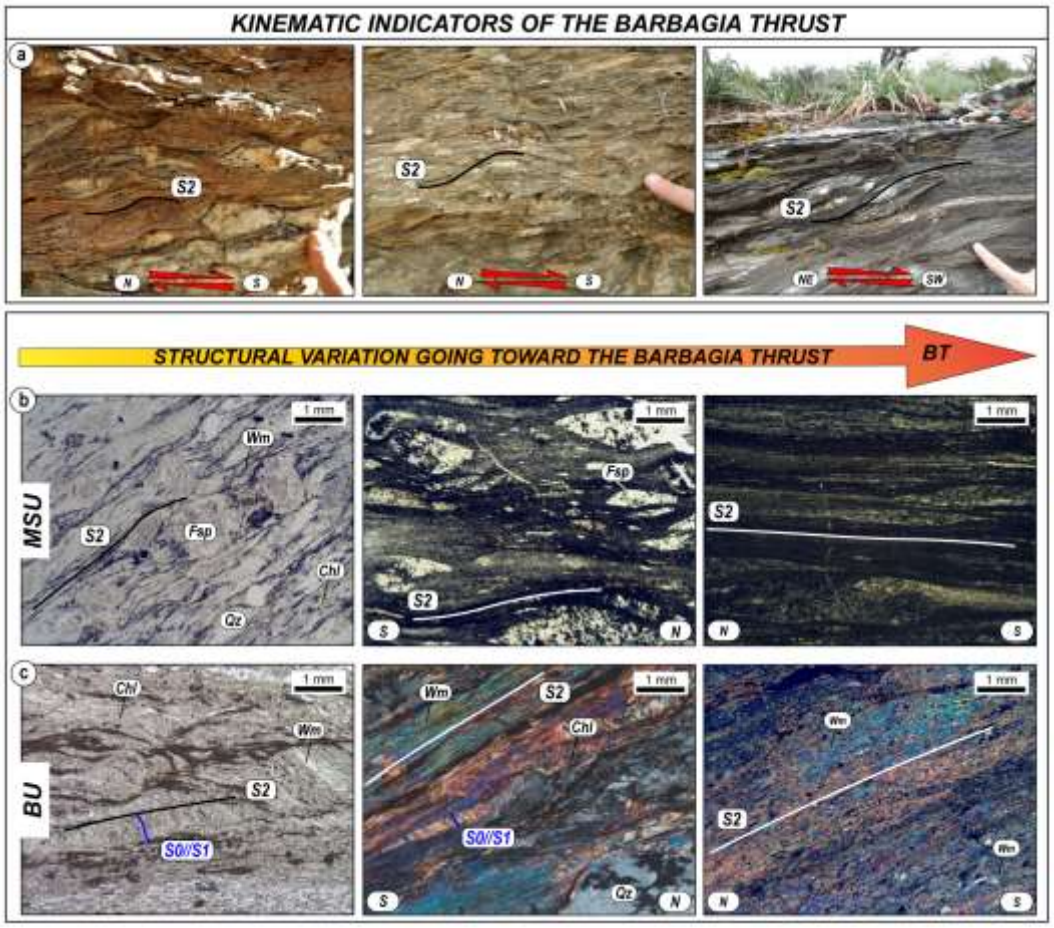

Figure 4.4: a) Mesoscopic kinematic indicators of mylonites belonging to the Barbagia Thrust indicating a top-to-the S-SW sense of shear; b, c) structural variation going toward the Barbagia Thrust in both units: b) variation from mylonites (on the left) to ultramylonites (on the right) in metavolcanic rocks belonging to the MSU; c) progressive variation of the foliation from spaced cleavage to a continuous cleavage moving toward the Barbagia Thrust in metasedimentary rocks.

4.5. Final remarks

The new geological map at 1:10.000 scale is the most detailed, currently available representation of the geo-structural setting of this sector of the Nappe Zone in the Sardinian Variscan belt. Two juxtaposed units have been distinguished: the lower one represented by the MSU and the upper one testified by the BU. The contact in between, the BT (Carosi & Pertusati, 1990; Carosi & Malfatti, 1995; Montomoli et al., 2018), is marked by a pluri-m-thick mylonitic zone affecting both units.

Detailed mapping, coupled with multi-scale structural observations, allowed the definition of a polyphase evolution (Fig. 4.5), consisting of three ductile deformation phases developed under a contractional tectonic regime and the fourth one under extensional conditions.

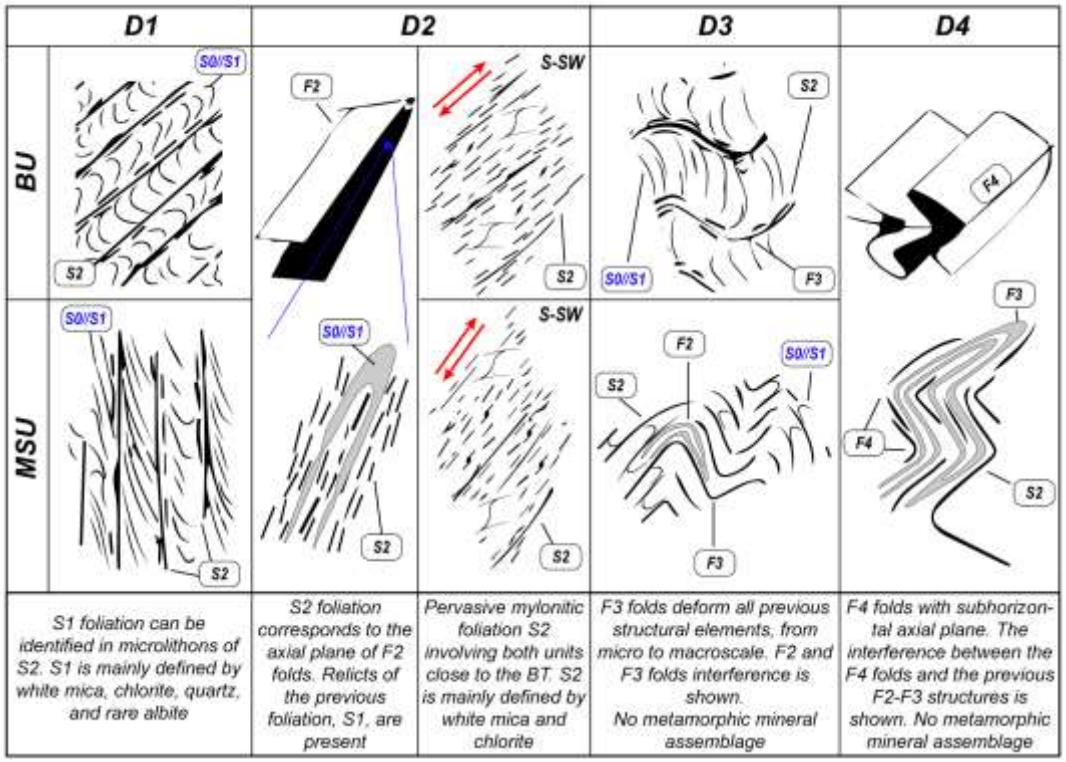

Figure 4.5: Synoptic reconstruction of the field and microstructural investigations of the deformation history of the Barbagia and Meana Sardo units.

The D_1 tectonic phase is associated with greenschist-facies paragenesis. In the study area, these structures were obliterated during the D_2 phase and, therefore, it is not possible to constrain with precision their kinematics and geometry. According to Carosi et al. (2004), the D_1 phase can be related to the early stage of collision. The prominent deformation phase (D_2) is responsible for the development of the main foliation (Fig. 4.6a), pervasive at all scales (S_2). It becomes more mylonitic moving toward the BT and displays several kinematic indicators with a main top-to-the S-SW sense of shear (Fig. 4.6a). Indeed, an increase in the strain gradient moving from the structurally higher parts of the BU and the structurally lower parts of the MSU toward the BT high-strain zone has been detected. The S_2 foliation is marked by greenschist-facies mineral assemblage (Wm + Chl). Both BLG and SGR mechanisms have been detected (Stipp et al., 2002; Law, 2014).

The presence of MSU and BU highly sheared rocks deformed under non-coaxial mylonitic conditions (Fig. 4.6b) and the emplacing of the MSU and BU with a top-to-the S-SW sense of shear during the N-S shortening agree with previous investigations (e.g., Conti et al., 2001; Carosi et al., 2004; Montomoli et al., 2018).

The D_2 phase is linked to the syn-nappe stacking and exhumation of the BU (Montomoli et al., 2018). After the crustal thickening and the nappe-stacking evolution, all the previous structural elements are widely deformed by weakly asymmetric to upright D_3 folds (Fig. 4.6a). Folds show nearly-vertical axial planes, and therefore no clear transport direction can be associated with this event. However, if we admit that the shortening direction had to be perpendicular to the axial planes and to the trend of fold axes, the D_3 phase had a similar shortening direction to the D_2. Restoring the original pre-Gennargentu Antiform attitude of the D_2 fold structures detected in the investigated area, F_2 shows a SW-S verging anticlinal antiforms and synclinal synforms, highlighting a top-to-the S-SW sense of transport. This also agrees with the S-SW sense of shear and the fold polarity detected within the Monte Santa Vittoria area, in the southern limb of the Barbagia Synform (Carosi et al., 2004; Montomoli et al., 2018). Thus, the presence of the BT mylonitic zone in the different sectors of the Barbagia Synform, with the same structural and kinematic features and the similar shortening direction between the D_2 and D_3 phase, confirms the post-nappe stacking folded structure. This architecture, in agreement with the model of Conti et al. (1999) and Carmignani et al. (1994), emphasizes the presence of large-scale structures acquired in a contractional setting during the late deformation stage of crustal thickening and not during the late orogenic extension. Also, the lack of metamorphic mineral growth during the D_3, is consistent with the coupling of BU with MSU under greenschist-facies conditions (D_1 and D_2) and a subsequent antiformal stacking during the regional horizontal shortening under upper-crustal conditions (D_3). During the orogenic extensional phase (D_4), folds with sub-horizontal axial planes (F_4) are recognizable. This geometry suggests the gravitational collapse of the thickened orogen. Different authors (Carmignani et al., 1994; Conti et al., 1999, 2001) highlighted the presence of low- to high-angle normal faults in correspondence of the antiforms limbs displaying an opposite sense of shear and leading to tectonic unroofing of the antiformal hinge zones. However, no clear BT-parallel extensional structures overprinting BT-related mylonite have been observed in the investigated area.

As a whole, the polyphase history recorded in this sector of the Nappe Zone in Sardinia summarized in this study, highlights the complex tectonic history that occurred during the evolution of an orogenic wedge. In particular, this area records a pre-, syn- to post-nappe stacking evolution developed under contractional conditions and a late-extensional deformation.

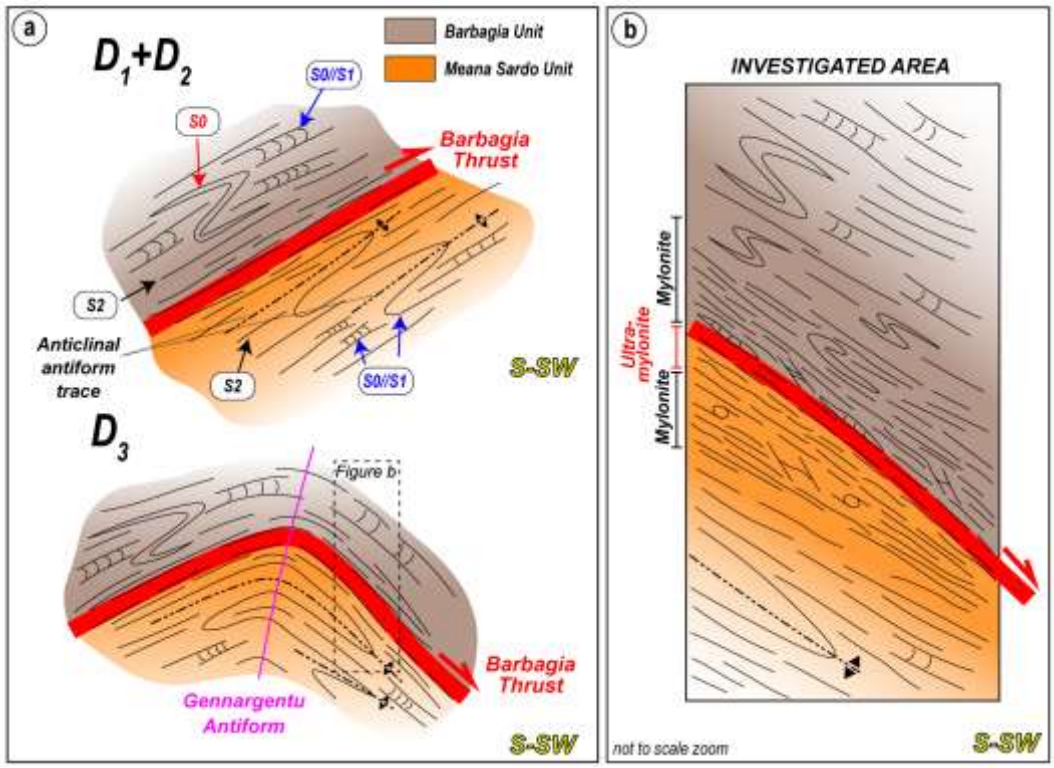

Figure 4.6: Sketch of the structural evolution derived from the obtained data. a) Structural features of the pre-, sin- and post-nappe stacking deformation under compressive conditions (D_1, D_2, D_3); b) simplified and not to scale structural features of the investigated sector. Far from the mylonitic zone, pre-D_2 structures are well-recognizable. The prominence of mylonite and, only in Meana Sardo Unit, ultramylonite, characterizes the high-strain zone of the Barbagia Thrust. The presence of S-SW dipping of the axial plane of F_2 folds due to the D_3 folding event has been highlighted.

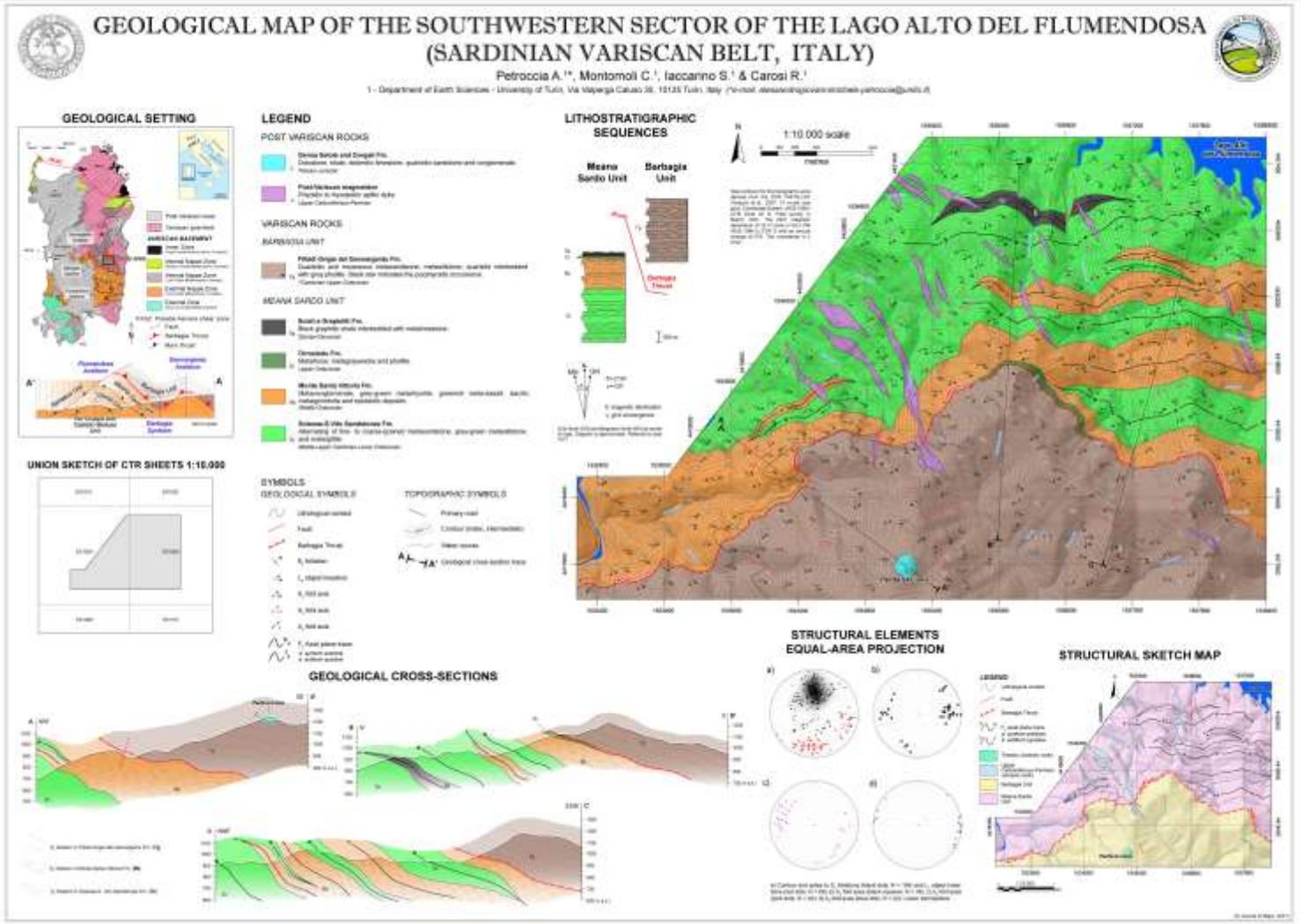
GEOLOGICAL MAP OF THE SOUTHWESTERN SECTOR OF THE LAGO ALTO DEL FLUMENDOSA
(SARDINIAN VARISCAN BELT, ITALY)
Petroccia A.[1]*, Montomoli C.[1], Iaccarino S.[1] & Carosi R.[1]
1 - Department of Earth Sciences - University of Turin, Via Valperga Caluso 35, 10125 Turin, Italy (*e-mail: alessandragiovanna.petroccia@unito.it)
GEOLOGICAL SETTING
LEGEND
POST VARISCAN ROCKS
VARISCAN ROCKS
BARBAGIA UNIT
MEANA SARDO UNIT
LITHOSTRATIGRAPHIC SEQUENCES
Meana Sardo Unit
Barbagia Unit
1:10.000 scale
UNION SKETCH OF CTR SHEETS 1:10.000
SYMBOLS
GEOLOGICAL SYMBOLS
TOPOGRAPHIC SYMBOLS
GEOLOGICAL CROSS-SECTIONS
STRUCTURAL ELEMENTS
EQUAL-AREA PROJECTION
STRUCTURAL SKETCH MAP

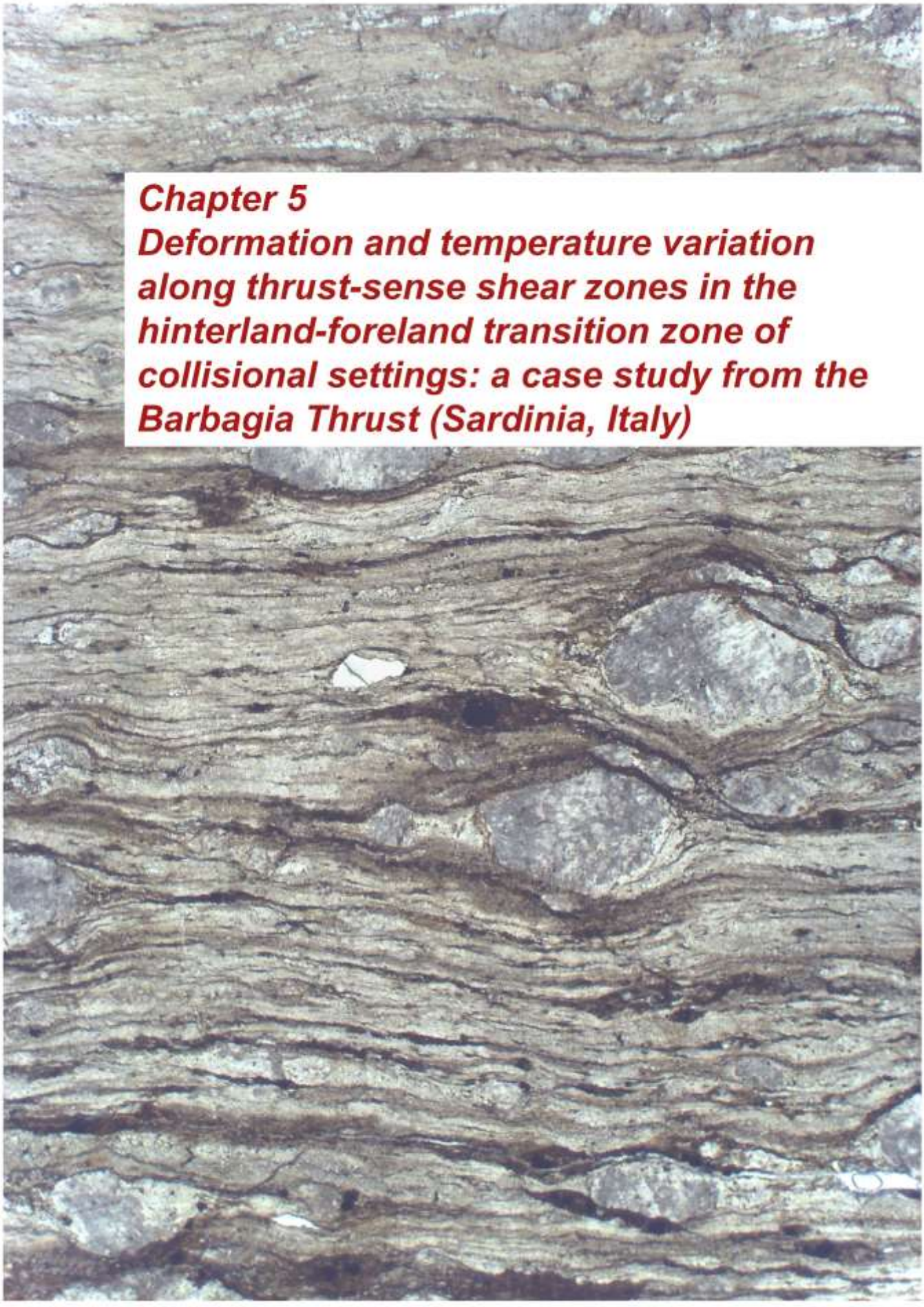

Chapter 5
Deformation and temperature variation along thrust-sense shear zones in the hinterland-foreland transition zone of collisional settings: a case study from the Barbagia Thrust (Sardinia, Italy)

5.1. Introduction

Hinterland-foreland transition zones are characterized by the presence of mylonitic rocks along km-scale ductile shear zones linked to thrust-sense shear zones, which lead to the formation of thrust sheets or tectonic nappes. Classically, these zones have been associated with a simple shear-dominated deformation (e.g., Coward & Kim, 1981; Mitra, 1994; Seno et al., 1998; Yonkee, 2005). However, quantitative studies have shown that the ductile deformation in the thrust-sense shear zone involves a significant component of pure shear deformation (e.g., Simpson & De Paor, 1993; Grasemann et al., 1999; Ring & Brandon, 1999; Bailey et al., 2007; Ring & Kumerics, 2008; Law et al., 2021). Therefore, shear zones in dynamics orogenic wedge settings require a quantitative assessment of the kinematic vorticity (Xypolias, 2010; Thigpen et al., 2010, 2013; Fossen & Cavalcante, 2017; Ghosh et al., 2020, Simonetti et al., 2020a, b).

Several processes can potentially be responsible for the dynamic weakening and strain localization in the crust, including (i) shear heating (e.g., Brun & Cobbold, 1980; Molnar & England, 1990; Camacho et al., 2001; Burg & Schmalholz, 2008; Thielmann & Kaus, 2012; Platt, 2015, 2018; Regenauer-Lieb et al., 2015), (ii) fabric development (e.g., Montési, 2013), and (iii) grain-size reduction by cataclasis or dynamic recrystallization (e.g., Montési & Zuber, 2002; Handy et al., 2007; Platt & Behr, 2011). Among them, thermal weakening (Takeuchi & Fialko, 2012; Willis et al., 2019), linked to shear heating, has been regarded as one of the main mechanisms in localizing deformation and for the development of shear zones (e.g., Schott et al., 2000; Thielmann & Kaus, 2012; Duretz et al., 2014). This mechanism is particularly applicable to the middle crust close to the brittle/ductile transition (e.g., Hirth et al., 2001; Behr & Platt, 2014; Platt, 2015). Thus, establishing the thermo-kinematic setting of shear zones is crucial because it is one of the most effective ways to test theoretical models of orogen tectono-metamorphic evolution against field observations (e.g., Sanderson, 1982; Ring et al., 2001; Law et al., 2004; Waters et al., 2018; Iaccarino et al., 2020; Thigpen et al., 2021).

Several works have used a multidisciplinary approach to unravel the deformation, structural, and thermal gradients of a region and, in turn, discriminate marginal and central areas within high-strain shear zones (Xypolias, 2010; Ring et al., 2015; Carosi et al., 2020; Grujic et al., 2020; Simonetti et al., 2020a, b, 2021). Field-based studies, combined with vorticity and kinematic analysis, are key for exploring shear zone evolution. There are several analytical techniques to determine both the kinematic vorticity and the deformation temperature in mylonitic rocks.

Whereas kinematic vorticity estimation can be generally obtained from all kinds of deformed rocks, low-grade metasedimentary sequences in the hinterland-foreland transition zone contain mineralogical assemblages that are not always suitable for conventional thermometric techniques.

The Raman Spectroscopy on Carbonaceous Material (RSCM; Beyssac et al., 2002, 2003, 2004) is based on the progressive transformation of carbonaceous material (CM) to graphite with increasing temperature. RSCM has generally been used as a geothermometer to determine the peak temperature reached during burial or tectonic thrust stacking (Chen et al., 2011; Scharf et al., 2013; Vitale Brovarone et al., 2013; Bellanger et al., 2015; Molli et al., 2018; Berger et al., 2020; Pérez-Cáceres et al., 2020; Montmartin et al., 2021; Nibourel et al., 2021), during contact metamorphism (Aoya et al., 2010; Mori et al., 2017; Beyssac et al., 2019; Skrzypek, 2021) or during frictional heating along fault planes after an earthquake (Fauconnier et al., 2014; Kaneki et al., 2016; Kuo et al., 2017, 2018; Nakamura et al., 2020; Muirhead et al., 2021). It is non-destructive and sensitive to thermal changes, enabling to constrain peak temperature in rocks from different geological contexts and metamorphic conditions (see Henry et al., 2019 for a complete review).

The hinterland-foreland transition zone of the Sardinian Variscan belt in Italy is a well-preserved low- to medium-grade Variscan basement that was not overprinted by subsequent Alpine orogenesis. It represents an excellent site to investigate a regional thrust-sense movement shear zone related to the nappe emplacement during the continental collision in the lower Carboniferous, i.e., the Barbagia Thrust (BT; Carosi & Pertusati, 1990; Carosi & Malfatti, 1995; Montomoli et al., 2018). The BT marks the boundary between the Internal and the External Nappe Zone of the Variscan belt, separating tectonic units with a complex history from tectonic units deformed at a higher structural level during the progressive propagation of deformation from the hinterland to the foreland (Montomoli et al., 2018). It played a critical role during nappe stacking and the exhumation of the crustal units. Few studies have addressed the BT structure, kinematics, and flow regime (e.g., Montomoli et al., 2018), and its thermal architecture is poorly understood.

5.2. Investigated areas and methods

To better constrain the structural architecture and thermal evolution of the BT, data have been collected in two thermally- and potentially kinematically-distinct sectors of the shear zone. The two investigated sectors, Area I and II, are located in the Barbagia region (central Sardinia), along with the northern and the southern limb of the Barbagia Synform (Figs. 5.1a, b, c). Area I and II are ~20 km apart.

The Internal Nappe Zone is represented by the structurally upper Barbagia Unit (BU), in the hangingwall (HW), overthrust on the Meana Sardo Unit (MSU), in the footwall (FW), belonging to the External Nappe Zone.

In this study, the thermo-structural evolution of the BT within the Nappe Zone has been investigated by combining detailed field observations, meso- and microstructural analysis, vorticity analysis, and finite strain estimations with a quantitative thermometric analysis by RSCM. Variations in both temperature conditions of shearing and magnitude of simple shear between these two domains allow us to examine any linkages and feedbacks between shear heating and thrust kinematics.

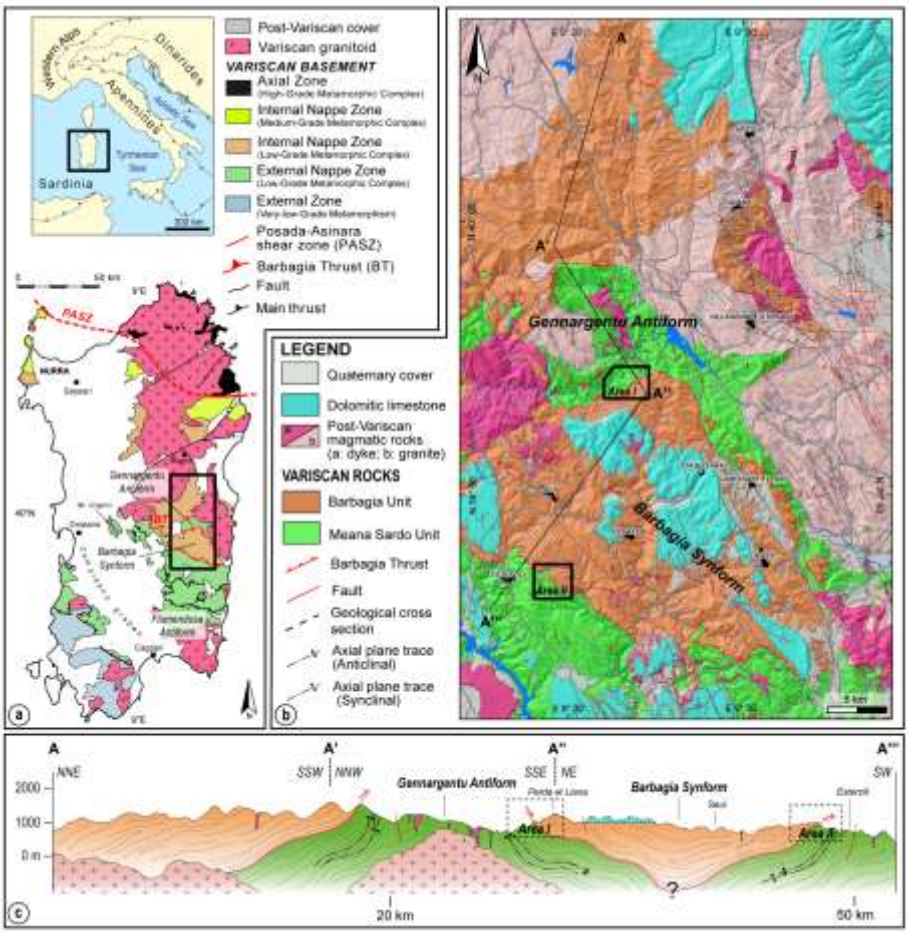

Figure 5.1: a) Geographic position and tectonic sketch map of the Sardinia island (modified from Carmignani et al., 1994). Location of Fig. 5.1b is indicated; b) schematic geological map of the Internal and External Nappe Zone in central Sardinia. The locations of Area I and Area II have been highlighted. The trace of the geological cross-section A-A''' is indicated (modified from Carmignani et al., 1994, 2016); c) geological A-A''' cross-section along the Internal and External Nappe Zone. The deep structure of the Barbagia Synform is uncertain. The horizontal and vertical exaggeration is for both 1.5:1.

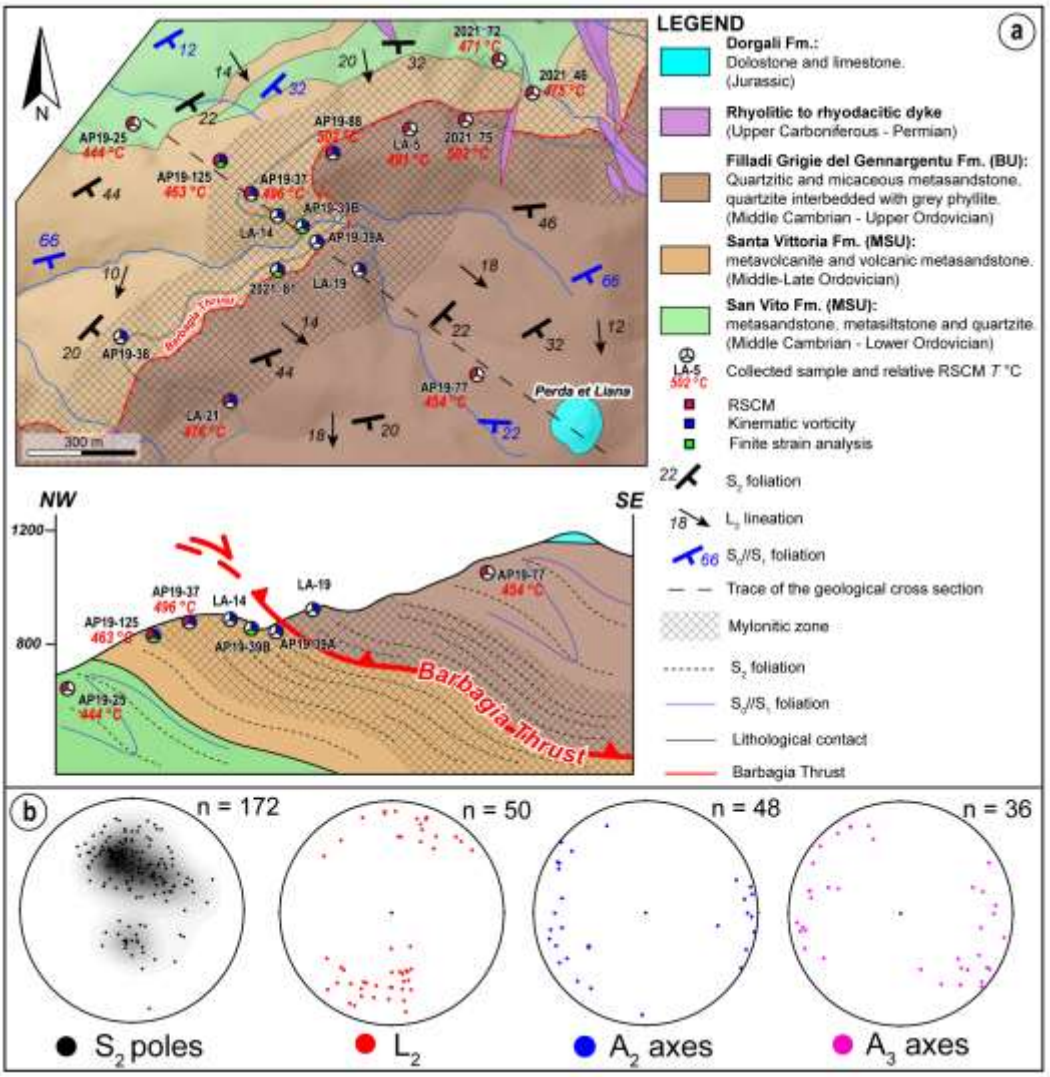

Figure 5.2: a) Geological map of Area I, derived from our original fieldwork and mapping. The trace of NW-SE oriented geological cross-section, shown below (the vertical exaggeration is 2:1), is indicated. On the cross-section the selected sample locations and the corresponding type of analysis are indicated; b) stereoplots (equal angle, lower hemisphere projections) of the main structural elements.

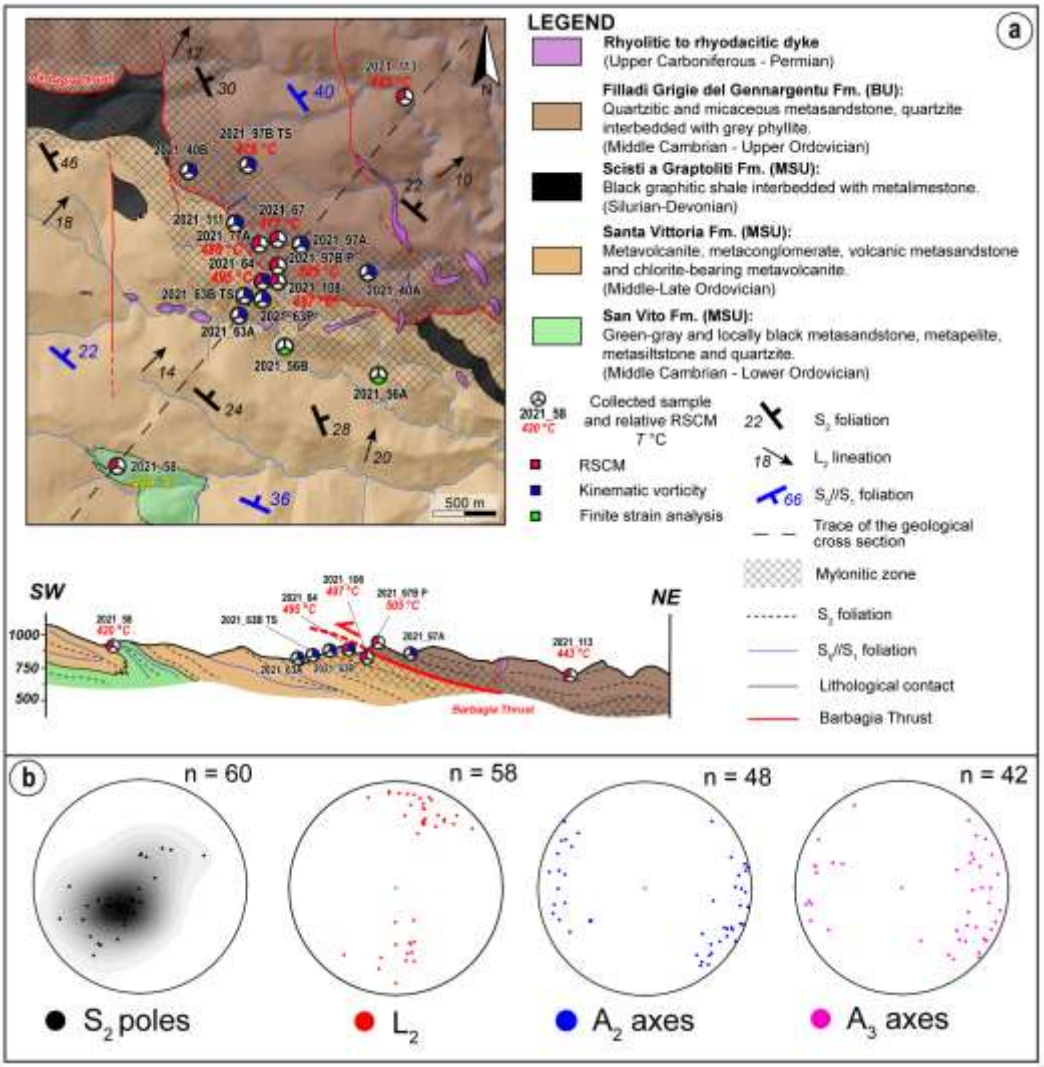

Figure 5.3: a) Geological map of Area II (modified and integrated from Carosi, 2004). The trace of the NW-SE oriented geological cross-section, shown below (no vertical exaggeration) is indicated. On the cross-section the selected sample locations and the corresponding type of analysis are indicated; b) stereoplots (equal angle, lower hemisphere projections) of the main structural elements.

5.3. Meso- and microstructural analysis results

In both Area I and II (Figs. 5.2a, b and 5.3a, b), four main phases of ductile deformation were observed based on overprinting criteria and structural observations from the meso- to microscale. Microstructural analyses were performed on field-oriented samples, cut perpendicular to the main foliation and parallel to the object lineation (approximating the XZ section of the finite strain ellipsoid). Folds have been described following Ramsay (1967). Dynamic deformation mechanisms for both quartz and feldspar have been described according to Pryor (1993), Piazolo & Passchier (2002), Stipp et al. (2002) and Law (2014). Foliations, kinematic indicators, and mylonites have been classified according to Passchier & Trouw (2005). Mylonite has been classified considering the percentage of the matrix as compared to porphyroclasts, varying from 50-90% for mylonitic rocks to more than 90% for ultramylonite. Mineral abbreviations are after Whitney & Evans (2010), except for white mica (Wm).

5.3.1. D_1 and D_2 deformation phases

Relicts of the original bedding (S_0) can be recognized as a compositional alternation or dismembered lentoid fragments only far from the BT (Figs. 5.4a). The D_1 phase is well-expressed far from the BT and mainly in FW. Fold systems related to the D_1 phase are only observed in Area II within the External Nappe Zone, far from the BT. They show a S-SW vergence and are moderately to strongly asymmetric. In most cases (Fig. 5.4b), the D_1 signature is represented by the S_1 foliation, parallel or at a moderate angle to the bedding (S_0). Often, due to complete transposition, it is nearly impossible to distinguish S_1 from S_0 (S_1//S_0). The S_1 can be recognized within the thickened hinges of F_2 folds and in microlithons (Figs. 5.4a, c). At the microscale, S_1 is a continuous foliation defined by syn-kinematic recrystallization of white mica (Fig. 5.4c), chlorite, quartz, calcite, opaque minerals, and rare albite. Moving toward the BT high-strain zone, a well-developed transposition of S_1, and rootless folds have been recognized.

Structures related to the D_2 phase are characterized by tight to isoclinal, overturned to recumbent folds (Fig. 5.4d), with a S-SW vergence, developed from micro- to map-scale. The interlimb angles of F_2 folds range from 60-2° (close to sub-isoclinal), and they generally show rounded and thickened hinges with stretched limbs (class 2 of Ramsay, 1967). The F_2 folds show an S_2 foliation parallel or sub-parallel to the relative fold axial planes, and it generally represents the main foliation at the outcrop-scale. S_2 mainly strikes E-W with both local NNW-SSE and NNE-SSW. In Area I, S_2 dips to the S with local variations toward the N due to late deformation (Fig. 5.2b), while in Area II, S_2 dips toward the N (Fig. 5.3b).

F_2 fold axes show the main E-W trend gently plunging with quite scattered values in both Area I and II. A well-visible N-S or NE-SW trend of the object lineation L_2 on the S_2 foliation is recognizable (Fig. 5.4e). The F_2 fold axes are nearly perpendicular to the L_2. Moving toward the BT, the main anisotropy gradually changes from a gradational to discretely spaced crenulation cleavage to a continuous S_2 foliation defined mainly by chlorite + white mica (Fig. 5.4f). The intensity of strain increases toward the tectonic contact, as does the mylonitic foliation. It is worth noting that the frequency of the occurrence of the D_1 structures decreases approaching the BT.

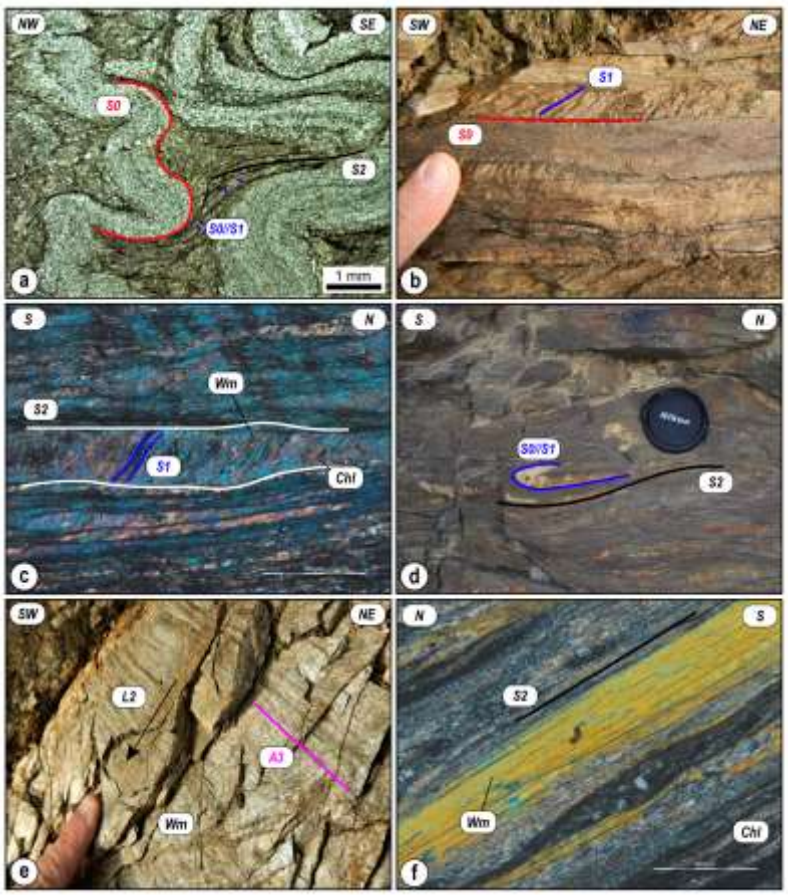

Figure 5.4: a) S_2 spaced foliation with S_0//S_1 preserved in microlithons. A relict of bedding (S_0), defined by the primary compositional alternation between quartz-rich and phyllosilicate-rich levels, is recognizable (PPL: parallel-polarised light) (San Vito Fm.; FW); b) selective S_1 foliation involving the S_0 compositional alternation in metasedimentary rock (Filladi Grigie del Gennargentu Fm.; HW); c) S_2 spaced foliation at the microscale. S_1 preserved in microlithons is defined by Wm + Chl (XPL: crossed-polarised light) (San Vito Fm.; FW); d) outcrop evidence of F_2 rootless fold. S_0//S_1 foliation is preserved in the hinge of F_2 folds. The S_2 cleavage is parallel to the F_2 axial plane (Filladi Grigie del Gennargentu Fm.; HW); e) L_2 object lineation, defined by Wm crystals and the intersection lineation, parallel to the A_3 fold axes, are displayed (San Vito Fm.; FW); f) S_2 fine-grained continuous foliation defined by Wm + Chl alternating with quartz-rich levels in metasedimentary rocks (XPL) (San Vito Fm.; FW).

5.3.2. The Barbagia Thrust

In both Area I and II, located along the northern and southern limb of the Barbagia Synform, the BT is characterized by a hm-thick mylonitic zone that shows a similar deformation pattern. The BT-related structures (D_2) overprint both metasedimentary and metavolcanic or metavolcanoclastic rocks of the FW and metasandstone, metasiltstone, and metapsammite of the HW (see the geological maps in Figs. 5.2a and 5.3a), transposing all previous structures. In the FW and HW of the BT, a variation in structural style moving toward the BT across the deformation gradient is present. The intensity of deformation increases toward the BT, where folds become tighter and lineation more pervasive; contemporaneously, the spacing between foliation domains decreases. Approaching the high-strain zone, the mylonitic foliation obliterates the previous S_1 foliation and microlithons. Although Area I and II are located in different sectors of the F_3 Barbagia Synform, they are characterized by the same shear sense.

Sheared metasedimentary rocks belonging to the FW (San Vito Fm.) and the HW (Filladi del Gennargentu Fm.) are characterized by a transition from a well-developed discrete smooth-spaced foliation with zonal cleavage domains (Fig. 5.5a) up to a continuous cleavage (Fig. 5.5b) approaching the BT. In samples from the high-strain zone, a penetrative continuous mylonitic foliation is found. The mylonitic S_2 foliation is defined by elongated quartz grains and phyllosilicate-rich levels, dominated by chlorite + white mica. Patchy undulose extinction and small new grains are recognizable in quartz. These structures suggest that bulging mechanisms (Fig. 5.5c; BLG II) with minor and local subgrain rotation recrystallization (Fig. 5.5d; SGR) are the main deformation mechanisms in quartz (Stipp et al., 2002; Law, 2014). Kinematic indicators with a top-to-the S-SW sense are represented by a meso- (Fig. 5.5e) and microscale *C'*-S fabric (Fig. 5.5f), asymmetric porphyroclasts and rare asymmetric displacement-controlled strain fringes around rigid objects, mainly constituted by pyrite. In the FW, metavolcanic and metavolcanoclastic rocks belonging to the Santa Vittoria Fm., a progressive transition from non-sheared rocks to mylonites to ultramylonites can be observed along the deformation gradient approaching the BT. This is coupled with a gradual variation from a disjunctive cleavage with sub-parallel cleavage domains to a continuous cleavage in the most intensely deformed ultramylonitic rocks. In mylonites, the main foliation is defined by the grain shape preferred orientation of feldspar, quartz, white mica, and chlorite. Feldspars show undulose extinction, evidence of brittle deformation, and locally flame perthite (Fig. 5.5g). In ultramylonite, the matrix is composed of ultra-fine-grained black bands made by phase-mixing of white mica surrounding rounded K-feldspar and plagioclase porphyroclasts.

The fine grain size (< 25 µm) of quartz in these rocks prohibits the identification of their recrystallization mechanisms (Fig. 5.5h). Kinematic indicators include *C'*-S fabrics, mica fish, and the asymmetry of porphyroclasts of quartz or feldspar crystals which indicate a top-to-the S-SW sense of shear.

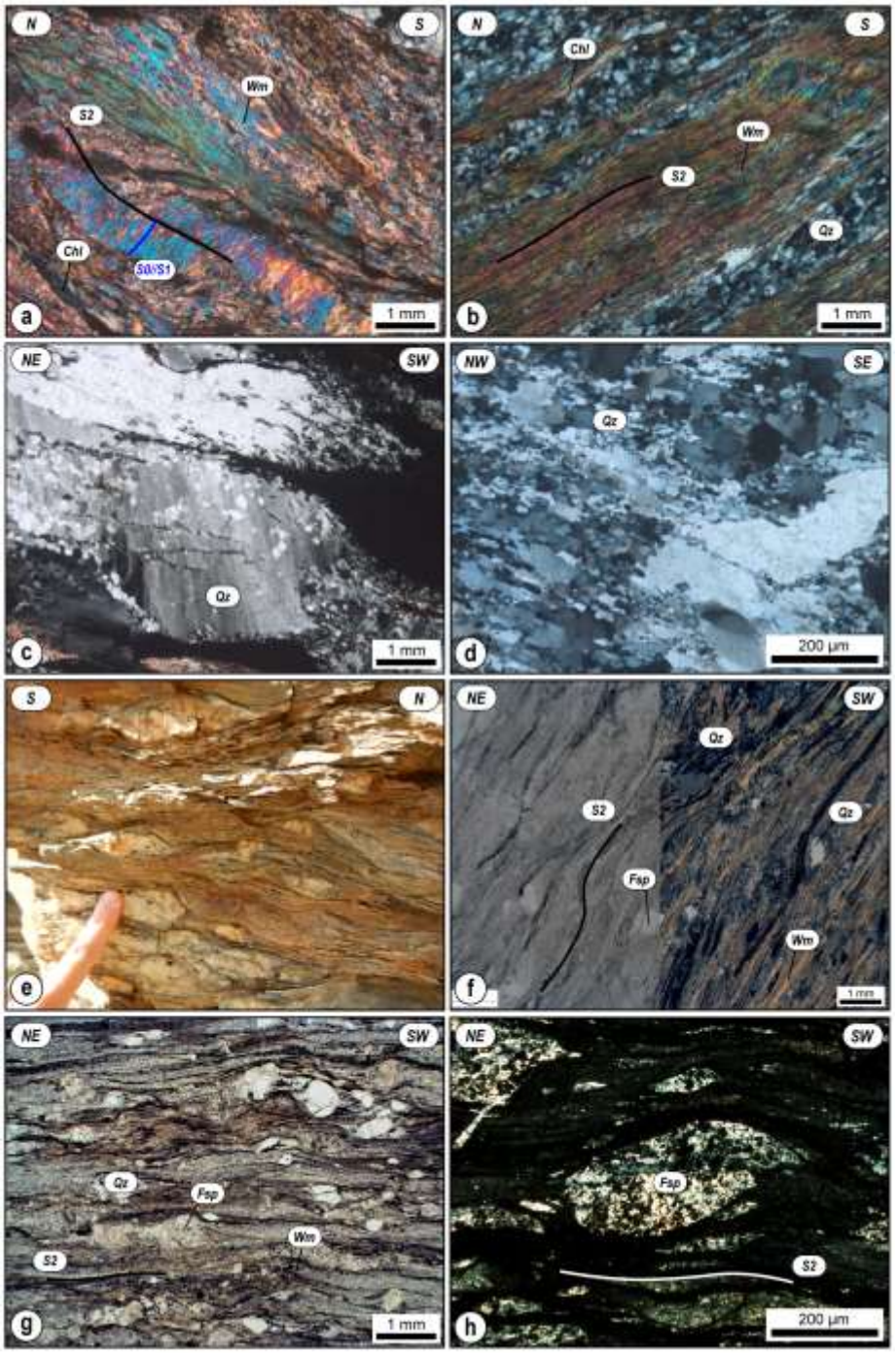

Figure 5.5: Meso- and microscale features across the Barbagia Thrust mylonitic zone. a) S_2 spaced foliation in metasedimentary rocks (San Vito Fm.; FW). Both S_1 and S_2 cleavages are defined by Wm + Chl (XPL); b) continuous cleavage in metasedimentary rocks (Filladi Grigie del Gennargentu Fm.; HW). S_2 cleavage is defined by both quartz and phyllosilicate-rich horizons (XPL) (Filladi Grigie del Gennargentu Fm.; HW); c) quartz with small new grains and undulose extinction indicative of BLG II mechanism (XPL) (Filladi Grigie del Gennargentu Fm.; HW); d) quartz with BLG II and minor local SGR mechanisms in a mylonite, subgrains, and new grains can be recognized (XPL) (Filladi Grigie del Gennargentu Fm.; HW); e) HW mylonites at the mesoscale: mylonitic fabric indicating a top-to-the S sense of shear (Filladi Grigie del Gennargentu Fm.); f) FW mylonite at the microscale: C'-S fabric is indicative of a top-to-the SW sense of shear (PPL and XPL) (San Vito Fm.; g) FW metavolcanoclastic mylonitic rocks. C'-S fabric and rotated porphyroclasts pointing to a top-to-the SW sense of shear (PPL) (Santa Vittoria Fm.); h) fine-grained continuous cleavage and σ-type porphyroclast in the FW ultramylonite indicating a top-to-the SW sense of shear (XPL) (Santa Vittoria Fm.).

5.3.3. D_3 and D_4 deformation phases

The D_3 phase is composed of m- to km-scale folds (i.e., Gennargentu Antiform and Barbagia Synform) that overprint and refold all previous structural elements, including the BT (Fig. 5.6a). They are commonly gentle, slightly asymmetric, and open (Figs. 5.6a, b), ranging from upright to steeply inclined and from metric to pluri-m long wavelengths. Locally kink-type folds occur (Fig. 5.6c). These folds display a S-SE vergence (Figs. 5.6a, b, c) with local variation to N. A_3 axes generally are coaxial to the A_2 axes and perpendicular to the L_2 object lineation in both investigated areas (Figs. 5.2b and 5.3b). In the F_3 hinge zones of less competent units, the S_3 axial-plane foliation is represented by a gradational crenulation cleavage (Fig. 5.6d). The main deformation mechanisms, as seen at the microscale, are pressure solution and kinking in phyllosilicate- rich domains (Fig. 5.6e). No metamorphic mineral assemblage related to these folds has been observed (Fig. 5.6e). D_4 produced gentle to open F_4 folds with sub-horizontal axes and axial planes (Fig. 5.6f). Locally, some minor-scale kink-folds occur. No metamorphic mineral assemblages related to the D_4 phase have been observed.

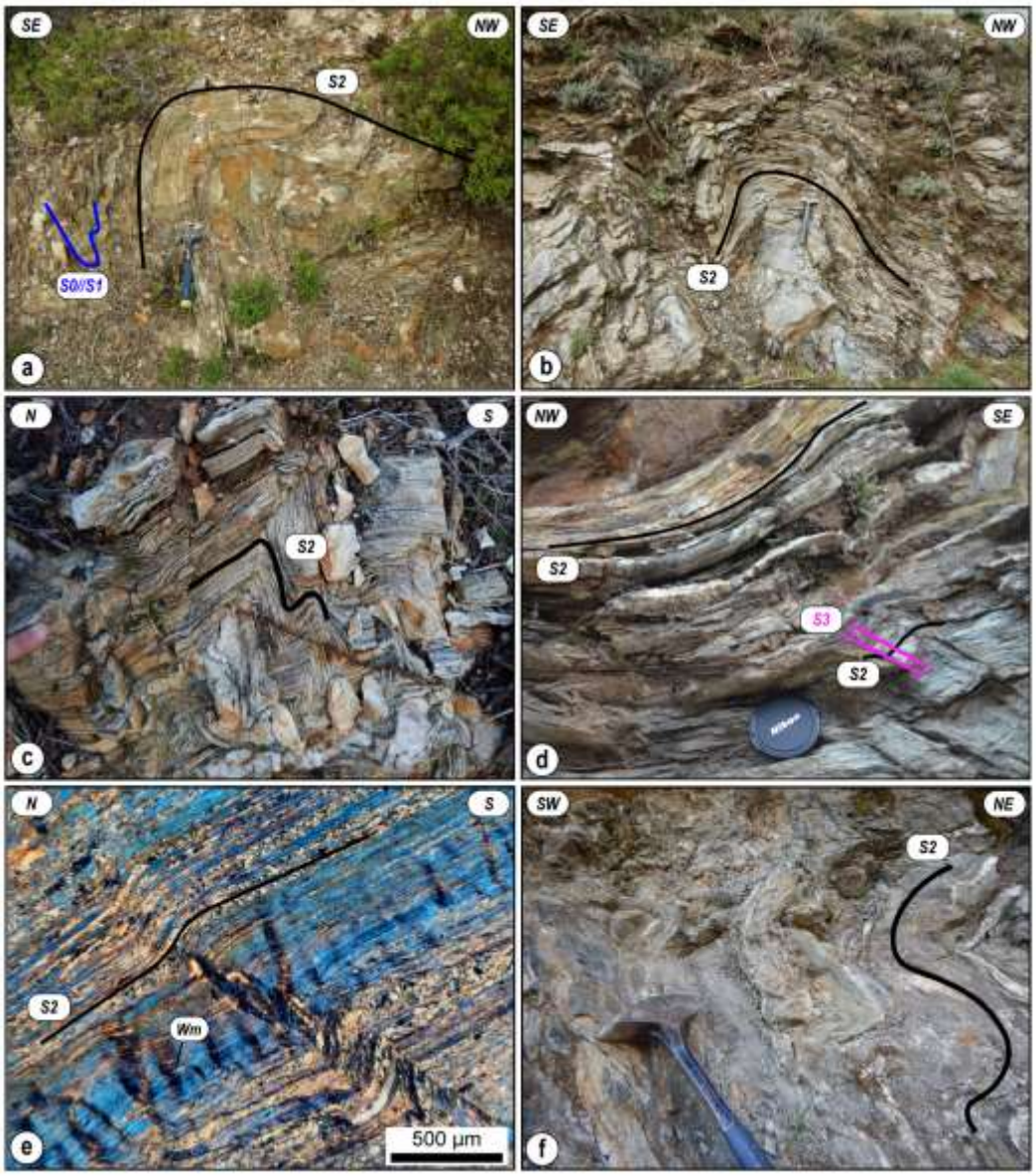

Figure 5.6: Outcrop aspect of the F_3 (a) asymmetric, (b) upright and (c) kink folds, showing mainly S-SE vergence; d) S_3 spaced foliation at mesoscale developed only in less competent layers in the hinge of F_3 fold; e) continuous S_2 foliation, defined by Wm + Chl, deformed by F_3 micro-kink folds (XPL); f) outcrop evidence of late open folds (F_4) with sub-horizontal axes and axial planes, deforming S_2 foliation.

5.4. Kinematic vorticity and finite strain results

In order to characterize the type of flow within the BT, kinematic vorticity analyses were performed on mylonitic samples in both Area I and II (Figs. 5.2a and 5.3a). In the present study, the *C'* shear band method (Kurz & Northrup, 2008; Gillam et al., 2013) and two different porphyroclasts-based methods, the porphyroclast aspect ratio method (PAR; Passchier, 1987; Wallis et al., 1993) and the rigid grain net method (RGN; Jessup et al., 2007), have been applied. A total of 19 samples (8 for HW and 11 for FW) were selected (Table 1). Examples of polar histograms related to *C'* shear band method (sample AP19-37), used to derive the angle *v*, are provided in figure 5.7a. For the RGN and PAR methods, an example of the same sample (sample AP19-37) is shown in figures 5.7b, and c, respectively. An example (sample AP19-39B) of the Fry diagram for both the XZ and YZ sections of the finite strain ellipsoid is presented in figure 5.7d. Full results are provided in Appendix 1, 2, and 3. The complete finite strain dataset (samples locations in Figs. 5.2a and 5.3a), obtained by the centre-to-centre method, is reported in Table 1.

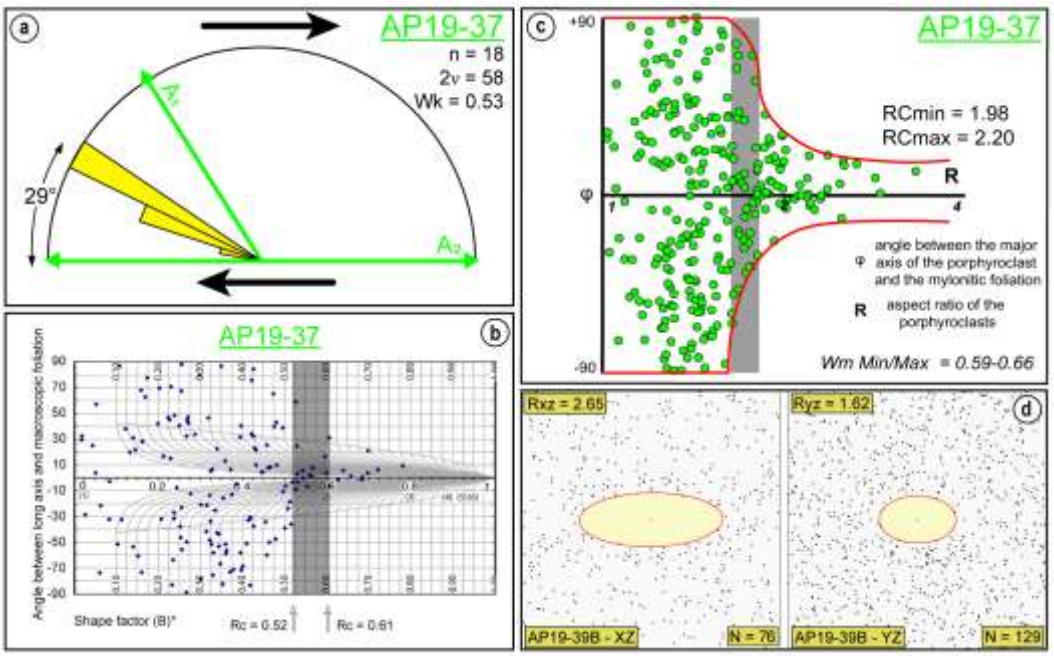

Figure 5.7: Example of vorticity analysis and finite strain results. a) Polar histogram used to derive the angle v, and the corresponding kinematic vorticity number, Wk. A1 = flow apophysis 1; A2 = flow apophysis 2; n = total number of data; b) and c) example of the plots for the porphyroclasts-based methods (b=RGN; c= stable porphyroclasts method). Rcmin and Rcmax = minimum and maximum critical axial ratio; Wm = mean kinematic vorticity number; d) Fry diagram for the XZ and YZ sections of the finite strain ellipsoid. N = number of centers considered in the analysis. The RXZ and RYZ axial ratios are shown.

Area I

			RSCM analysis									Kinematic vorticity and finite strain analysis												
				Aoya et al., 2010				Beyssac et al., 2002								RGN	Porphyroclasts method					Finite strain analysis			
SAMPLE NAME	UNIT	DISTANCE FROM THE BT (m)	n.	R2	SD	SE (°C)	RSCM °C	SD	SE (°C)	RSCM °C	N	v ANGLE (°)	Wk	N	Wm	Rc *min*	Rc *max*	Wk min	Wk max	Wk mid	R_{xz}	R_{yz}	R_{xy}	K
AP19-77	BU	*350*	10	0.40	5.7	1.9	*454*	5.6	1.9	*464*	-	-	-	-	-	-	-	-	-	-	-	-	-	-
LA-21	BU	*156*	12	0.35	18.1	5.5	*476*	16.8	5.1	*486*	18	28	0.56	-	-	-	-	-	-	-	-	-	-	-
LA-19	BU	*80*	-	-	-	-	-	-	-	-	9	19	0.79		-	-	-	-	-	-	-	-	-	-
LA-5	BU	*52*	12	0.32	17.2	5.2	*491*	15.6	4.7	*498*	-	-	-	-	-	-	-	-	-	-	-	-	-	-
2021_75	BU	*22*	11	0.30	14.0	4.4	*502*	12.4	3.9	*508*	-	-	-	-	-	-	-	-	-	-	-	-	-	-
AP19-88	BU	*18*	11	0.30	13.4	4.2	*502*	11.9	3.8	*508*	22	16	0.85	-	-	-	-	-	-	-	-	-	-	-
AP19-39A	MSU	*10*	-	-	-	-	-	-	-	-	11	11	0.93	-	-	-	-	-	-	-	-	-	-	-
2021_81A	MSU	*16*	-	-	-	-	-	-	-	-	14	19	0.79	-	-	-	-	-	-	-	3.30	1.26	2.62	6.23
AP19-39B	MSU	*60*	-	-	-	-	-	-	-	-	22	20	0.77	-	-	-	-	-	-	-	2.65	1.62	1.64	1.03
AP19-38	MSU	*84*	-	-	-	-	-	-	-	-	18	25	0.64	-	-	-	-	-	-	-	-	-	-	-
LA-14	MSU	*122*	-	-	-	-	-	-	-	-	-	-	-	164	0.56 - 0.65	2.11	2.33	0.63	0.69	0.66	-	-	-	-
AP19-37	MSU	*126*	10	0.31	17.4	5.8	*496*	15.6	5.2	*503*	18	29	0.53	280	0.52 - 0.61	1.98	2.20	0.59	0.66	0.63	-	-	-	-
2021_46	MSU	*160*	15	0.35	13.5	3.6	*475*	12.5	3.3	*483*	-	-	-	-	-	-	-	-	-	-	-	-	-	-
2021_72	MSU	*178*	16	0.36	17.7	4.6	*471*	16.4	4.2	*480*	-	-	-	-	-	-	-	-	-	-	-	-	-	-
AP19-125	MSU	*280*	10	0.38	5.2	1.7	*463*	4.9	1.6	*472*	22	30	0.50		-	-	-	-	-	-	2.18	1.42	1.54	1.27
AP19-25	MSU	*560*	10	0.41	8.2	2.7	*444*	8.1	2.7	*455*	-	-	-	-	-	-	-	-	-	-	-	-	-	-

Area II

			RSCM analysis									Kinematic vorticity and finite strain analysis												
				Aoya et al., 2010				Beyssac et al., 2002								RGN	Porphyroclasts method					Finite strain analysis			
SAMPLE NAME	UNIT	DISTANCE FROM THE BT (m)	n.	R2	SD	SE (°C)	RSCM °C	SD	SE (°C)	RSCM °C	N	v ANGLE (°)	Wk	N	Wm	Rc *min*	Rc *max*	Wk min	Wk max	Wk mid	R_{xz}	R_{yz}	R_{xy}	K
2021_113	BU	*360*	12	0.42	8.3	2.5	*443*	8.2	2.5	*454*	-	-	-	-	-	-	-	-	-	-	-	-	-	-
2021_97B TS	BU	*220*	16	0.35	16.3	4.2	*476*	14.8	3.8	*485*	15	29	0.53	-	-	-	-	-	-	-	-	-	-	-
2021_97A	BU	*180*	-	-	-	-	-	-	-	-	17	28	0.56	-	-	-	-	-	-	-	-	-	-	-
2021_40A	BU	*135*	-	-	-	-	-	-	-	-	18	25	0.64	-	-	-	-	-	-	-	-	-	-	-
2021_67	BU	*122*	11	0.35	11.7	3.7	*477*	10.7	3.4	*485*	-	-	-	-	-	-	-	-	-	-	-	-	-	-
AP19-77A	BU	*55*	10	0.33	8.6	2.9	*486*	7.8	2.6	*494*	-	-	-	-	-	-	-	-	-	-	-	-	-	-
2021_40B	BU	*52*	-	-	-	-	-	-	-	-	12	20	0.77	-	-	-	-	-	-	-	2.42	1.36	1.78	2.17
2021_97B P	BU	*40*	12	0.29	6.5	2	*505*	5.7	1.7	*511*	-	-	-	-	-	-	-	-	-	-	-	-	-	-
2021_111	BU	*12*	-	-	-	-	-	-	-	-	7	13	0.90	-	-	-	-	-	-	-	-	-	-	-
2021_108	MSU	*10*	10	0.31	7.2	2.4	*497*	6.4	2.1	504	-	-	-	-	-	-	-	-	-	-	-	-	-	-
2021_64	MSU	*35*	12	0.31	5.8	1.7	*495*	5.2	1.6	502	14	14	0.88	-	-	-	-	-	-	-	-	-	-	-
2021_63B P	MSU	*180*	-	-	-	-	-	-	-	-	12	23	0.69	-	-	-	-	-	-	-	-	-	-	-
2021_63B TS	MSU	*235*	-	-	-	-	-	-	-	-	16	28	0.56	-	-	-	-	-	-	-	-	-	-	-
2021_63A	MSU	*254*	-	-	-	-	-	-	-	-	24	30	0.5	-	-	-	-	-	-	-	-	-	-	-
2021_56B	MSU	*288*	-	-	-	-	-	-	-	-	-	-	-	-	-	-	-	-	-	-	1.96	1.49	1.23	0.39
2021_56A	MSU	*300*	-	-	-	-	-	-	-	-	-	-	-	-	-	-	-	-	-	-	2.25	1.63	1.38	0.61
2021_58	MSU	*650*	18	0.48	5.5	1.3	*420*	5.7	1.4	429	-	-	-	-	-	-	-	-	-	-	-	-	-	-

Table 1: Results of the RSCM estimations (both Aoya et al. (2010) and Beyssac et al. (2002) calibrations results are indicated), kinematic vorticity, and the finite strain (see Figs. 5.2 and 5.3 for samples location). Samples, divided according to the corresponding tectonic unit, are listed according to the distance with respect to the Barbagia Thrust. The number of spectra (n), mean R2 ratio (Beyssac et al., 2002) for n spectra with corresponding standard deviation (SD), and calculated temperature with standard error (SE= SD/√n.) have been indicated.

5.4.1. Area I

In Area I, a total of 9 samples (3 for HW and 6 for FW, respectively; Fig. 5.2a) analyzed with the *C'* shear band method gives (Table 1) a vorticity number ranging from 0.50 to 0.93, with a mean of 0.71. In sample AP19-37, from the FW, we found, applying the stable porphyroclasts method, a minimum Rc of 1.98 and a maximum Rc of 2.20 corresponding to *Wk* values of 0.59 and 0.66 (Table 1), respectively. In sample LA-14, from the FW, minimum and maximum Rc values are 2.11 and 2.33, corresponding to *Wk* between 0.63 and 0.69 (Table 1). The overlapping but different range of vorticity (Fig. 5.8a) in these samples may be due to (i) different analytical uncertainties associated with input data and/or (ii) the different strain memory. Finite strain results in Area I indicate an axial ratio of 2.18, 2.65, and 3.30 on the XZ sections, 1.42, 1.62, and 1.26 on YZ sections of the finite strain ellipsoid and the shape parameter of the strain ellipsoid (*K*) is 1.27, 1.03 and 6.23 for samples AP19-125, AP19-39B, and 2021_81A, respectively (Fig. 5.8b).

Mylonite in the middle part of the shear zone (samples AP19-39B) is close to plane strain conditions, whereas mylonite closest to the core of the BT (sample 2021_81A) is in the prolate field (Fig. 5.8b).

5.4.2. Area II

Data from Area II, obtained from 9 samples analyzed by the *C'* shear band method (5 for HW and 4 for FW, respectively; see Fig. 5.3a for sample location and Table 1 for results), give a vorticity number ranging from 0.50 to 0.90, with a mean of 0.67. In Area II, finite strain results indicate an axial ratio of 1.96, 2.25, and 2.42 on the XZ sections and 1.49, 1.63, 1.36 on YZ sections of the finite strain ellipsoid and the shape parameter of the strain ellipsoid (*K*) is 0.39, 0.61 and 2.17 for samples 2021_56B, 2021_56A, and 2021_40B, respectively. In the Flinn diagram (Fig. 5.8b), the two farthest samples with respect to the core of the BT (samples 2021_56A and 2021_56B) fall in the oblate field near the plane strain conditions. Finite strain in mylonite in the external part of the shear zone (AP19-125) plots close to plane strain conditions, whereas in samples closest to the core of the BT (sample 2021_40B) is in the prolate field (Fig. 5.8b).

Estimated values in both Area I and II reveal an important contribution of pure shear during thrust-sense ductile deformation (Fig. 5.8a). Moreover, the results highlight in both areas a strong increase of the component of simple shear along the deformation gradient in both units, approaching the BT high-strain zone (Fig. 5.8a, Table 1).

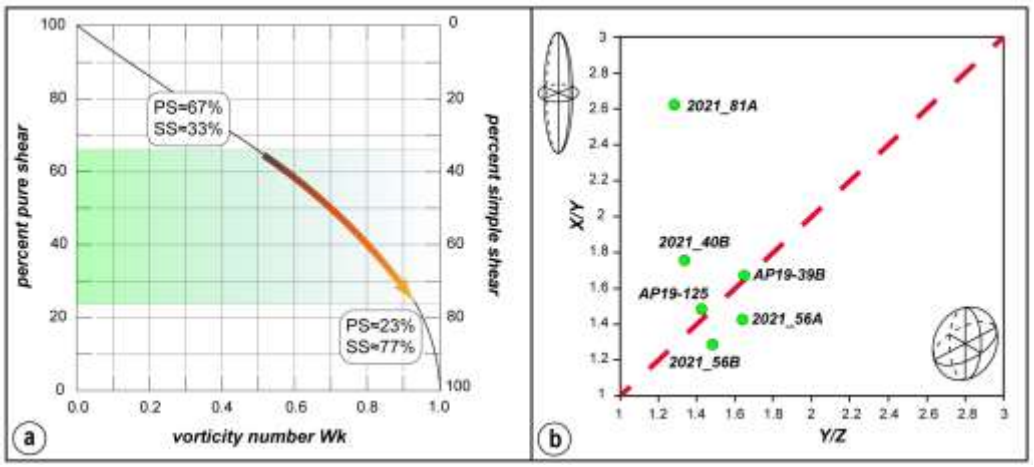

Figure 5.8: a) Diagram showing the relative percentage of simple shear obtained from the selected samples of both areas. The simple shear component increases (highlighted by the arrow) according to the deformation gradient; b) Flinn diagram showing the analyzed samples (green dots) finite strain results (for sample location see Figs. 5.2a and 5.3a).

5.5. RSCM estimates

The peak temperature was obtained using RSCM. This method is based on the progressive transformation of CM during the increase of temperature, and it is not affected by the retrograde history (Beyssac et al., 2002; Beyssac & Lazzeri, 2012). The RSCM temperature estimates discussed in the following sections were derived from Aoya et al. (2010). The temperature results, calculated with both Beyssac et al. (2002) and Aoya et al. (2010) calibrations, are given in Table 1. A total of 18 samples from both Area I and Area II (Figs. 5.2a and 5.3a for sample location) collected at different structural positions were selected for RSCM analysis. Representative spectra and corresponding RSCM temperatures are reported in figures 5.9a and b, respectively.

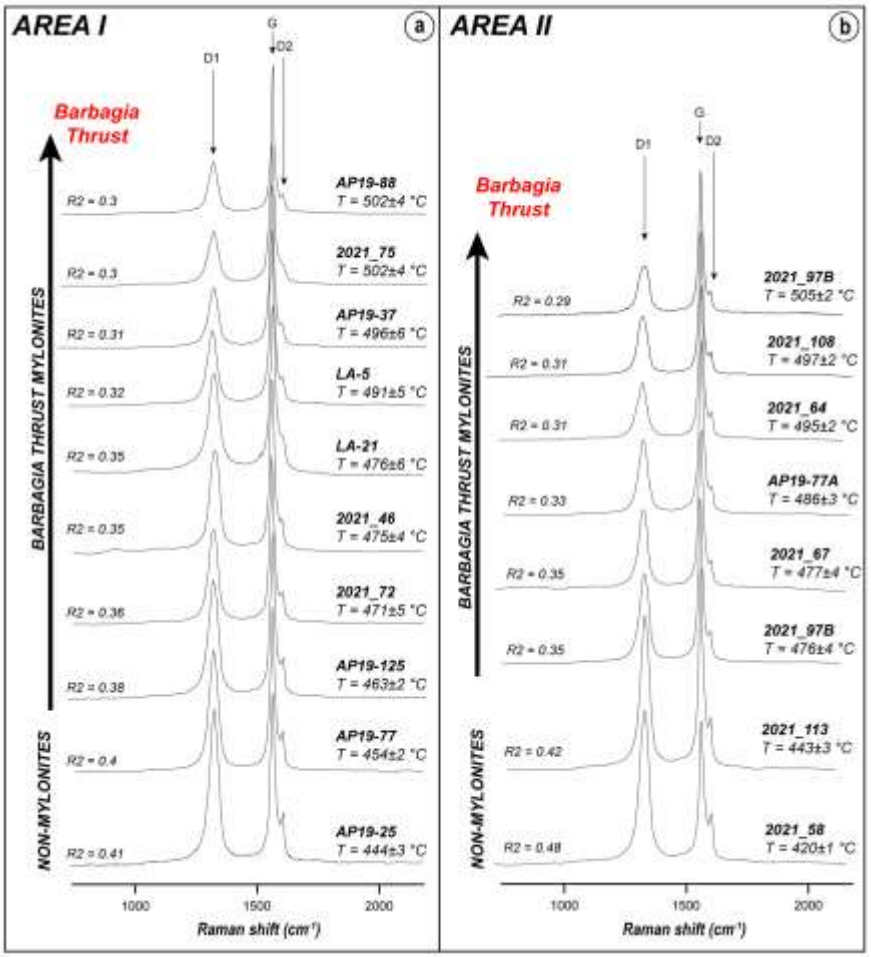

Figure 5.9: Representative raman spectra of carbonaceous material for each sample obtained in non- and mylonitic rocks of both investigated areas for Area I (a) and Area II (b). For each spectrum, the R2 ratio and the corresponding RSCM T (°C) with the relative simplified error have been indicated. Samples are ordinated according to structural distance from the Barbagia Thrust.

5.5.1. Area I

In Area I, the R2 parameter ranges from 0.30 to 0.41, with an average of 0.35. The R2 parameter varies from 0.30 to 0.40 and from 0.31 to 0.41 for the HW and FW, respectively (Table 1). A systematic increase in temperature moving from the structurally higher parts of the HW, or from the structurally lower parts of the FW, moving into the BT core, from ~455 up to 508 °C (Fig. 5.9a) has been detected. In particular, within the HW, temperature increases along the deformation gradient from a minimum of ~454 up to 502 °C close to the BT. The Raman spectra of the FW follow the same pattern and temperature increases from ~444 °C up to ~496 °C for the sample nearest to the BT. The lowest temperatures in Area I have been found in non-mylonitic samples, where relict S_1 foliation is observable in microlithons (Fig. 5.10a). No systematic differences in the obtained RSCM *T* results have been detected from graphite lying on S_1 or S_2. Samples with the highest temperature have been found in mylonitic rocks within the core of the BT (Fig. 5.10b).

5.5.2. Area II

In Area II, the R2 parameter ranges from 0.29 to 0.48, with an average of 0.36. The R2 parameter varies from 0.42 to 0.29 and from 0.48 to 0.31 for the HW and FW, respectively (Table 1). Moving from the structurally higher sectors of the HW, or from the structurally lower one of the FW, toward the BT, a general increase in temperature, from ~420 up to 505 °C (Fig. 5.9b), has been highlighted. Along the deformation gradient, temperature increases from ~420 up to 497 °C and ~443 up to 505 °C for FW and HW, respectively. As for Area I, the lowest temperatures in Area II have been detected in non-mylonitic samples (Fig. 5.10a) and no differences have been detected from graphite lying on S_1 or S_2. Samples with the highest temperature have been found in mylonites from both HW and FW (Fig. 5.10b).

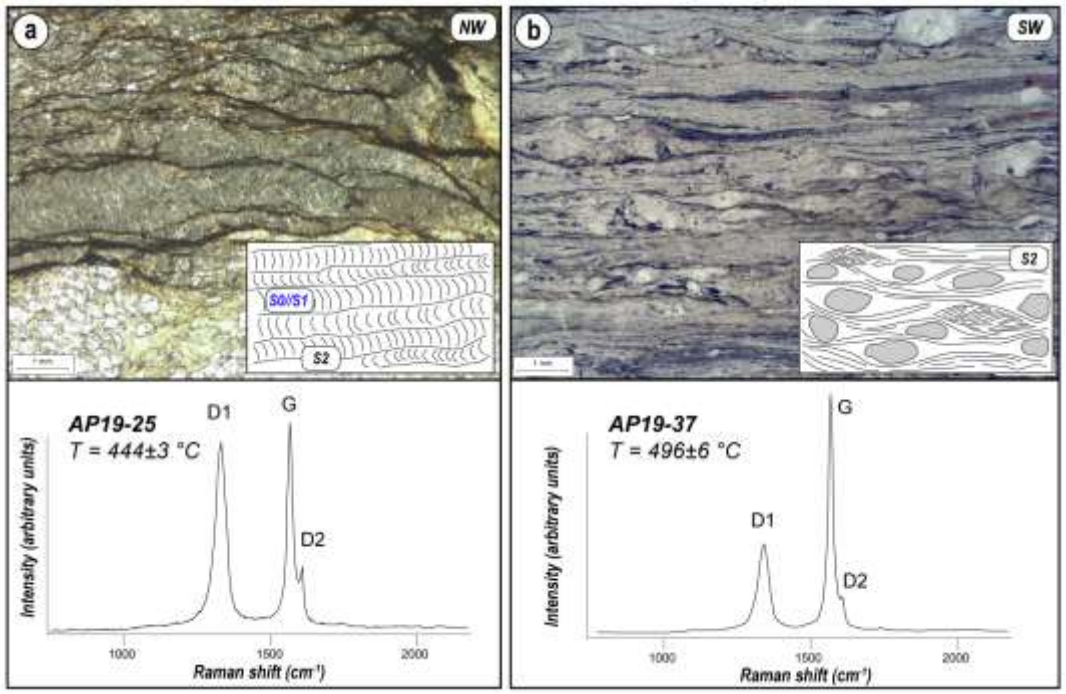

Figure 5.10: Example from Area I of the variation of RSCM temperature in different deformed rocks. Thin sections (PPL) and representative Raman spectra for carbonaceous material from FW samples AP19-25 (a) and AP19-37 (b), respectively outside and inside the mylonitic zone (see Fig. 5.2a for the position of the samples). Note that the RSCM T (°C) is higher in the mylonite.

5.6. Discussion

5.6.1. Geometry and deformation regime of the BT

Detailed meso- and microstructural analyses have unraveled the tectonic history of two different sectors (Area I and Area II) of the BT in the Sardinian Variscan belt (Fig. 5.1b). This region has undergone a polyphase evolution consisting of four ductile deformation phases. Sedimentary bedding S_0 is only observed in a few areas where a strong lithological contrast is present. The D_1 structures are detectable far from the BT and mainly in the FW. The S_1 foliation is defined by quartz + white mica + chlorite, indicating a greenschist-facies condition. The main structures of the study area are controlled by the D_2 deformation phase. This phase is linked to the syn-nappe stacking and exhumation of the HW (Carosi et al., 2004; Montomoli et al., 2018). An increase in shear deformation along with the progressive transposition of previous D_1 structures approaching the BT has been highlighted. The observed deformation gradient in Area I appears strikingly similar to that reported along the BT in the Area II (Carosi et al., 2004; Montomoli et al., 2018).

The S_2 foliation, parallel to the boundaries of the shear zone, and the F_2 fold axes, perpendicular to the L_2 object lineation, are coeval with the overthrust of the Internal Nappe Zone onto the External Nappe Zone (Carosi et al., 2004). The syn-kinematic mineral assemblage (chlorite + white mica) along the S_2 mylonitic foliation is indicative of greenschist-facies metamorphic conditions. This is in agreement with the main dynamic recrystallization mechanism of quartz, indicative of temperature ranges ~400-450 °C (BLG II and local SGR; Piazolo & Passchier 2002; Stipp et al., 2002). These data are corroborated by the presence of undulose extinction, local flame perthite, and brittle deformation in feldspar, indicating ~400-500 °C (Pryer, 1993). The observed relationships between mineral assemblage growth and deformation and dynamic recrystallization mechanisms are broadly consistent with those reported by Montomoli et al. (2018), but with some differences. Whilst, the syn-kinematic minerals observed during the D_2 phase are the same as previous authors, the observed quartz recrystallization mechanism indicates slightly higher temperatures of deformation. However, the lack of Grain Boundary Migration (GBM) in quartz, as highlighted by Conti et al. (1998), Montomoli et al. (2018), and this work, indicates that deformation probably did not exceed ~500 °C. Kinematic indicators, both at the meso- and microscale, in Area I and II, reveal a top-to-the S-SW sense of shear. This also agrees with the S-SW F_2 fold vergence detailed by previous authors (Carosi, 2004; Carosi et al., 2004; Montomoli et al., 2018). The whole architecture of the Nappe Zone is affected by regional-scale F_3 folds (D_3). The D_3 phase is characterized by pressure solution, indicating an upper structural level deformation. Also, the presence of the BT mylonitic zone in the different sectors of the Barbagia Synform, with the same structural and kinematic features, indicates that F_3 folding deformed this tectonic contact. Similar structural results and the same shear sense were obtained from both zones, confirming the post-nappe stacking folded structure (i.e., Barbagia Synform). Subsequent post-collision extensional tectonics was characterized by the development of open folds (F_4).

5.6.2. RSCM temperature variation along the BT

Orogenic systems are partially characterized by successive and moderate overprinting thermal events (e.g., Brown, 1993; Delchini et al., 2016; Beyssac et al., 2019). One of them is the progressive increase of temperature along shear zones (Thigpen et al., 2010). There are several methods for investigating the thermal architecture of a low-temperature portion of an orogenic belt, including vitrinite reflectance (Ferreiro Mählmann et al., 2012), illite and chlorite crystallinity (Merriman et al., 1995; Jaboyedoff et al., 2001; Maino et al., 2015; Vidal et al., 2016), and RSCM thermometry (Beyssac et al., 2002; Rahl et al., 2005; Aoya et al., 2010; Lahfid et al., 2010; Kouketsu et al., 2014).

Montomoli et al. (2018) performed both illite and chlorite crystallinity measurements on samples transecting the BT, but found no systematic changes in those parameters across the structural profile. Compared to the illite and chlorite crystallinity measurements, RSCM thermometer, in the absence of extreme fluid-rock interaction or deformation (Moris-Muttoni et al., 2022 and references therein), may be more sensitive to the temperature variation recording peak temperature (e.g., Beyssac et al., 2002; Aoya et al., 2010; Lahfid et al., 2010). RSCM temperatures across the BT on both strongly and weakly deformed samples have been taken from two different structural sectors of the same shear zone. An increase in temperature moving from the structurally higher parts of the HW, or from the structurally lower parts of the FW, toward the BT core has been highlighted. The lowest RSCM temperature from non-mylonitic samples of both FW and HW (Figs. 5.11a) is slightly different in Area I and II. Based on the geological framework, this *T* is linked to the maximum temperature reached during collisional shortening and regional metamorphism in the HW and FW. RSCM temperatures range from ~420 to ~450 °C, in agreement with the documented metamorphic mineral assemblage and recrystallization mechanism of quartz and feldspar. In comparison, mylonites return higher RSCM temperatures ranging from ~470 to ~500 °C (Fig. 5.11a). The detected T_{RSCM} shift between non-mylonitic to mylonitic rocks is in the range of ~50-70 °C.

Several factors could cause this rise in temperature towards the core of shear zones: (i) graphite precipitation from a hydrothermal fluid; (ii) detrital graphite; (iii) strain reorganization of graphite; and (iv) shear heating. Fluids have previously been involved to explain the presence of CM with unusual crystallinity (Vitale Brovarone et al., 2020; Skrzypek, 2021). CM grains found in low-grade metamorphic rocks but indicating higher temperatures have been explained by the precipitation of higher-crystallinity (lower R2) CM from hydrothermal fluids (Kříbek et al., 2008) or detrital origin (Galy et al., 2008). Whilst fluid-rock interaction during shear deformation or detrital origin of graphite can not be completely excluded, the presence of a systematic increase in the CM crystallinity from the boundary to the core of the shear zone, in both areas, and the paucity of meso- and/or microscale evidence for fluids (e.g., veins stockwork) make it to appear unlikely.

The RSCM data reported here show a persistent and systematic increase in *T* with increasing strain intensity moving into the BT high strain shear zone. Several contributions have demonstrated that strain could reorganize the structure of graphite (Kitamura et al., 2012; Furuichi et al., 2015; Nakamura et al., 2015, 2017, 2020; Kouketsu et al., 2019; Kedar et al., 2020; Lyu et al., 2020). This strain-induced mechanism is similar to lattice modification and recrystallization in the ductile deformation of minerals (Wang et al., 2019).

If strain could reorganize the structure of the CM, the obtained T_{RSCM} may not be systematic in the temperature increase. However, the strain-driven crystallization of CM is most effective in low-grade metamorphic rocks (~200-350 °C), where the deformation could strongly modify the internal structure of CM (Wang et al., 2019). Obtained lowest temperatures come from non-mylonitic samples and are associated with *T* of ~420-450 °C (Fig. 5.11a), linked to collisional shortening and regional metamorphism.

Thus, these samples are characterized by medium crystalline and organized graphite that could be difficult to deform and give us an increase in temperature of ~50-70 °C due to strain-induced mechanism. Despite this, obtained results cannot completely exclude this factor. Shear heating has been shown to produce temperature increases in shear zones (Molnar & England, 1990; Camacho et al., 2001; Burg and Gerya, 2005; Mako & Caddick, 2018; Waters et al., 2018; Thigpen et al., 2021). The amount of heat generated during shear heating varies as a result of several factors: (i) convergence rate, (ii) strain rate, and (iii) width. Mako & Caddick (2018) used numerical models to calculate shear heating magnitudes as high as ~200 °C, but they suggest that natural shear zones would probably produce much lower values. Thus, several authors (Jamieson & Beaumont, 2013; Mako & Caddick, 2018; Waters et al., 2018; Iaccarino et al., 2020) highlight that shear heating, in most common natural shear zones, produces relatively little heat compared to the surrounding rocks, probably on the order of ~10-60 °C. In particular, shear heating for low initial temperature (~300-400 °C) is strongly dependent on convergence velocity (Waters et al., 2018). Shear heating > 100 °C is only achievable with high convergence velocities (~3-5 cm/year), whereas lower convergence velocities (~1 cm/year) can only produce heating > 50 °C, according to the calculations of Mako & Caddick (2018). The strain rate and the width of the shear zone can also play an important role in the potential magnitudes of shear heating (Mako & Caddick, 2018). Integrating the strain rate values obtained by Montomoli et al. (2018) along the BT (10-12-10-14 s^{-1}) with the measured width of the shear zone in both transects (~600 m) in the Mako & Caddick (2018, their figure 9) graphs, it is possible to predict the potential temperature increase due to shear heating across the BT shear zone. Considering a shear zone activity ranging between 5-10 My and the known strain rate values of Montomoli et al. (2018), for non-mylonitic rocks of initial temperature of ~400-450 °C, these integrated models of shear heating predict a *T* increase of ~50 °C. Moreover, the calculations of Mako & Caddick (2018) also imply that the observed maximum-*T* conditions are only possible for lower convergence velocities (≤ 3 cm/year). In summary, obtained T_{RSCM} estimates derived both from Area I and II indicate that the temperature shift between the mylonitic and non-mylonitic rocks is approximately ~50-70 °C (Fig. 5.11a), in agreement with the numerical

simulations. The displacement of the ductile shear zone is directly related to the strain rate, the width of the shear zone (Molnar & England, 1990; Waters et al., 2018), and the thermal architecture. The amount of erosion before the development of the BT is not known. However, temperatures of ~450 °C, obtained by the RSCM method in the HW metasediments imply depths of ~18 km when coupled with plausible thermal gradients of 25 °C km^{-1} (Casini et al., 2012; Montomoli et al., 2018). In the above scenario, taking a thrust dip reference value of ~35°, as roughly equivalent to the syn-orogenic dip of the BT, the minimum magnitude of displacement of the BT has been calculated, obtaining ~31 km of displacement (vertical depth/sin(thrust dip angle)). This result is confirmed by the distance calculated on the basis of cartographic evidence (estimated parallel to the shear plane) of ~20-30 km, which is comparable to the amount reported by Carosi & Malfatti (1995). As highlighted by different authors (Burg & Gerya, 2005; Waters et al., 2018), the fault displacement represents another important parameter to be taken into account while discussing shear heating. Along shear zones with a considerable displacement, as in this case, combined with a relatively short duration of ductile shearing, the most plausible heat source is shear heating (Mako & Caddick, 2018). It is also worth noting that, even if the RSCM absolute error is about ± 50 °C (Beyssac et al., 2002, 2004), a systematic thermal increase following the deformation gradient and toward the BT in both Area I and II has been detected. Nevertheless, in the southernmost area, the thermal variation from non- to strongly deformed rocks is larger than the absolute error of the method and thus increases the reliability of the obtained data. However, the meaning of the detected thermal gradient across the BT is still uncertain.

Fluid circulation, strain reorganization and shear heating may be equally responsible for the increase in the obtained RSCM temperatures. Obviously, the driving factor strongly changes the interpretation of the geological data. Nevertheless, due to the magnitude of the recorded increase in temperature that fits well with the model predictions, the obtained results appear to be consistent with a shear heating model. A number of works have documented that shear heating has strongly influenced the thermal structure of shear zones; as the Main Central Thrust in the Himalayas (Molnar & England, 1990), the South Tibetan Detachment System in the Everest region (Waters et al., 2018); for the Central and the Western Alps (Burg & Gerya, 2005; Schmalholz & Duretz, 2015); in the Davenport shear zone, central Australia (Camacho et al., 2001); the Norumbega fault zone, Central Maine (Mako & Caddick, 2018); for the northern Scandian orogenic wedge (i.e., Moine, Ben Hope, Naver, and Skinsdale Thrust; Thigpen et al., 2021) or for generic subduction zones (Peacock, 1992).

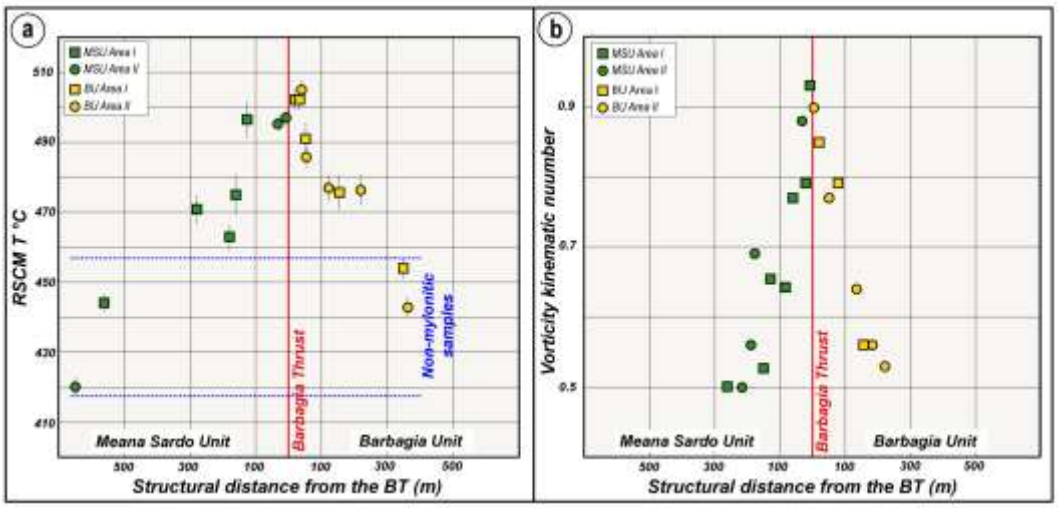

Figure 5.11: a) Distribution of RSCM T (°C) compared with the sample structural distance with respect to the BT; b) distribution of estimated vorticity kinematic number against the structural distance from the Barbagia Thrust. Both graphs show increasing RSCM T (°C) and Wk values (i.e., increase in simple shear) toward the shear zone.

5.6.3. Kinematics of the BT

The deformation regime and the finite strain of the BT have been defined. The kinematic vorticity data obtained by the *C'* shear bands method (Kurz & Northrup, 2008), PAR, and the RGN method (Jessup et al., 2007) have allowed quantification of the flow regime as a non-coaxial flow. Concerning the uncertainties in the estimation of the vorticity parameter, all methods, based on different assumptions, return consistent results from both Area I and II. The object lineation within the BT is gently plunging and generally parallel to the dip of the main foliation, and thus is compatible with a thrust-sense movement. The obtained data highlight that the simple shear component increases progressively towards the centre of the BT, from both HW and FW rocks and in both Area I and II (Fig. 5.11b). A variation of simple shear from ~33% up to ~77% has been recognized. Mylonites and less deformed rocks record a flow regime dominated by pure shear, whereas ultramylonites in the center of the shear zone record an increasing amount of simple shear. This is associated with a change of the finite strain ellipsoid from close to the plane strain up to prolate conditions. Obtained results are in good agreement with the previous work on the BT. In fact, asymmetric F_2 folds observed in both nappes with the axial plane parallel to the mylonitic foliation are linked to the BT non-coaxial deformation (Carosi et al., 2004). According to the description by Fossen (2016), it is possible to suggest that the presence of this kind of fold accommodates the component of shortening perpendicular to the BT.

Contemporaneous pure and simple shearing, due to the overthrust of the Internal Nappe Zone onto the External Nappe Zone, may explain the F_2 folds. Finite strain data suggest a variation from general flattening to prolate ellipsoid, in agreement with an increase of simple shear in thrust-sense shear zones (Vitale & Mazzoli, 2008; Fossen, 2016). A higher Rxz value is inferred from ultramylonitic/within core samples compared to values from the other mylonitic samples, corroborating both field and microstructural observations. This implies that the core of the BT accommodated a higher amount of strain with respect to the shear zone peripheries (Fossen & Cavalcante, 2017). Higher *Wk* values within the centre of the BT, and a prolate strain ellipsoid are associated with higher T_{RSCM}, whereas lower *Wk* values, far from the BT core, and plane strain conditions are associated with samples showing lower T_{RSCM}.

The progressive increase in temperature towards the BT, coupled with the increase of simple shear, could indicate a syn-shearing temperature imprint. This broad correlation between T_{RSCM} and the deformation gradient could imply that the flow path was accompanied by a progressive localization of deformation in the core of the shear zone, due to thermal weakening, during the ductile deformation (Vitale & Mazzoli, 2008). Although the lacking of absolute timing constraints, obtained results fit well with the Type II shear zone growth model proposed by Fossen & Cavalcante (2017). In this case, following the hypothesis of the shear heating model discussed above, the deformation has been progressively localized in the central part of the shear zone due to thermal weakening. The result, as in the study case of the BT, is a shear zone with a deformation gradient increasing toward the centre and associated with systematic variations in kinematic vorticity, finite strain and *T* based on RSCM (Fig. 5.12).

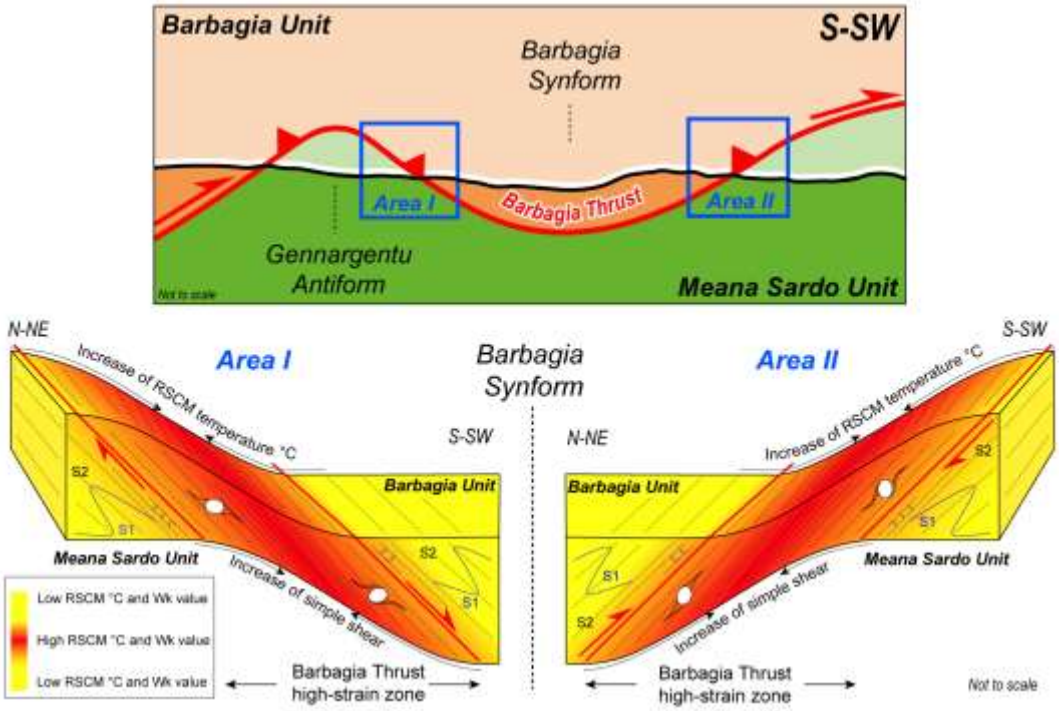

Figure 5.12: On the top, the current stage of the architecture of the belt is shown by a simplified cross-section across the Internal and External Nappe Zone. The approximated position of the investigated areas and the simplified present-day topography have been highlighted. The sense of shear is the same in both areas, pointing to a top-to-the S-SW. On the bottom, not to scale representations of the Barbagia Thrust along with the northern and southern limb of the Barbagia Synform, have been displayed. The given "finite" shape is not referred to the shear displacement but is due to the late fold (F_3) linked to D_3 deformation (Barbagia Synform). The progressive strain partitioning and gradient, from fold structures to a mylonitic foliation (approaching the Barbagia Thrust high-strain zone), have been highlighted, mirrored by the increase of both simple shear and the RSCM T (°C).

5.7. Conclusions

This study shows the importance of studying regional-scale shear zones with a multidisciplinary approach. Quantitative constraints on deformation and peak temperature in two sectors of the BT have been provided (Fig. 5.12). The strictly similar thermo-kinematic results and the same sense of shear obtained from two different sectors along the BT (Area I and Area II) confirm the post-nappe stacking folded structure (i.e., Barbagia Synform) of the belt (Fig. 5.12). Valuable information can only be obtained if different and independent techniques are integrated to constrain temperature and deformation in terms of peak temperature, finite strain, and kinematics of the flow. Detecting a thermal gradient and, whenever possible, identifying the process that produces heating in a thrust-sense shear zone in collisional systems is one of the primary results of this work.

A combination of structural investigations at different scales and of RSCM analyses reveals an increase in finite strain and of the simple shear component coupled with the systematic increase in T_{RSCM}, approaching the high-strain zone from the structurally higher parts of the HW or from the structurally lower parts of the FW (Fig. 5.12). Regarding the nature of the heating, obtained thermal results document that the paleothermal architecture of the BT best fits with a tectonic scenario of shear heating. The heating quantified along the BT (~50 °C) is in agreement with the shear heating magnitudes calculated by numerical and mechanical studies. By integrating different methodologies, obtained results show that the BT represents a major tectonic boundary that drove exhumation, divides the internal sector of the Sardinian orogenic wedge from the external one, and represents a change from hinterland- to foreland-style deformation.

Appendix

Appendix 1: Polar histograms used for estimating the kinematic vorticity. *v* = angle between the *C'* planes and the shear zone boundary; A1= flow apophysis 1; A2 = flow apophysis 2; n = total number of data; *Wk* = kinematic vorticity number.

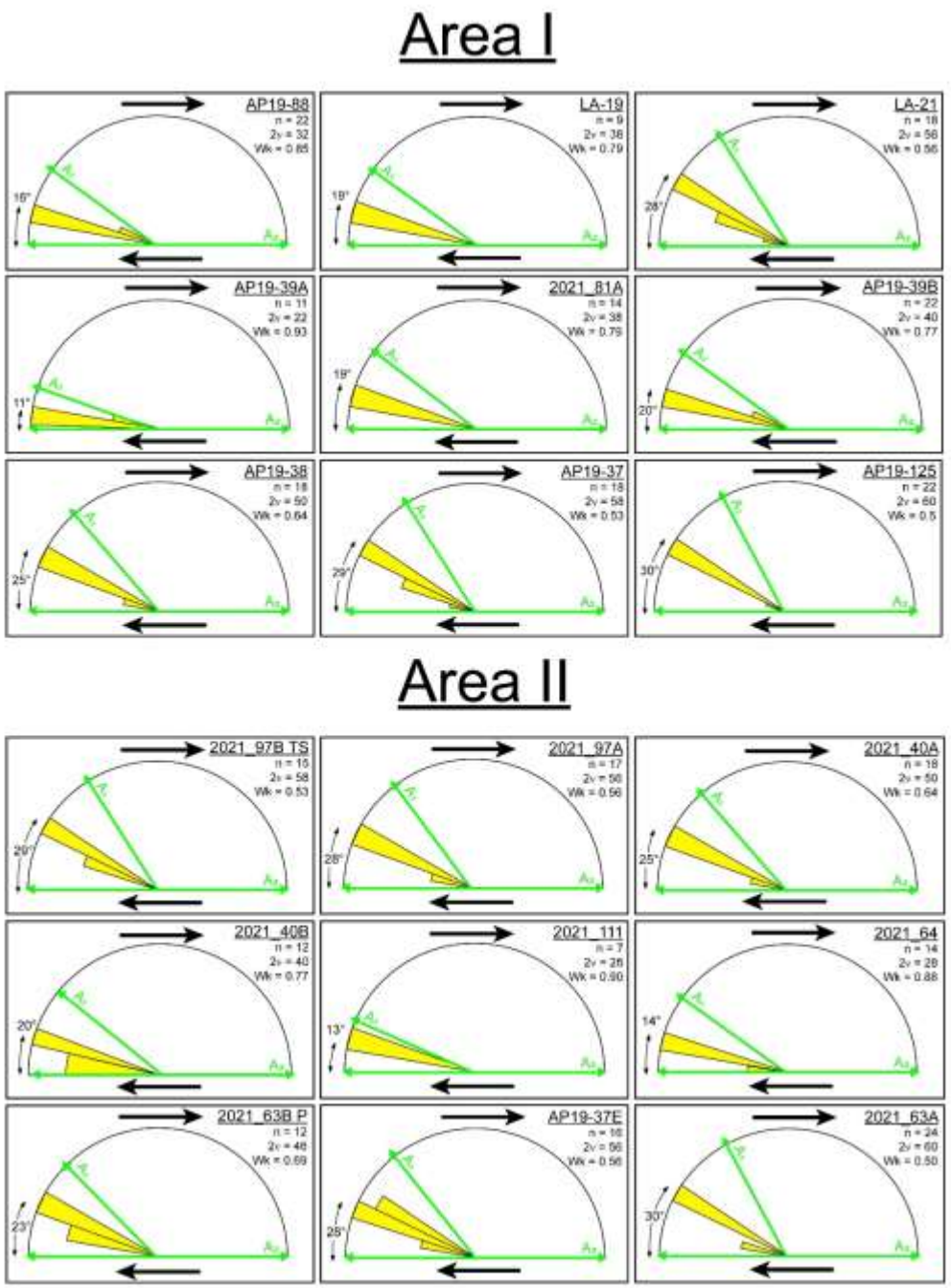

Appendix 2: Diagrams showing the porphyroclasts distribution for both RNG and PAR methods. Rc= critical axial ration; RCmin = minimum critical axial ration; RCmax = maximum critical axial ratio; *Wm*min = vorticity number calculated with RCmin; *Wm*max = vorticity number calculated with RCmax.

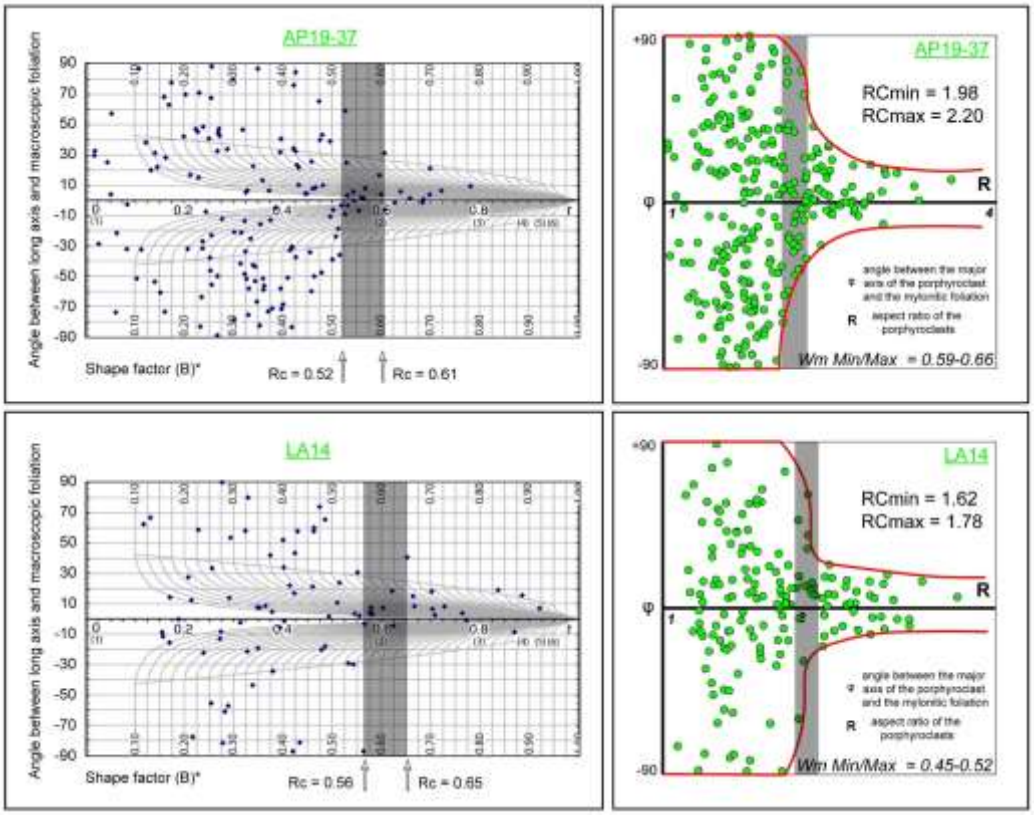

Appendix 3: Finite strain diagrams based on the centre-to-centre method of Fry (1979).

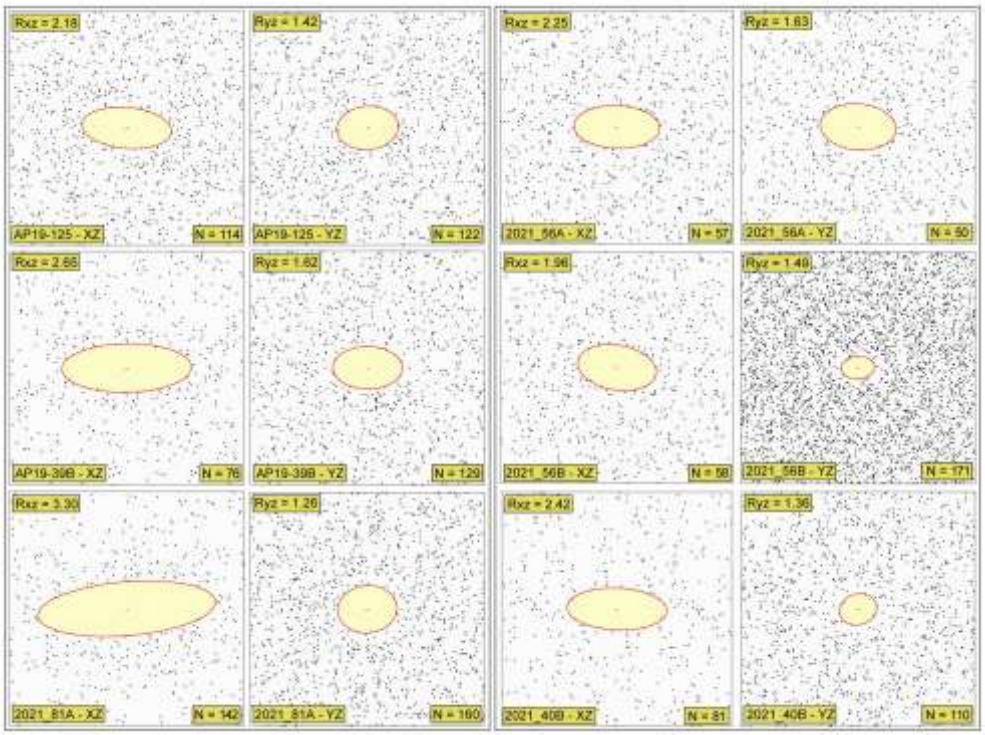

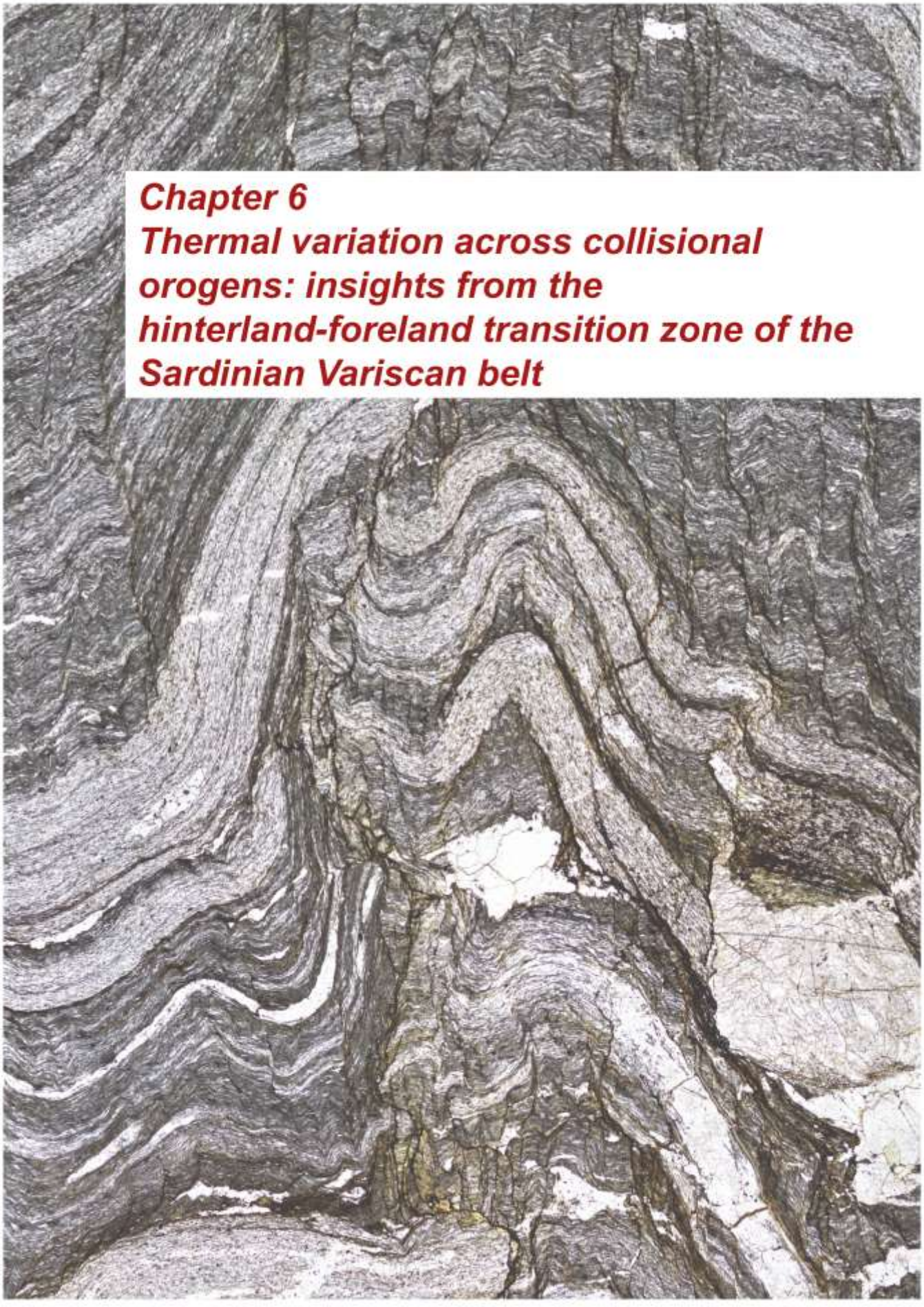

Chapter 6
Thermal variation across collisional orogens: insights from the hinterland-foreland transition zone of the Sardinian Variscan belt

6.1. Introduction

Different factors control the tectonic architecture of orogenic wedges in collisional belts, such as the detachment zones, the efficiency of erosion or the temperature distribution (Agard, 2021; Avouac, 2003; Graveleau et al., 2012; Jamieson & Beaumont, 1998, 2013; Jamieson et al., 1996, 1998, 2002; Konstantinovskaia & Malavieille, 2005, 2011). Quantitative constraints about the thermal variation in space and time are necessary for understanding and modeling paleo-wedges (Girault et al., 2020; Jaquet et al., 2018; Thigpen et al., 2021). However, except along a few favorable crustal sections (e.g., Beyssac et al., 2007; Long et al., 2016; Grujic et al., 2020), thermal estimations are often scattered and not continuously quantified across the chain, leaving large volumes of metasediments uninvestigated. Unlike the hinterland, where metamorphic conditions can be approached by quantitative petrological investigations based on mineral parageneses, in the hinterland-foreland transition zones, where the metamorphic grade is lower, reconstructing the thermal architecture could be challenging. The main problems are related to the presence of high-variance mineral assemblages, i.e., the low number of phases, and to the small grain size of metamorphic minerals. These characteristics imply significant uncertainties in the thermobarometric estimates of low-grade rocks, representing a limitation for quantitative thermal investigations at the belt scale (Frey, 1987; Merriman & Frey, 1999; Merriman & Peacor, 1999). However, since the hinterland-foreland transition zones are made of nappes or tectonic units which occupy most of the collisional belt, they represent a natural laboratory to investigate the thermal variation and distribution necessary for the orogenic wedge comprehension.

Different geothermometers have been developed for low-grade metamorphic conditions, including crystallinity of illite or chlorite (Frey & Robinson, 1999; Jaboyedoff et al., 2001; Carosi et al., 2003; Vidal et al., 2016), vitrinite reflectance (Ferreiro Mählmann et al., 2012), calcite-dolomite thermometer (e.g., Bickle & Powell, 1977), chlorite + quartz + H_2O thermometer or K-white mica + quartz + H_2O barometer (Vidal & Parra, 2000; Dubacq et al., 2010), and Raman Spectroscopy on Carbonaceous Material (RSCM; Beyssac et al., 2002). The latter is based on the crystallinity of the Carbonaceous Material (CM). The advantage in using RSCM lies in its irreversibility, meaning that the CM structure is generally insensitive to retrogression, recording the highest temperature (T °C) experienced by the rocks, as well as the availability of different calibrations in large temperature ranges (Aoya et al., 2010; Beyssac et al., 2002; Lahfid et al., 2010).

Here, a complete *T* mapping based on RSCM across the hinterland-foreland transition zone of the Variscan belt exposed in Sardinia (Italy) has been presented, defining the peak temperature distribution during the nappe formation, thrusting, shear heating and post-nappe stacking deformation in a natural fossil orogenic wedge within the Variscan chain.

6.2. Investigated area and methods

The investigated area comprises: (i) the upper-greenschist-facies rocks belonging to the Internal Nappe Zone (near the Lula and Bitti villages; Fig. 6.1b; see Costamagna et al., 2012 for the *P-T* condition in the area); (ii) the Barbagia Unit (BU; Internal Nappe Zone; Fig. 6.1b) consisting of quartzitic and micaceous metasandstone alternating with metasiltstone, interbedded with grey phyllite referred to the Filladi Grigie del Gennargentu Fm. (Postgotlandiano Auct., Vai & Cocozza, 1974); (iii) the Meana Sardo Unit (MSU; Fig. 6.1b), associated with the External Nappe Zone, and made up of Middle Cambrian to Lower Ordovician silicoclastic succession (Arenarie di Solanas-San Vito Fm.; Calvino, 1959), Middle-Upper Ordovician metavolcanic rocks belonging to the Monte Santa Vittoria Fm. (Carmignani et al., 1994) and black graphitic shale with interbedded metalimestone layers (Scisti a Graptoliti Fm.), Silurian to Lower Devonian in age and covered by deformed Lower Carboniferous synorogenic flysch deposits (metaconglomerate, metasandstone, phyllite and quartzite with large olistolithic bodies; Carmignani et al., 1994).

The T_{RSCM} contour map was calculated using a linear interpolation algorithm with the Inverse Distance Squared Weighting (v.surf.idw tool), providing surface interpolation using numerical approximation (weighted averaging) techniques from vector point data. The isotherms were extrapolated by r.surf.contour tool in the QGIS 3.10.9 Coruña environment. Due to the emplacement of km-scale intrusive granitic bodies and the possible re-heating of CM, we sampled, as far as possible, at a minimum distance of approximately 100-200 m from its thermo-metamorphic aureola and from the associated pluri-m dykes, to exclude the occurrence of contact metamorphism overprinting. In addition to these considerations, no quartz annealing microstructures are present in the investigated samples confirming the absence of re-heating. Table 1 summarises the results of the spectrum decomposition for both samples analyzed in this work and previously discussed in Chapter 5 (see Appendix 1 for the name and position of investigated samples). In Appendix 2, representative examples of obtained Raman spectra in the investigated area are given. For each spectrum, the R2 ratio, the position of the graphite G band and D1, D2 defects bands and the corresponding T_{RSCM} (°C) with the relative simplified error is reported.

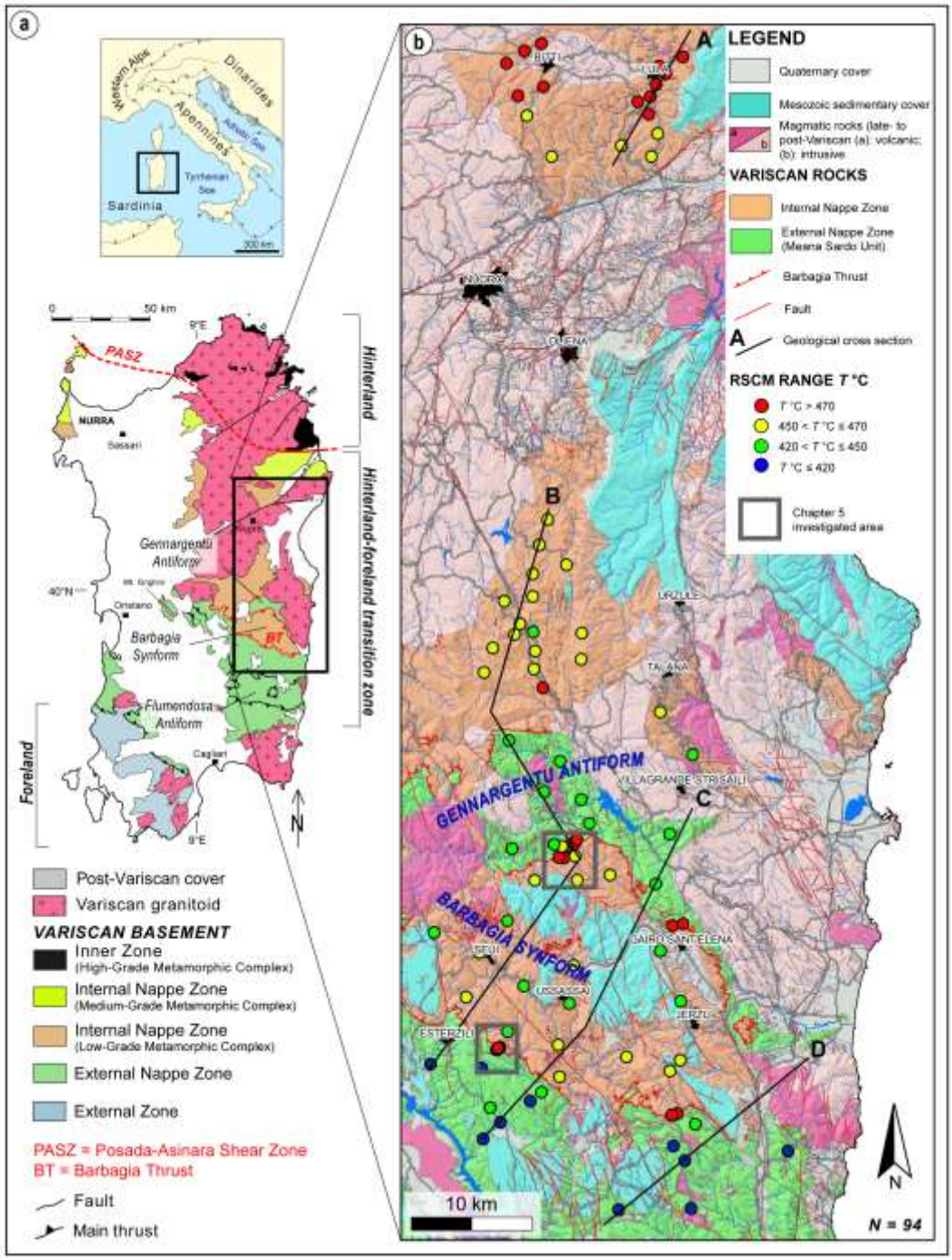

Figure 6.1: a) Geographic position and tectonic sketch map of the Sardinia island (modified from Carmignani et al., 1994). Location of figure 6.1b is highlighted by a black rectangle; b) schematic geological map of the Internal and External Nappe Zone showing peak metamorphic temperatures estimated through RSCM thermometry and trace of the cross-sections presented in figure 6.2. The location of Chapter 5 investigated areas is displayed by the grey rectangles.

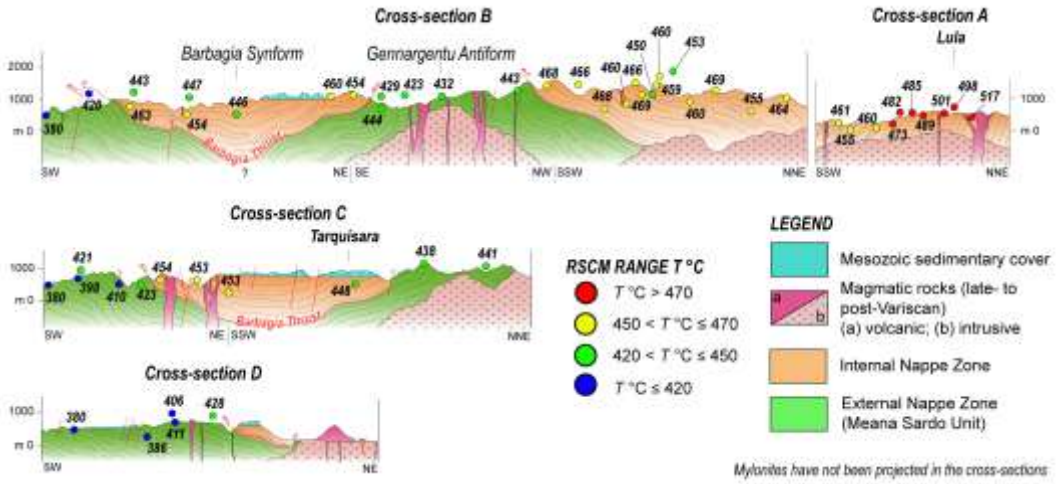

Figure 6.2: Original data plotted on the geological cross sections compiled after Carmignani et al. (1994, 2015), and the 1:50.000 geological maps of Jerzu and Muravera (CARG project, Pertusati et al., 2002). Symbols for T_{RSCM} refer to samples projected on the cross-section topography.

6.3. RSCM results

The obtained dataset consists of 76 samples (52 and 20 for Internal and External nappes, respectively, and four mylonites), integrated with the 18 samples from Chapter 5. All temperatures have been plotted on the geological map (Fig. 6.1b) and along four structure-orthogonal cross-sections (Fig. 6.2). A T_{RSCM} contour map of the entire investigated area was developed (Fig. 6.3), without considering the mylonitic samples as they were interpreted in Chapter 5 as related to shear heating rather than to the nappe-stacking regional metamorphism.

In the northernmost sector, i.e., the upper-greenschist-facies rocks of the Internal Nappe Zone, a southward decrease in T_{RSCM} from ~520 to ~450 °C is detectable (Fig. 6.3). The BU was investigated both in the northern limb of the Gennargentu Antiform and along the Barbagia Synform (Fig. 6.1b). The MSU was unraveled both in correspondence of the core of the Gennargentu Antiform and in the southern sector of the Barbagia Synform (Fig. 6.1b). A general southward decrease in T_{RSCM} from ~470-440 °C down to ~440-380 °C is observable in both BU and MSU, respectively (Fig. 6.3). The T_{RSCM} of the BU within the northern limb of the Gennargentu Antiform are homogeneous (~460 °C), and no evident systematic variations are recognizable (Fig. 6.3). The thermal distribution within the Barbagia Synform, made by the BU in the core, is less clear, but a decrease in T_{RSCM} from the northern sectors is recognizable (Fig. 6.3).

The MSU displays T_{RSCM} of ~435 °C and ~400 °C inside the Gennargentu Antiform and in the southernmost investigated sector, respectively (Fig. 6.3). A systematic decrease in T_{RSCM} from ~430 down to ~380 °C in the southernmost part of the MSU is present (Fig. 6.3).

A noticeable thermal difference between BU and MSU is highlighted by individual samples (Fig. 6.1b), as well as T_{RSCM} contour map and isotherms pattern (Fig. 6.3). In correspondence of the Gennargentu Antiform, the T_{RSCM} difference between both nappes is slightly lower (~10-20 °C) compared to the southernmost area, where it is above the absolute error of the RSCM method (~30-70 °C).

Sample	***Tectonic unit***	***n***	***R2***	***T(°C)***	***SE = STDEV/√(n- 1) ≤ 8***	***SD***
BI20	Internal Nappe Zone (upper-greenschist facies rock)	10	0.25	526	16	6
AP19-3	Internal Nappe Zone (upper-greenschist facies rock)	10	0.27	515	18	6
LU18	Internal Nappe Zone (upper-greenschist facies rock)	11	0.27	517	11	4
AP19-8	Internal Nappe Zone (upper-greenschist facies rock)	12	0.31	498	11	3
BI18	Internal Nappe Zone (upper-greenschist facies rock)	11	0.30	503	19	6
LU23	Internal Nappe Zone (upper-greenschist facies rock)	12	0.30	501	9	3
AP19-7	Internal Nappe Zone (upper-greenschist facies rock)	14	0.32	489	16	5
BI8	Internal Nappe Zone (upper-greenschist facies rock)	11	0.32	491	12	4
BI2	Internal Nappe Zone (upper-greenschist facies rock)	12	0.32	488	18	5
LU11	Internal Nappe Zone (upper-greenschist facies rock)	12	0.33	485	11	3
LU1	Internal Nappe Zone (upper-greenschist facies rock)	12	0.34	482	18	6
LU9	Internal Nappe Zone (upper-greenschist facies rock)	10	0.36	473	17	6
LU10	Internal Nappe Zone (upper-greenschist facies rock)	12	0.36	470	11	3
LU4	Internal Nappe Zone (upper-greenschist facies rock)	13	0.39	460	15	4
LU15	Internal Nappe Zone (upper-greenschist facies rock)	12	0.38	461	11	3
LU3	Internal Nappe Zone (upper-greenschist facies rock)	12	0.39	455	14	4
BI7	Internal Nappe Zone (upper-greenschist facies rock)	13	0.41	453	16	5
AP19-118	Internal Nappe Zone (Barbagia Unit)	9	0.38	464	19	7
2021_3	Internal Nappe Zone (Barbagia Unit)	12	0.40	455	9	3
2021_5	Internal Nappe Zone (Barbagia Unit)	10	0.40	454	20	7
AP19-161B	Internal Nappe Zone (Barbagia Unit)	12	0.37	469	8	2
AP19-19	Internal Nappe Zone (Barbagia Unit)	12	0.39	460	15	5
2021_9	Internal Nappe Zone (Barbagia Unit)	10	0.39	459	11	4
2021_8	Internal Nappe Zone (Barbagia Unit)	10	0.41	450	6	2
2021_10	Internal Nappe Zone (Barbagia Unit)	14	0.37	466	12	3
AP19-110	Internal Nappe Zone (Barbagia Unit)	10	0.37	468	11	4
2021_11	Internal Nappe Zone (Barbagia Unit)	15	0.38	460	11	3
AP19-187	Internal Nappe Zone (Barbagia Unit)	10	0.38	463	17	6
2021_12	Internal Nappe Zone (Barbagia Unit)	16	0.37	468	20	6
2021_60	Internal Nappe Zone (Barbagia Unit)	12	0.38	462	8	2
AP19-164	Internal Nappe Zone (Barbagia Unit)	10	0.37	468	18	6
2021_31a	Internal Nappe Zone (Barbagia Unit)	12	0.35	477	13	4
AP19-26	Internal Nappe Zone (Barbagia Unit)	13	0.40	453	11	3

Sample	Tectonic unit	n	R2	T(°C)	SE = STDEV/√(n- 1) ≤ 8	SD
BA3	External Nappe Zone (Meana Sardo Unit)	12	0.44	437	9	3
2021_53	External Nappe Zone (Meana Sardo Unit)	16	0.45	432	6	2
AP19-68	External Nappe Zone (Meana Sardo Unit)	14	0.47	423	2	1
AP19-72	External Nappe Zone (Meana Sardo Unit)	10	0.45	429	9	3
AP19-163B	External Nappe Zone (Meana Sardo Unit)	12	0.43	441	7	2
AP19-23	External Nappe Zone (Meana Sardo Unit)	12	0.41	450	6	2
AP19-41	External Nappe Zone (Meana Sardo Unit)	9	0.43	438	3	1
AP19-45	Internal Nappe Zone (Barbagia Unit)	7	0.37	469	15	6
2021_22	Internal Nappe Zone (Barbagia Unit)	12	0.38	460	13	4
BA9	Internal Nappe Zone (Barbagia Unit)	12	0.37	466	3	1
AP19-74	Internal Nappe Zone (Barbagia Unit)	10	0.41	446	9	3
2021_48	Internal Nappe Zone (Barbagia Unit)	10	0.43	441	7	2
2021_50	Internal Nappe Zone (Barbagia Unit)	17	0.40	454	8	2
AP19-47	Internal Nappe Zone (Barbagia Unit)	13	0.41	448	11	3
AP19-122	Internal Nappe Zone (Barbagia Unit)	11	0.39	458	6	2
AP19-165	Internal Nappe Zone (Barbagia Unit)	12	0.41	447	7	2
AP19-180	Internal Nappe Zone (Barbagia Unit)	11	0.36	471	12	4
AP19-48	Internal Nappe Zone (Barbagia Unit)	15	0.42	443	10	3
AP19-49A	Internal Nappe Zone (Barbagia Unit)	10	0.44	434	6	2
AP19-163A	Internal Nappe Zone (Barbagia Unit)	12	0.41	449	13	4
AP19-167	Internal Nappe Zone (Barbagia Unit)	12	0.40	453	10	3
AP19-162	Internal Nappe Zone (Barbagia Unit)	12	0.40	453	17	5
AP19-49B	Internal Nappe Zone (Barbagia Unit)	11	0.41	449	8	3
AP19-50	Internal Nappe Zone (Barbagia Unit)	11	0.41	450	8	3
AP19-24	Internal Nappe Zone (Barbagia Unit)	11	0.40	454	19	6
2021_66	External Nappe Zone (Meana Sardo Unit)	8	0.57	380	8	3
AP19-56	External Nappe Zone (Meana Sardo Unit)	7	0.48	423	2	1
AP19-58	External Nappe Zone (Meana Sardo Unit)	10	0.50	409	8	3
AP19-55	External Nappe Zone (Meana Sardo Unit)	10	0.46	428	9	3
AP19-70	External Nappe Zone (Meana Sardo Unit)	8	0.55	388	2	1
AP19-59	External Nappe Zone (Meana Sardo Unit)	14	0.47	421	2	1
AP19-140	External Nappe Zone (Meana Sardo Unit)	4	0.53	398	9	5
AP19-76	External Nappe Zone (Meana Sardo Unit)	10	0.57	380	10	3
AP19-54	External Nappe Zone (Meana Sardo Unit)	10	0.51	410	6	2
AP19-126	External Nappe Zone (Meana Sardo Unit)	12	0.50	411	2	1
AP19-75	External Nappe Zone (Meana Sardo Unit)	10	0.56	386	9	3
2021_59	External Nappe Zone (Meana Sardo Unit)	8	0.57	380	8	3
AP19-46	Mylonite	10	0.36	471	9	3
2021_74	Mylonite	12	0.28	513	2	1
AP19-52	Mylonite	11	0.34	479	9	3
AP19-53	Mylonite	13	0.36	473	7	2

Table 1: Results of the RSCM estimations with the Aoya et al. (2010) calibration. The number of spectra (n), mean R2 ratio for n spectra with the corresponding standard deviation (SD) and calculated temperature with standard error (SE= SD/√n) have been indicated. See Chapter 5 for the other used samples.

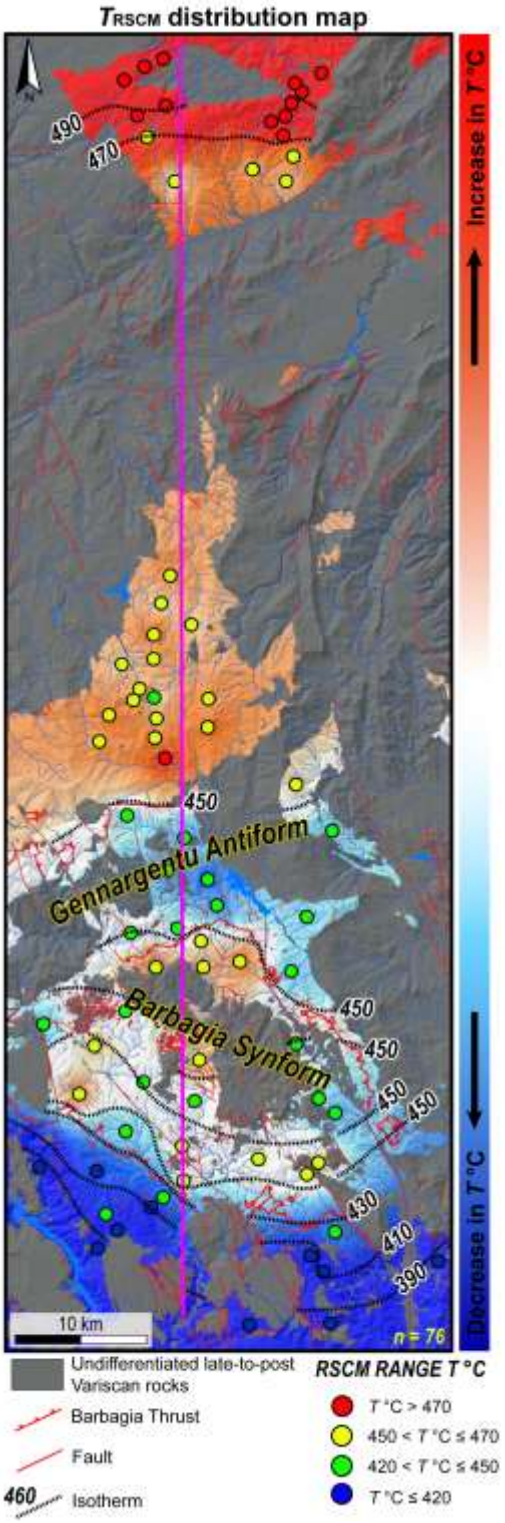

Figure 6.3: T_{RSCM} contour map and isotherms of the investigated area. The trace of the simplified tectonic cross-section shown in Figure 6.4 has been displayed in purple.

6.4. Discussion and conclusions

Using RSCM, a high-resolution description of the thermal architecture of the hinterland-foreland transition zone of the Sardinian Variscan belt is described. In the northernmost investigated sector of the Internal Nappe Zone, the derived T_{RSCM} within the Lula and Bitti villages (Figs. 6.1b and 6.2) are in agreement with those obtained with thermodynamic modeling estimations (~450-470 °C) on nearby samples by Costamagna et al. (2012), highlighting the reliability of the obtained RSCM data. The presence of garnet, plagioclase, biotite and white mica in the northernmost rocks is in agreement with the obtained T_{RSCM} of ~500-520 °C and *P-T* data from Franceschelli et al. (1989). The central Nappe Zone, where the juxtaposed BU onto the MSU crops out, is characterized by a more complex thermal architecture (Fig. 6.3). The BU displays a general T_{RSCM} of ~470-440 °C whereas the MSU has T_{RSCM} of ~440-380 °C. According to previous authors (Montomoli et al., 2018), obtained data fit with greenschist-facies metamorphism for both nappes reached during the burial and the pre-nappe stacking event associated with the early collisional stage. Previous investigations do not document a thermal difference between the BU and MSU (Franceschelli et al., 1992; Carosi et al., 2010; Montomoli et al., 2018). However, the T_{RSCM} coverage highlights a systematic difference between them of ~10-20 °C within the Gennargentu Antiform and ~30-70 °C in the southernmost sector (Figs. 6.3 and 6.4). At the belt scale, the thermal boundary between nappes follows the BT orientation developed during the nappe stacking (Figs. 6.3 and 6.4). New data coupled with the existing high- T_{RSCM} (~480-500 °C) reached along the BT were linked to shear heating during syn-nappe stacking and not the regional metamorphism (Chapter 5). The BT must be considered a major tectonic boundary that divides the internal sector from the external one of the Varisican orogenic wedge in Sardinia (Montomoli et al., 2018), dividing two major zones characterized by nappes showing different thermal conditions (Figs. 6.3 and 6.4). After the crustal thickening and the syn-collisional exhumation, all the previous structural elements were widely deformed by large-scale folds (i.e., the Gennargentu Antiform and the Barbagia Synform; Conti et al., 1999). Restoring the original pre-antiform and pre-synform attitude of the nappes, and if we assume that the peak temperature has been reached during the burial and the collisional metamorphism, the core of the Gennargentu Antiform could represent the deepest portion of the MSU, whereas the southernmost area the shallowest. Similarly, the deeper part of the BU is observable both in the northern limb of the Barbagia Synform and in the Gennargentu Antiform. This is widely confirmed by the general northward temperature increase inside the nappes (Fig. 6.4).

The T_{RSCM} shifting between the MSU and the BU is higher in the southernmost sector (~30-70 °C) than within the Gennargentu Antiform (~10-20 °C). The post-nappe stacking folded structure is also highlighted by the presence of the BT with the same structural and kinematic features and high- T_{RSCM} (Chapter 5; Fig. 6.4) in the two limbs of the Barbagia Synform.

The Upper Carboniferous-Permian intrusions cross-cut the main structures in the metamorphic basement and the associated isotherms architecture, pointing out how this thermal pattern was recorded during the collisional stage. The presence of a systematic and regular path in T_{RSCM} recognized across the entire hinterland-foreland transition zone in Sardinia allows the exclusion of any possible significant post-collisional contact metamorphism overprints in the investigated samples.

Orogenic wedge construction and its later evolution are driven by many factors, e.g., rheology, strain rates and erosion, which also control the wedge's thermal evolution and influence how strain is accommodated (Jaquet et al., 2018). Involving large-scale nappes, or tectonic units, covering most of the chain, the hinterland-foreland transition zone in collisional belts represents a key area to understand the nappe tectonics and the thermal architecture of orogenic wedges. In the Nappe Zone of the Sardinian Variscan belt, our data provide quantitative thermal constraints at the belt scale with a relative uncertainty of less than 10-15 °C, highlighting a complex thermal orogenic wedge architecture previously unrecognized. Obtained results highlight a scenario of: (i) syn-nappe stacking metamorphism and peak temperature acquisition during the collisional stage; (ii) syn-collisional exhumation of the Internal Nappe Zone associated with shear heating along thrust-sense structures (Chapter 5); (iii) subsequent regional-scale folding during the latest stage of collision, that drove the present-day thermal architecture.

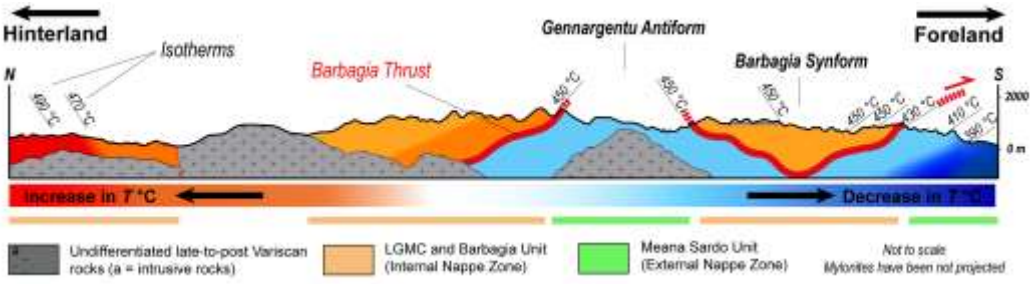

Figure 6.4: Thermal architecture of the study area in a cross-section view (see Fig. 6.3). Green and orange bars refer to the spatial extension of the Internal (orange) and External (green) nappes. The thick red line, that marks the Barbagia Thrust, suggests the role of shear heating along the shear zone. The spatial distribution of the isotherms occurrence is displayed.

Appendix

Appendix 1: Position and name of the analysed samples for the northern and central-southern investigated area (Chapter 5 non-mylonitic samples are included). The last one represents the analyzed mylonitic samples (Chapter 5 mylonites are excluded).

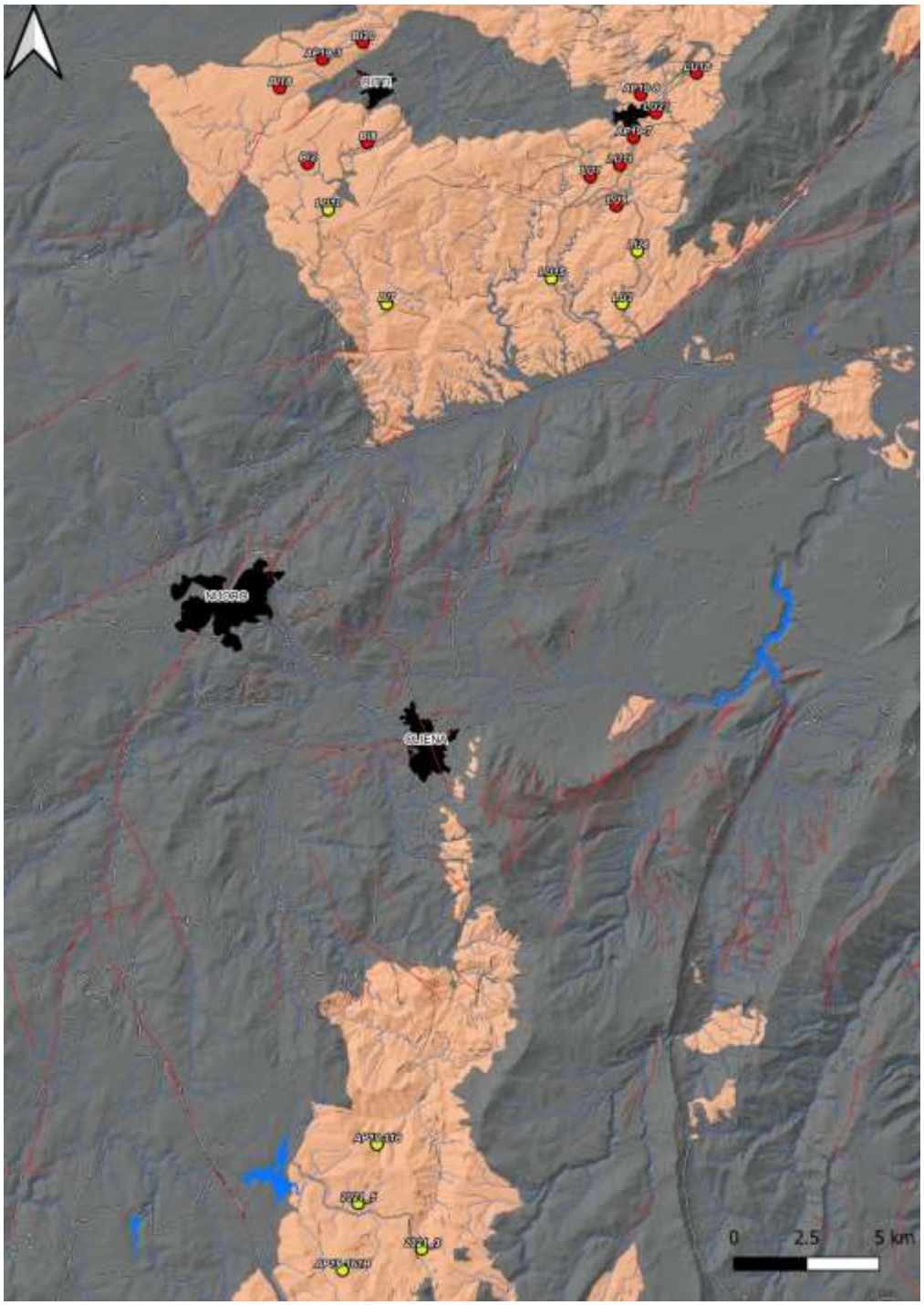

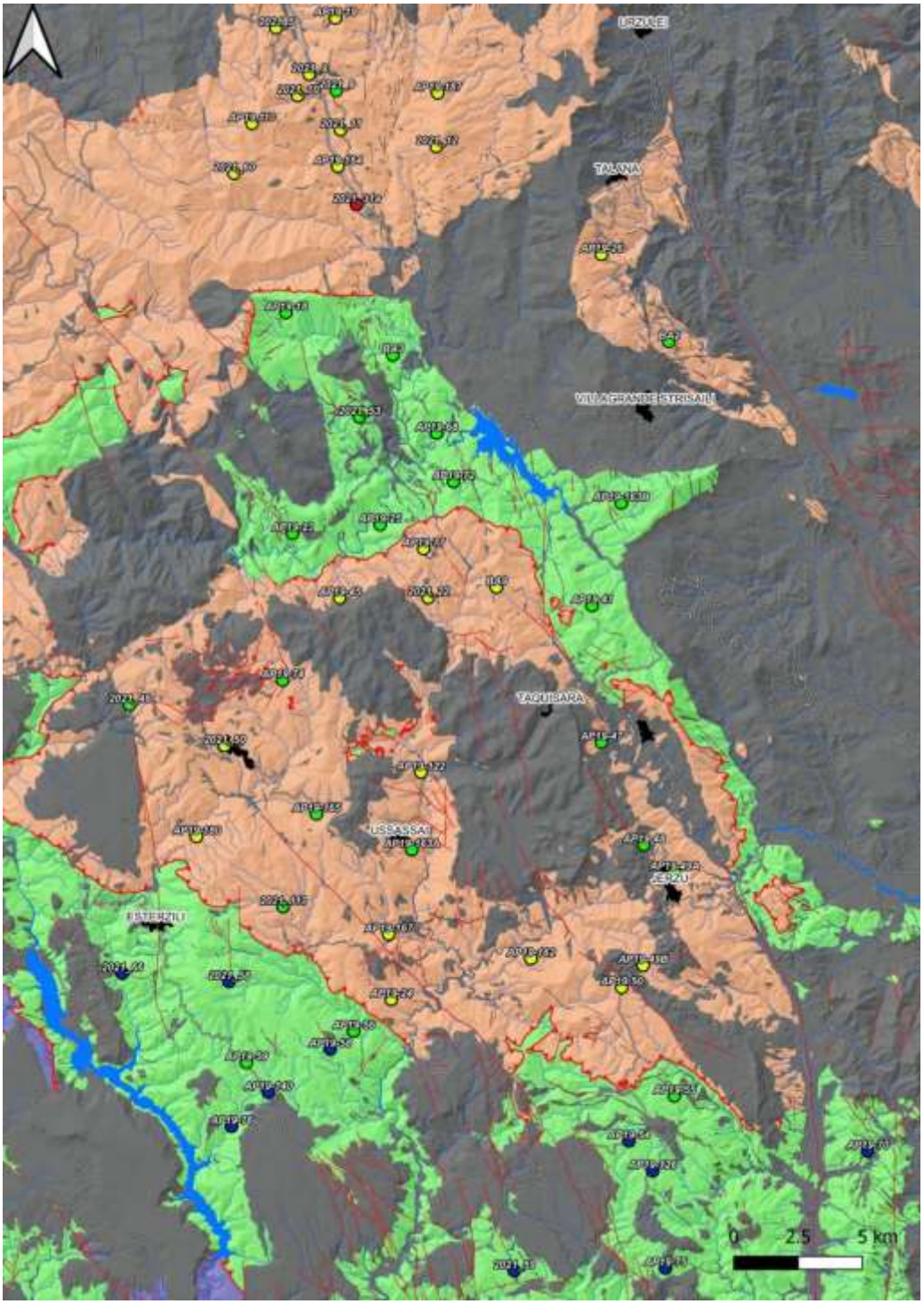
TALANA
VILLAGRANDE STRISAILI
TAQUISARA
0
2.5
5 km

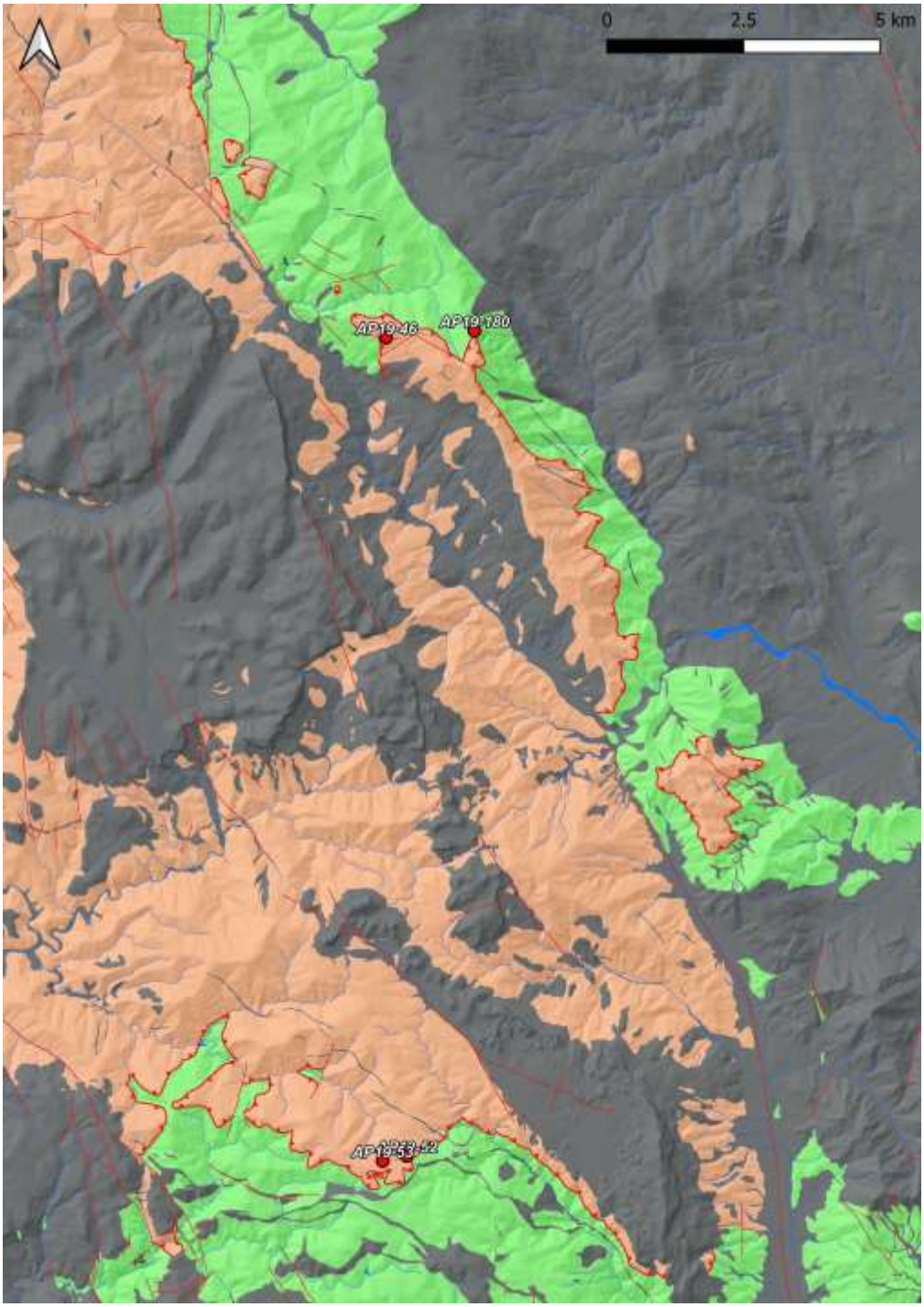
0
2.5
5 km
AP19-46
AP19-180

Appendix 2: Examples of representative Raman spectra of carbonaceous material obtained in the investigated area. For each spectrum, the R2 ratio and the corresponding T_{RSCM} (°C) with the relative simplified error have been indicated.

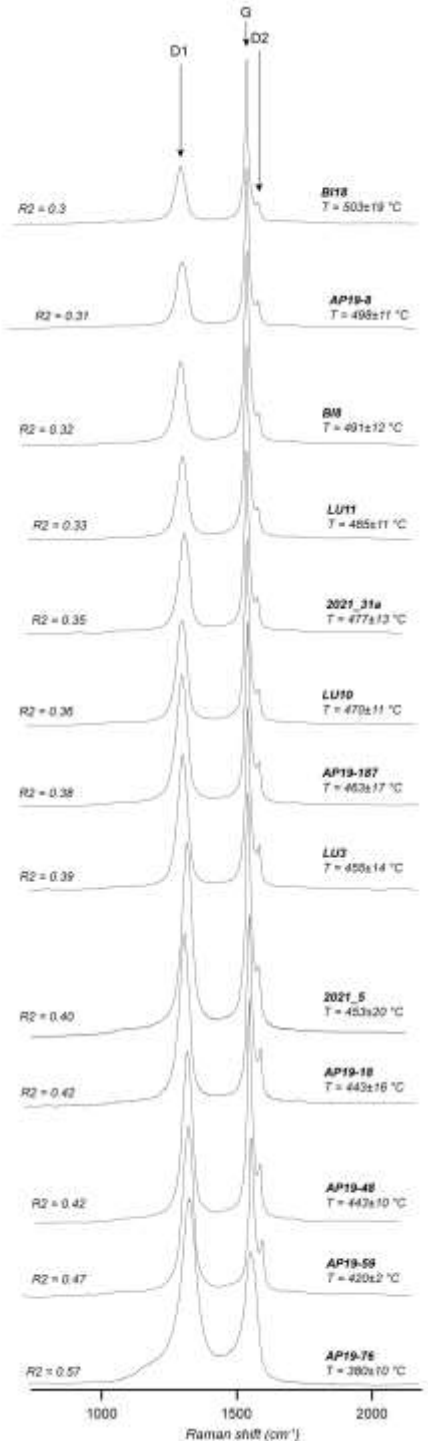

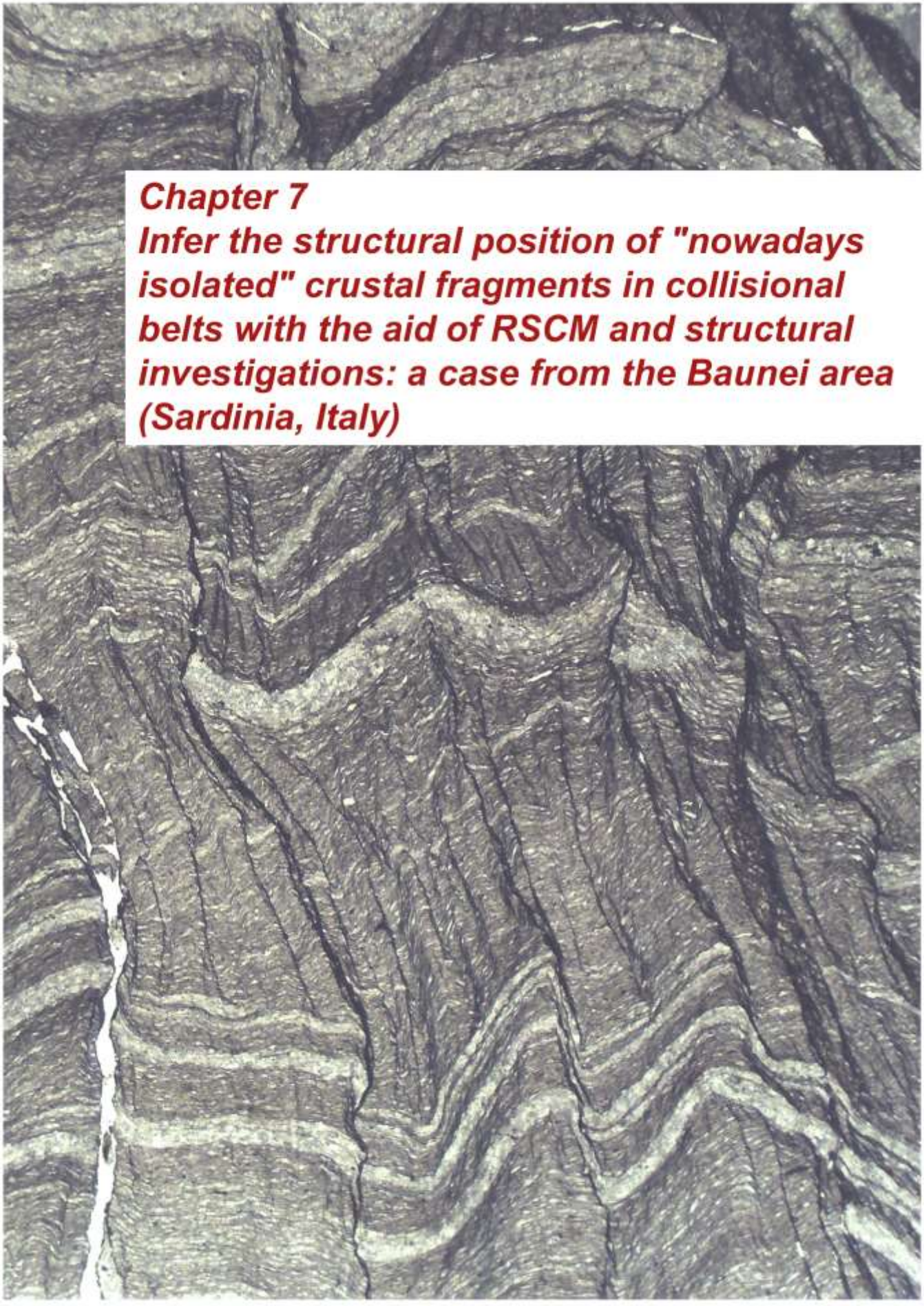

Chapter 7
Infer the structural position of "nowadays isolated" crustal fragments in collisional belts with the aid of RSCM and structural investigations: a case from the Baunei area (Sardinia, Italy)

7.1. Introduction

The concept of "structural level", i.e., the change of the deformation style (or regime), depends on the crustal depth linked to the related changes in temperature and pressure (Fossen, 2016). Faults and brittle features are prominent in the upper structural level (0-15 km), whereas, going deeper in the crust, ductile deformation and shear zones progressively drive the entire architecture (Fossen, 2016; Fossen & Cavalcante, 2017). Orogenic belts are natural laboratories to explore the relationship between deformation processes and tectonic structures at various scales across different depths within the crust (e.g., Gapais et al., 2005; Bastida et al., 2010; Sharib et al., 2021). In particular, the hinterland-foreland transition zone of collisional belts is characterized by metasediments that underwent nappe-stacking deformation, complex folding, low-grade metamorphism and thrust-sense shearing from different structural positions (Bell, 1978; Alsop, 1992; Schavemaker et al., 2012; Bastida et al., 2014; Hansberry et al., 2014; Vasquez-Serrano et al., 2021). Although most of the deformation has been concentrated within the thrust-sense movement shear zones that mark the boundaries between nappes, non-coaxial deformation far from the shear zone, i.e., in a shallow structural level, is accommodated by superposed generations of shear-related folds (Platt, 1983; Ez, 2000; Alsop & Holdsworth, 2004; Carreras et al., 2005; Bastida et al., 2014; Carreras & Druguet, 2019). In fact, ductile shear zones could be associated, in the upper structural framework, with contemporaneous folding, with axial surfaces sub-parallel to the shear zone boundaries (Hudleston, 1977; Ramsay et al., 1983; Passchier & Williams, 1996; Carreras et al., 2005; Nabavi & Fossen, 2021). Although field observation is fundamental in understanding the relationship between different deformative structures, at least a thermal constraint is needed to fix tectonic and structural elements within the crust or the nappe pile. In addition, the presence of post-collisional tectonic events (e.g., granitic intrusions, brittle fragmentation; Caggianelli et al., 2013) often strongly modify the present-day architecture of the belt, creating isolated metamorphic septa, which are challenging to be correlated within the crust and among each other.

This is the case of the Baunei area belonging to the Internal Nappe of the Sardinian Variscan belt (Fig. 7.1a; Carmignani et al., 1994). Due to the presence of low-grade metasediments rich in carbonaceous material, we performed Raman Spectroscopy on Carbonaceous Material (RSCM; Beyssac et al., 2002) as a primary method of investigation. Integrating our results with the existing RSCM coverage from the Internal Nappe Zone (Chapters 5 and 6), a westward decrease in temperature of ~50 °C has been highlighted.

To understand the meaning of this strike-parallel temperature decrease that does not follow the belt gradient and the reason of this cold isolated septum, i.e., the Baunei area, structural investigations at different scales have been performed.

The lack of mylonites and the presence of complex superpositions of fold generations with a vergence compatible with the sense of shear along the basal tectonic contact (i.e., the Barbagia Thrust, BT; Montomoli et al., 2018; Chapter 5), coupled with lower T_{RSCM} allows to define this isolated fragment as a structurally upper portion belonging to the Internal Nappe Zone. The present study highlights the importance of integrating T_{RSCM} with different scales of structural investigations to unravel low-grade basements and infer the structural position across the crust or the nappe pile of currently isolated belt fragments.

7.2. Investigated area and methods

The investigated area within the Baunei town is entirely located in the Barbagia Unit (BU) succession belonging to the Internal Nappe Zone. This unit (also known as 'Postgotlandiano'; Vai & Cocozza, 1974) consists of metasandstone interbedded with phyllite and quartzite, referred to as a single metasedimentary formation (Filladi Grigie del Gennargentu Fm.). The protolith age is from Cambrian to Ordovician (Carmignani et al., 1994; Pertusati et al., 2002). The post-Variscan magmatic rocks are represented by rhyolitic to rhyodacitic aplitic pluri-m dykes and km-scale intrusive granite surrounding the Baunei area (Upper Carboniferous-Permian; Carmignani et al., 2001). Due to the presence of the stratotype of the Genna Selole Fm. in the Baunei area, the Jurassic sequence has been deeply investigated by Dieni et al. (1983). The area is characterized by dolostone, shale and dolomitic limestone (Costamagna & Barca, 2004).

RSCM, due to the irreversible process of the increase in crystallinity with the heating of the Carbonaceous Material (CM), records the highest temperature experienced by the rocks (Beyssac et al., 2002).

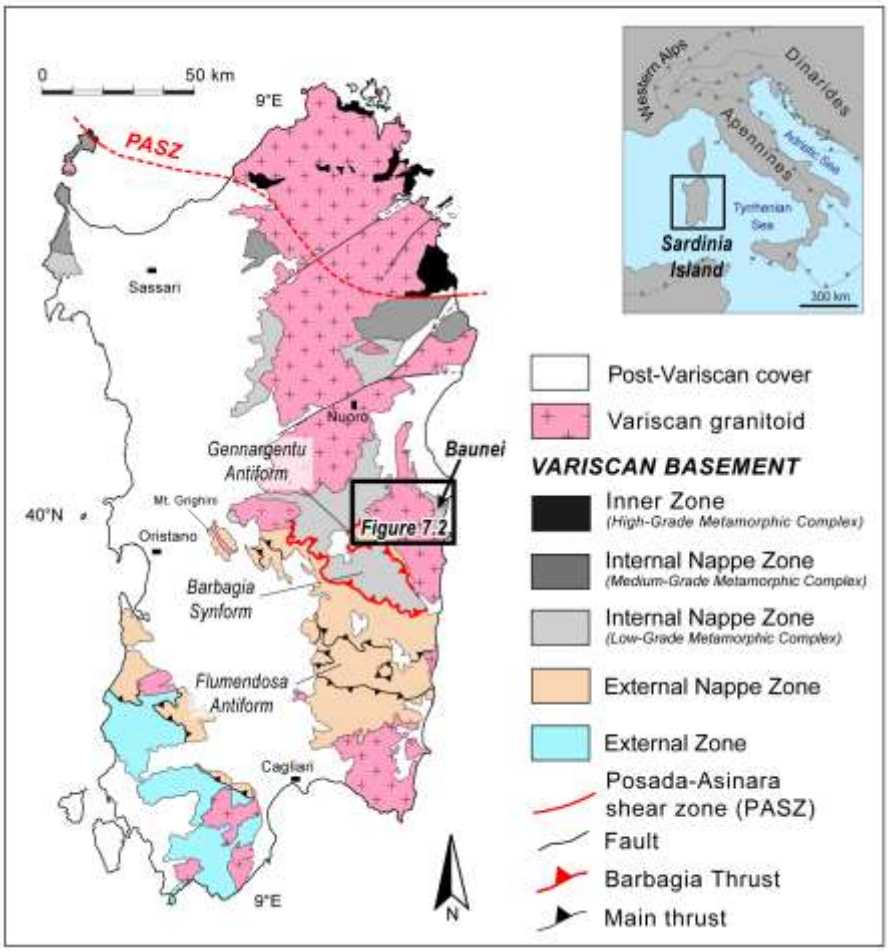

Figure 7.1: Tectonic map of the Sardinia island (modified after Carosi et al., 2020). The geographic position of the island has been provided.

7.3. RSCM thermometry

A total of six samples from the Baunei area were investigated by RSCM. A minimum of 10 spectra for each sample on CM perfectly embedded and non-damaged during polishing were obtained, with acquisition times from 30 to 60 s. The standard deviation for each sample (SD), necessary to assess the potential within-sample structural heterogeneity, following the procedures proposed by Beyssac et al. (2002), is provided. All investigated samples show a maximum standard error (SE=SD/√(n-1)) < 8. See Table 1 for sample details and T_{RSCM} results. The R2 parameter ranges between 0.47-0.50 with an average of 0.48. A homogeneous *T* distribution between ~408-423 °C, with an average of 420 °C, has been detected. No systematic differences in the obtained T_{RSCM} results have been detected from graphite lying in different structural positions.

Sample	n	R2	T(°C)	SD	SE = SD/√(n - 1) ≤ 8
AP19-161A	13	0.47	422	9	3
BA1	12	0.47	423	2	1
BA5	12	0.47	423	3	1
BA8A	12	0.47	422	4	1
BA8B 2	12	0.50	408	7	2
BA10	12	0.48	417	3	1

Table 1: Results of the RSCM estimations with the Aoya et al. (2010) calibration for the Baunei area. The number of spectra (n), R2 ratio with the corresponding standard deviation (SD), and calculated temperature (T °C) with standard error (SE) have been indicated.

Obtained results have been integrated with the existing T_{RSCM} coverage from Chapters 5 and 6 (see all data on the geological map in Fig. 7.2a), using a linear interpolation algorithm with the Inverse Distance Squared Weighting (v.surf.idw tool) in the GIS environment to derive a T_{RSCM} contour map of the interested sector (Fig. 7.2b). A progressive and systematic decrease in T_{RSCM} from W to E, i.e., toward the Baunei area, and from ~460 down to ~410 °C within the Internal Nappe Zone is recognizable (Fig. 7.2b). It is important to note that the thermal variation is BT-parallel (Figs. 7.2a, b), therefore perpendicular to the tectonic transport and the metamorphic gradient of the belt (Carmignani et al., 1994). The Baunei area is also colder than the MSU belonging to the External Nappe Zone, outcropping in the core of the Gennargentu Antiform (Fig. 7.2b). The presence of a systematic and homogeneous *T* recognized across the Baunei septum allows the exclusion of any possible significant post-collisional contact metamorphism overprint in the investigated samples.

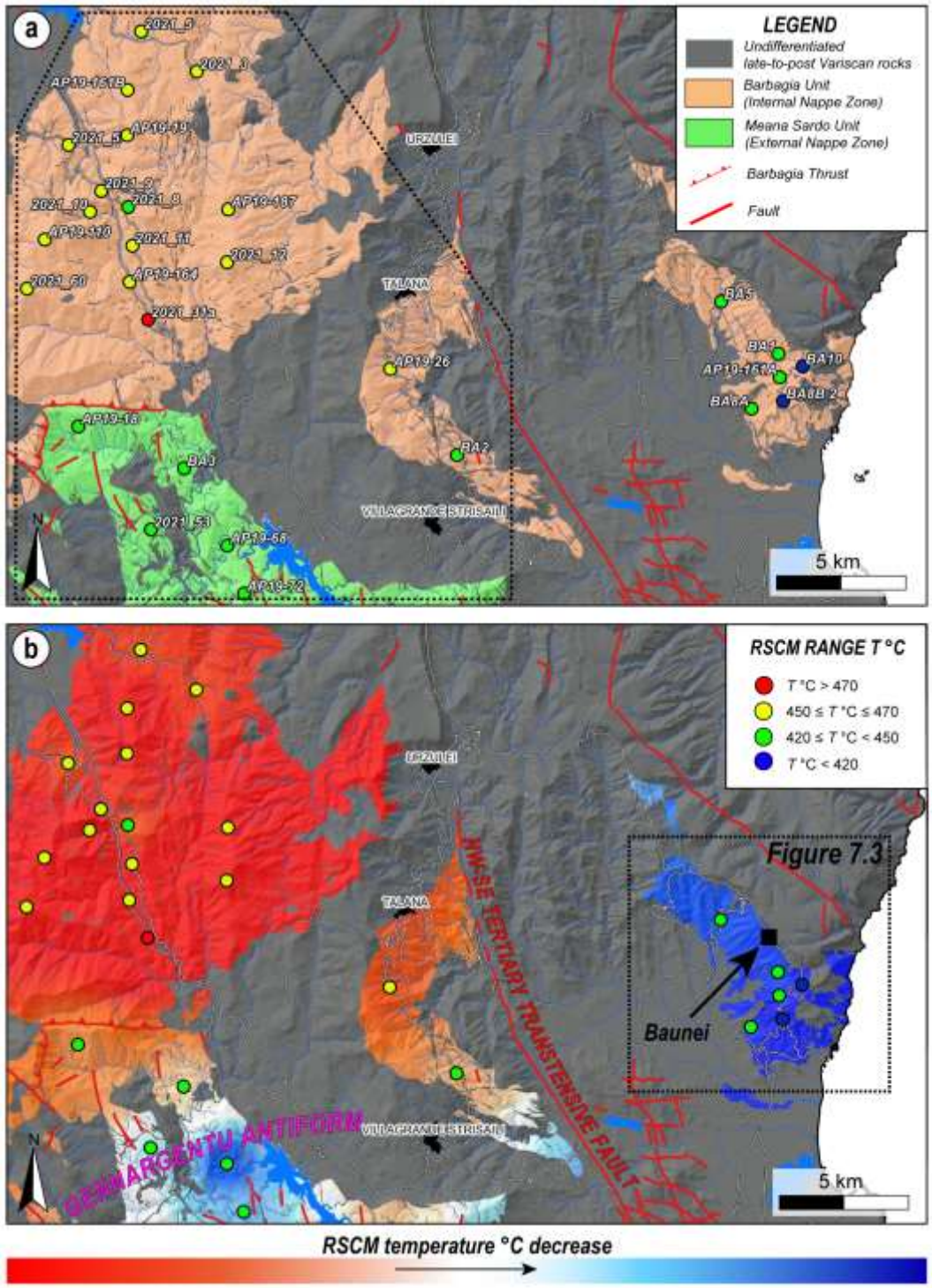

Figure 7.2: Geological map (a) and T_{RSCM} contour map (b) of the investigated area. Chapters 6 studied area has been highlighted. The trace of the main tertiary transtensive fault is displayed.

7.4. Structural analysis of the Baunei area

To understand the meaning of the obtained lower T_{RSCM}, structural investigations at different scales in the Baunei septum have been performed (Fig. 7.3). The structural architecture comprises four ductile phases, hereafter referred to as, besides the original bedding (S_0), D_1, D_{2a} and D_{2b} and D_3. The entire area is affected by late brittle deformation. Mineral abbreviations are after Warr (2021), meso- and microstructural elements have been classified according to Passchier & Trouw (2005), Fossen (2016) and Law (2014).

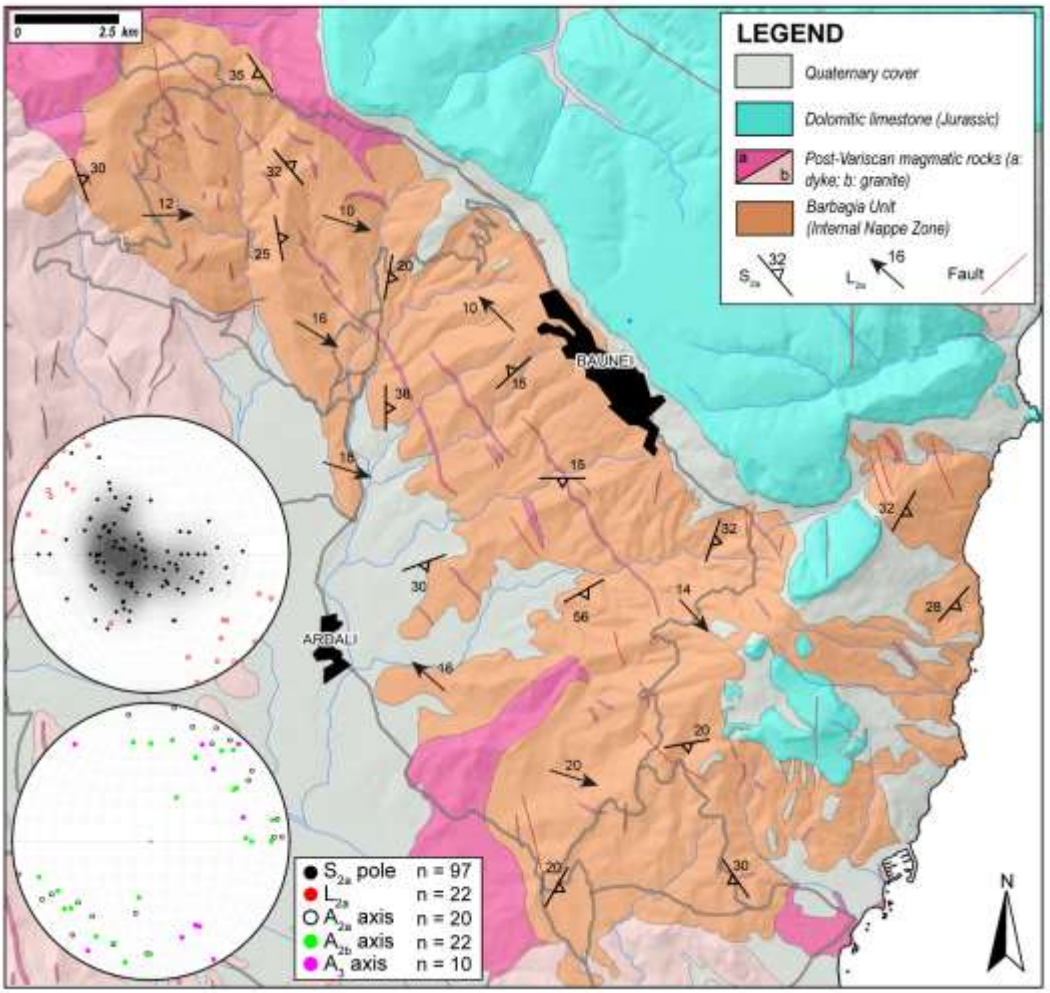

Figure 7.3: Geological sketch map of the study area (Baunei area, see Fig. 7.2b). Stereoplot (equal area, lower hemisphere projections) of the main structural elements are given.

7.4.1. D_1 deformation phase

The original bedding (S_0) is observable only where a strong lithological contrast is present. Relicts of the S_0 can be recognized as dismembered quartz lentoid fragments (Fig. 7.4a) or compositional alternation. The D_1 is represented by the S_1 foliation, generally parallel or at a moderate angle to the bedding. Due to complete transposition, it is often impossible to distinguish S_1 from S_0 (S_1//S_0). No evident mesoscopic folds linked to the D_1 phase are detectable in the field. The S_1 is defined by syn-kinematic recrystallization of white mica, chlorite, quartz, and rare albite, and can be recognized within the thickened hinges of F_2 folds and in S_2 microlithons from micro- to macro-scale (Fig. 7.4b).

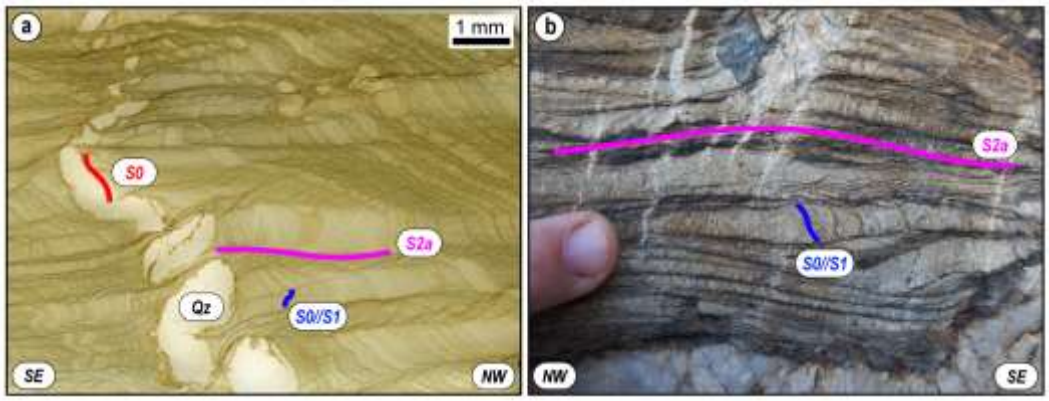

Figure 7.4: (a) Micro- and (b) mesoscale photos illustrating the multilayer sequence affected by the crenulation cleavage S_2. The relict S_1 foliation and, locally, the original bedding S_0 are recognizable.

7.4.2. D_2 deformation phase

The D_2 has been subdivided into two separate deformative events (D_{2a}-D_{2b}), still displaying similar structural features, metamorphic syn-kinematic mineral assemblage, and sense of transport but showing overprinting relationships.

7.4.2.1. D_{2a} deformation phase

The D_{2a} tectonic phase overprints older structures and can be detected all over the studied outcrops. The F_{2a} folds affect both the S_0 and the S_1 cleavage. F_{2a} folds are tight to isoclinal, overturned to recumbent, with a main S-SE-vergence (Fig. 7.5a). They vary from centimetric to pluri-metric in size and generally show rounded and thickened hinges with stretched limbs (Fig. 7.5a). Locally, rootless folds with stretched and broken limbs have been detected. According to Ramsay's classification (Ramsay, 1967), F_{2a} folds can be ascribed mainly to classes 1B (parallel) and 2 (similar).

A_{2a} axes and intersection lineations between S_{2a} foliation and folded S_0//S_1 surfaces show a NE-SW trend gently plunging with quite scattered values both toward the SW and the NE. The object lineations L_{2a} trend about N150 and plunge towards the N-NW and S-SE, nearly perpendicular to A_{2a} fold axes (Fig. 7.3). Parallel to F_{2a} axial planes, a well-developed S_{2a} axial plane foliation, striking E-W to N50E has been recognized. It is the main planar structural element identified in the whole study area. The dipping varies from sub-horizontal to about 70° towards the N-NW and S-SE (Fig. 7.3). The S_{2a} foliation is often ascribable to a crenulation cleavage, characterized by smooth cleavage domains showing a gradational to discrete transition to the microlithons where the S_1 foliation is still preserved (Fig. 7.5b). In more fine-grained rocks, the S_{2a} is a continuous and pervasive foliation (Fig. 7.5c). S_{2a} is characterized by syn-kinematic white mica and chlorite, elongated quartz crystals, and detrital re-oriented micas. The largest quartz grains are affected by undulatory extinction, deformation lamellae, deformation bands and bulging (BLG; Fig. 7.5d).

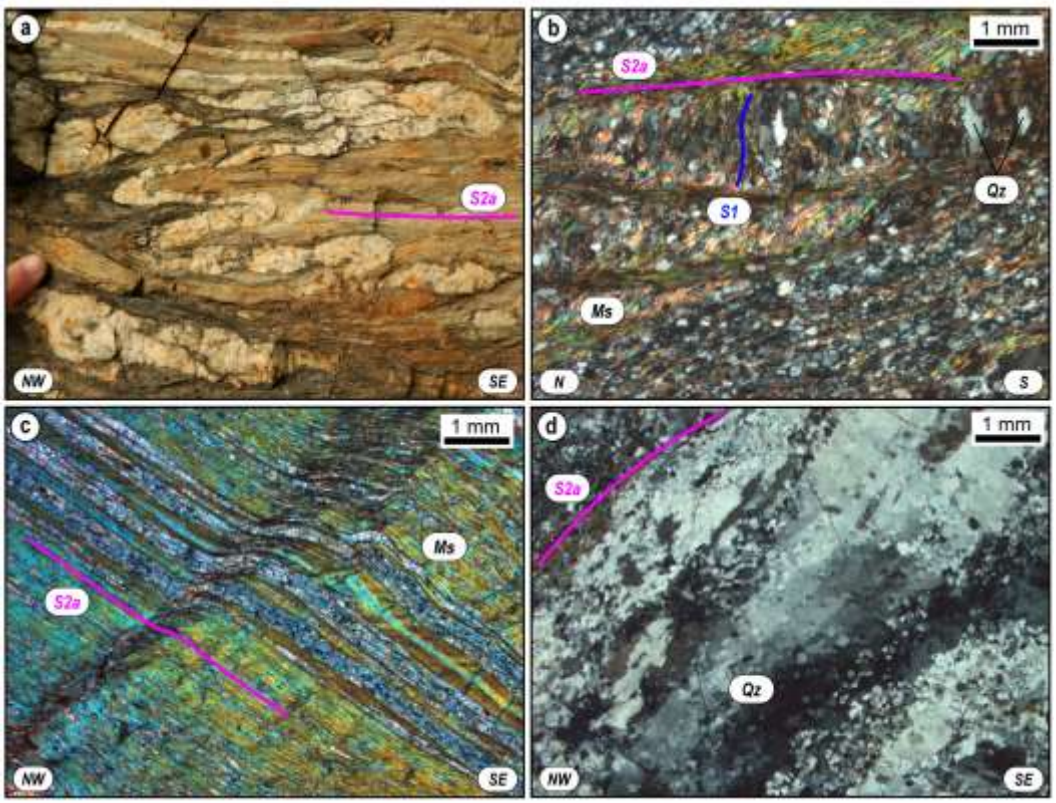

Figure 7.5: a) isoclinal F_{2a} folding highlighted by a more competent level, which develops an S_{2a} axial plane foliation; b) S_{2a} crenulation cleavage made of white mica and S_1 microlithons made of white mica and quartz (XPL: crossed-polarized light); c) S_{2a} foliation made of white mica levels and quartz-rich levels (XPL); d) S_{2a} quartz-rich levels affected by undulatory extinction (XPL).

7.4.2.2. D_{2b} deformation phase

D_{2b} folds range from centimetric to decametric in size and are concentrated in deformation belts of pluri-cm size (Fig. 7.6a). They are a S-SW-verging fold system developed from micro- to outcrop-scale (Fig. 7.6a). Folds have generally rounded hinges, and vary from tight, to close and isoclinal. The more competent layers are affected by boudinage and shear deformation along the F_{2b} fold limbs (Fig. 7.6a). The A_{2b} fold axes and the S_{2b}/S_{2a} intersection lineation show a generally NE-SW and W-E trend gently plunging with quite scattered values both toward the S-SE and the N-NE (Fig. 7.3). The F_{2b}-F_{2a} interference pattern shows parallel axes and sub-orthogonal axial planes (Fig. 7.6b; Type 3 Ramsay, 1967). The F_{2b} folds show an S_{2b} foliation parallel or subparallel to F_{2b} fold axial planes. The S_{2b} is generally a spaced crenulation cleavage present only in the F_{2b} hinge zone (Fig. 7.6c). This event is highlighted by local syn-kinematic white mica and chlorite, the re-orientation of the pre-existing grains and pressure solution (Fig. 7.6c).

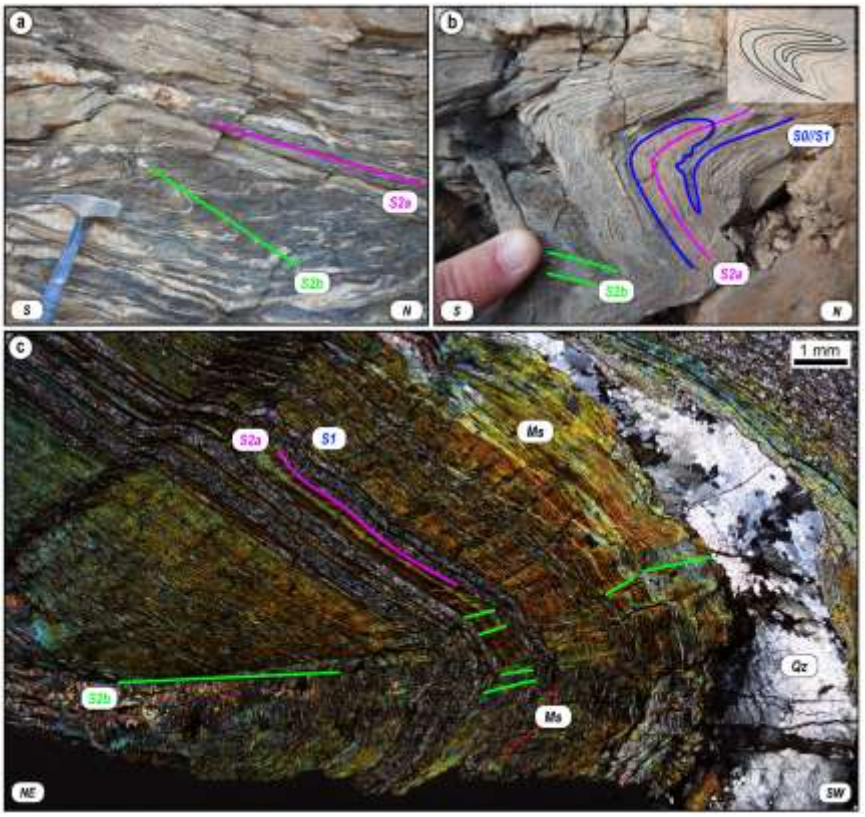

Figure 7.6: a) pluri-cm deformation band characterized by overturned F_{2b} folds affecting S_{2a} and locally developing an S_{2b} axial plane foliation; b) type 3 interference fold pattern affecting S_{2a} foliation with the local development of an S_{2b} crenulation cleavage; c) microscale evidence of S_{2b} spaced crenulation cleavage made of white mica, deforming S_{2a} foliation. S_1 is locally recognizable within microlithons (XPL).

7.4.3. D_3 phase and brittle deformation

The F_3 folds, occurring at scales ranging from outcrop- to macroscopic scale, are commonly gentle to open (Fig. 7.7a), from m- to pluri-m-long wavelength, parallel or slightly asymmetric folds. They are from upright to slightly inclined with a S-SE vergence (Fig. 7.7a). F_3 folds re-orient and deform the original attitude of the previous structural elements, causing a variation in the orientation of the S_{2a} and L_{2a} from S-SE to N-NW. A_3 fold axes plunge at low angles toward NE or SW, with scattered values (Fig. 7.3). The D_3 is almost coaxial with D_{2a} and D_{2b} phases. Generally, F_3 folds do not produce a pervasive axial plane foliation. However, a local and poorly pervasive crenulation cleavage, preferentially in originally clay-rich lithotypes, is recognizable (Fig. 7.7b). In thin-section, the main deformation mechanism is characterized by pressure solution (Fig. 7.7c), without metamorphic recrystallization. Sub-vertical to vertical transcurrent to normal fault network deforms all the previous ductile structures (e.g., S_1-S_{2a}; Fig. 7.7d). Locally, pluri-cm-thick cataclasites are recognizable. The field evidence of the fault distribution highlights one major fault system showing a main N150-N130 and a minor N-S.

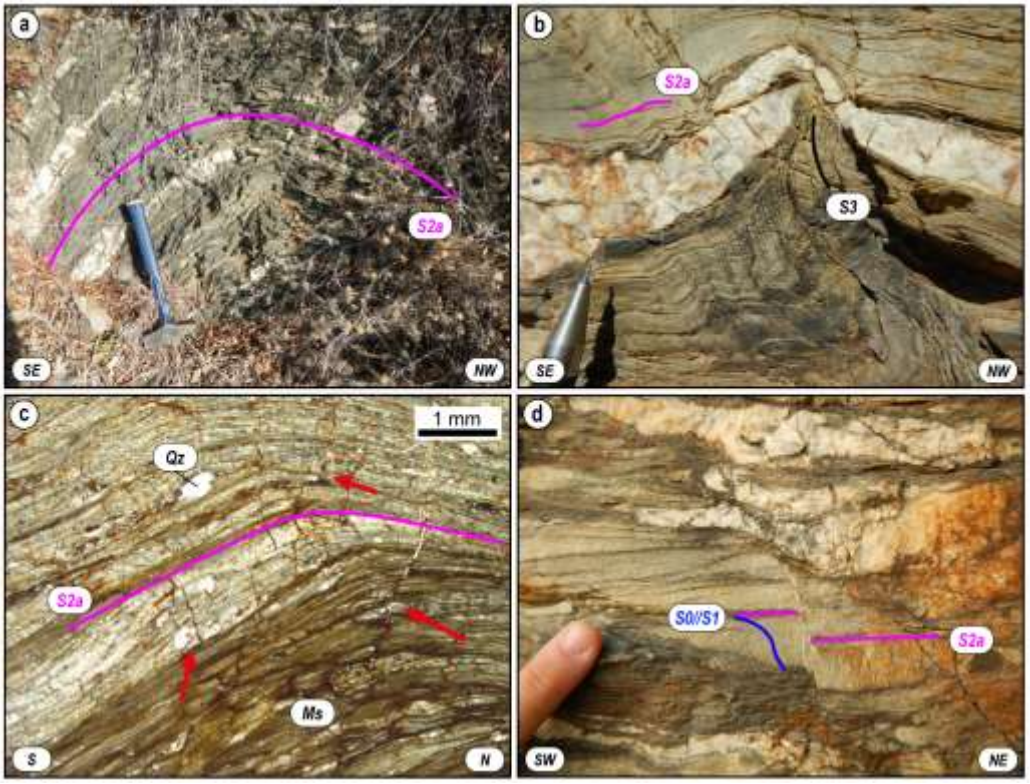

Figure 7.7: a) open F_3 folds affecting the S_{2a} foliation; b) S_3 crenulation cleavage produced by F_3 folding in clay-rich rock; c) microscale evidence of F_3 folding; d) brittle structures affecting metasediments with a normal sense of displacement.

7.5. Discussion

The classical deformation sequence recognized in the central sector of the Internal Nappe Zone in Sardinia (Carosi et al., 2004, Montomoli et al., 2018) is consistent with pre-, syn- and post-nappe stacking structures. The D_1 is related to the early stage of collisional history (Carosi et al., 2004). In contrast, the D_2 phase is linked to the syn-nappe stacking and the BT activity, with the overthrust of the Internal Nappe Zone on the External one. Based on meso- and microstructural observations in the Baunei area, a polyphase deformation history developing within a framework of a single protracted orogenic process, from pre- to post-nappe stacking, has been highlighted, resulting in four different contractional deformation phases (D_1, D_{2a}, D_{2b}, D_3; Fig. 7.8a).

The ongoing of the deformation during thrust-sense movement can lead to the superposition of similar-verging structures formed at different times but under the same deformation regime and metamorphic conditions (Oriolo et al., 2022). According to Carosi et al. (2004), the D_2 deformation phase is responsible for the development of the main foliation pervasive in all the Internal Nappe Zone (S_2) and asymmetric folds generated during shearing far from the BT. In the Baunei area, belonging to the Internal Nappe Zone, both D_{2a} and D_{2b} phases are characterized by complex folds patterns with a mainly S-vergence (Fig. 7.8a), in agreement with the sense of shear detected along the basal tectonic contact, i.e., the BT (Fig. 7.8b; Carosi et al., 2004; Montomoli et al., 2018). The S_{2a} syn-kinematic mineral assemblage (chlorite + white mica) indicates greenschist-facies metamorphic conditions and is in line with the obtained T_{RSCM} of Chapters 5 and 6. The same sense of tectonic transport, the coaxiality, and the similar mineral greenschist-facies assemblage of the D_{2b} enables to infer the D_2 as the ongoing of deformation during the syn-nappe stacking. Also, no mylonites have been detected during both D_{2a} and D_{2b}, but generally, D_2 is associated with it. The lack or presence of mylonite related to the shear deformation depends on the structural distance from the shear zone, i.e., the structural level of deformation across the crust (Fig. 7.8b; Vasquez-Serrano et al., 2021). Thus, the Baunei septum seems to record the shallow crustal deformation related to the BT shear activity (Fig. 7.8b).

All the previous structural elements are widely deformed by weakly asymmetric to upright D_3 folds. Admitting that the shortening direction had to be perpendicular to the axial planes and to the trend of fold axes, the direction of tectonic transport was essentially the same for all the D_{2a}, D_{2b} and D_3 events (Chapter 4). Metamorphic conditions do not seem to vary significantly between D_1 and D_2, while distinct evidence of cooling is seen from D_2 to D_3, from blastesis to dissolution (Montomoli et al., 2018; see also previous chapters).

This result, in agreement with the model of Conti et al. (1999) and Carmignani et al. (1994), emphasizes the presence of large-scale structures acquired in a contractional setting during the late deformation stage of crustal thickening. Also, the lack of metamorphic mineral growth during the D_3 is consistent with regional horizontal shortening under upper-crustal conditions.

After the nappe-stacking evolution, during the lower Carboniferous-Permian, the basement was widely intruded by the Sardo-Corso batholith (Casini et al., 2012). The presence of homogeneous *T* obtained in the Baunei area, similar but lower to the previously recognized across the entire hinterland-foreland transition zone in Sardinia (Chapter 6), allows the exclusion of possible significant post-collisional contact metamorphism overprinting in the investigated samples. The metamorphic basement was subsequently affected by normal to transtensive tertiary faults (Carmignani et al., 2001, 2016; Oggiano et al., 2009, 2011; Dieni et al., 2011). Evidence of this brittle deformation has been observed as NW-SE and N-S oriented normal faults in the investigated area. From a regional scale point of view, the Baunei septum is tectonically divided by km-scale normal faults in its eastward side, close to the Talana septum. These structures have strongly deformed the Internal Nappe Zone, leading to the exposition of different portions across the nappe pile, i.e., the Baunei area.

To summarise, the lower *T* respecting the existing RSCM coverage (Chapters 5 and 6), coupled with the presence of a complex superposition of similar-looking folds instead of mylonites, allow to ascribe the Baunei area as a shallow sector belonging to the Internal Nappe Zone (Fig. 7.8b). The reason of the present-day exposure of this septum could be explained by the presence of tertiary normal faults that drag down the Baunei area from the nappe pile. This study shows the importance of integrating RSCM with a combination of structural investigations at different scales to obtain reliable information about the thermo-structural architecture of isolated septa and unravel their meaning across the crust and in the function of the deformation style.

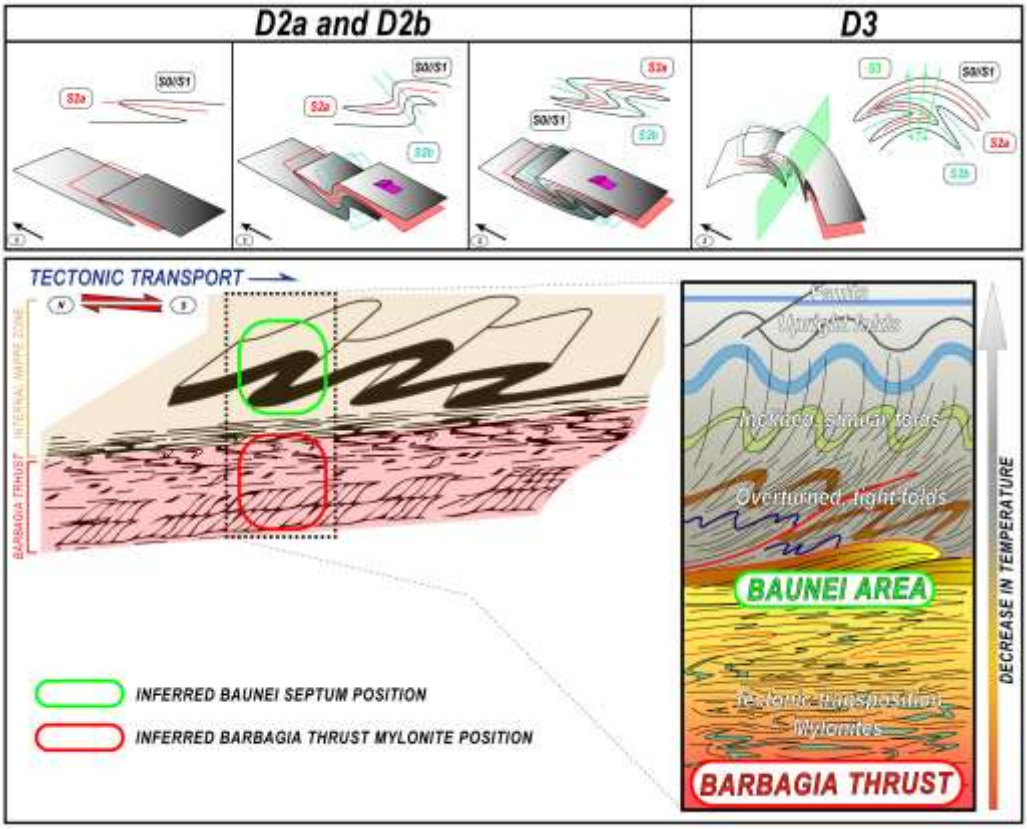

Figure 7.8: a) *Synoptic reconstruction of the contractional deformation history of the Baunei septum; b) Inferred position of the Baunei septum in both the nappe pile and in the crust.*

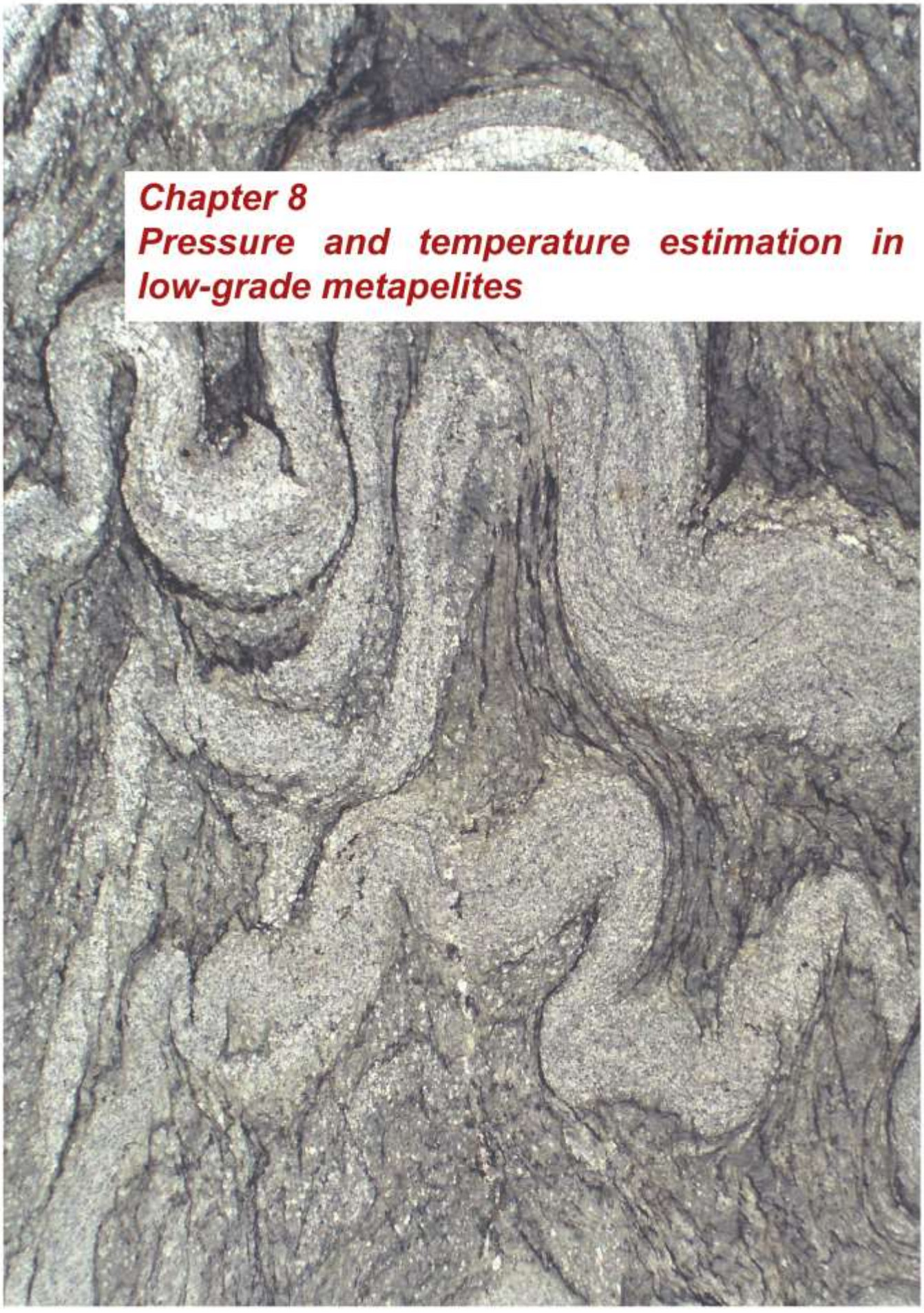

Chapter 8
Pressure and temperature estimation in low-grade metapelites

8.1. Introduction

Knowledge of collisional orogenic belts relies on the accurate determination of pressure (*P*) - temperature (*T*) conditions attained during burial and exhumation (Miyashiro, 1961). Quantitatively estimating the *P-T* conditions of individual samples allows geologists to develop robust tectonic models and simulate Earth's processes (e.g., Spear et al., 2016; Lanari & Duesterhoeft, 2019). *P-T* determinations are based on accurate thermobaric estimates within systems assumed to be at the chemical equilibrium (Spear et al., 2016; Engi et al., 2017; Lanari & Hermann, 2020). Two main modeling strategies are available for *P-T* determination (Holland & Powell, 2010; Lanari & Duesterhoeft, 2019 and references therein): inverse and forward modeling. Conventional thermobarometry (empirical) and multi-equilibrium thermobarometry (semi-empirical) are inverse methods in which mineral compositions are used to determine metamorphic conditions (e.g., Cathelineau, 1988; Powell & Holland, 1988, 1994; Berman, 1991; Gordon, 1992; Vidal & Parra, 2000; Bourdelle et al., 2013; Bourdelle & Cathelineau, 2015; Vidal et al., 2016). These thermobarometers assume that the chosen mineral compositions represent a single frozen-in equilibrium state. Comparatively, forward modelling relies on internally-consistent thermodynamic databases, and is based on experimentally or empirically calibrated *T*- and/or *P*-dependent equilibria between minerals considered to be in equilibrium. The first generation of internally consistent thermodynamic databases and solution models, also known as activity-composition (a-*X*) relations, led to the growth of multi-equilibrium thermobarometry. By contrast, in forward models, equilibrium mineral assemblages can be predicted at any *P-T* conditions by minimizing the total Gibbs free energy of a system with a specific bulk composition of interest (*X*; Powell & Holland 1990; Powell et al., 1998; De Capitani & Petrakakis, 2010; Yakymchuk, 2017). This approach is considered the most robust because *P-T* conditions may be constrained using both mineral compositions and the mineral assemblage (Connolly, 2005; Powell & Holland, 2008, 2010; see reviews by Holland & Powell, 2011 and Lanari & Duesterhoeft, 2019). Phase diagrams showing the equilibrium mineral assemblages at any specified *P-T-X* conditions permit the additional calculation of mineral modes and isopleths (e.g., Spear, 1988; Spear et al., 2016). Alternatively, *P-T* conditions may be determined using empirically calibrated thermobarometers, which are based on various parameters. These include the concentration of trace elements in a phase (trace element thermometry, e.g., Zr-in-Rt or Ti-in-Qz; Tomkins et al., 2007), the degree of crystallinity of different phases (e.g., graphite with Raman Spectroscopy on Carbonaceous Material thermometry, RSCM; Beyssac et al., 2002; Aoya et al., 2010), or the elastic anisotropy of a host-inclusion system (elastic barometry; Kohn, 2014).

Low-grade metamorphic rocks, particularly metapelites (metamorphosed clay-rich sedimentary rocks), are abundant in collisional belts, i.e., orogenic wedges (Frey, 1987; Frey & Robinson, 1999). Elucidating their metamorphic conditions is fundamental for comprehending ancient and actual tectono-metamorphic processes at convergent plate margins. Despite the significant occurrence of such rocks and the impressive progress in modeling over the last two decades, relatively fewer methods, compared to metamorphism at a higher pressure and temperature conditions, are available for *P-T* determination in low-grade metapelites (Thompson, 1957; Frey, 1987; Merriman & Frey, 1999; Merriman & Peacor, 1999; Bourdelle, 2021). The main barriers to robust *P-T* determination in low-grade rocks include: (i) the presence of a mosaic of local equilibria rather than a well-equilibrated assemblage; (ii) high variance assemblages involving few index minerals; and (iii) small grain size. Chemically-zoned minerals (e.g., chlorite) and detrital phases are often present at low-grade conditions and, in using phase equilibrium forward models, a reactive bulk composition which discards detrital phases or the interior of zoned minerals that do not participate in the reactions is required (e.g., Lanari & Engi, 2017). The development and refinement of inverse thermodynamic methods starting with conventional thermobarometry and progressing to multi-equilibrium, improved with quantitative high-resolution X-ray micro-mapping techniques and programs (Lanari et al., 2014), offer new opportunities to study low-grade rocks. Low-grade rocks are generally associated with a low number of phases exchanging a small number of elements (e.g., quartz, K-white mica, chlorite, albite in a system SiO_2-Al_2O_3-FeO-MgO-Na_2O-K_2O-H_2O) and result in large stability fields in the *P-T* space. Several authors have tried to address this challenge situation by developing solution models that can reproduce the compositions observed in nature (Vidal et al., 2005; Dubacq et al., 2010). An alternative strategy consists of the integration of different approaches, e.g., chlorite + quartz + H_2O thermometer (Vidal et al., 2006; Grosch et al., 2012; Cantarero et al., 2014, 2018) and K-white mica + quartz + H_2O barometer (Dubacq et al., 2010; Ganne et al., 2012; Lanari et al., 2012), to derive the *P-T* conditions. Although it seems to be the less critical problem, several complexities arise in investigating the chemical variability of small mineral grains. However, several aids come from the development of methods based on the crystallinity of different phases, independently from their chemistry and size (e.g., illite and chlorite; Merriman et al., 1990, 1995; Jaboyedoff et al., 2001; Vidal et al., 2016 and graphite with RSCM; Beyssac et al., 2002; Aoya et al., 2010). Thus, investigating low-grade metamorphism requires alternative strategies and complex petrological models (Cantarero et al., 2014, 2018; Scheffer et al., 2016; Vidal et al., 2016). The typical and most used approach to study low-grade rocks is the inverse method and the ones based on the crystallinity of the phases (e.g., Agard et al., 2010; Lanari et al., 2012, 2014; Pourteau et al.,

2013; Scheffer et al., 2016; Di Rosa et al., 2017, 2019; Verdecchia et al., 2019; Pérez-Cáceres et al., 2020; Sanità et al., 2022). Forward methods such as mineral assemblage diagrams are also applied to low-grade rocks in order to derive the *P-T* conditions and path and develop tectonic models (e.g., Lo Pó et al., 2015; Boedo et al., 2016; Balen et al., 2017; Franceschelli et al., 2017), but the strengths and limitations of doing so have never been deeply discussed and need a critical study and examination.

The Sardinian Variscan belt, due to the presence of several metamorphic constraints in its high-grade complex and the lack of *P-T* conditions of the low-grade metasediments from the Nappe Zone or the hinterland-foreland transition zone, represents a good area to compare these approaches. This chapter evaluates the reliability of thermodynamic databases for phase diagram modeling of low-grade metapelites. Moreover, it assesses whether *P-T* conditions from phase equilibrium diagrams are consistent or different from those derived from the inverse method combined with RSCM.

8.2. Investigated area and methods

The investigated samples come from both the Barbagia Unit (BU; Fig. 8.1b) and the Meana Sardo Unit (MSU; Fig. 8.1b), belonging to the Internal and External nappes. After a careful investigation of more than 100 thin sections across the hinterland-foreland transition zone, three samples (2021_5 and AP19-49 from the Internal Nappe Zone; AP19-76 from the External Nappe Zone; Fig. 8.1b) were selected for microstructural and mineral chemistry analysis. They have been previously investigated by RSCM thermometry (Chapter 6). Mineral compositions and quantitative compositional maps were obtained with a JEOL JXA 8200 electron probe micro-analyzer (EPMA) located at the Institute of Geological Sciences of the University of Bern, Switzerland, following the procedure described in Lanari et al. (2017). Analytical conditions for the mapping were 15 KeV accelerating voltage, 10 nA specimen current and 90 ms dwell time. X-ray maps of Al, Fe, K, Mg, and Na were acquired by wavelength-dispersive spectrometry (WDS), whereas Ca, P, Si, and Ti were by energy-dispersive spectroscopy (EDS). The program XMapTools 4 (Lanari et al., 2014, 2019) was used for classification and analytical standardization.

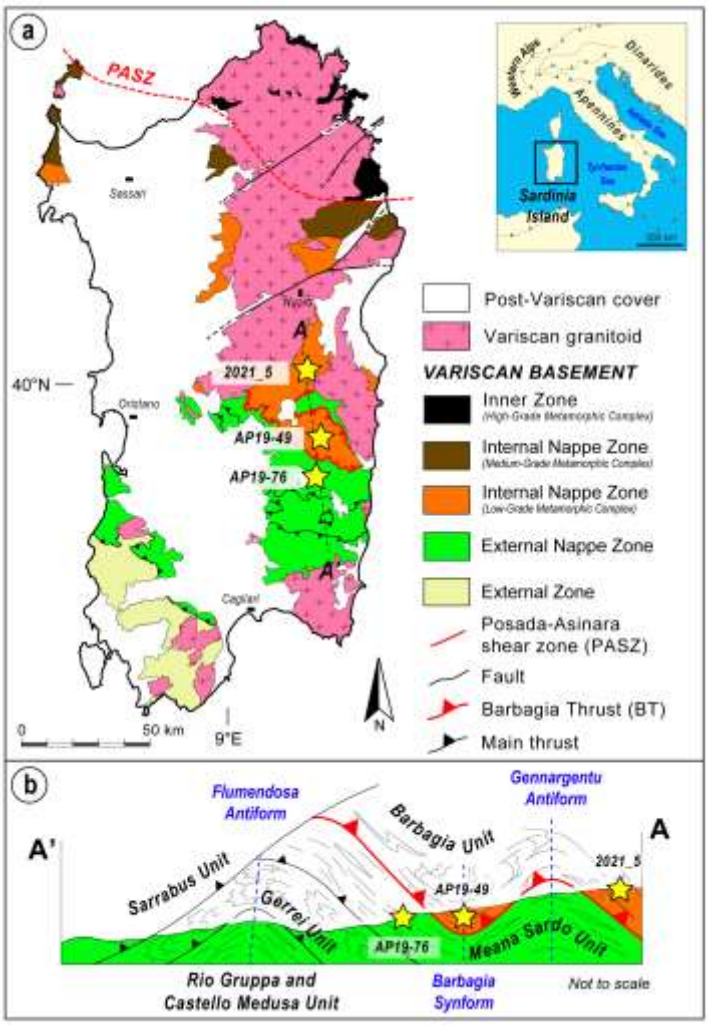

Figure 8.1: a) Tectonic sketch map of the island of Sardinia (modified after Carosi et al., 2020). b) Schematic geological cross-section (A-A') along the Nappe Zone (modified after Carmignani et al., 1994; Conti et al., 1999, 2001). The position of the three investigated samples is indicated in both figures.

8.3. Samples

Samples 2021_5 (Fig. 8.2a) and AP19-49 (Fig. 8.2b) are phyllites from the northern and central sectors, respectively, belonging to the Internal Nappe Zone, whereas sample AP19-76 (Fig. 8.2c) is a phyllite from the External Nappe Zone. All samples are characterized by a similar mineral assemblage, with white mica, quartz, and chlorite (± rutile, apatite, zircon). Albite is present in samples 2021_5 and AP19-76. The main foliation (S_p) is defined by the grain shape preferred orientation (GSPO) of micas and quartz and forms a crenulation cleavage recognizable in all samples. A continuous to spaced cleavage, S_{p-1}, characterized by the same previous assemblage, is preserved within the microlithons.

Sample 2021_5 contains 35 vol% quartz, 34% K-white mica, 16% chlorite, and 14% albite with the accessory minerals accounting for ~1% (Fig. 8.2a). In sample AP19-49, quartz constitutes 22 vol%, K-white mica 54%, chlorite 23%, and accessories 1% (Fig. 8.2b), and in the AP19-76 sample (Fig. 8.2c), quartz constitutes 15 vol%, K-white mica 66%, chlorite 18%, albite 0.5%, and accessories 0.5%. Representative microprobe analysis of both K-white mica and chlorite for all three samples are reported in Table 1-2.

2021_5					***AP19-49***					***AP19-76***				
K-white mica					*K-white mica*					*K-white mica*				
	High-Si (P1)		*Low-Si (P2)*			*High-Si (P1)*		*Low-Si (P2)*			*High-Si (P1)*		*Low-Si (P2)*	
SiO_2	46.98	46.40	46.70	46.38	SiO_2	47.77	47.28	46.78	47.13	SiO_2	47.04	46.05	45.73	46.36
Al_2O_3	33.68	32.69	36.31	35.77	Al_2O_3	31.54	30.10	31.02	32.29	Al_2O_3	34.30	34.67	35.99	36.07
FeO_{TOT}	2.03	2.73	1.32	1.38	FeO_{TOT}	2.29	3.19	2.52	1.93	FeO_{TOT}	1.08	1.18	1.01	1.13
MnO	0.00	0.01	0.02	0.00	MnO	0.00	0.05	0.00	0.03	MnO	0.00	0.00	0.02	0.00
MgO	0.80	0.97	0.63	0.59	MgO	1.29	1.92	1.76	1.66	MgO	0.79	0.84	0.72	0.83
CaO	0.00	0.00	0.00	0.01	CaO	0.01	0.00	0.01	0.01	CaO	0.02	0.03	0.03	0.01
Na_2O	0.53	0.44	0.86	0.45	Na_2O	0.13	0.11	0.17	0.15	Na_2O	0.70	0.59	0.66	0.77
K_2O	10.45	10.63	9.59	9.54	K_2O	9.73	10.94	10.86	10.58	K_2O	9.59	9.89	9.77	9.70
Atom site distribution (11 anhydrous-oxygen basis)														
Si	3.15	3.15	3.08	3.09	Si	3.24	3.23	3.20	3.19	Si	3.16	3.11	3.07	3.08
Al	2.66	2.62	2.82	2.81	Al	2.52	2.42	2.50	2.57	Al	2.71	2.76	2.84	2.82
Fe	0.11	0.15	0.07	0.08	Fe	0.13	0.18	0.14	0.11	Fe	0.06	0.07	0.06	0.06
Mg	0.08	0.10	0.06	0.06	Mg	0.13	0.20	0.18	0.17	Mg	0.08	0.08	0.07	0.08
K	0.89	0.92	0.81	0.81	K	0.84	0.95	0.95	0.91	K	0.82	0.85	0.84	0.82
Na	0.07	0.06	0.11	0.06	Na	0.02	0.02	0.02	0.02	Na	0.09	0.08	0.09	0.10
XMg	0.41	0.39	0.46	0.43	XMg	0.50	0.52	0.55	0.61	XMg	0.57	0.56	0.56	0.57

2021_5				***AP19-49***			***AP19-76***			
Chlorite				*Chlorite*			*Chlorite*			
	Low-vacancies (C1)	*High-vacancies (C1)*			*Low-vacancies (C1)*	*High-vacancies (C2)*		*Low-vacancies (C1)*		*High-vacancies (C2)*	
SiO_2	23.16	22.92	24.58	SiO_2	25.52	26.45	SiO_2	24.06	23.81	24.51	24.38
Al_2O_3	23.27	23.32	22.84	Al_2O_3	21.48	23.04	Al_2O_3	23.53	23.79	23.03	23.73
FeO	33.21	28.72	32.46	FeO	29.02	27.35	FeO	29.53	29.95	28.76	29.04
MnO	0.16	0.17	0.17	MnO	0.33	0.31	MnO	0.16	0.17	0.13	0.17
MgO	7.54	7.72	7.73	MgO	10.21	9.57	MgO	9.64	9.83	10.08	9.34
CaO	0.05	0.01	0.04	CaO	0.18	0.20	CaO	0.03	0.03	0.02	0.04
Na_2O	0.02	0.02	0.06	Na_2O	0.06	0.07	Na_2O	0.06	0.01	0.04	0.01
K_2O	0.03	0.03	0.05	K_2O	0.10	0.10	K_2O	0.08	0.04	0.20	0.10
Atom site distribution (14 anhydrous-oxygen basis including Fe3+)											
Si	2.56	2.61	2.68	Si	2.77	2.82	Si	2.61	2.57	2.66	2.64
Al(T_2)	1.44	1.38	1.32	Al(T_2)	1.23	1.18	Al(T_2)	1.39	1.43	1.34	1.36
Al(M_1)	0.44	0.38	0.32	Al(M_1)	0.23	0.18	Al(M_1)	0.39	0.43	0.34	0.36
Mg(M_1)	0.14	0.14	0.16	Mg(M_1)	0.25	0.22	Mg(M_1)	0.19	0.18	0.21	0.18
Fe(M_1)	0.35	0.30	0.38	Fe(M_1)	0.39	0.35	Fe(M_1)	0.32	0.31	0.34	0.31
V(M_1)	0.07	0.18	0.14	V(M_1)	0.13	0.25	V(M_1)	0.10	0.08	0.11	0.15
Mg(M_2+M_3)	1.10	1.17	1.09	Mg(M_2+M_3)	1.40	1.30	Mg(M_2+M_3)	1.37	1.40	1.42	1.33
Fe(M_2+M_3)	2.72	2.44	2.58	Fe(M_2+M_3)	2.24	2.09	Fe(M_2+M_3)	2.36	2.40	2.27	2.32
Al(M_2+M_3)	0.15	0.37	0.29	Al(M_2+M_3)	0.28	0.53	Al(M_2+M_3)	0.23	0.18	0.26	0.32
XMg	0.29	0.32	0.30	XMg	0.39	0.38	XMg	0.37	0.37	0.38	0.36

Tables 1-2: Representative compositions of K-white mica and chlorite obtained by EPMA (WDS spot analyses).

K-white mica shows a muscovite composition with minor pyrophyllite and celadonite content for all the investigated samples (Guidotti, 1984). No chemical differences from the microstructural position of the K-white mica grains are detectable (Figs. 8.3a, b), i.e., between microlithon (S_{p-1}) and the main foliation (S_p). Two generations of K-white mica were made (P1 and P2) based on Si atoms per formula units (a.p.f.u.) (Table 1). The Si-content ranges from 3.17-3.13 a.p.f.u. and 3.10-3.05 in sample 2021_5; 3.30-3.23 and 3.20-3.10 in sample AP19-49; and 3.16-3.11 and 3.09-3.05 in sample AP19-76. The high- and low-Si-content refers to the first (P1) and second (P2) generations of K-white mica. The *XMg* (*XMg* = Mg/(Mg+Fe)) values are in the range of 0.50-0.38; 0.62-0.45, and 0.58-0.50 for samples 2021_5, AP19-49, and AP19-76, respectively. Finely interlayered paragonite is also observed in sample AP19-76.

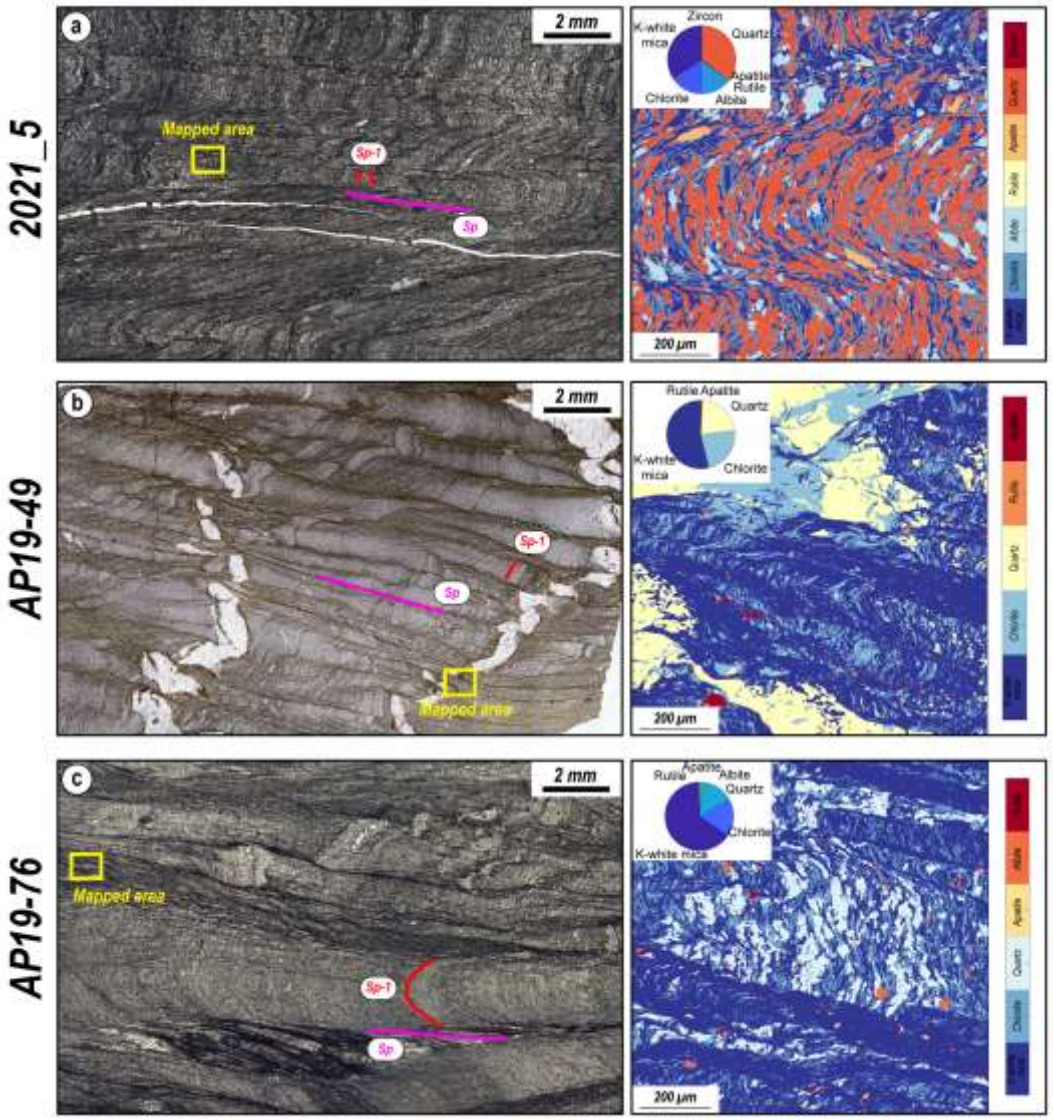

Figure 8.2: Thin section scans and mineral distribution images obtained by classification of X-ray maps for the three analyzed samples: a) 2021_5; b) AP19-49; c) AP19-76.

The chlorite composition in all the investigated samples lies between clinochlore+daphnite, sudoite, and amesite in the Vidal & Parra (2000) end-member diagram. Chlorite is typically homogeneous, except in sample AP19-49 where variable compositions occur in different areas (Fig. 8.3b). No clear chemical variations were found between chlorites from different microstructural positions. Two groups of chlorite have been distinguished using the number of vacancies (C1 and C2; Tab. 2), inferred to be high-temperature (low-vacancies, C1) or low-temperature (high-vacancies, C2) related chlorites.

Chlorite shows Si a.p.f.u. and *XMg* of 2.75-2.55 and 0.33-0.26 for sample 2021_5; 2.90-2.62 and 0.40-0.34 for sample AP19-49; and 2.70-2.56 and 0.39-0.34 for sample AP19-76.

Plagioclase is albitic, with *XAb* (=Na/(Na+Ca+K)) between 0.95-0.99 in all samples.

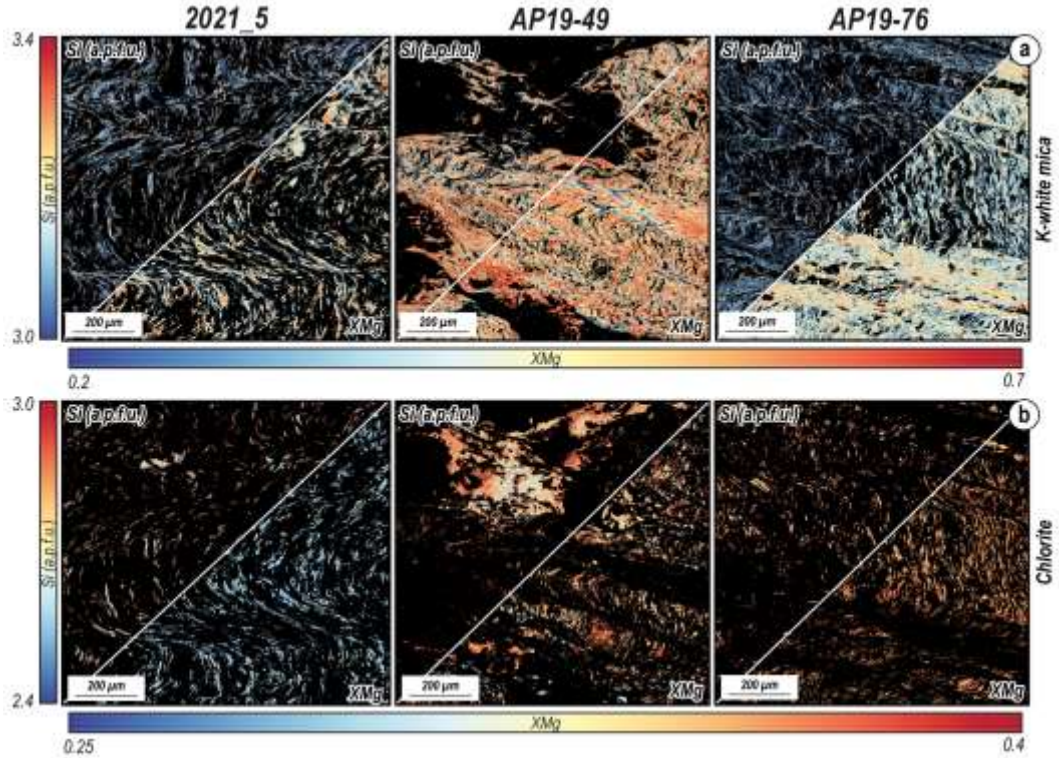

Figure 8.3: a) Maps of Si (a.p.f.u.) and XMg in K-white mica for the three analyzed samples; b) Si (a.p.f.u.) and XMg values maps of chlorite for the three analyzed samples.

8.3.1. Petrochemical interpretation

Available thermobarometric approaches require that white mica and chlorite either grow in equilibrium or re-equilibrate at a given stage of the metamorphic history. Due to the presence of compositional zoning, quantitative compositional mapping is an important tool for assessing local equilibria (Vidal et al., 2006; Lanari et al., 2012). All selected samples show similar microstructural characteristics and mineral assemblages. Despite the presence in each sample of two generations of both K-white mica and chlorite, indicating the possible record of two distinct stages of mineral growth or re-equilibration, one of them (AP19-49) shows a chlorite's microtexture and composition, respecting the other seems to be late or post-kinematic (Fig. 8.3b).

Thus, considering the importance of unraveling samples that display the greatest possible equilibrium texture, the sample AP19-49, showing evidence of probable late chlorite not grown during the assemblage phases, has been excluded.

8.4. *P-T* conditions

8.4.1. Multi-equilibrium involving chlorite and white mica

The chlorite-K-white mica-quartz-water multi-equilibrium approach of Vidal et al. (2005, 2006) was applied using the program ChlMicaEqui 1.5 (Lanari, 2012). These calculations are based on the thermodynamic database of Berman (1988), which contains modifications from Vidal et al. (2005, 2006) for chlorite, and Parra et al. (2002) and Dubacq et al. (2010) for white mica. This method is based on the convergence of the equilibria involving chlorite and mica end-members in the presence of quartz and water (see Vidal et al., 2006 for details). It requires the knowledge of the composition of chlorite and K-white mica and the assumption that they formed close to chemical equilibrium conditions at a given stage of their metamorphic history. Representative spot analyses of both generations of chlorite and white mica are reported in Tables 1-2. For sample 2021_5 we got conditions of 410 °C and 0.6 GPa, 429 °C - 0.4 GPa (Figs. 8.4a, b) for H*T*-C1 and L*T*-C2 (see above). For sample AP19-76, we got 398 °C - 0.4 Gpa, 387 °C - 0.4 GPa (Figs. 8.4c, d) for H*T*-C1 and L*T*-C2 (see above).

The main limitation of this approach is the assumption of chemical equilibrium between the compositions of chlorite and white mica selected for thermobarometry. An alternative strategy that does not require assuming equilibrium between chlorite and white mica is applied below to address this limitation.

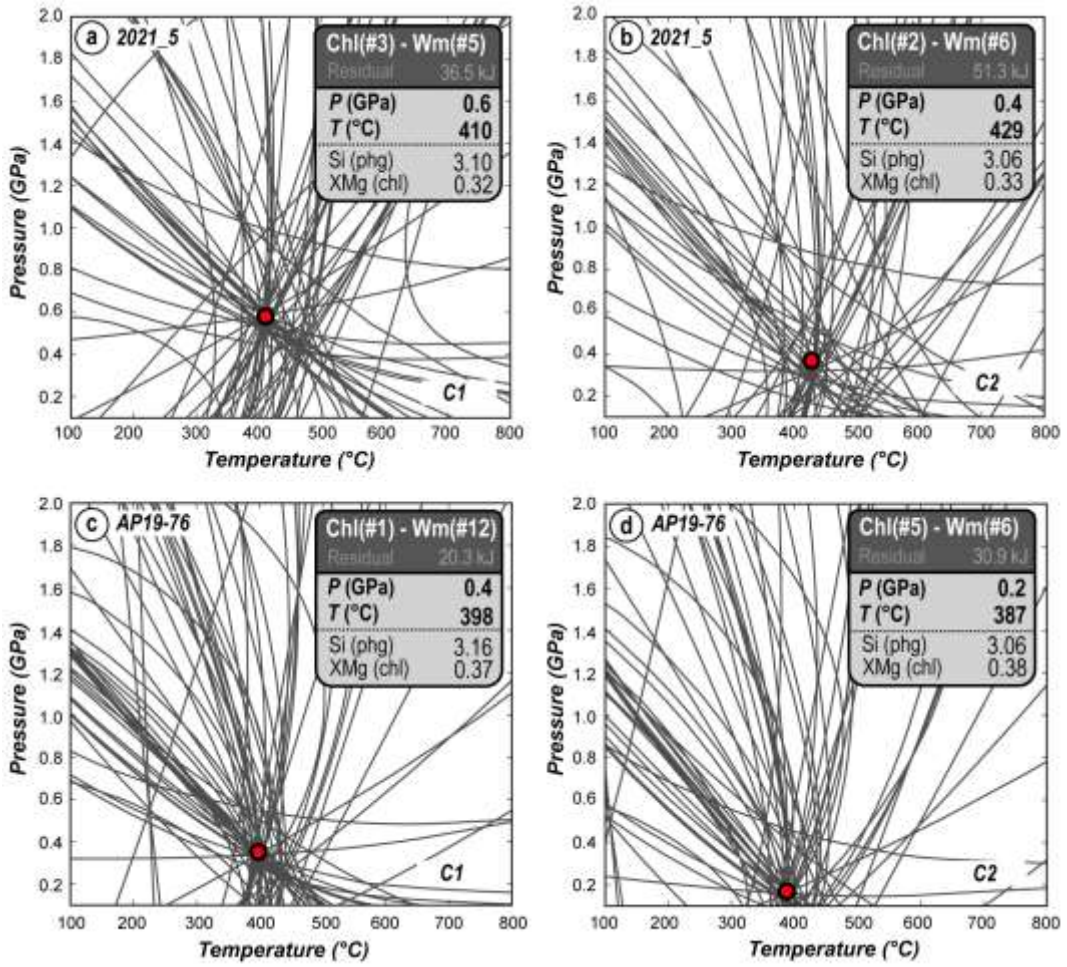

Fig. 8.4: Multi-equilibrium of chlorite and white mica calculations using C1 (a,c) and C2 (b,d) compositional groups for samples 2021_5 and AP19-76, respectively

8.4.2. Hybrid approach combining RSCM and white-mica barometry

In this section, pressure conditions of K-white mica formation are obtained using the approach of Dubacq et al. (2010) at the maximal temperature of metamorphism (T_{max}) obtained by RSCM.

Raman Spectroscopy on Carbonaceous Material (RSCM; Beyssac et al., 2002) thermometry has been used to determine peak temperature conditions in the overall Sardinian hinterland-foreland transition zone (Chaper 6). This method is based on the progressive transformation of carbonaceous material into graphite (CM) during an increase in temperature (see Henry et al., 2019 for a complete review). The T_{max} estimates were derived with the Aoya et al. (2010) calibration due to the specific laser applied during the analysis.

Table 3 summarizes the results of the spectral decomposition for both analyzed samples. Representative spectra are depicted in Figure 5. The two estimated temperatures are 453 ± 20 °C and 380 ± 10 °C for samples 2021_5 and AP19-76, respectively (Chapter 6; Figs. 8.5a, b). It is important to note that the analyzed samples are consistent with the temperature detected across the belt and do not represent an anomaly in the thermal structure of the chain (Chapter 6).

Sample name	*T*°C (Aoya et al., 2010)				
	n. Spectra	R2	*T°C*	*SD*	SE (°C)
2021_5	10	0.40	453	6.9	20
AP19-76	10	0.57	380	3.4	10

Table 3: Results of the RSCM estimations with the Aoya et al. (2010) calibration. The number of spectra (n), R2 ratio with the corresponding standard deviation (SD), and calculated temperature (T °C) with standard error (SE) have been indicated.

The equilibrium condition of K-white mica-quartz-water is represented by a divariant *P-T* line along which only the amount of water in the interlayer site content varies (Dubacq et al., 2010). This technique can be used as a barometer for a given temperature (Lanari et al., 2012). Combining T_{max} with the high-Si (P1) content K-white mica generation, *P-T* conditions of 0.5-0.8 GPa at 453 ± 20 °C for sample 2021_5 and 0.4-0.5 GPa, 380 ± 10 °C for sample AP19-76 (Figs. 8.5a, b) have been obtained. Assuming the same temperature range for the second generation of K-white mica (P2), as also suggested by the multi-equilibrium results presented above, both samples display lower-pressure conditions (Figs. 8.5a, b).

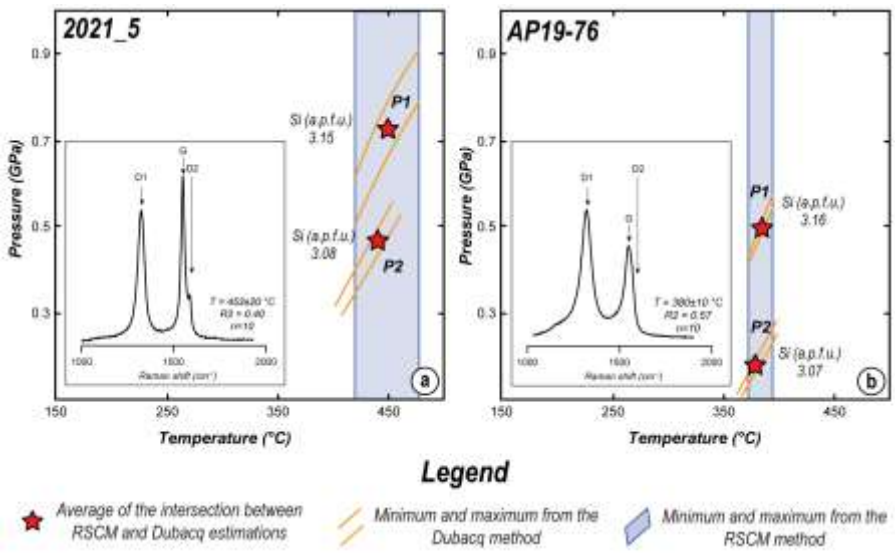

Figure 8.5: Hybrid approach combining RSCM and white-mica barometry from Dubacq et al. (2010) applied to samples from the 2021_5 (a) and AP19-76 (b) samples. In each sample, the P-T lines calculated were projected for the high-Si (P1) and low-Si (P2) compositional groups vs the T_{max} range.

8.4.3. Summary of the inverse methods

The *P-T* conditions were derived by comparing all the obtained results with different methods. They all indicate similar results. The *P-T* peak (P1+C1+RSCM) is at 420-450 °C, 0.6-0.8 GPa and 370-400 °C, 0.4-0.5 GPa, for the Internal and External nappes, respectively (Figs. 8.6a, b). Both samples display a second stage of K-white mica and chlorite (P2+C2), associated with similar temperature conditions but lower pressure values. The second stage is constrained at 0.4-0.5 GPa for the Internal nappes and 0.2 GPa for the External nappes, respectively (Figs. 8.6a, b).

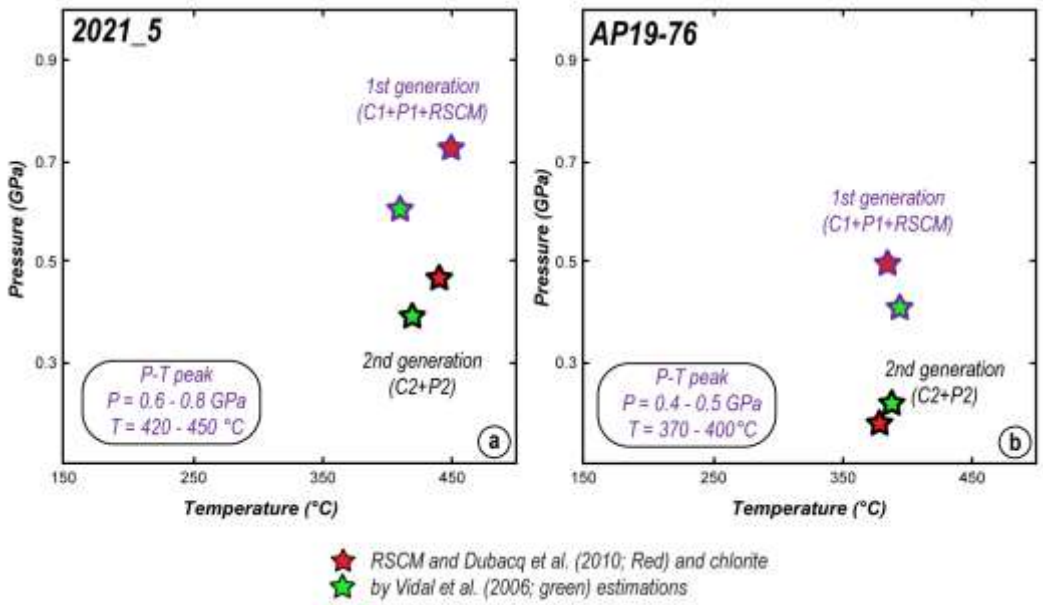

Figure 8.6: P-T diagram summarizing the obtained metamorphic results with both multi-equilibrium involving chlorite and white mica and the hybrid approach combining RSCM and white-mica barometry for the Internal (a) and the External (b) nappes.

8.5. Phase equilibrium modeling

The following part of this study tests the ability of forward models to predict the mineral assemblage and mineral compositions observed in the chosen natural samples. The construction of equilibrium phase diagrams strongly depends on the selected database and solution models, the use of an appropriate chemical system, and the choice of a bulk composition representative of the sample or a specific stage (reactive bulk composition).

Phase diagrams were computed in the system Na_2O-K_2O-FeO-MgO-Al_2O_3-SiO_2-H_2O (NKFMASH) using Theriak-Domino (De Capitani & Brown, 1987; De Capitani & Petrakakis, 2010). The CaO component was ignored due to the absence of a Ca-rich phase in the

analyzed samples. TiO_2 is not considered in the calculations because Ti is only contained in rutile. FeO includes both Fe^{2+} and Fe^{3+}. The influence of Fe^{3+} has not been considered in the calculations because in a graphite-bearing metapelite with no magnetite and/or hematite, Fe^{3+} will be mostly contained in K-white mica and chlorite (Forshaw & Pattison, 2021). The Fe^{3+} could also be in chlorite, and its increase reflects the incorporation of the Fe^{3+}-sudoite component with decreasing temperature (Vidal et al., 2006, 2016).

To provide a thorough evaluation of different options, we tested six different databases:

(i) Ds62 (dataset of Holland & Powell, 2011; solution models as in White et al., 2014);

(ii) Ds55-tc33 (Holland & Powell, 1998; solution models as in Pattison & Debuhr, 2015),

(iii) Ds55-tc32 (Holland & Powell, 1998; solution models as Holland & Powell, 1998),

(iv) Jun92 (Berman, 1988; solution models as in De Capitani & Petrakakis, 2010);

(v) Vidal14 (Berman, 1988; solution models as in Pourteau et al., 2014);

(vi) SPaC (Berman, 1988; solution models as in Spear & Pyle, 2010).

8.5.1. Bulk composition

The bulk composition used for modeling can influence the topology and phase proportions predicted in a *P-T* phase diagram (e.g., Palin et al., 2016) but does not influence the predicted mineral compositions near the equilibrium conditions (Lanari & Hermann, 2021). In this study, local bulk compositions were calculated from the compositional maps, corrected for mineral density, and considering only areas with similar compositional zoning patterns (Lanari & Engi, 2017). The selected map width was 1000x1000 µm, at least 8-10 times greater than the 'average' size of the largest grains (Lanari & Engi, 2017; see Figs. 8.2a, c and Fig. 8.3). This criterion ensures that the composition is reasonably representative of the entire composition of the domain as long as the section is uniform in the mineral assemblage. The obtained reactive bulk composition is presented in Table 5. Sample 2021_5 is similar in composition to the worldwide median pelite of Forshaw & Pattison (2023), whilst sample AP19-76 is comparatively enriched in Al_2O_3, TiO_2, and K_2O, and depleted in SiO_2 and CaO.

	Sample	SiO_2	TiO_2	Al_2O_3	FeO_{TOT}	MnO	MgO	CaO	Na_2O	K_2O	Total
wt%	2021_5	61.25	1.77	19.54	5.19	-	1.29	0.06	0.80	3.88	94.57
	AP19-76	49.18	2.93	26.78	8.06	-	2.56	0.07	0.43	6.34	96.78

Table 4: Reactive bulk compositions (wt%) used for the thermodynamic modeling.

8.5.2. Prediction of mineral assemblages

The reliability of the phase diagram approach is directly linked to its ability to predict an observed mineral assemblage at various *P-T* conditions. If an exact match cannot be obtained, the degree of discrepancy and therefore the model uncertainty increase. K-Wm + Chl + Qz + Ab and K-Wm + Pa + Chl + Qz + Ab represent the mineral assemblage for the investigated samples 2021_5 and AP19-76, respectively. Only database Ds62 predicts all minerals found in the natural assemblage for sample 2021_5; this occurs in a *P-T* range of 350-450 °C and 0.1-0.3 GPa (shown as the red field in Fig. 8.7a). No exact match for the observed mineral assemblage can be found in diagrams calculated within any other database. Phases that are missed (-) or predicted as extra (+) in each database have been highlighted in Figures 8.7a, b.

In both samples, it is important to highlight that: (i) the stability of biotite, in all databases, occurs at *T* > 450-500 °C; (ii) albite is generally not predicted by the models but is present in both samples; (iii) paragonite is not predicted to be stable in the samples containing paragonite; and (iv) chloritoid is predicted to be stable above at higher pressure conditions (generally above 0.5-0.6 GPa), but was never observed in the samples.

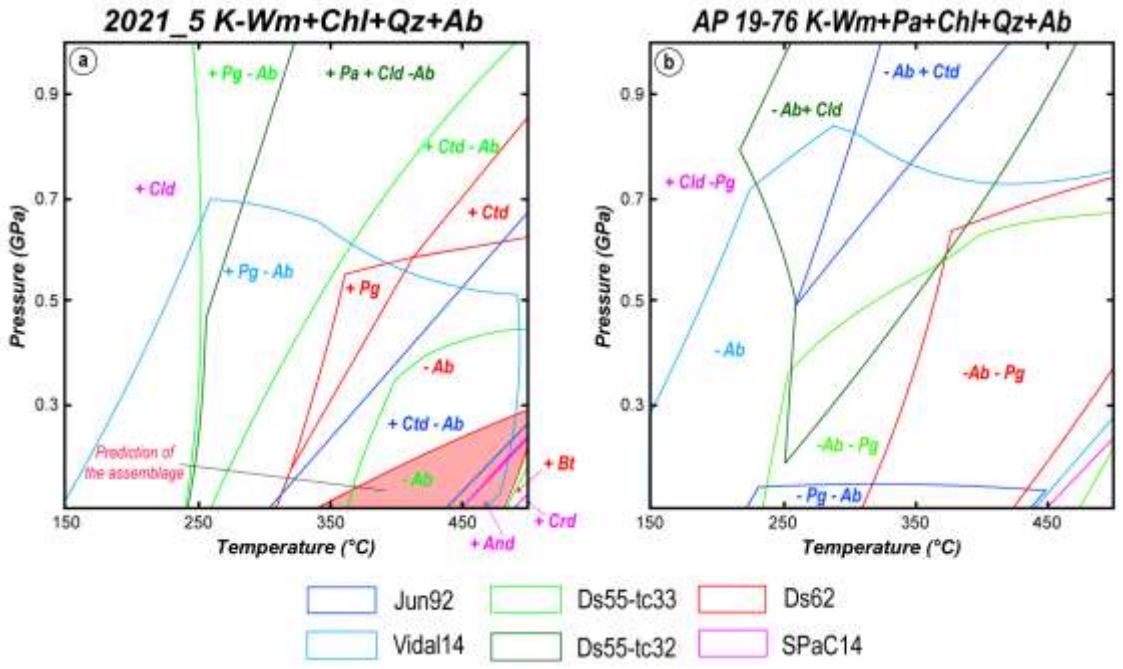

Figure 8.7: P-T diagram showing the predicted mineral assemblage for the Internal (a) and the External (b) nappes. The respective phases that are missed (-) or predicted as extra (+) are indicated with different colours in the function of the respectively used database.

8.5.3. Prediction of mineral compositions

When predicted mineral assemblage fields are large, compositional isopleths of minerals can be used to better constrain *P-T* conditions (Powell & Holland, 2008). Phase diagrams have been calculated in a *P-T* range of 150-500 °C and 0.1-10 Gpa. Isolines for Si (in a.p.f.u.) and *XMg* are plotted in Figures 8.8 and 8.9 for both K-white mica and chlorite, to highlight possible consistency between each investigated database and associated solution models. The average "observed values" taken from the chemical spot analyses (Tables 1 and 2), integrated with the minimum and maximum of the peak *P-T* groups obtained from XMapTools, were used to define a compositional range.

The predicted composition of K-white mica is similar for both samples. The Si in K-white mica (3.15 ± 0.01 and 3.13 ± 0.03 for sample 2021_5 and AP19-76, respectively) is predicted by the model in the selected *P-T* range using databases Ds62, Ds55-tc33, Ds55-tc32, and Jun92 (Figs 8.8, 8.9). Despite the latter, Ds55-tc33, Ds55-tc32 and Ds62 highlighted H*P*-L*T* conditions for both sample compositions. In both samples, the isopleths of *XMg* are temperature dependent. Similarly, the *XMg* (0.40 ± 0.01 and 0.56 ± 0.01 for sample 2021_5 and AP19-76, respectively) is predicted in the model using Ds62, Ds55-tc33, and Ds55-tc32 databases. The only difference is that in sample AP19-76 also Vidal14 predicts the composition (Fig. 8.9).

The predicted composition of the chlorite is similar to the observed Si content, but different to the observed *XMg* (Figs 8.8, 8.9). The Si in chlorite (2.58 ± 0.02 and 2.59 ± 0.02 for sample 2021_5 and AP19-76, respectively) is predicted in the model for the selected *P-T* range when databases Ds62, Jun92, Vidal14, and SPaC are used. The Ds55-tc33 and Ds55-tc32 databases did not predict the in Si of chlorite natural values. All databases predicted the *XMg* in chlorite within the predicted *P-T* range (Figs 8.8 and 8.9). Jun92 and SPaC14 predict the Si at L*P* conditions, whereas Vidal14 isopleths are similar in both samples (Figs 8.8 and 8.9). The observed *XMg* (0.30 ± 0.02 and 0.37 ± 0.01 for sample 2021_5 and AP19-76, respectively) is predicted by all databases. *XMg* isopleths span a range of compositions across the entire *P-T* space. The random isopleth position and orientation highlight the strong differences in the prediction of *XMg* in chlorite.

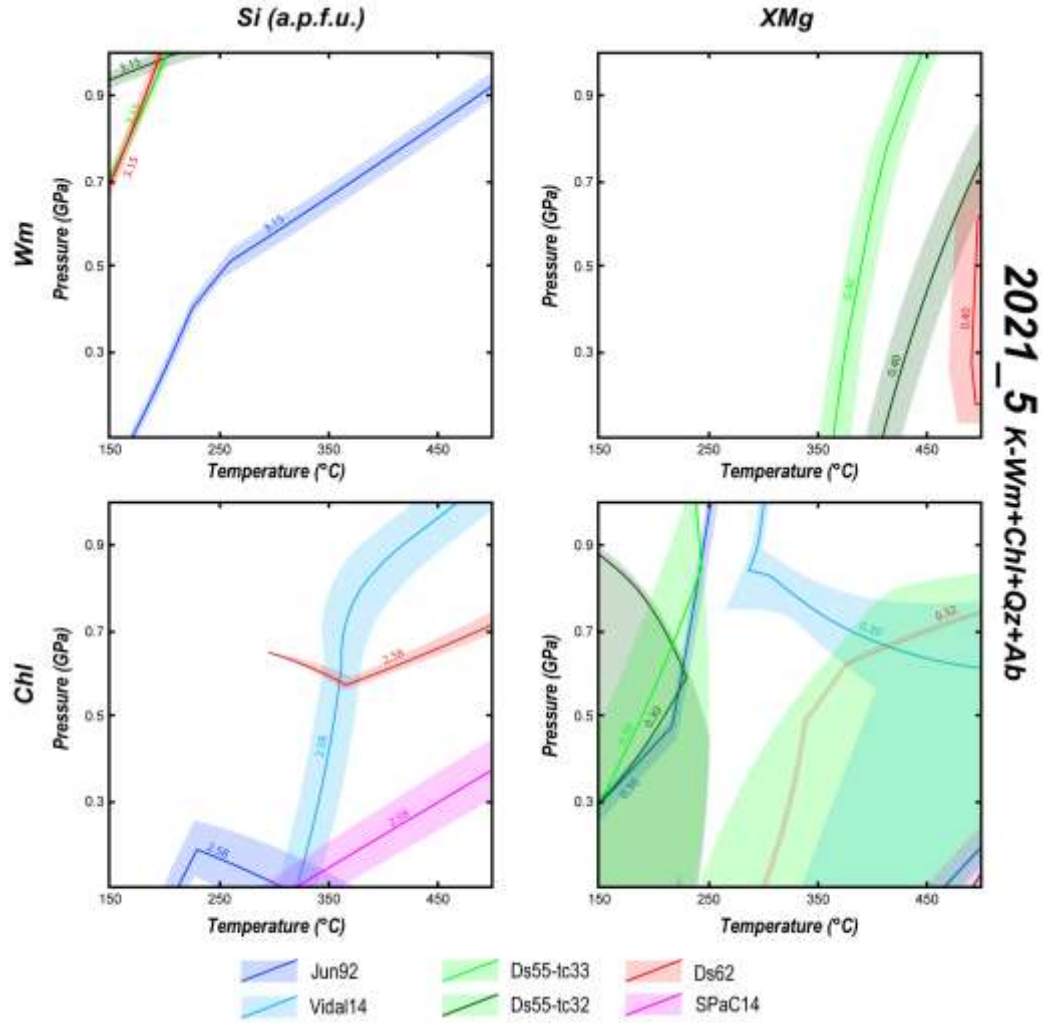
Si (a.p.f.u.)
XMg
Wm
Chl
Pressure (GPa)
Temperature (°C)
2021_5 K-Wm+Chl+Qz+Ab
Jun92
Vidal14
Ds55-tc33
Ds55-tc32
Ds62
SPaC14

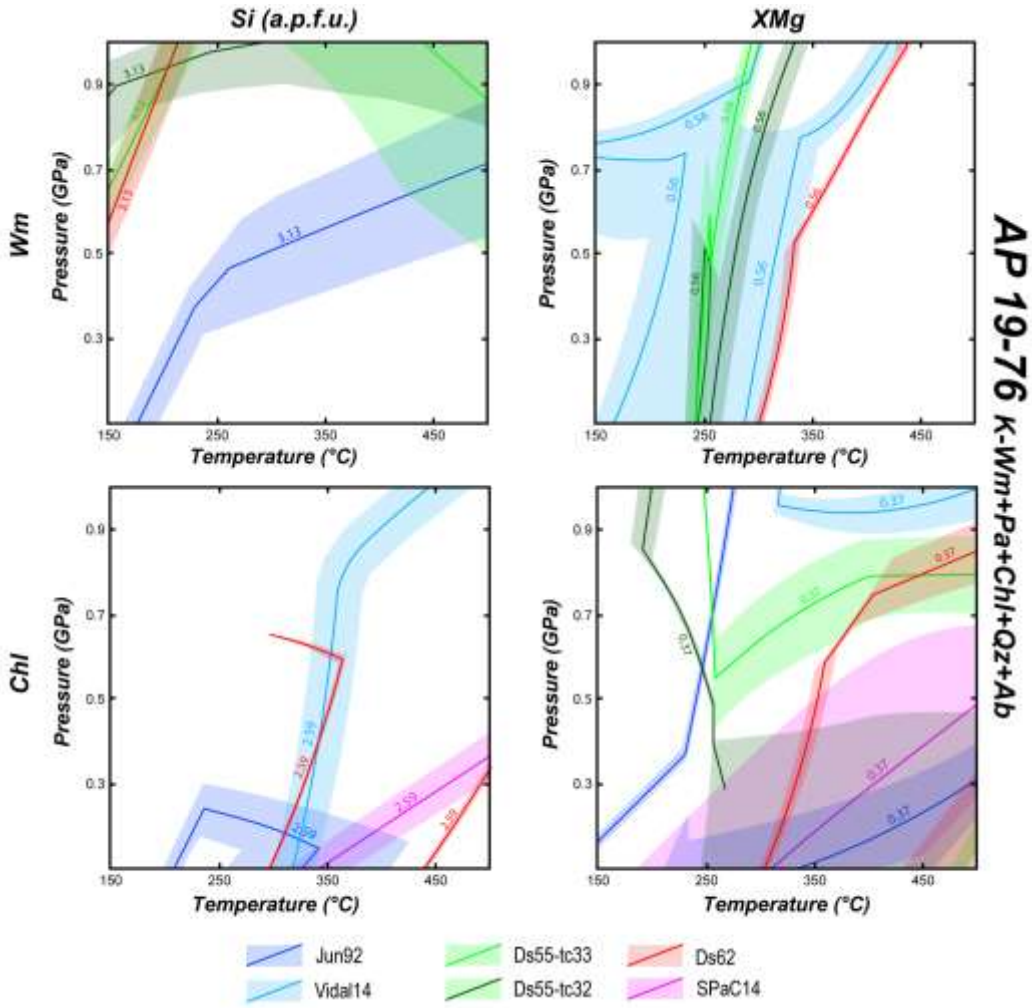

Figure 8, 9: P-T phase diagrams for sample 2021_5 and AP19-76. Predicted compositional isopleths of Si and XMg for both K-white mica and chlorite from different databases. The shaded region shows minimum and maximum values around the mean value (thick line).

8.6. Discussion

8.6.1. P-T condition integrating inverse modeling and RSCM

Estimating the *P-T* conditions of crystallization in low-grade metamorphic rocks is challenging. In metapelites, chlorite and white mica are the most useful, yet they are stable over a wide range of metamorphic conditions. Modeling assemblages with these two phases is complicated as complex chemical substitutions are involved (Holland et al., 1998; Vidal et al., 2001; Parra et al., 2002; Dubacq et al., 2010; Trincal & Lanari, 2016), and direct experimental constraints of these equilibria are rare (Parra et al., 2005). High-variance assemblages (low number of phases) are promising targets for multi-equilibrium (inverse approach), provided that at least two independent equilibria can be found.

This advantage is particularly evident in low-grade metamorphic rocks that often lack index minerals and for which thermobarometry is otherwise challenging (e.g., Parra et al., 2002; Lanari et al., 2012; Pourteau et al., 2013; Cantarero et al., 2014). In contrast to the phase diagram approach, generally used for higher metamorphic conditions and for rocks with a lower variance, these methods do not require a reactive bulk composition. Also, extrapolation from H*T* and H*P* of empirical or semi-empirical models to L*T* samples may be erroneous. Several researchers have obtained *P-T* conditions in low-grade rocks using the integration of chlorite-K-white mica-quartz-water and K-white mica-quartz-water multi-equilibrium approaches (e.g., Ganne et al., 2012; Lanari et al., 2012, 2014; Giuntoli et al., 2018; Sanità et al., 2022). *P-T* estimates obtained using inverse models rely on the assumption of a frozen-in state of equilibrium. Although the equilibrium among mineral phases cannot be proven, microtextural relationships (e.g., Waters & Lovegrove, 2002; Pattison & Spear, 2018) and compositional criteria based on quantitative compositional maps (e.g., Vidal et al., 2006; Lanari et al., 2012; Scheffer et al., 2016) may help the investigations. In this study, one sample has been excluded from the analysis, based on complex zoning and microtexture, elucidated by compositional mapping.

The first quantification of *P-T* on the two investigated samples was obtained with the chlorite-K-white mica-quartz-water multi-equilibrium approach. This method is based on the assumption that both chlorite and K-white mica are “represented” by their compositions used for modelling-formed in equilibrium. To avoid assumptions on the chemical equilibrium between K-white mica and chlorite, we applied the K-white mica-quartz-water multi-equilibrium approach for the white mica with the highest Si-content at the T_{max} obtained by RSCM. Both techniques have been used individually in various geological environments. RSCM, in particular, has been used in the last two decades to determine the peak temperature across different frameworks and chains (e.g., Bellanger et al., 2015; Delchini et al., 2016; Lahfid et al., 2019; Balansa et al., 2022; Herviou et al., 2022). However, developing any tectonic model and geodynamic interpretation is impossible without pressure constraints. Both methods gave similar results in investigated case, displaying two distinct *P-T* points linked to the different generations of chlorite and K-white mica.

This chapter shows that a detailed analysis of low-grade metamorphic rocks conducted integrating *P-T* estimates realized using the multi-equilibrium thermodynamic approach based on available solid solution models (Vidal et al., 2005, 2006; Dubacq et al., 2010) with T_{max} estimates from RSCM thermometry. The resulting thermal peak estimates are consistent between chlorite and white mica methodologies.

8.6.2. Phase diagrams at low-grade conditions

8.6.2.1. Mineral assemblage

Although the forward approach can be seen as a more straightforward way to obtain the *P-T* condition for metapelites, several complications in low-grade rocks are present. The construction of equilibrium phase diagrams for specific bulk rock composition, producing isochemical phase diagrams, requires choosing (i) a database, (ii) an appropriate chemical system, and (iii) a reactive bulk composition representative of the sample volume assumed to have been chemically reactive and in equilibrium. These choices are critical as they strongly affect the results (e.g. Symmes & Ferry, 1992; Tinkham & Ghent, 2005; Pattison & Debuhr, 2015; Waters, 2019).

Detrital or authigenic phases are common in pelitic sediments, including clay (e.g., kaolinite and smectite), dioctahedral mica (e.g., muscovite and paragonite), chlorite and plagioclase. Thus, detrital minerals are widespread and challenging to recognize in low-grade metapelites. The presence of detrital minerals and the observation of compositional zoning in metamorphic minerals demonstrate that large-scale (e.g., thin-section scale) thermodynamic equilibrium is rarely attained in nature (Tracy et al., 1982; Carlson et al., 2015; Lanari et al., 2017). This question the use of a measured bulk-rock composition as an approximation of the reactive bulk composition at low-grade conditions. The improvement of compositional mapping helped the community to highlight possible detrital grains, or part of the grains (e.g., Lanari et al., 2012). Their presence is directly related to the low-temperature conditions that do not help the complete re-equilibration and total recrystallization. Consequently, it can be challenging to identify a spatial domain suitable to determine a reactive bulk composition for the forward thermodynamic modeling. The over- or under-estimation of different phases in predicting the mineral assemblage using different databases in the forward approach has been discussed in section 8.4.2. The problem with high-variance assemblages is that if the assemblage is not reproduced in the model, the absence of a mineral or the presence of another one not observed in the rock can influence the modeled mineral compositions and, therefore the *P-T* results. Each mineral is discussed separately below.

Albite, a common phase in low-grade metapelite, has often been identified as a detrital phase (Frey, 1987; Frey & Robinson, 1999). However, albite appears to be in textural equilibrium with the other minerals in the analyzed samples. Despite this, the absence of albite in the models is in line with a detrital origin. However, if albite is in equilibrium and not detrital, as the textural evidence highlights, there should be fractionation issues and problems, such as

the distribution of the Na in the bulk rocks system. Thus, if the albite is not detrital and the model is at fault, then the phase diagram predicts too much paragonite. However, if the albite is detrital, the model will be wrong.

Paragonite is not predicted to be stable in sample AP19-76 which contains paragonite but is observed in sample 2021_5 where it is not expected to be stable in the model. Following the Na problem related to the albite, it could be strictly linked to the underestimation or overestimation of the paragonite prediction. If the phase diagram does not predict stable albite, all the Na of the system will be destined to the paragonite. However, if it is produced more stable paragonite than the amount found in the natural sample, this will have consequences concerning the Al/Si ratio, and the database will force muscovite to contain more Al. This will be an important problem when using the Si in white mica parameter.

Chloritoid stability and prediction are strongly related to the Al and Fe content within the sample. However, the lack of this phase inside the studied samples is well-sustained by the good chloritoid prediction in the obtained phase diagram for pressure conditions generally above 0.7 GPa.

Biotite is predicted to be stable for all databases at T > 450-500 °C. This result is consistent with the lack of biotite in all samples investigated across the low-grade hinterland-foreland transition zone (Chapters 5 and 6). It is important to highlight that the Bt-in line can occur under different conditions, depending on K-Si content, but for low-grade metapelites, its ingress is well-constrained, as predicted by the obtained phase diagrams.

To summarize, the main problem in the mineral assemblage prediction is related to the distribution of Na in the bulk rock system, i.e., albite-paragonite Na-partitioning. This element distribution affects the prediction of the albite and paragonite phases in the phase diagram and strongly influences the repartitioning of the Al/Si in the K-white mica. It could be crucial when authors use the content of Si in K-white mica as a fixed point in our *P-T* space.

8.6.2.2. Mineral compositions

The low-grade metapelites are associated, as previously discussed, with a high variance assemblage that is referred to few minerals and system components, resulting in a more straightforward mass balance of the system. These are reflected when using a few compositional isopleths and solution models. The presence of fewer parameters on which we can rely when constraining *P-T* conditions with the phase diagram approach leads to simpler topologies but significant uncertainties related to the predicted large fields.

Two parameters or variables that could be used in these simpler systems using chlorite and K-white mica have been tested.

K-white mica

The amount of Si in white mica is commonly used for pressure determination within the geological community. This parameter is based on experimental data obtained at high-pressure conditions. Tschermak substitution ($Al^{IV} + Al^{VI} = Si^{IV} + Fe^{VI}$, Mg^{VI}) in phengite is known to be sensitive to pressure conditions in K-feldspar- or talc-bearing assemblages (Massonne & Schreyer, 1987, 1989; Massonne, 1995) and in H*P*-L*T* metapelites (Saliot & Velde, 1982; Massonne, 1992; Bousquet et al., 1998, 2002; Agard et al., 2001). Therefore, the maximum Si values of highly substituted early phengite are generally used to estimate the peak pressure experienced by rocks. The obtained Si-in-phengite compositional isopleths (a.p.f.u.), shown on the *P-T* grid, highlight that all the databases indicated different positions of the natural composition of the K-white mica. Despite the *XMg* could be partially influenced by the K-white mica-chlorite exchange, the fractionating of the K-white mica does not shift the Si isopleths (Airaghi et al., 2017). The *XMg* is challenging because it is often very small in value and could be affected by Fe^{3+} (Guidotti et al., 1994; Guidotti & Sassi, 2002; Forshaw & Pattison, 2021). However, the Si and the Al will be strongly involved in the model by the strong partition of the Na in the K-white mica (see the previous paragraph). Although the Si a.p.f.u. in K-white mica is extensively used as a geobarometer, significant difficulties when considering this parameter have been observed.

Chlorite

Although chlorite is widespread in different rock types, few thermodynamic models with low-*T* end-members are available (e.g., Berman, 1988). The inaccuracy of this approach is due in most cases to uncertainties in the *P-T* data employed for the calibration, to the inaccuracy of the thermodynamic properties of chlorites end-members, to the choice of the mixing model, and to the difficulty in measuring the Fe^{3+} content and in accounting for it in solid-solution models (cf. Grosch et al. 2012). Thus, both Si and *XMg* in chlorite suffer from the lack of experimental data. This is strongly related to the different orientations of all the isopleths from different databases. Vidal et al. (2005) proposed, through an experimental approach coupled with the study of natural samples, a thermodynamic model for aluminous chlorites, based on a four-thermodynamic-component solid solution model (Mg-sudoite, Mg-amesite, clinochlore, and daphnite). *XMg* in chlorite is both pressure- and temperature-dependent. It has been modelled without considering the Fe_2O_3. The Fe^{3+} content could strongly influence the structural formula of chlorites and, consequently, the *P-T* estimates.

Theoretically, it could impact the *XMg* of chlorite, whereas the Si does not change much. However, in graphite-bearing metapelites, as the investigated samples, the amount of Fe_2O_3 in the bulk is <10%. In both Si and *XMg* no database can precisely predict the chlorite's natural composition and highlight a *P-T* condition for both samples.

Metapelites are nowadays incorporated into the mountain and occur in almost all geological terranes worldwide. The sensitivity of their mineral assemblages and the compositions of key mineral constituents to changes in *P* and/or *T* conditions makes these rocks highly valuable for thermobarometry. Thus, an important question for future studies is: can we use forward modeling in low-grade metapelites? The right answer is probably no now because the limitations and problems of different databases must be considered. In addition, more work is necessary to understand this point better and to improve the thermodynamic modeling with a forward approach in low-grade rocks. People generally ignore something to obtain reasonable results in medium- and high-grade rocks by forward modeling. However, using phase diagrams in low-grade rocks to develop tectonic interpretation could be significantly dangerous because no database could really predict and model the natural assemblage and composition. Although Willner et al. (2015) demonstrated that pseudosections could be an ideal tool to constrain the *P-T* of very-low- to low-grade metamorphic rock sequences and Willner et al. (2013) highlighted that crystals are small and unzoned at these *P-T* conditions, our results are not in agreement with these considerations. Thus, despite the geological community still produced tectonic interpretations based on the isopleths and phase diagram approach on low-grade metapelites (e.g., Lo Pó et al., 2015; Boedo et al., 2016; Balen et al., 2017; Franceschelli et al., 2017), as shown in Fig. 8.10, these values are often entirely out respecting the natural values. In particular, several problems also could derive from the massive use of Si in K-white mica for barometric estimations and the development of widespread tectonic models and interpretations (e.g., overpressure, high-pressure). Quantitative thermobarometry discrepancies are caused by incorrect thermodynamic properties or/and by inadequate reactive bulk composition (e.g., Pan et al., 2020). Also, working with databases and solution models developed on H*T* and H*P* conditions in low-grade rocks may be dangerous. New thermodynamic experiments and algorithms at the low-*PT* are needed to develop proper thermodynamic databases and models and increase the reproducibility of the published estimates for low-grade rocks. Thus, based on the phase diagram results, tectonic interpretations on low-grade rocks must be validated and tested by integrating different parallel methodologies and approaches (e.g., multi-equilibrium and RSCM).

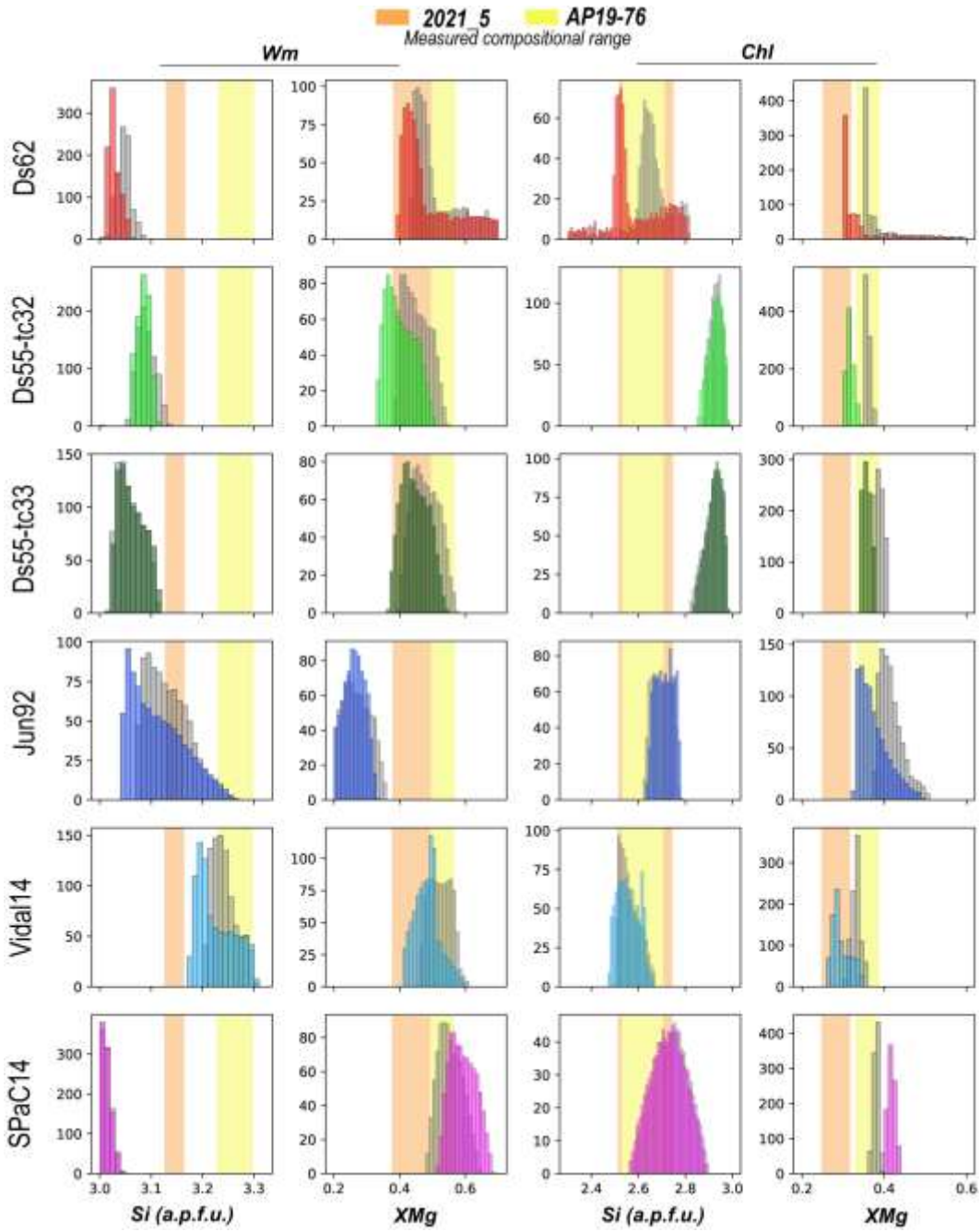

Figure 8.10: Diagrams comparing the observed compositional range of Si and XMg in K-white mica and chlorite for both samples (2021_5 and AP19-76) with the predicted values from the different databases (coloured for sample 2021_5 and shaded for sample AP19-76).

8.6.3. Regional interpretation

The polyphase deformation history recorded in the hinterland-foreland transition zone in Sardinia is regarded as the result of pre-, syn- to post-nappe stacking evolution developed under contractional conditions (D_1 to D_4; Chapter 5, 6), highlighting a complex tectonic history occurring during the growth of the orogenic wedge. During the D_1 and D_2 phases, blastesis of chlorite and K-white mica grains occur. Using the multi-equilibrium approach on chlorite and K-white mica, integrated with RSCM, the *P-T*-peak conditions of 0.6-0.8 GPa and 420-450 °C and 0.4-0.5 GPa and 370-400 °C from the Internal and External nappes have been obtained. Taking a typical correlation of pressure vs depth in a collisional framework (1 GPa = 33 km), the paleo-crustal depth of Internal and External nappes was ~20-26 and ~13-17 km. Assuming that the obtained *P-T* peak is related to the D_1 event (D_{p-1} of this work = to D_1), referring to the early stage of collision and burial (Carosi et al., 2004; Montomoli et al., 2018), it could be highlighted a difference in the pressure of ~0.2-0.3 GPa and ~8 km in depth, between Internal and External nappes. The *P-T* conditions of the Internal Nappe Zone sample are similar to those obtained in the LGMC by Costamagna et al., 2012, but with slightly lower pressure. Indeed, the presented data agree with the progressively northward increase in pressure and temperature going towards the hinterland (Cruciani et al., 2013, 2022). Both nappes show a decrease in pressure conditions associated with the second generation of chlorite and K-white mica. The retrograde path indicates a decompression with no relevant temperature changes, with values of 0.4-0.5 and 0.2 GPa for the Internal and External nappes, respectively. No significative heating during the D_2 exhumation phase was identified, whereas the quantity of the decrease in pressure between both nappes is similar (~0.2 GPa), indicating an isothermal decompression. The D_2 phase, linked to the syn-nappe stacking deformation and exhumation of the Internal Nappe Zone, is related to the BT activity (Montomoli et al., 2018 and references therein). Instead, the exhumation path recognized in the External Nappe Zone could be linked to the activity of more external thrust due to the migration of the deformation from the hinterland toward the foreland, e.g., the tectonic contact between Meana Sardo and Gerrei units (Carmignani et al., 1994). The provided *P-T* results allow the re-interpretation of the low-grade Sardinian Nappe Zone as fully equilibrated in greenschist-facies conditions, experiencing moderate pressure during the building up of the Variscan belt in Sardinia and subsequent exhumation (Fig. 8.11).

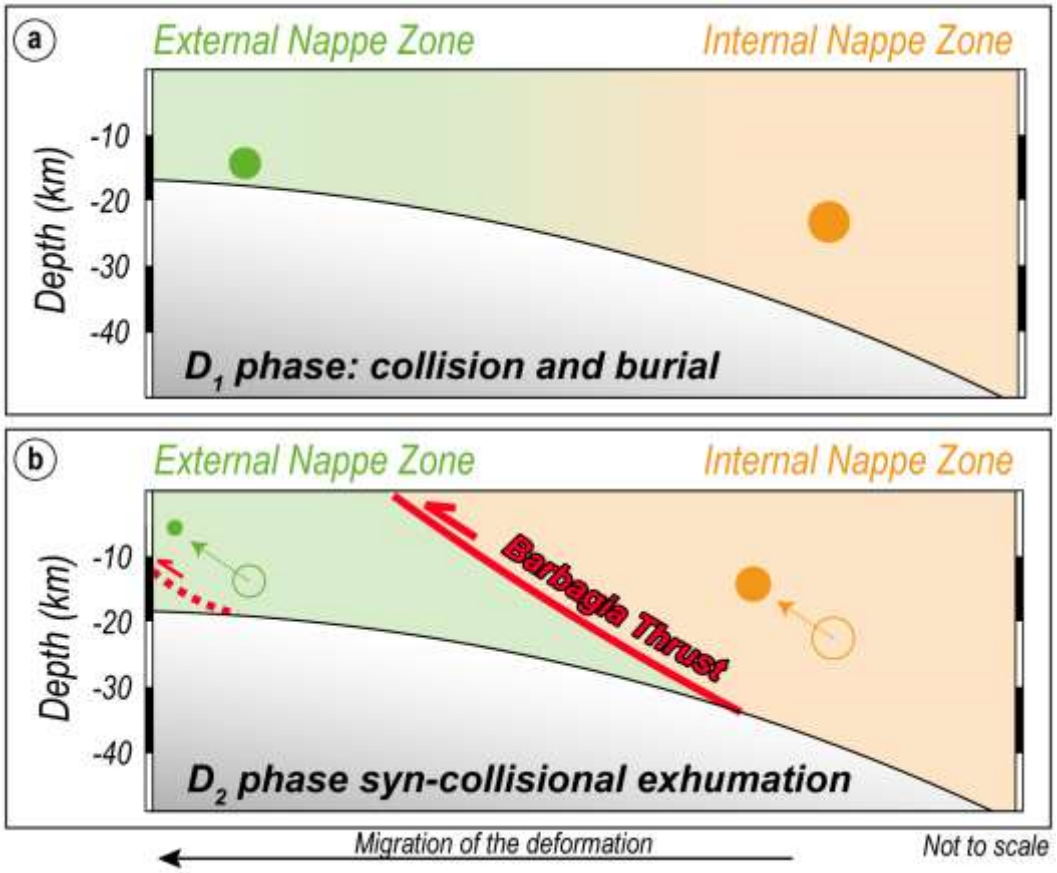

Figure 8.11: Tectonic sketch from the D_1 to the D_2 deformation phase. The path of both the Internal and External nappes is indicated

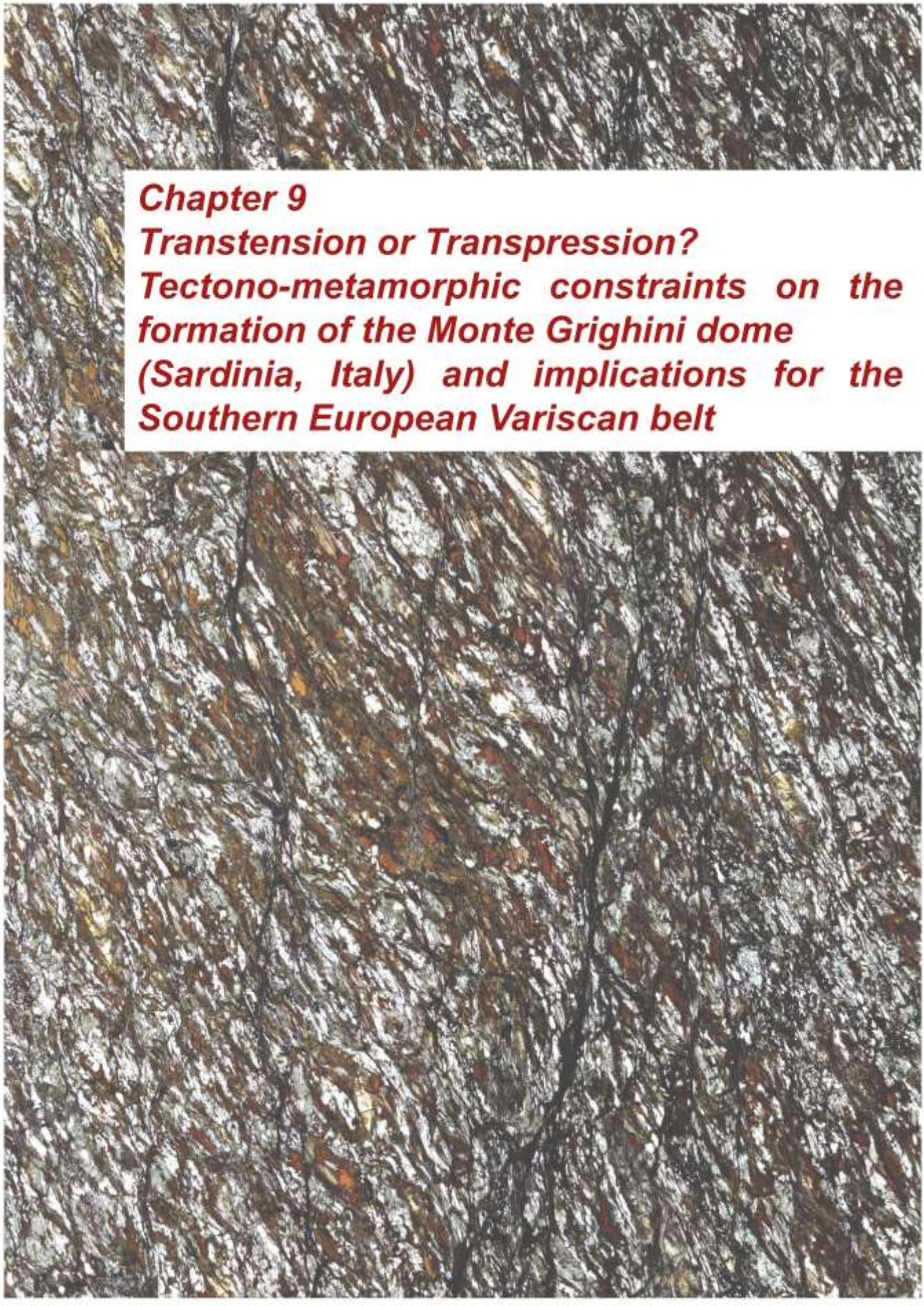

Chapter 9
Transtension or Transpression? Tectono-metamorphic constraints on the formation of the Monte Grighini dome (Sardinia, Italy) and implications for the Southern European Variscan belt

9.1. Introduction

Dome-shaped structures, characterized by a core of high-grade metamorphic or granitic rocks surrounded by low-grade ones, are important tectonic features in orogens (Burg, 2004; Whitney et al., 2004, 2013; Platt et al., 2015; Cao et al., 2022). Their origin and tectonic setting are still debated, and several mechanisms have been proposed for their formation, tectonic regime and exhumation (Coney, 1980; Whitney et al., 2004). During the 1980's and 1990's, the formation of domes was mostly associated with metamorphic core complexes (MCCs; Coney, 1980; Coney & Harms, 1984; Lister & Davis, 1989) as inferred in the Basin and Range province (western North America). More recently, several studies highlighted the importance of strike-slip tectonics, i.e., transtension or transpression tectonics for their formation (Druguet, 2001; Denèle et al., 2007, 2009; Gebelin et al., 2009; Zhang et al., 2017). These processes involve large-scale high-temperature (H*T*) ductile shear zones, which weaken the crust and contribute to the exhumation and the emplacement of intrusions (Druguet, 2001; Rosenberg & Handy, 2005). For these reasons, a multidisciplinary approach is necessary to better constrain domes formation (e.g., Aguilar et al., 2015; Broussolle et al., 2015; Zhang et al., 2017; Cao et al., 2022; Fu et al., 2022).

The Variscan orogeny in Europe is characterized by numerous dome-shaped structures that developed from the collisional stage at ~360-350 Ma until orogenic collapse at ~300-290 Ma (Vanderhaeghe & Teyssier, 2001; Faure et al., 2009; Gapais et al., 2015; Vanderhaeghe et al., 2020; Cochelin et al., 2021; Vanardois et al., 2022a, b). The development of the Variscan chain was also widely affected by the development of crustal-scale strike-slip shear zones during the late-Carboniferous ~340-300 Ma (Arthaud & Matte, 1977; Matte, 2001; Carosi & Palmeri, 2002; Di Vincenzo et al., 2004; Carreras & Druguet, 2014; Franke et al., 2017; Simonetti, 2021).

The tectono-metamorphic history of the Monte Grighini dome and its non-coaxial deformation, integrating field observations, meso- and microstructural data, kinematics of the flow, *P-T* estimations coupled with *in-situ* U–(Th)–Pb (texturally- and chemically-controlled) geochronology on monazite has been unraveled. Comparing this area with other similar sectors in the southern European Variscan belt (e.g., Carosi et al., 2020, 2022; Simonetti, 2020a, b, 2021), a tectonic model in the framework of the East Variscan Shear Zone during the Upper-Carboniferous has been proposed (EVSZ; Matte, 2001; Corsini & Rolland, 2009; Padovano et al., 2012, 2014; Simonetti, 2021).

9.2. Investigated area and methods

The Monte Grighini dome, exposed in the Variscan belt in Sardinia (Figs. 9.1a, b), is a NW-SE elongated dome belonging to the hinterland-foreland transition zone (Musumeci, 1992).

Authors have interpreted this dome as developed in a transtensional regime at ~305-295 Ma, where the exhumation was driven by the Monte Grighini shear zone (MGSZ; Cruciani et al., 2016). However, Elter et al. (1990) ascribed the Monte Grighini dome as a late-Carboniferous strike-slip shear zone. Also, due to the presence of several similarities between the MGSZ and the Posada-Asinara shear zone (PASZ) in northern Sardinia and within the framework of the southern European Variscan belt (Matte, 2001; Carosi et al., 2020, 2022; Simonetti, 2021 for a review), a re-investigation of the extensional regime associated with the MGSZ is necessary.

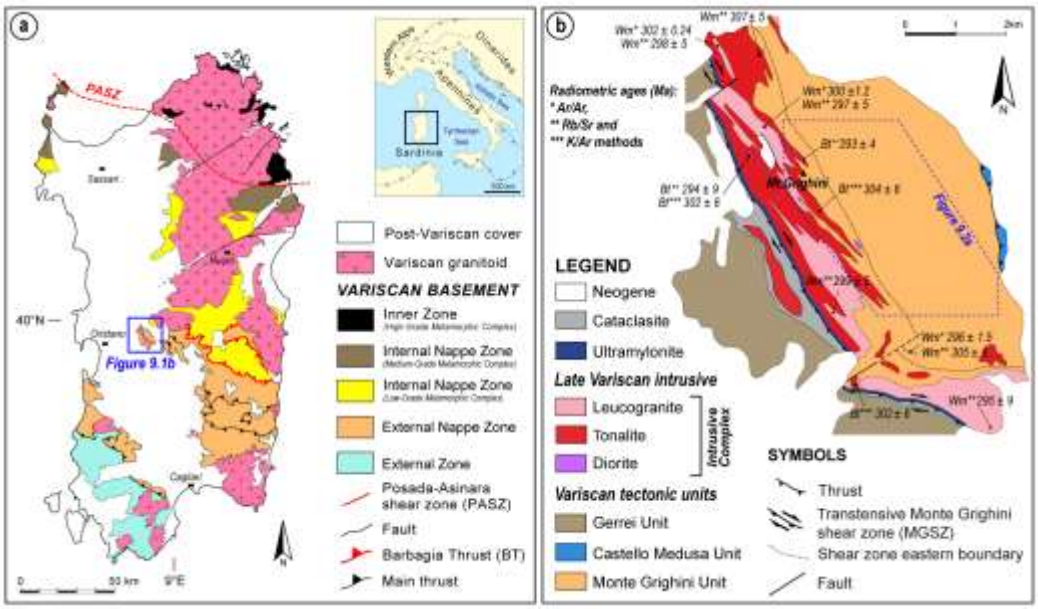

Figure 9.1: a) Tectonic sketch map of Sardinia (modified after Carosi et al., 2020). The location of the investigated dome is marked by a blue box; b) simplified Monte Grighini dome geological map (modified after Musumeci et al., 2015; Cruciani et al., 2016). Previous radiometric ages, the method used for dating, and the studied mineralogical phase are shown in the inset. The dashed blue line indicates the perimeter of the investigated area (Fig. 9.2a).

The *C'* shear band method (Kurz & Northrup, 2008; Gillam et al., 2013) with two different porphyroclasts-based methods has been integrated: (a) the porphyroclast aspect ratio method (PAR; Passchier, 1987; Wallis et al., 1993) and (b) the rigid grain net method (RGN; Jessup et al., 2007) in order to estimate the amount of pure and simple shear components.

To constrain the deformation regime (e.g., transpression/transtension; Fossen et al., 1994; Fossen & Tikoff, 1998), the angle $\theta = (\arcsin Wk)/2$ (Xypolias, 2010), between the maximum Instantaneous Stretching Axis (ISA max) in the horizontal plane and the shear zone boundary has been calculated.

Pressure-temperature (*P-T*) conditions were estimated using phase equilibrium modeling. Phase diagrams were computed in the 10-component NCKFMASHTO (Na_2O-CaO-K_2O-FeO-MgO-Al_2O_3-SiO_2-H_2O-TiO_2-Fe_2O_3) system using Theriak–Domino (De Capitani & Brown, 1987; De Capitani & Petrakakis, 2010) and the internally consistent dataset of Holland & Powell (2011; update ds62; February 2012) and associated solution models of White et al. (2014), excepting for the plagioclase model of Holland et al. (2021). The bulk composition for modelling was determined using an X-ray map of a representative area of the thin section. X-ray maps of Al, Fe, K, Mg, and Na were acquired in a single scan by wavelength-dispersive spectrometry (WDS), whereas Ca, P, Si, and Ti were measured at the same time by energy-dispersive spectroscopy (EDS). The program XMapTools v4 (Lanari et al., 2014) was used to process compositional maps. Local bulk compositions were generated from the oxide weight-percentage maps by averaging pixels with a density correction (Lanari & Engi, 2017). The *P-T* condition has been inferred with compositional isopleth thermobarometry. The results of phase equilibrium modeling were compared with those of the conventional Ti-in-Bt geothermometer (Henry et al., 2005).

Before isotopic monazite dating, grain locations, internal features (e.g., inclusions) and their textural position were investigated through a scanning electron microscope hosted at the University of Torino (Italy). The further step was to analyze the chemistry and the zoning of each monazite crystal using the JEOL 8200 Super Probe electron microprobe hosted at the University of Milano (Italy). Monazite chemistry and X-ray compositional maps are necessary for defining the compositional zoning required for the correct interpretation of monazite grains and relative ages. Monazite crystals were analyzed *in-situ*, on 30 µm-thick thin sections, by the Laser Ablation Inductively Coupled Plasma-Mass Spectrometry (LA-ICP-MS) at the Università di Perugia (Italy).

9.3. Field data and mesoscale observations

A non-numerical progression in the description of deformation phases and structural elements has been used (e.g., S_p, S_{p-1}). Abbreviations are: (S) for syn-metamorphic surfaces or axial plane foliation; (A) for fold axes; (L) for object lineations; (F) for folds; and (D) for the deformation phases. The suffix ‘p’ denotes ‘principal’. Four ductile deformation phases were detected.

Figures 9.2a and b show the geological map and the cross-section based on fieldwork performed as part of this study, integrated with existing cartographic data (Musumeci et al., 2015).

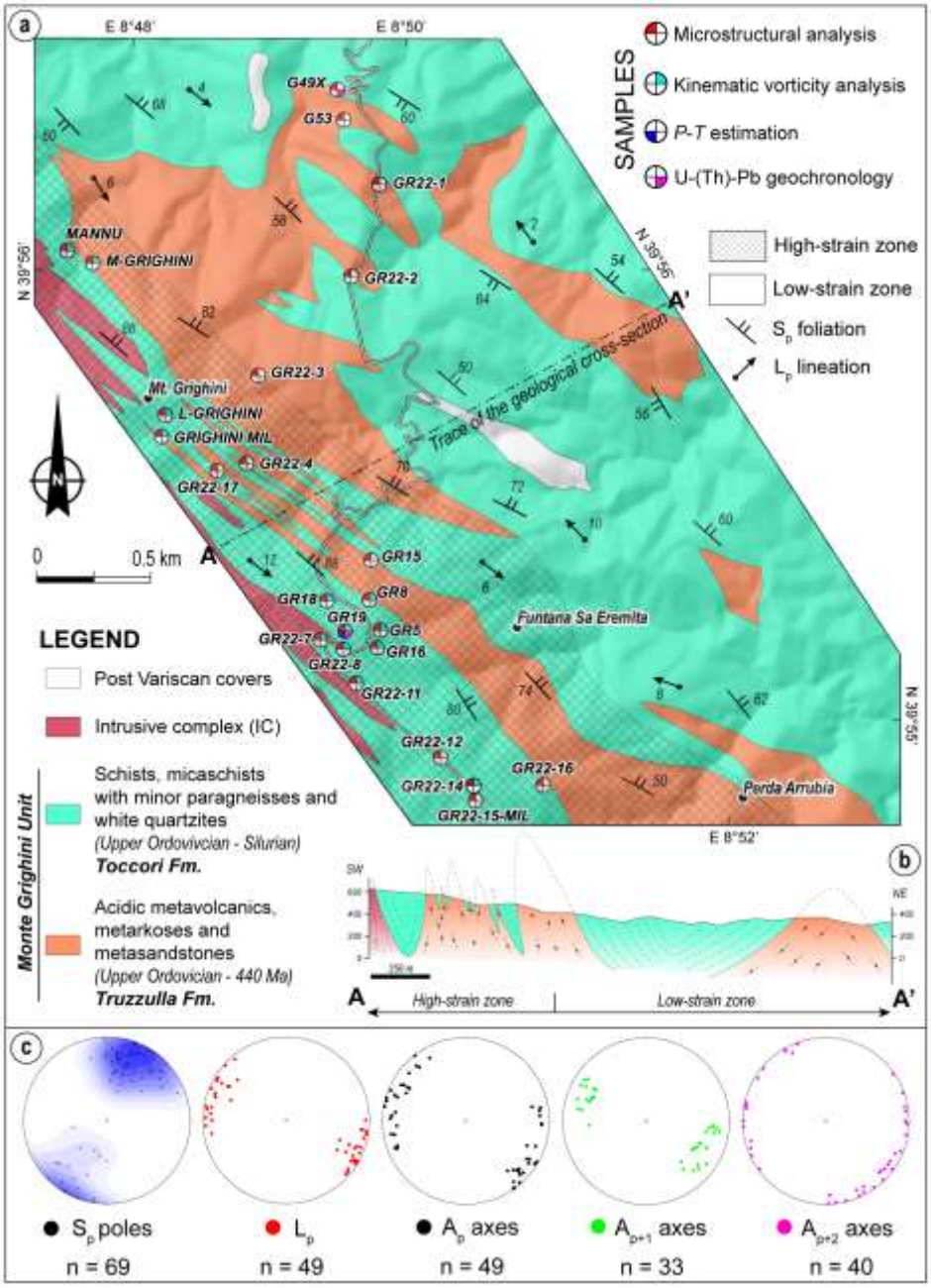

Figure 9.2: a) Simplified geological map of the investigated sector of the dome (see Fig. 9.1b for its position). Samples selected for study and the corresponding types of analysis are shown; b) SW-NE oriented geological cross-section; c) stereoplots (equal areal, lower hemisphere projections) of the main structural elements.

The oldest detectable deformation phase (D_{p-1}) is testified by a relict foliation (S_{p-1}), observable only in correspondence of the hinges of D_p folds (Fig. 9.3a). Structures related to the D_p phase are characterized by tight to isoclinal (Fig. 9.3a) folds. A_p fold axes show a W-E to NW-SE plunging with quite scattered values (Fig. 9.2c). The F_p folds are associated with an S_p foliation parallel or sub-parallel to the relative fold axial planes (Fig. 9.3a), and it represents the main planar structural element in the overall area. The S_p foliation shows a general NW-SE strike and dips at moderately (Fig. 9.3b) to mostly high/sub-vertical angles (Fig. 9.3c) both to the N-NE and to the S-SW (Fig. 9.2c). S_p changes from a disjunctive cleavage with sub-parallel cleavage domains, in the northeastern part of the area, to a mylonitic continuous foliation, toward the westernmost sector; i.e., approaching the MGSZ. The L_p object lineation is defined by elongate biotite, sillimanite and muscovite crystals and by millimeter- to centimeter-scale quartz ribbons. The L_p shows a N90-N120 main trend and gently plunges toward both NW and SE (Fig. 9.2c) with low to sub-horizontal angles (Fig. 9.3b). The D_p tectonic phase is characterized by a deformation partitioned into domains alternating between prevailing folding and shearing deformation (low- and high-strain zones, respectively). Moving southwestward, i.e., toward the MGSZ, the strain increases and is characterized by non-coaxial deformation. Shear sense indicators have been observed both at meso- and microscale on sections parallel to the XZ plane of the finite strain ellipsoid and are linked to the D_p. They are mainly represented by *C*-*C'*-S fabric (Fig. 9.3d) and rotated porphyroclasts. All indicate a top-to-the NW sense of shear. F_{p+1} folds, affecting the S_p foliation, are the main evidence of D_{p+1} phase in the study area. The F_{p+1} folds are commonly gentle to slightly asymmetric upright folds (Fig. 9.3e), ranging from metric to pluri-m long wavelengths. Locally kink and/or chevron-type folds are detectable. Fold axes, A_{p+1}, generally trend parallel both to the F_p fold axes and to the L_p object lineation (Fig. 9.2c), with higher plunging values. A D_{p+1}-related crenulation cleavage (S_{p+1}) is locally recognizable. The F_p-F_{p+1} fold interference pattern shows parallel axes and sub-orthogonal axial planes (Fig. 9.3e). D_{p+2} produced gentle to open F_{p+2} folds with sub-horizontal axes and axial planes (Fig. 9.3f). A_{p+2} axes plunge at low angles toward E-W to NW-SE with very high dispersion (Fig. 9.2c). D_{p+2} phase is not associated with the development of foliations and lineations.

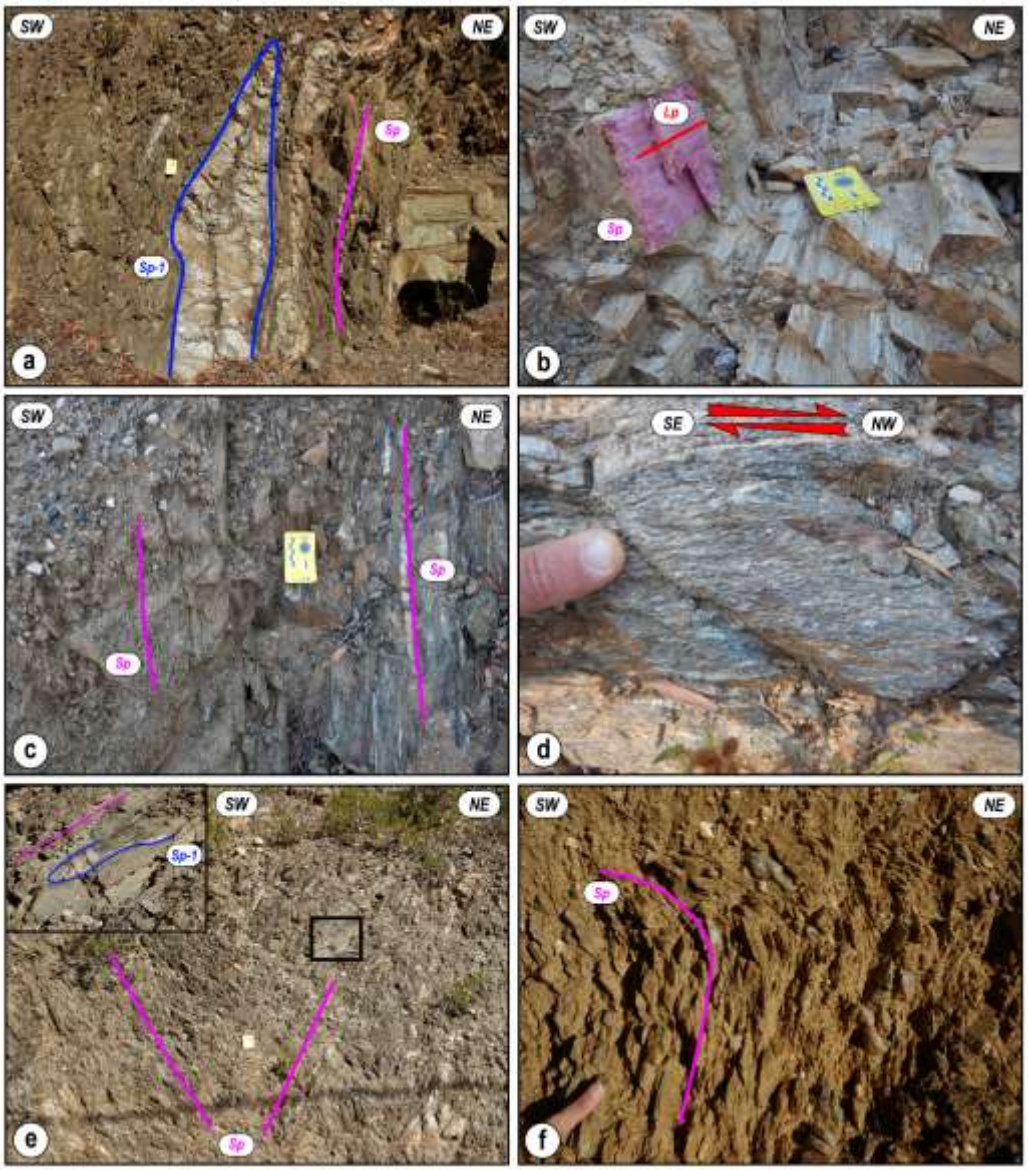

Figure 9.3: a) Outcrop evidence of F_p folds in the Toccori Fm. deforming an older relict foliation (S_{p-1}); b) L_p sub-horizontal object lineation along the moderately dipping S_p is displayed; c) sub-vertical S_p foliation. The contact between the intrusive rock belonging to the IC (on the left) and the Toccori Fm. schist (on the right) is parallel to the S_p; d) mylonite from the Toccori Fm. at the mesoscale: C'-S fabric is indicative of a top-to-the NW sense of shear; e) upright F_{p-1} fold, deforming the S_p attitude. A zoom of the F_p fold and the S_{p-1} foliation located in the NE limb of the F_{p+1} fold is displayed; f) evidence of late open folds (F_{p+2}) with sub-horizontal axes and axial planes, deforming S_p foliation.

9.4. Microstructures

Microstructural investigations have been performed on 24 samples (see Fig. 9.2a for the sample location). Foliations have been classified according to Passchier & Trouw (2005). Quartz dynamic recrystallization microstructures are defined according to Law (2014). Mineral abbreviations are after Warr (2021).

Porphyroids and metavolcanic rocks belonging to the Truzulla Fm. are generally strongly deformed and characterized by a porphyroclastic microstructure (Fig. 9.4a) with millimetre-sized K-feldspar (Fig. 9.4b) and subordinate plagioclase porphyroclasts. The S_p disjunctive cleavage is marked by white mica, biotite and rare chlorite. Quartz and phyllosilicate grains are oriented parallel to the main schistosity (S_p), wrapping around feldspar porphyroclasts (Fig. 9.4b). Asymmetric K-feldspar porphyroclasts, showing a top-to-the NW sense of shear, are recognizable (Fig. 9.4b). Quartz shows lobate grain boundaries suggesting dynamic recrystallization by grain boundary migration (GBM), indicative of temperature > 500 °C (Law, 2014). In some samples, overprinting by subgrain rotation (SGR) recrystallization is found.

Metasediments belonging to the Truzulla Fm. are characterized by a disjunctive cleavage (S_p), sub-parallel cleavage domains, and a continuous schistosity mainly made of biotite, white mica and quartz. The S_p foliation wraps around garnet and staurolite (Fig. 9.4c). A sporadic internal foliation (S_{p-1}), made of orientated quartz, white mica, ilmenite, and graphite, varies from discordant to concordant with the external one (Fig. 9.4c). This suggests that garnet and staurolite could be inter- to early syn-tectonic (syn-S_p) minerals with respect to the S_p (i.e., between the D_{p-1} and D_p phase and during the early D_p phase). Quartz presents irregular, lobate and ameboid grain boundaries compatible with GBM recrystallization (Law, 2014). Samples collected within the high-strain zone display a top-to-the NW sense of shear, marked by mica-fish (Fig. 9.4d), *C'*-*C*-S fabric, and asymmetric strain shadows around porphyroclasts.

Schist and paragneiss from the Toccori Fm. are characterized by the alternating millimeter-scale quartzo-feldspathic and muscovite-biotite-sillimanite-rich layers (Fig. 9.4e). Prismatic sillimanite, biotite and white mica define the S_p schistosity. However, fine-grained fibrolite also occurs (Fig. 9.4e). Kinematic indicators, pointing to a top-to-the NW sense of shear, such as *C*-*C'*-S fabric (Fig. 9.4e) and mica-fish, are present. Quartz shows evidence of GBM and, more rarely, chessboard extinction, which implies high-*T* recrystallization (*T* > 650°C; Law, 2014; Fig. 9.4f).

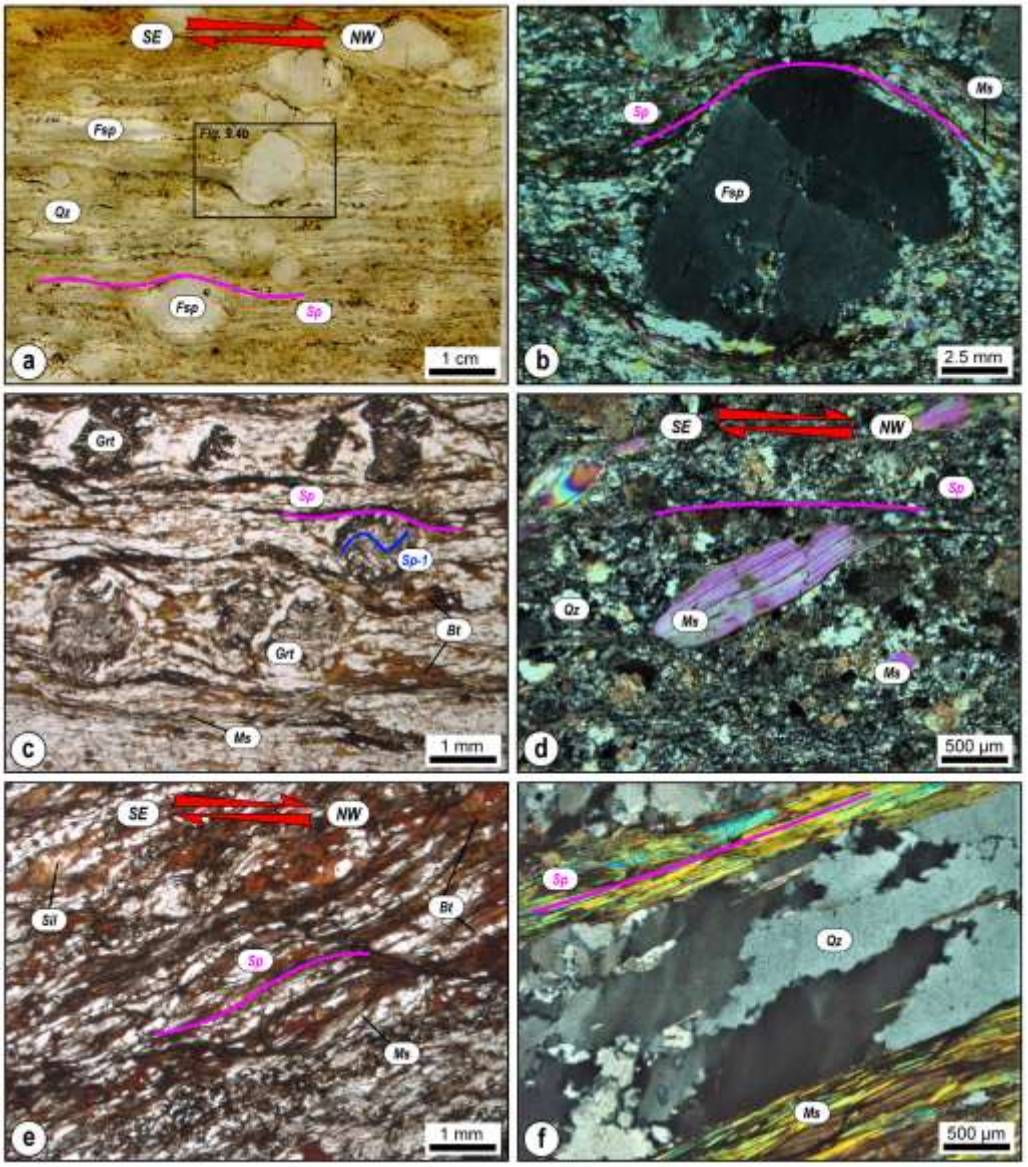

Figure 9.4: a, b) Sheared metavolcanic rock belonging to the Truzulla Fm. showing a dextral sense of shear (top-to-the NW; a is PPL: plane-polarized light; b is XPL: crossed-polarized light). σ-type porphyroclast shows a top-to-the NW sense of shear; c) garnet porphyroclast showing an internal foliation S_{p-1} (blue line) both discordant and locally concordant with the S_p foliation. Garnet is wrapped by the main foliation S_p (violet line) defined by white mica+ biotite (PPL); d) mica-fish in Truzulla Fm. rock showing a top-to-the NW sense of shear (XPL); e) C'-S fabric in sillimanite-bearing schist, indicating a top-to-the NW sense of shear (PPL); f) dynamically recrystallized quartz showing lobate and irregular grain boundaries indicative of GBM and chessboard extinction (XPL).

9.5. *P-T*-D-*t* estimates

9.5.1. Kinematic of the flow

The full dataset of the kinematic vorticity analysis is reported in Table 1.

	Kinematic vorticity analysis											
	C' shear bands method			Rigid grain net method			Porphyroclasts method					
SAMPLE NAME	N	v ANGLE (°)	Wk	N	Wm	Wm mid	Rc *min*	Rc *max*	Wk min	Wk max	Wk mid	θ
GR22-5	-	-	-	68	0.39-0.44	0.42	1.48	1.7	0.37	0.49	0.43	13
GR22-7	23	32	0.44	-	-	-	-	-	-	-	-	13
GR22-8	10	31	0.47	-	-	-	-	-	-	-	-	14
GR22-11	15	30	0.5	-	-	-	-	-	-	-	-	15
GR22-14	27	30	0.5	-	-	-	-	-	-	-	-	15
L-GRIGHINI	-	-	-	64	0.43-0.47	0.45	1.63	1.81	0.45	0.53	0.49	15
M-GRIGHINI	-	-	-	60	0.37-0.45	0.41	1.52	1.72	0.4	0.49	0.45	13
GR5	20	32	0.44	-	-	-	-	-	-	-	-	13
GR8	22	33	0.41	-	-	-	-	-	-	-	-	12
GR9	10	32	0.44	-	-	-	-	-	-	-	-	13
GR16	11	30	0.5	-	-	-	-	-	-	-	-	15
GR18	6	33	0.41	-	-	-	-	-	-	-	-	12
GR19	19	31	0.47	-	-	-	-	-	-	-	-	14
GRIGHINI MIL	14	30	0.5	-	-	-	-	-	-	-	-	15
MANNU	16	31	0.47	-	-	-	-	-	-	-	-	14

Table 1: Results of kinematic vorticity investigations: number of data (N), angle between C' planes and the shear zone boundary (v), Wk value (Wk), mean value of Wk in a range (Wm) and the average of its range (Wm mid); minimum critical axial ratio (Rcmin), maximum critical axial ratio (Rcmax), minimum value of Wk (Wkmin), maximum value of Wk (Wkmax), mean value of Wk (Wkmid) and angles between the maximum ISA in the horizontal plane and the shear zone boundary (θ).

Twelve samples (see Fig. 9.2a for samples location) analyzed with the *C'* shear band method gave vorticity numbers ranging from 0.41 to 0.50, with a mean of 0.46. Vorticity analysis using the porphyroclasts-based method on three samples (GR22-5, L-GRIGHINI and M-GRIGHINI) gives values comprised between 0.37-0.47 and 0.37-0.53 for RGN and PAR, respectively. The datasets collected by the two-types porphyroclasts-based methods are comparable and fit with the *C'* shear bands approach results. Considering all data obtained by different methods, the *Wk* value ranges between 0.37-0.53 (Fig. 9.5a).

Although different methods have been used, vorticity values are relatively homogeneous and do not show drastic variation along the strain gradient. The obtained vorticity values indicate that the MGSZ experienced general shear (Forte & Bailey, 2007; Fig. 9.5a) during deformation, which involved 77-64% pure shear and 23-36% simple shear components (Fig. 9.5b). Calculated *θ* angles between the maximum Instantaneous Stretching Axis (ISA max) in the horizontal plane and the shear zone boundary vary between 12-15°. These values indicate a pure shear dominated transpression deformation (Fig. 9.5c).

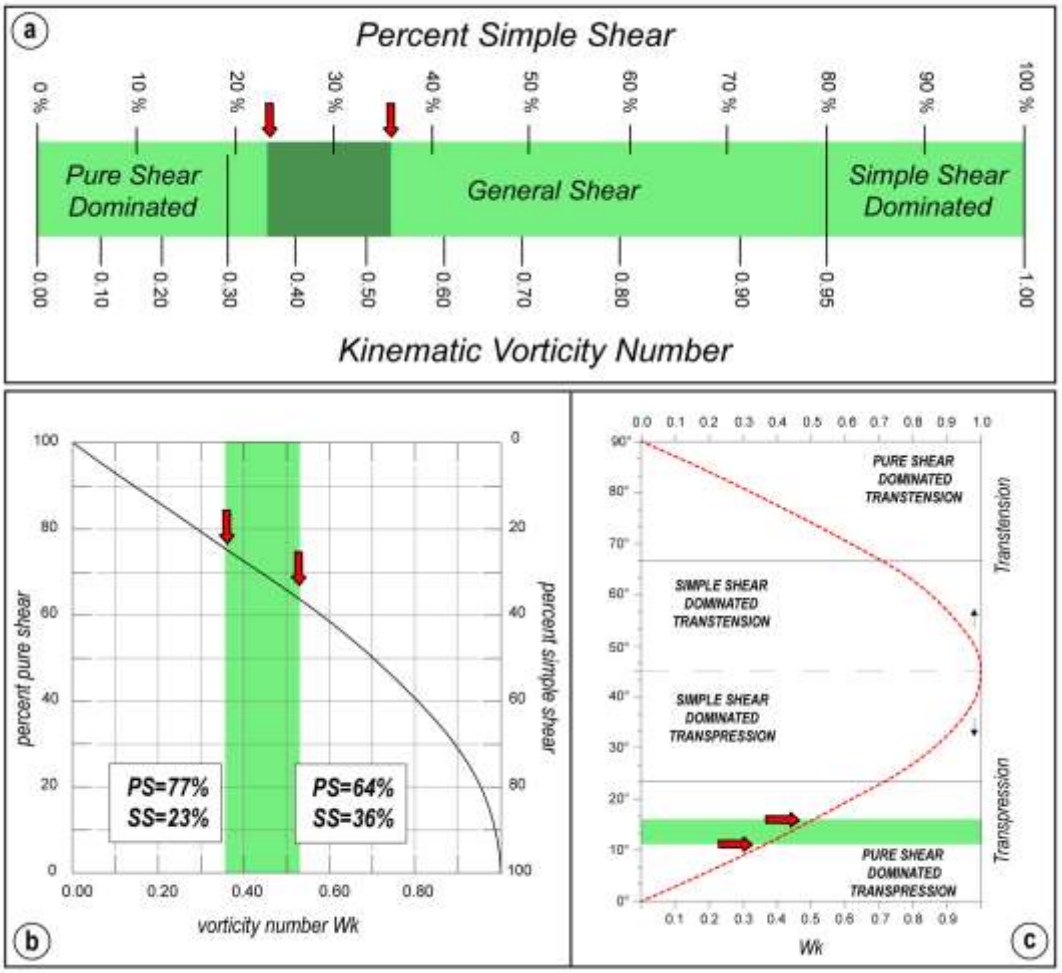

Figure 9.5: a) Scale relations between the kinematic vorticity number Wk number and the percent of simple shear. Zones of pure shear, general shear and simple shear dominated deformations are marked (modified after Forte & Bailey, 2007); b) relationship between kinematic vorticity number Wk and the percentage of pure shear (PS) and simple shear (SS) (modified after Law et al., 2004); c) relationship between the orientation of the maximum instantaneous stretching axis (ISA max) with respect to the shear zone boundary (angle θ) versus the Wk number (modified after Fossen & Tikoff, 1993). Samples fall in the field of pure shear dominated transpression.

9.5.2. Mineral compositions

Sample GR19, a sillimanite-bearing mylonitic schist (Fig. 9.6a) from the Toccori Fm. (see Fig. 9.2a for the sample location), was chosen for *P-T* investigation. GR19 contains (Fig. 9.6b; vol%): quartz (36%), white mica (26%), biotite (22%), sillimanite (14%), with plagioclase and ilmenite as the main accessory minerals (2% in total). Selected mineral compositions in sample GR19, derived from XMapTools, are reported in Table 2.

Mineral:	***Biotite***				***White Mica***	
Position:	***Sp***		***Post-Sp***		***Sp***	
wt%	*N of pixel = 65*	*N of pixel = 100*	*N of pixel = 88*	*N of pixel = 91*	*N of pixel = 112*	*N of pixel = 255*
SiO_2	35.14	34.69	34.69	34.86	45.31	44.77
TiO_2	2.65	2.37	2.79	2.73	0.60	0.56
Al_2O_3	20.02	20.12	19.36	19.49	36.19	35.61
FeO	19.08	19.96	21.31	21.20	1.08	1.04
MgO	6.97	7.37	6.70	6.67	0.45	0.44
CaO	0.06	0.06	0.05	0.05	0.05	0.05
Na_2O	0.13	0.13	0.13	0.14	0.83	0.85
K_2O	9.25	9.41	9.30	9.32	9.97	9.80
Total	93.30	94.11	94.33	94.46	94.48	93.12
Cations						
Si	2.70	2.68	2.69	2.70	3.03	3.04
Ti	0.16	0.14	0.16	0.15	0.03	0.03
Al^{VI}	0.52	0.50	0.46	0.48	1.91	1.89
Al^{IV}	1.32	1.32	1.31	1.30	0.96	0.96
Fe_{tot}	1.06	1.13	1.17	1.17	0.07	0.06
Mg	1.01	1.02	0.98	0.97	0.05	0.05
Ca	0.01	-	-	-	-	-
Na	0.02	0.02	0.02	0.02	0.11	0.11
K	0.93	0.93	0.92	0.92	0.85	0.85
Sum	7.73	7.74	7.71	7.71	7.01	6.99
XMg	0.39	0.40	0.36	0.36	0.42	0.42

Table 2: Representative mean values of the mineral compositions from XMapTools of sample GR19. Structural formulae were calculated for biotite and white mica = 11 O.

According to Guidotti (1984) and Keller et al. (2005) classification, white mica is a muscovite with minor pyrophyllite content. It is homogeneous in composition, with mean Si contents of 3.04 ± 0.03 a.p.f.u. and *XMg* (*XMg* = Mg/(Mg+Fe)) of 0.42 ± 0.04. Whilst two generations of biotite can be distinguished using microstructural criteria; these different generations do not show drastically different compositions. After the Tischendorf et al. (2004) classification, biotite is classified mainly as siderophyllite with minor annite composition (see Appendix 1a). Biotite parallel to the S_p shows *XMg* of 0.39 ± 0.01, whereas the post-kinematic (i.e., post-D_p) biotite displays *XMg* of 0.35 ± 0.02. The Ti a.p.f.u. in biotite has a mean value of 0.14 ± 0.03. Plagioclase is albitic in composition (*XAn* = 0.04-0.07).

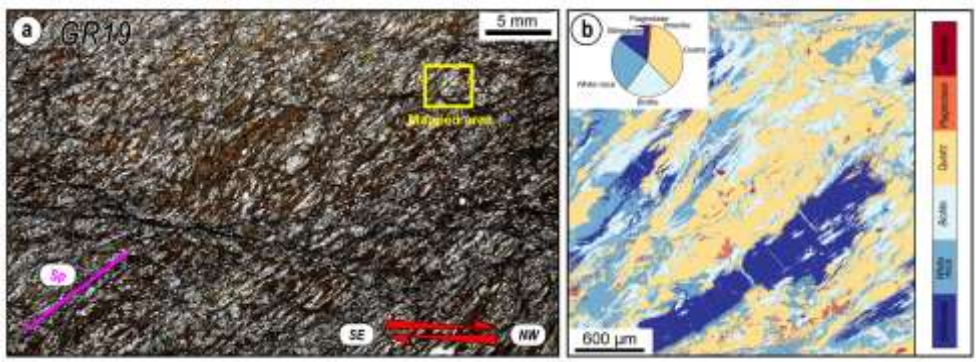

Figure 9.6: a) Thin section scan of sample GR19. The area mapped using EPMA is indicated in yellow (PPL); b) processed X-ray map of sample GR19 showing the distribution of different minerals. The inset pie-chart depicts the volume % for each phase.

9.5.3. P-T constraints

Figure 9.7 shows the *P-T* equilibrium phase diagram for sample GR19, calculated for 0.1-1 GPa and 500-700 °C. The sillimanite-*in* curve is located in the pressure range of ~0.3-0.7 GPa and between ~560-700 °C. Biotite is completely consumed above 680 °C. Rutile is stable above the upper sillimanite-*in* line, while ilmenite is predicted in the sillimanite stability field. The observed mineral assemblage (labeled as Pl–Ms–Bt–Ilm–Sil; Fig. 9.7a) is represented by a field restricted in a *P-T* range of 0.3-0.7 GPa and 560-670 °C, delimited by the disappearance of staurolite and by the stability boundary of sillimanite (Fig. 9.7a). According to the syn-S_p biotite compositional isopleths (*XMg* = 0.39-0.40), joined with the compositions of white mica (Si = 3.03-3.05 a.p.f.u.; *XMg* = 0.41-0.43), the inferred *P-T* conditions are compatible with the observed mineral assemblage stability field (Fig. 9.7b). Similar temperature results (*T* = 625 ± 25 °C; Appendix 1b, c) have been obtained using Ti-in-Bt conventional geothermometry (Henry et al., 2005), consistent with the phase diagram results (Fig. 9.7b).

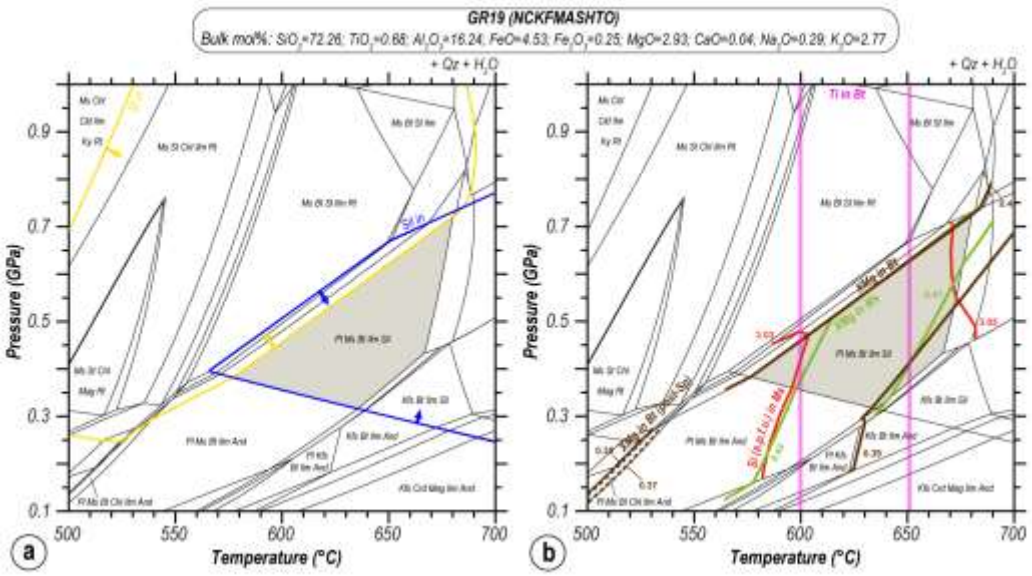

Figure 9.7: P-T equilibrium phase diagram for the high-temperature mylonitic sample GR19. The inferred equilibrium assemblage is highlighted in grey. a) Yellow and blue lines mark the staurolite-out and sillimanite-in reactions, respectively; b) the intersection of compositional isopleths of biotite and white mica. The Ti-in-Bt range has been provided in purple.

9.5.4. Monazite textural position and chemistry

Two samples, inside and outside the high-strain mylonitic zone (GR19 and G49X, respectively; see Fig. 9.2a for the sample position), were chosen for *in-situ* geochronology of monazite. Sample G49X has been previously investigated for the *P-T* estimations by Cruciani et al. (2016). A total of seven monazite grains, two for sample GR19 and five for sample G49X were investigated. Selected analyses of monazite and the spot analysis position are available in Appendix 2, 3.

Monazites from the sample G49X are between ~40 and ~120 μm in length. They generally occur among quartz, biotite, and white mica in the S_p, while in two cases (Mnz 6a and Mnz 7b), they occur as inclusions within garnet. The monazites from GR19 are between ~20 and ~60 μm in length. Most of the monazites in the mylonite are very small and difficult to unravel. The crystals located along the S_p foliation are generally within biotite- or sillimanite-rich domains along the mylonitic foliation. One monazite (Mnz 11) has a sillimanite mineral inclusion. This crystal is particularly interesting due to the sillimanite growing contemporaneous with the shearing event. Backscattered electron (BSE) images show clear zoning in most grains with domains of different grey tones (see Appendix 2). X-ray compositional maps reveal that such zoning is well controlled by the different distributions of *X*(HREE + Y) and *X*(LREE) + Th. *X*(HREE+Y) is defined as (HREE+Y)/REE, whereas *X*(LREE) is LREE/REE. The electron microprobe analysis (see Appendix 2, 3) revealed two chemical domains (I and II), based on Y, Th, and REE content. In sample G49X, Domain I (Figs. 9.8a, b) is characterized by cores with medium-Y content ranging from 0.022 to 0.035 (a.p.f.u.), low-Th values from 0.01 to 0.026 (a.p.f.u.) and *X*(HREE + Y) low amounts varying from 0.044 to 0.067. Domain II (Figs. 9.8a, b) is characterized by medium-high-Y rims/grains, $0.028 < Y < 0.057$ (a.p.f.u.), low-medium-Th values from 0.05 to 0.055 (a.p.f.u.) and $0.071 < X(\text{HREE} + Y) < 0.094$. The monazites enclosed in garnet crystals follow the same zoning pattern of many matrix crystals and are chemically similar, in which the cores show medium/low-Y and *X*(HREE + Y), and the rims are enriched in these same elements. In sample GR19, Domain I (Figs. 9.8a, b), as documented by X-ray maps (see Appendix 2, 3), occurs only in Mnz 11, where a medium-Y (Y = 0.033) and low-medium-Th (Th = 0.013) core is recognizable. Medium- to high-Y values ($0.042 < Y < 0.061$ a.p.f.u.), medium-Th values from 0.018 to 0.041 (a.p.f.u.) and *X*(HREE + Y) between $0.069 < X(\text{HREE} + Y) < 0.095$ are well preserved and represent the main features of Domain II (Figs. 9.8a, b). This domain has been observed both as a continuous rim around cores or as a homogeneous medium-high-Y content grain. The sillimanite inclusion is inside the Y-rich rim correlated with Domain II.

In summary, based on the previously described textural and chemical arguments, monazite, in both samples, shows two main growth domains/generations (Figs. 9.8a, b), i.e., (i) Domain I, representing the core of the grains both in garnet and along the mylonitic foliation, with low-medium-Y contents; (ii) Domain II, forming continuous to rarely discontinuous high *X*(HREE + Y) rims or homogeneous grains, occurring mostly in the matrix. Taking into account the resolution of the applied method, no significant difference between the monazite chemistry and obtained ages has been highlighted.

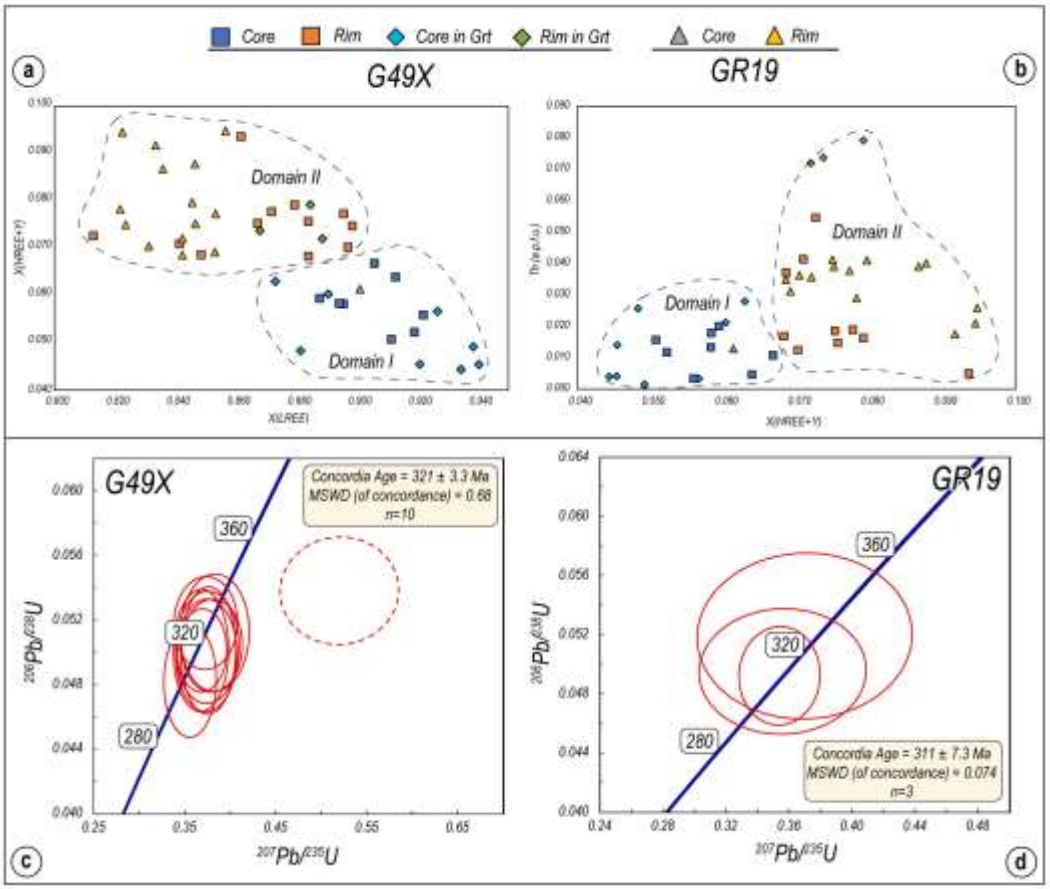

Figure 9.8: Chemical monazite variations in sample G49X and GR19: a) X(HREE + Y) vs. X(LREE) plot and in (b) X(Y+HREE) vs. Th plot. In both diagrams, monazite compositional domains (I and II) and the microstructural position of the analyzed grains are highlighted; (c) and (d) $^{206}Pb/^{238}U$ versus $^{207}Pb/^{235}U$ concordia diagrams for sample G49X and GR19. In sample G49X the dashed line indicates a spot not aligned along the concordia line.

9.5.5. In-situ U–(Th)–Pb geochronology and ages

The measured isotopic data are reported in Appendix 2 (see also for the laser spot analysis position). A total of seven monazite grains covering the whole textural-chemical variability were selected for *in-situ* dating, obtaining data from a total of 13 spots (10 and 3 for samples

G49X and GR19, respectively). The obtained results are plotted in a $^{206}Pb/^{238}U$ versus $^{207}Pb/^{235}U$ concordia diagram (Figs. 9.8c, d). The concordia calculation gives values of 321 ± 3.3 and 311 ± 7.3 Ma for G49X and GR19, respectively (Figs. 9.8c, d). The monazite crystal with a sillimanite inclusion (Sample GR19 in Mnz 11) produced ages of ~315-310 Ma. Results are similar for the two samples, with no detected variation between different chemical domains and ages, according to the precision of the applied datings method.

9.6. Discussion

9.6.1. P-T-D-t tectono-metamorphic evolution

After field observations integrated with meso- and microstructural investigations, four ductile deformation phases have been highlighted. The D_{p-1} structures were associated with the S_{p-1} relict foliation both in the hinge of F_p folds or as an internal foliation in the barrovian index minerals. The S_{p-1} foliation could be ascribed as the only evidence of the nappe stacking event (D_1 and D_2 deformation phases of Cruciani et al. (2016). Thermobarometric data from the D_1 of the MGU indicate *T* ~490-540 °C and *P* ~0.7-0.9 GPa (Cruciani et al., 2016) at the late stage of nappe stacking. The D_p phase controls the whole architecture of the study area. Obtained data highlight, as previous authors did before (Columbu et al., 2015), an increase in strain and in the amount of kinematic indicators going toward the MGSZ. The principal structures of the study area are controlled by the D_p deformation phase, linked to the MGSZ activity, in which the strain is partitioned into F_p tight and isoclinal folds (low-strain zone) and shear zone domains (high-strain zone) approaching the shear zone. The development of shear domains that gradually increase in number and dimension moving toward the MGSZ, i.e., southwestward, has been recognized and highlighted. Instead, D_p folds become smaller and less frequent, while the mylonitic foliation becomes gradually more penetrative and continuous (strain partitioning). The presence of a sub-vertical S_p foliation, parallel to the boundaries of the shear zone, and F_p fold axes, parallel to the sub-horizontal L_p mineral lineation, is compatible with the simultaneous development of D_p shear and F_p fold domains linked to the MGSZ activity. Kinematic indicators, both at the meso- and microscale, point to a top-to-the NW sense of shear, in agreement with the previous interpretations (Elter et al., 1990; Musumeci, 1992). Despite Cruciani et al. (2016) linked the S_2 foliation of the Monte Grighini Unit far from the MGSZ, to syn-nappe emplacement, southward thrusting, and folding (Carosi & Pertusati, 1990; Carosi et al., 1991, 2002, 2004; Conti et al., 1998, 2001), no evidence of southward thrust-sense deformation has been detected. In addition, the steeply dipping foliation and the sub-horizontal lineation do not fit with the thrust deformation. The kinematic of the flow allows the characterization of the deformation in terms of the percentage of pure and simple shear components of the D_p phase.

The geometry and kinematics of the MGSZ are compatible with a transpressive regime as a consequence of dextral shear deformation with a shortening component perpendicular to the shear zone boundaries. F_p and F_{p+1} fold axes parallelism suggest that the transpressive regime was probably active until the end of the D_{p+1} deformation phase (i.e., the D_3 for Cruciani et al., 2016). Although D_p and D_{p+1} have been defined as different events, both deformation events are linked to the same deformation regime and result from continuous deformation, suggesting that the basement continued to undergo sub-horizontal shortening up to the final stages of collision. Subsequent post-collision and post-transpression gravitational instability were characterized by the development of open folds (F_{p+2}). An increase in metamorphic grade can be recognized going from NE to SW, in agreement with Cruciani et al. (2016). The syn-kinematic S_p mineral assemblage (sillimanite + biotite, biotite + white mica) parallel to the S_p mylonitic foliation is indicative of medium- to high-temperature amphibolite-facies.

Phase equilibrium modeling suggested equilibration conditions roughly at ~0.4-0.6 GPa and ~625 °C, pointing to a high temperature and low-pressure (H*T*/L*P*) thermal regime. Taking into account the uncertainties of our and previous *P*-*T* estimations (Cruciani et al., 2016), the shear event could be associated with a *T* ~625 ± 25 °C and a *P* ~0.4 ± 0.1 GPa. The investigated mylonitic sample clearly shows sillimanite oriented parallel to the S_p, suggesting that ductile deformation was still active in H*T* conditions within the sillimanite-stable condition. Obtained metamorphic data are also supported by the quartz chessboard extinction microstructures (~650 °C) and by the Ti-in-Bt temperatures (625 ± 25 °C). The growth of fibrolitic sillimanite at the expense of the prismatic ones, and the presence of post-S_p biotite, testify a retrograde path, probable during the late stages of the transpression. These conditions are consistent with the retrograde path observed by Cruciani et al. (2016). The growth of andalusite, testified by Cruciani et al. (2016), confirms that the sillimanite-bearing S_p assemblage was affected by exhumation to relatively shallower crustal levels.

The timing has been constrained by *in-situ* U–(Th)–Pb monazite dating. Even though some monazite chemical features contrasts are observed between them, both studied samples record a similar and comparable timing on the S_p both inside and outside the mylonitic zone. This indicates a partitioning of deformation and the contemporaneity between folding and shearing events during the transpressive activity of the D_p event. The obtained ages of ~315 Ma have mainly been detected in high-Y and low-Th inner rims and in monazites along the S_p. This supported the growth of monazites during retro-metamorphism and garnet breakdown. Also, the monazite crystal with sillimanite inclusions (Sample GR19, Mnz 11), compatible with domain II of the Mnz chemical groups, indicates ages of ~315-310 Ma.

This age is fundamental to constrain the shear event. The syn-tectonic emplacements of the IC at ~305-295 Ma (Del Moro et al., 1991) within the MGSZ and the presence of mylonitic and foliated granites highlight that the deformation linked to the dextral wrenching was still active until ~300 Ma.

The investigated dome and the associated MGSZ have been classically described with a transtensional model (Musumeci, 1992; Cruciani et al., 2016). However, the sub-vertical H*T* mylonitic foliation associated with a sub-horizontal mineral lineation in the MGSZ prevents the full investigation of this transtensional hypothesis and fits better with a transpressive regime (Fossen & Tikoff, 1998). The performed study demonstrated that the mylonitic stage (D_p corresponding to the D_4 phase for Cruciani et al., 2016) took place in an H*T* amphibolite-facies condition under a transpressive deformation regime. Also, structural and geochronological constraints highlight the contemporaneous shear-and-fold deformation that affected the Monte Grighini dome over a time span of ~15 Ma, based on both the structural and geochronological constraints. This enhanced strain partitioning and, consequently, strain localization in crustal-scale ductile shear zones probably favored the intrusions emplacing during the late stages of the pure-shear dominated transpression (Fig. 9.9a).

9.6.2. The MGSZ: a glance for late-Carboniferous transpressive deformation

Late Variscan transpressive shear zones played a fundamental role in the architecture of the Sardinian Variscan belt, accommodating the internal deformation due to continental collision in the inner portion of the chain (~325-305 Ma, Di Vincenzo et al., 2004; Carosi et al., 2012, 2020; Cruciani et al., 2022). In fact, a similar architecture obtained in the MGSZ has been described in the northern sector of the Sardinia island, where an amphibolite-facies transpressive shear zone, i.e., the Posada-Asinara shear zone (PASZ; Carosi et al., 2012, 2020, 2022) crops out. The amphibolite-facies condition of both shear zones is testified by the presence of syn-kinematic sillimanite + biotite or biotite + white mica parallel to the mylonitic foliation. The PASZ developed under decreasing temperature and pressure, starting at ~325 Ma and active for ~25 My. It is important to note that Carosi et al. (2020) constrained the timing of the activity of the PASZ with the same *in-situ* approach on monazites used for this work. The MGSZ and the PASZ show a similar ductile, transpressive deformation characterized by a similar percentage of pure shear deformation. Obtained new data, following the previous hypothesis of Elter et al. (1990), enhance the potential similitude and the correlation of the MGSZ to the regional-scale PASZ in the Sardinian Variscan belt.

This possibility is significant for recognizing a similar shear zone of the PASZ in the Nappe Zone, far from the inner zone of the Variscan belt. Texturally-controlled geochronological data indicate that similar ages of the transpression onset of the MGSZ have been obtained in different sectors of the Southern European Variscan belt (Simonetti, 2021; Carosi et al., 2022; Fig. 9.9b). In particular, similar features and ages of transpressive tectonic were collected, as well as in Sardinia (Carosi et al., 2020), also in the Maures-Tanneron Massif (MTM; Simonetti et al., 2020b) and in the External Crystalline Massif (Simonetti et al., 2018, 2020a, 2021; Jacob et al., 2021; Fréville et al., 2022; Vanardois et al., 2022). All these fragments have been associated with the East Variscan shear zone (EVSZ; Matte, 2001; Fig. 9.9b) framework. The EVSZ should be considered a network of interconnected transpressive shear zones displaying a similar evolution (Simonetti, 2021). The oldest ages (~340 Ma; Simonetti et al., 2018, 2021) of the transpressive deformation have been discovered in the External Crystalline Massif, whereas within the MTM (~323 Ma) and Sardinia island (~325-300 Ma), ages are younger. The MGSZ shows slightly younger ages (~315-300 Ma) with respect to the PASZ in Sardinia (Fig. 9.9c). According to Simonetti et al. (2020a), it is, therefore, possible that transpressional deformation along the EVSZ preferentially started to be accommodated in the lower and migmatitic crust (External Crystalline Massif; Simonetti et al., 2021; Bühler et al., 2022; Vanardois et al., 2022a, b) and later shifted between medium- and high-grade complex, as in northern Sardinia and MTM (Carosi et al., 2020, 2022; Simonetti et al., 2020b). Up to now, the transpressive shear linked to the EVSZ has been generally recognized at the boundary between the medium- and the high-grade rocks or within the migmatitic complex. However, the scenario of the MGSZ emphasizes that the EVSZ represents a network of interconnected transpressive shear zones that also deformed the nappe zone of the Variscan belt, far from the metamorphic core of the belt. Thus, a progressive renjuvement of the shear activity toward the marginal and external portions of the EVSZ is recognizable.

Summarizing, this study has both local and regional implications for the meaning of this dome-shaped structure within the Variscan belt in Sardinia and its role in the late-Carboniferous Variscan belt framework. Meso- and microstructural data highlight that the principal structures of the D_p phase are controlled by a deformation in which the strain is partitioned into folds and shear zone domains (high- and low-strain zones). The kinematic of the flow highlights a pure shear dominated transpressive regime associated with a sub-vertical mylonitic foliation and a sub-horizontal lineation. The mylonitic event of the MGSZ, based on equilibrium phase diagram modeling, developed under H*T*-L*P* amphibolite-facies conditions.

In-situ U–(Th)–Pb geochronology on monazite highlights the contemporaneous folding and shearing event during the transpressive activity. The onset and the progressive evolution of the MGSZ with the associated syn-kinematic intrusions lasted from ~315 up to ~300 Ma, in a time span of ~15 My. The MGSZ shows striking structural, kinematics and chronological similarities with other dextral ductile transpressive shear zones occurring in the Sardinian Variscan chain (e.g., the PASZ) and other fragments of the Variscan basements in Southern Europe. Due to its position within the chain (i.e., hinterland-foreland transition zone or Nappe Zone) and the obtained ages, the MGSZ could be ascribed as one of the youngest and most external transpressive shear zone active in the EVSZ framework. This chapter described a network of interconnected transpressive shear zones related to the EVSZ that also deformed the nappe zone of the Variscan belt.

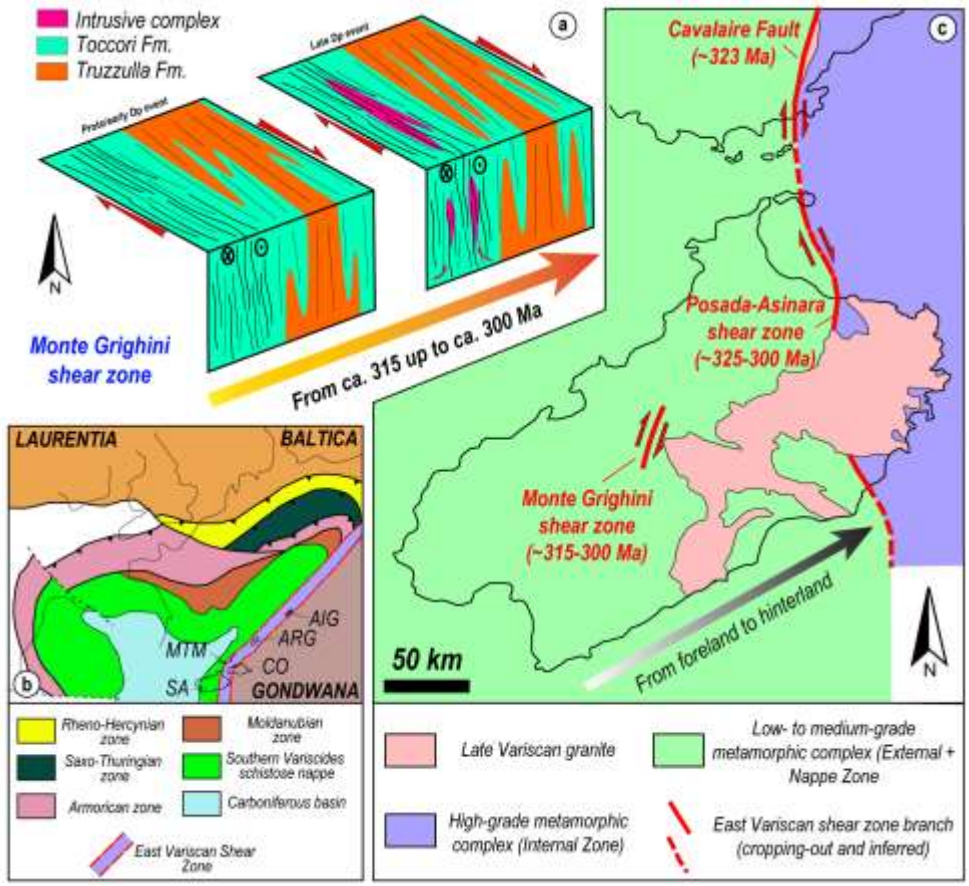

Figure 9.9: a) Simplified scheme of the tectonic evolution of MGSZ deduced from structural observations and the P-T-t results. The late syn-D_P intrusions have been provided; b) sketch maps of the Southern European Variscan belt during the late Carboniferous (modified from Corsini & Rolland, 2009; SA = Sardinia; MTM = Maures–Tanneron Massif; CO = Corsica; ARG = Argentera Massif; AIG = Aiguilles Rouge Massif); c) inferred lateral relationships between the branches of EVSZ during the late Carboniferous (modified from Simonetti et al., 2020a).

Appendix

Appendix 1: On the left, a diagram showing the biotite composition (on the top) and the probability density plot temperatures for the Ti-in-Bt temperature distribution. The mean and the StDev are shown (625 ± 25 °C; Henry et al., 2005). X-ray map of the analysed thin section shows the temperature variation (Ti-in-Bt; on the right).

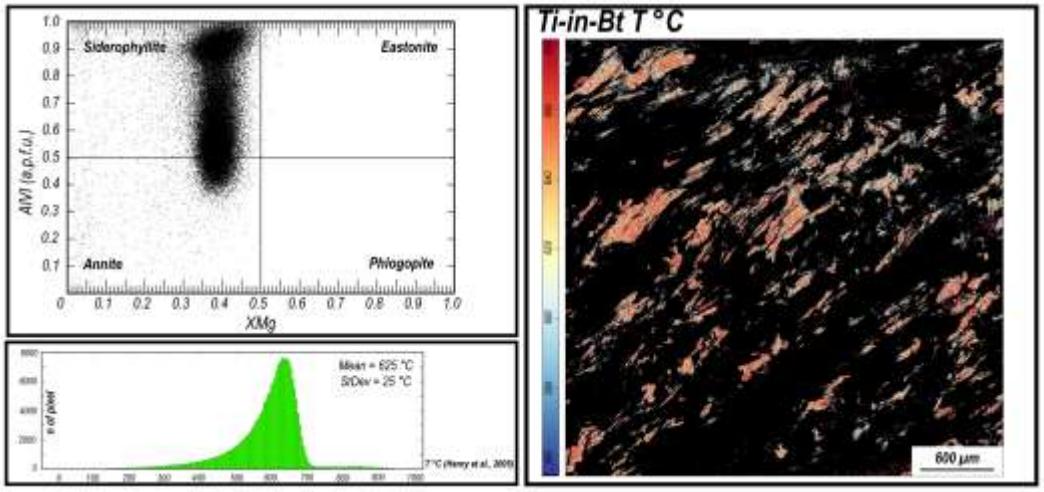

Appendix 2: Textural position, Back-scattered electron images and Th, Y chemical maps of selected monazites. Red dots represent the spots of quantitative chemical analyses. Compositional maps of Th and Y made by electron microprobe with spot location and the corresponding $^{208}Pb/^{232}Th$ (Th) and $^{206}Pb/^{238}U$ (U) ages are shown.

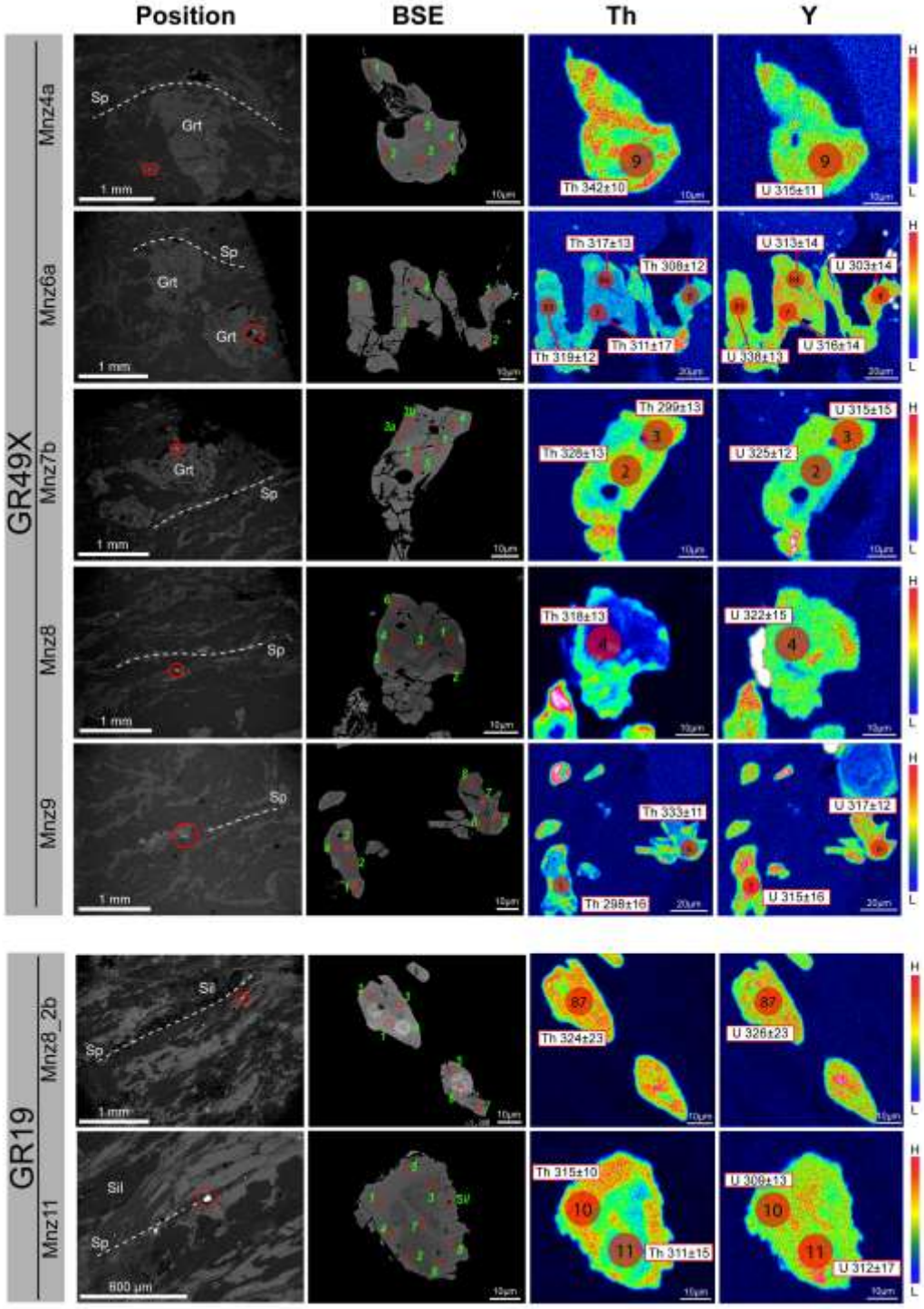

Appendix 3: Chemical analysis of the monazite selected for geochronology. Structural formula calculated based on 4 oxygens.

No. Spot	1	2	3	4	5	6	1	2	3	4	5	1	2	3a	3b	4	5
Sample	GR49X	GR49X	GR49X	GR49X	GR49X	GR49X	GR49X	GR49X	GR49X	GR49X	GR49X	GR49X	GR49X	GR49X	GR49X	GR49X	GR49X
Wt%	Mnz4a	Mnz4a	Mnz4a	Mnz4a	Mnz4a	Mnz4a	Mnz6a	Mnz6a	Mnz6a	Mnz6a	Mnz6a	Mnz7a	Mnz7a	Mnz7a	Mnz7a	Mnz7a	Mnz7a
Spot position	RIM	RIM	RIM	RIM	CORE	RIM	CORE	CORE	CORE	CORE	CORE	CORE	CORE	RIM	RIM	RIM	CORE
Textural position	// Sp	// Sp	// Sp	// Sp	// Sp	// Sp	in Grt	in Grt	in Grt	in Grt	in Grt	in Grt	in Grt	in Grt	in Grt	in Grt	in Grt
P2O5	30.26	29.80	29.94	30.00	30.01	29.72	30.01	29.68	29.41	30.37	30.53	29.90	29.55	30.50	30.43	30.41	30.42
SiO2	0.19	0.10	0.06	0.08	0.06	0.19	0.05	0.16	0.03	0.00	0.06	0.14	0.14	0.11	0.05	0.11	0.12
ThO2	2.06	2.08	1.37	1.87	1.19	1.62	0.44	1.54	0.36	0.16	0.46	2.83	3.05	1.62	1.47	2.43	2.36
UO2	0.68	0.24	0.43	0.54	0.33	0.55	0.34	0.23	0.33	0.40	0.27	0.87	0.46	0.35	0.37	0.67	0.38
Al2O3	0.05	0.00	0.00	0.01	0.03	0.07	0.06	0.05	0.00	0.00	0.02	0.05	0.00	0.02	0.00	0.00	0.00
La2O3	13.13	13.63	14.13	13.29	14.00	13.84	17.46	15.43	16.11	18.09	17.45	14.52	14.32	14.02	14.81	14.31	15.32
Ce2O3	27.41	27.57	28.63	28.69	29.09	27.88	31.03	30.17	30.91	31.69	31.48	28.46	28.17	29.67	27.76	28.51	28.91
Pr2O3	2.95	2.87	2.87	3.27	2.92	2.89	2.69	3.24	3.35	3.22	2.97	2.99	2.98	3.44	2.91	2.98	2.78
Nd2O3	12.36	12.69	12.79	12.62	12.66	12.65	10.36	11.10	10.83	10.02	10.64	11.52	11.33	11.71	11.60	10.85	11.33
Sm2O3	2.52	2.71	2.53	2.76	2.45	2.39	1.55	1.96	1.50	1.53	1.38	1.99	1.74	1.90	1.97	1.97	1.50
Gd2O3	2.13	2.40	2.49	2.50	2.11	2.55	0.62	0.97	1.16	0.85	0.94	1.51	1.47	1.49	1.89	1.42	1.39
Dy2O3	0.59	0.91	0.60	0.49	0.56	0.63	0.01	0.25	0.44	0.62	0.09	0.38	0.60	0.73	0.81	0.75	0.53
Y2O3	1.78	1.58	1.35	1.35	1.43	1.52	1.66	1.34	1.64	1.41	1.47	1.06	1.61	2.00	1.95	2.07	1.59
CaO	0.74	0.68	0.38	0.60	0.31	0.47	0.32	0.40	0.24	0.17	0.18	0.83	0.72	0.50	0.44	0.69	0.55
SUM	96.85	97.76	97.57	98.07	97.14	96.96	96.60	96.51	96.31	98.55	97.94	97.05	96.14	98.06	96.46	97.17	97.17
Cations																	
P	1.013	1.005	1.008	1.005	1.011	1.004	1.010	1.006	1.003	1.009	1.014	1.008	1.006	1.011	1.021	1.015	1.016
Si	0.008	0.004	0.002	0.003	0.002	0.007	0.002	0.006	0.001	0.000	0.002	0.005	0.006	0.004	0.002	0.004	0.005
Th	0.019	0.019	0.012	0.017	0.011	0.015	0.004	0.014	0.003	0.001	0.004	0.026	0.028	0.014	0.013	0.022	0.021
U	0.006	0.002	0.004	0.005	0.003	0.005	0.003	0.002	0.003	0.004	0.002	0.008	0.004	0.003	0.003	0.006	0.003
Al	0.002	0.000	0.000	0.000	0.002	0.003	0.003	0.002	0.000	0.000	0.001	0.002	0.000	0.001	0.000	0.000	0.000
La	0.191	0.200	0.207	0.194	0.205	0.204	0.256	0.228	0.239	0.262	0.253	0.213	0.212	0.203	0.216	0.208	0.223
Ce	0.397	0.402	0.417	0.416	0.424	0.407	0.452	0.442	0.456	0.455	0.452	0.415	0.415	0.425	0.403	0.411	0.418
Pr	0.042	0.042	0.042	0.047	0.042	0.042	0.039	0.047	0.049	0.046	0.042	0.043	0.044	0.049	0.042	0.043	0.040
Nd	0.175	0.181	0.182	0.178	0.180	0.180	0.147	0.159	0.156	0.140	0.149	0.164	0.163	0.164	0.164	0.153	0.160
Sm	0.034	0.037	0.035	0.038	0.034	0.033	0.021	0.027	0.021	0.021	0.019	0.027	0.024	0.026	0.027	0.027	0.020
Gd	0.028	0.032	0.033	0.033	0.028	0.034	0.008	0.013	0.015	0.011	0.012	0.020	0.020	0.019	0.025	0.019	0.018
Dy	0.008	0.012	0.008	0.006	0.007	0.008	0.000	0.003	0.006	0.008	0.001	0.005	0.008	0.009	0.010	0.010	0.007
Y	0.037	0.033	0.029	0.028	0.030	0.032	0.035	0.029	0.035	0.029	0.031	0.022	0.034	0.042	0.041	0.043	0.033
Ca	0.031	0.029	0.016	0.026	0.013	0.020	0.014	0.017	0.010	0.007	0.007	0.035	0.031	0.021	0.019	0.029	0.023
SUM	1.991	1.998	1.994	1.997	1.992	1.995	1.995	1.995	1.999	1.995	1.990	1.994	1.994	1.992	1.986	1.989	1.987
X(LREE)	0.867	0.872	0.897	0.884	0.906	0.884	0.934	0.921	0.927	0.938	0.940	0.881	0.873	0.889	0.885	0.868	0.890
X(HREE+Y)	0.075	0.078	0.070	0.068	0.067	0.076	0.044	0.045	0.057	0.049	0.045	0.048	0.063	0.072	0.079	0.074	0.060

No. Spot	1	2	3	4	5	6	1	2	3	4	5	6	7	8
Sample	GR49X	GR49X	GR49X	GR49X	GR49X	GR49X	GR49X	GR49X	GR49X	GR49X	GR49X	GR49X	GR49X	GR49X
Wt%	Mnz8	Mnz8	Mnz8	Mnz8	Mnz8	Mnz8	Mnz9	Mnz9	Mnz9	Mnz9	Mnz9	Mnz9	Mnz9	Mnz9
Spot position	RIM	RIM	CORE	CORE	RIM	RIM	CORE	RIM	CORE	RIM	CORE	RIM	CORE	CORE
Textural position	// Sp	// Sp	// Sp	// Sp	// Sp	// Sp	// Sp	// Sp	// Sp	// Sp	// Sp	// Sp	// Sp	// Sp
P2O5	30.31	30.12	30.05	30.35	29.88	30.16	30.30	30.66	30.07	30.03	30.44	30.21	30.75	30.75
SiO2	0.03	0.21	0.07	0.13	0.34	0.20	0.13	0.08	0.00	0.00	0.16	0.09	0.09	0.07
ThO2	1.81	4.09	1.73	1.31	6.04	4.60	2.22	1.13	1.47	0.55	1.99	0.57	0.52	0.38
UO2	0.46	0.28	0.20	0.22	0.38	0.49	0.59	0.75	0.94	0.26	0.25	0.32	0.44	0.23
Al2O3	0.07	0.03	0.00	0.02	0.05	0.11	0.06	0.01	0.03	0.00	0.07	0.00	0.08	0.07
La2O3	15.20	12.81	15.53	15.09	12.89	13.44	14.04	14.68	15.73	16.72	14.66	15.52	16.16	16.17
Ce2O3	29.10	26.59	29.68	31.02	24.66	26.84	27.48	27.90	28.38	28.98	28.07	29.14	30.13	30.64
Pr2O3	2.79	2.92	3.03	3.34	2.87	3.09	2.95	3.01	2.74	2.56	2.90	2.80	3.06	2.89
Nd2O3	10.76	11.57	11.45	11.49	11.90	11.54	12.13	11.45	11.78	11.04	12.37	11.06	10.82	10.76
Sm2O3	1.69	2.44	1.66	1.83	2.24	1.73	2.53	2.08	1.97	1.71	2.08	1.92	1.59	1.72
Gd2O3	1.68	2.22	1.15	1.42	2.57	1.63	2.16	1.76	1.79	1.54	1.67	1.49	1.62	1.25
Dy2O3	0.64	0.48	0.48	0.16	0.71	0.48	0.39	0.91	0.49	0.54	0.71	0.75	0.55	0.47
Y2O3	2.24	1.44	1.33	1.46	1.30	1.96	1.12	2.75	1.29	2.19	1.22	2.19	1.62	1.52
CaO	0.48	0.94	0.46	0.34	1.25	0.93	0.61	0.65	0.56	0.45	0.61	0.43	0.34	0.38
SUM	97.25	96.15	96.83	98.19	97.08	97.20	96.71	97.81	97.23	96.57	97.19	96.50	97.77	97.30
Cations														
P	1.013	1.015	1.012	1.009	1.005	1.008	1.017	1.014	1.012	1.011	1.016	1.014	1.018	1.020
Si	0.001	0.008	0.003	0.005	0.013	0.008	0.005	0.003	0.000	0.000	0.006	0.004	0.004	0.003
Th	0.016	0.037	0.016	0.012	0.055	0.041	0.020	0.010	0.013	0.005	0.018	0.005	0.005	0.003
U	0.004	0.002	0.002	0.002	0.003	0.004	0.005	0.007	0.008	0.002	0.002	0.003	0.004	0.002
Al	0.003	0.002	0.000	0.001	0.002	0.005	0.003	0.000	0.001	0.000	0.003	0.000	0.004	0.003
La	0.221	0.188	0.228	0.219	0.189	0.196	0.205	0.211	0.231	0.245	0.213	0.227	0.233	0.234
Ce	0.420	0.388	0.432	0.446	0.359	0.388	0.399	0.399	0.413	0.422	0.405	0.423	0.431	0.439
Pr	0.040	0.042	0.044	0.048	0.042	0.044	0.043	0.043	0.040	0.037	0.042	0.040	0.044	0.041
Nd	0.152	0.165	0.163	0.161	0.169	0.163	0.172	0.160	0.167	0.157	0.174	0.157	0.151	0.151
Sm	0.023	0.033	0.023	0.025	0.031	0.024	0.035	0.028	0.027	0.023	0.028	0.026	0.021	0.023
Gd	0.022	0.029	0.015	0.018	0.034	0.021	0.028	0.023	0.024	0.020	0.022	0.020	0.021	0.016
Dy	0.008	0.006	0.006	0.002	0.009	0.006	0.005	0.011	0.006	0.007	0.009	0.010	0.007	0.006
Y	0.047	0.031	0.028	0.031	0.027	0.041	0.024	0.057	0.027	0.046	0.025	0.046	0.034	0.032
Ca	0.020	0.040	0.020	0.015	0.053	0.039	0.026	0.027	0.024	0.019	0.026	0.018	0.014	0.016
SUM	1.991	1.987	1.992	1.993	1.991	1.990	1.987	1.993	1.993	1.996	1.989	1.993	1.989	1.989
X(LREE)	0.879	0.848	0.911	0.919	0.813	0.841	0.888	0.862	0.895	0.898	0.894	0.896	0.913	0.922
X(HREE+Y)	0.079	0.069	0.051	0.052	0.073	0.071	0.059	0.094	0.058	0.075	0.058	0.077	0.064	0.056

No. Spot	1	2	3	4	5	6	7		1	2	3	4	5	6	7	8
Sample	GR19	GR19	GR19	GR19	GR19	GR19	GR19		GR19	GR19	GR19	GR19	GR19	GR19	GR19	GR19
Wt%	Mnz8_2b	Mnz8_2b	Mnz8_2b	Mnz8_2b	Mnz8_2b	Mnz8_2b	Mnz8_2b		Mnz11	Mnz11	Mnz11	Mnz11	Mnz11	Mnz11	Mnz11	Mnz11
Spot position	RIM	RIM	RIM	RIM	RIM	RIM	RIM		RIM	RIM	RIM	RIM	RIM	RIM	RIM	CORE
Textural position	// Sp	// Sp	// Sp	// Sp	// Sp	// Sp	// Sp		// Sp	// Sp	// Sp	// Sp	// Sp	// Sp	// Sp	// Sp
P2O5	29.84	29.75	29.89	30.15	30.01	30.73	31.13		30.00	30.41	30.35	30.08	29.69	30.29	30.33	30.34
SiO2	0.14	0.08	0.06	0.10	0.07	0.09	0.14		0.06	0.00	0.02	0.16	0.12	0.05	0.07	0.07
ThO2	3.92	3.81	4.31	4.33	4.53	3.25	3.53		4.17	1.95	2.87	4.00	4.48	2.33	4.46	1.44
UO2	0.52	0.56	0.47	0.31	0.73	0.29	0.65		0.46	0.27	0.41	0.43	0.54	0.26	0.20	0.32
Al2O3	0.00	0.04	0.07	0.01	0.02	0.10	0.07		0.00	0.03	0.03	0.05	0.06	0.03	0.03	0.35
La2O3	13.46	13.26	13.66	13.86	13.33	13.49	13.51		13.21	14.13	13.88	13.00	13.10	13.96	13.57	15.04
Ce2O3	27.24	27.75	26.98	26.30	25.89	27.30	27.16		27.17	28.09	26.40	27.22	26.16	26.68	26.29	29.02
Pr2O3	2.92	3.03	2.75	2.71	2.64	3.01	2.97		2.79	3.10	2.91	3.10	2.57	3.14	2.87	2.98
Nd2O3	11.30	10.62	11.66	11.08	11.31	11.56	11.76		11.36	10.86	11.34	10.98	11.16	11.59	11.09	12.09
Sm2O3	1.96	2.06	1.86	1.86	1.70	2.12	1.98		2.17	1.92	1.91	2.03	1.82	2.13	2.15	1.98
Gd2O3	1.42	1.41	1.22	1.86	1.44	1.50	1.57		1.62	1.28	2.00	1.31	1.87	1.64	1.73	1.50
Dy2O3	0.47	0.49	0.80	0.88	0.54	0.63	0.42		0.51	0.65	0.59	0.52	0.36	0.76	0.77	0.55
Y2O3	2.16	1.97	2.26	2.33	2.20	2.29	1.95		2.28	3.07	2.80	2.08	2.25	2.91	2.52	1.58
CaO	1.03	1.01	1.05	1.08	1.23	0.82	0.89		1.08	0.72	1.01	0.97	1.15	0.81	0.96	0.50
SUM	96.37	95.83	97.04	96.87	95.64	97.19	97.73		96.88	96.49	96.52	95.92	95.34	96.59	97.05	97.76
Cations																
P	1.008	1.010	1.005	1.011	1.015	1.019	1.023		1.009	1.016	1.015	1.014	1.010	1.013	1.013	1.008
Si	0.005	0.003	0.002	0.004	0.003	0.004	0.006		0.002	0.000	0.001	0.006	0.005	0.002	0.003	0.003
Th	0.036	0.035	0.039	0.039	0.041	0.029	0.031		0.038	0.018	0.026	0.036	0.041	0.021	0.040	0.013
U	0.005	0.005	0.004	0.003	0.006	0.003	0.006		0.004	0.002	0.004	0.004	0.005	0.002	0.002	0.003
Al	0.000	0.002	0.003	0.001	0.001	0.005	0.003		0.000	0.002	0.001	0.002	0.003	0.001	0.002	0.016
La	0.198	0.196	0.200	0.202	0.196	0.195	0.193		0.194	0.206	0.202	0.191	0.194	0.203	0.198	0.218
Ce	0.398	0.407	0.392	0.381	0.379	0.391	0.386		0.395	0.406	0.382	0.397	0.385	0.386	0.380	0.417
Pr	0.042	0.044	0.040	0.039	0.038	0.043	0.042		0.040	0.045	0.042	0.045	0.038	0.045	0.041	0.043
Nd	0.161	0.152	0.165	0.157	0.161	0.162	0.163		0.161	0.153	0.160	0.156	0.160	0.164	0.156	0.169
Sm	0.027	0.028	0.025	0.025	0.023	0.029	0.026		0.030	0.026	0.026	0.028	0.025	0.029	0.029	0.027
Gd	0.019	0.019	0.016	0.024	0.019	0.019	0.020		0.021	0.017	0.026	0.017	0.025	0.021	0.023	0.020
Dy	0.006	0.006	0.010	0.011	0.007	0.008	0.005		0.006	0.008	0.008	0.007	0.005	0.010	0.010	0.007
Y	0.046	0.042	0.048	0.049	0.047	0.048	0.040		0.048	0.064	0.059	0.044	0.048	0.061	0.053	0.033
Ca	0.044	0.043	0.045	0.046	0.053	0.035	0.037		0.046	0.031	0.043	0.041	0.050	0.034	0.041	0.021
SUM	1.994	1.993	1.996	1.993	1.991	1.987	1.983		1.995	1.993	1.994	1.989	1.993	1.994	1.990	1.996
X(LREE)	0.842	0.847	0.836	0.823	0.822	0.853	0.853		0.833	0.857	0.831	0.846	0.822	0.846	0.827	0.901
X(HREE+Y)	0.072	0.069	0.075	0.087	0.075	0.078	0.069		0.077	0.092	0.095	0.070	0.080	0.095	0.088	0.061

Appendix 4: Isotopic results and geochronological data from the monazites of selected samples (GR19 and G49X)

Sample	Analysis	Spot number	Spot position	Grain textural position	Mnz Grain	Isotopic Ratios						Age (Ma)			
						$^{207}Pb/^{235}U$	1σ abs	$^{206}Pb/^{238}U$	1σ abs	$^{208}Pb/^{232}Th$	1σ abs	$^{206}Pb/^{238}U$	1σ abs	$^{208}Pb/^{232}Th$	1σ abs
G49X	Output_1_10	9	RIM	// Sp	Mnz4a	0.369	0.018	0.0501	0.0017	0.01707	0.00049	315	11	342	10
	Output_1_6	7	CORE	in Grt	Mnz6a	0.375	0.023	0.0503	0.0023	0.01549	0.00086	316	14	311	17
	Output_1_8	8	RIM	in Grt	Mnz6a	0.356	0.019	0.0482	0.0023	0.01537	0.00059	303	14	308	12
	Output_1_7	84	CORE	in Grt	Mnz6a	0.374	0.022	0.0498	0.0023	0.01583	0.00065	313	14	317	13
	Output_1_9	85	CORE	in Grt	Mnz6a	0.52	0.043	0.0538	0.0022	0.01589	0.00061	338	13	319	12
	Output_1_1	2	CORE	in Grt	Mnz7b	0.373	0.023	0.0518	0.0019	0.01637	0.00052	325	12	328	10
	Output_1_2	3	RIM	in Grt	Mnz7b	0.368	0.02	0.0501	0.0025	0.01493	0.00064	315	15	299	13
	Output_1_3	4	CORE	// Sp	Mnz8	0.383	0.025	0.0512	0.0024	0.01585	0.00065	322	15	318	13
	Output_1_4	5	RIM	// Sp	Mnz5	0.376	0.02	0.0501	0.0026	0.01485	0.00082	315	16	298	16
	Output_1_5	6	RIM	// Sp	Mnz6	0.38	0.022	0.0504	0.0019	0.0166	0.00054	317	12	333	11
GR19	Output_1_3	87	CORE	// Sp	Mnz8_2b	0.37	0.045	0.0519	0.0037	0.0162	0.0012	326	23	324	23
	Output_1_1	10	RIM	// Sp	Mnz11	0.354	0.017	0.0492	0.0022	0.01568	0.00049	309	13	315	10
	Output_1_2	11	RIM	// Sp	Mnz11	0.356	0.035	0.0495	0.0028	0.01548	0.00074	312	17	311	15

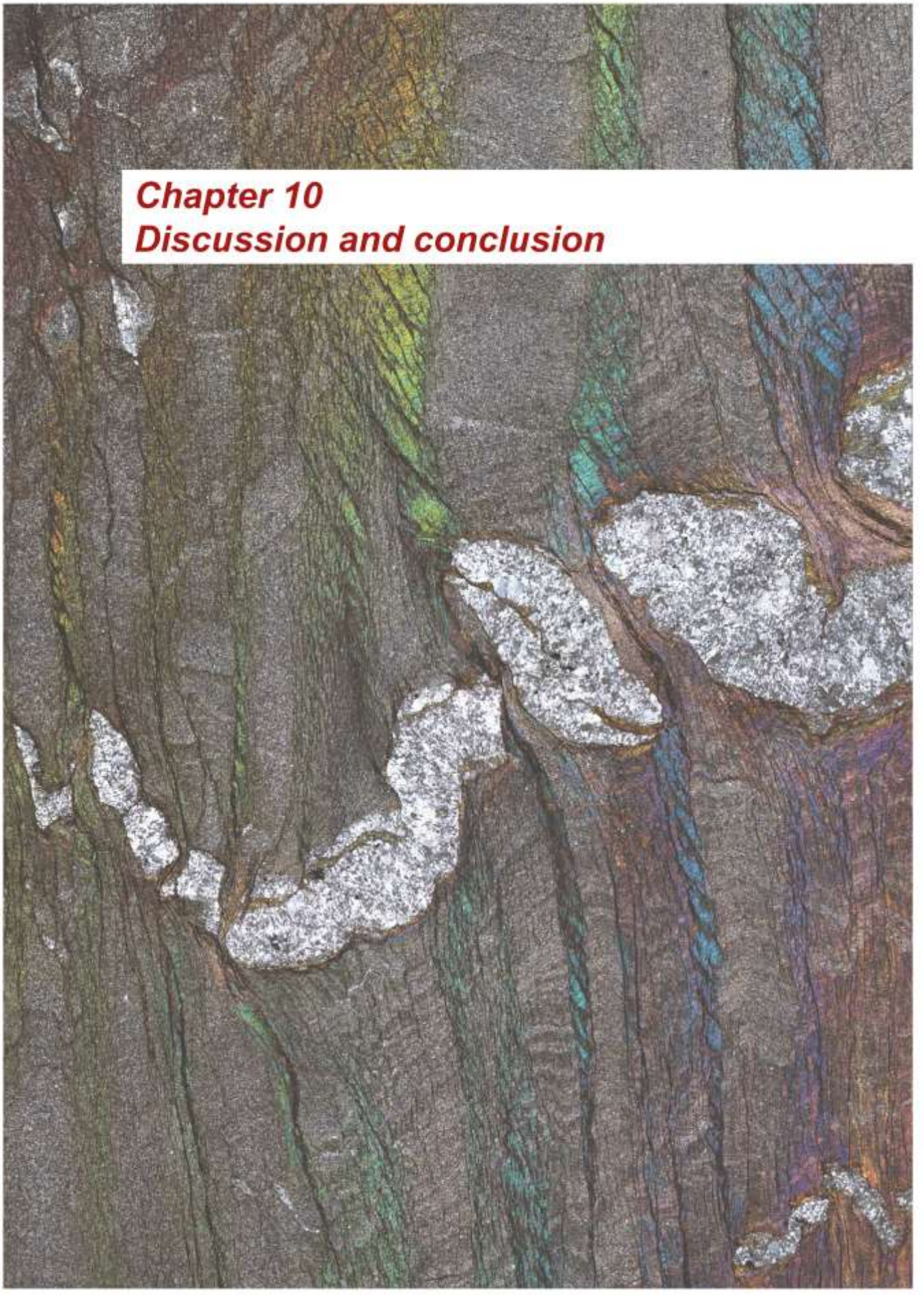

Chapter 10
Discussion and conclusion

10.1. Tectono-metamorphic evolution of the hinterland-foreland transition zone in Sardinia

The combination of structural investigations at different scales (from meso- to microscale) and the thermal architecture obtained by Raman Spectroscopy on Carbonaceous Material (RSCM) integrated with the *P-T* estimations through both inverse and forward modeling allows the definition of the tectono-metamorphic evolution of the overall investigated area. The polyphase deformation history recorded in the hinterland-foreland transition zone of the Variscan belt in Sardinia is regarded as the result of pre-, syn- to post-nappe stacking evolution developed under contractional (D_1 to D_3) and extensional conditions (D_4), highlighting a complex tectonic history occurring during the growth and the collapse of the orogenic wedge (Fig. 10.1). The following paragraph discusses a general overview of the deformation phases linked to the newly obtained and already existing *P-T-t* data of both investigated sectors of the belt (Internal and External nappes and the Monte Grighini Unit).

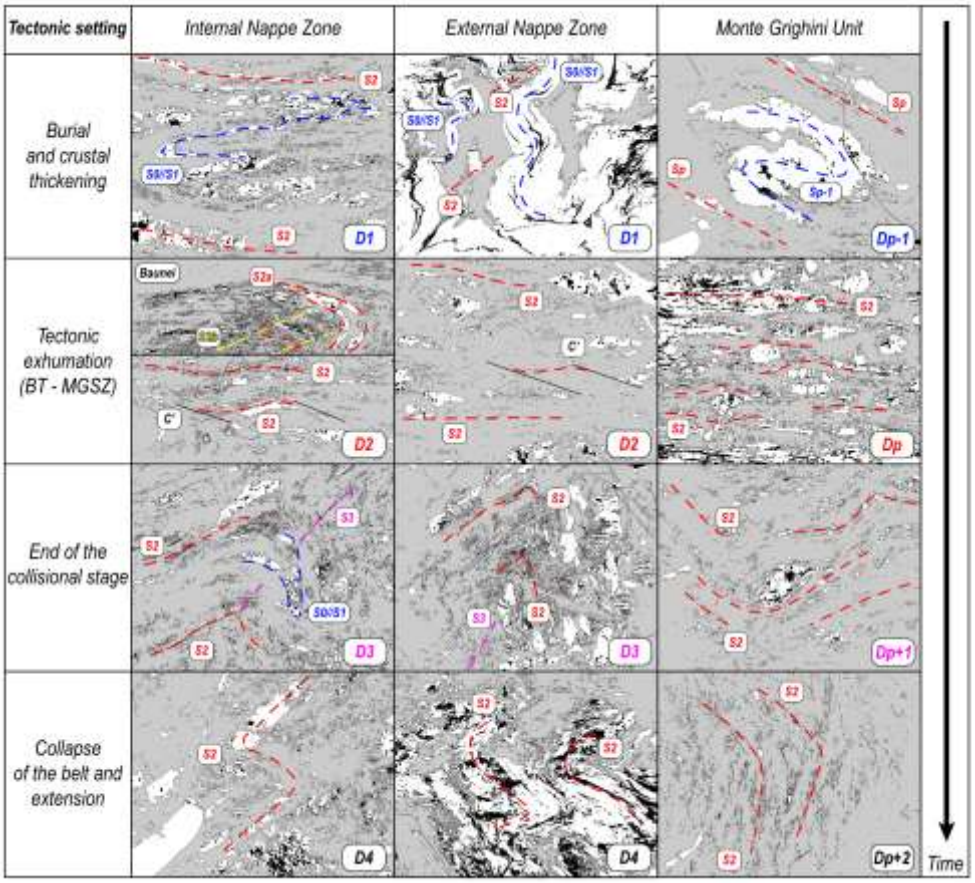

Figure 10.1: Synoptic resume of deformation history of the Barbagia, Meana Sardo and Monte Grighini units.

10.1.1. D_1 early collisional phase

Deforming the primary bedding S_0, far from the main tectonic contacts, the D_1 event is well-recognizable, both at micro- and mesoscale in the hinge of the D_2 folds, in S_2 microlithons or, when present, as a relict internal foliation in mineral phases (Fig. 10.1). According to previous authors, this event has been associated with the burial and the pre-nappe stacking during the early collisional stage and the orogenic wedge growth (Carmignani et al., 1994; Carosi et al., 2004; Conti et al., 1999, 2001; Montomoli et al., 2018). Previous investigations do not document a thermal difference between the Barbagia and Meana Sardo units (BU and MSU) belonging to the Internal and External nappes, respectively (Franceschelli et al., 1992; Montomoli et al., 2018). By high-resolution RSCM thermometric investigations at the belt scale and assuming that the recorded peak temperature may be associated with the maximum reached burial, the obtained results highlight a thermal difference between the Internal and External nappes, i.e., between the BU and MSU. The BU displays a general T_{RSCM} of ~470-440 °C, whereas the MSU has T_{RSCM} of ~440-380 °C (Chapters 5 and 6). Also, using RSCM at the belt scale, a complex and articulated thermo-structural architecture characterized by the presence of "anomalous" thermal sectors, i.e., the Baunei area, has been highlighted and subsequently investigated from the structural point of view (Chapter 7). The obtained temperatures are in agreement with the observed greenschist-facies assemblage (chlorite + white mica + albite + quartz) and with the recognized quartz recrystallization mechanism. Using an inverse and a hybrid approach, combining RSCM with the multi-equilibrium of the K-white mica and comparing them with the chlorite-white mica-quartz-water thermometer, the *P-T*-peak conditions of 0.6-0.8 GPa and 420-450 °C and 0.4-0.5 GPa and 370-400 °C from the Internal and External nappes have been constrained (Chapter 8).

Taking a typical relation of pressure vs depth in a collisional framework (1 GPa = 33 km), the paleo-crustal depth of Internal and External nappes was ~20-26 and ~13-17 km, respectively (Fig. 10.2). Assuming that our *P-T* peak is related to the D_1 event, referring to the early stage of collision and burial (Carosi et al., 2004), a difference in the pressure of ~0.2-0.3 GPa and ~8 km in depth between the two nappes has been highlighted (Fig. 10.2). The *P-T* conditions of the BU are similar to those obtained in the northern sector of the Internal Nappe Zone, near to Lula village, by Costamagna et al. (2012), but with slightly lower pressure (~0.2 GPa). Comparing our baric results reached during the D_1 with the existing ones close to the hinterland (Fig. 10.2), a northward, progressive increase in pressure and, consequently, depth (up to 1.7-1.9 GPa) is recognizable (Cruciani et al., 2013, 2022; Scodina et al., 2021).

The D_1 event has been only constrained in the northern sector of the Internal Nappe Zone between 330 and 390 Ma (Carosi et al., 2012, 2020; Di Vincenzo et al., 2004).

In the Monte Grighini dome, the D_1 has been observed rarely due to the strong transposition linked to the D_2 phase (Fig. 10.1). The existing thermobarometric data from the D_1 of the Monte Grighini dome indicate *T* ~490-540 °C and *P* of 0.7-0.9 GPa (Cruciani et al., 2016) linked to the burial during the collisional stage. Maximum *P* was reached during the D_1 collisional stage during the subduction of the continental crust (Cruciani et al., 2022). Comparing obtained results from the Internal and External nappes, the Monte Grighini dome is still hotter than the surrounding nappes, remaining an anomaly within the hinterland-foreland transition zone. However, *P* constraints are similar to both the MSU and BU.

10.1.2. D_2 syn-collisional phase and exhumation

The D_2 deformation phase at the belt scale is linked to the syn-collisional exhumation but is driven by different tectonic mechanisms. In the hinterland-foreland transition zone made by the BU and MSU, the D_2 is strictly associated with the Barbagia Thrust (BT) shear activity, the tectonic contact that marks the boundary between the Internal and External nappes. The D_2 is responsible for the development of the main foliation, pervasive at all scales (S_2). The intensity of deformation increases toward the BT and displays several kinematic indicators with a main top-to-the S-SW sense of shear, in agreement with previous investigations (e.g., Carosi & Malfatti, 1995; Conti et al., 1998, 2001; Carosi et al., 2004; Montomoli et al., 2018; see also Chapter 5). The S_2 foliation, parallel to the boundaries of the shear zone, and the F_2 fold axes, perpendicular to the L_2 object lineation, are coeval with the overthrust of BU on MSU (Carosi et al., 2004).

The syn-kinematic mineral assemblage (chlorite + white mica) along the S_2 mylonitic foliation indicates greenschist-facies metamorphic conditions. This is in agreement with the main dynamic recrystallization mechanism of quartz, indicative of temperature ranges ~400-450 °C (BLG II and local SGR; Piazolo & Passchier, 2002; Stipp et al., 2002).

These data are corroborated by the undulose extinction, local flame perthite, and brittle deformation in feldspar, indicating ~400-500 °C (Pryer, 1993). Integrating structural investigation with RSCM, a deformation and thermal gradient from the border to the core of the shear zone has been recognized (Chapter 5). The BT is linked to a flow regime dominated by pure shear the boundary to one dominated by simple shear approaching to the core of the shear zone, associated with a variable simple shear amount, from ~33% up to ~77%.

This is also associated with a change in the finite strain ellipsoid, from close to plane strain up to constrictional conditions, indicating that the core of the BT accommodated a higher amount of strain with respect to the shear zone peripheries (Fossen & Cavalcante, 2017). The obtained results are in good agreement with the previous works on the BT. In fact, asymmetric F_2 folds observed in both nappes with axial planes parallel to the mylonitic foliation are linked to the BT non-coaxial deformation (Carosi et al., 2004).

According to Fossen (2016), it is possible to suggest that this kind of fold accommodates the component of shortening perpendicular to the BT. The lack or presence of mylonite related to the shear deformation strongly depends on the structural distance from the shear zone, i.e., the structural level of deformation across the crust. This has been well observed investigating the Baunei septum from the structural point of view, recording the shallow crustal deformation related to the BT shear activity (Chapter 7).

The progressive increase in temperature towards the BT, coupled with the rise of the simple shear, could indicate a syn-shearing temperature increase. This broad correlation between T_{RSCM} and the deformation gradient could imply that the flow path was accompanied by a progressive localization of deformation in the core of the shear zone, due to thermal weakening, during the ductile deformation (Fossen & Cavalcante, 2017). The D_2 event has also been constrained under the metamorphic point of view by the same approach used for the D_1. The retrograde path indicates a decompression with no relevant temperature changes, with values of 0.4-0.5 and 0.2 GPa for the Internal and External nappes, respectively (Chapter 8). Due to the assumptions and limitations linked to the applied methodologies, no significative heating during the D_2 exhumation phase was identified, whereas the amount of decreasing pressure between both nappes is similar (~0.2 GPa; Fig. 10.2). The D_2 phase, linked to the syn-nappe stacking deformation and syn-collisional exhumation of the Internal Nappe Zone, is related to the BT activity (Montomoli et al., 2018 and references therein).

Instead, during the progressive deformation moving toward the foreland, the exhumation path recognized in the External Nappe Zone could be linked to the activity of more external thrusts, e.g., the tectonic contact between Meana Sardo and Gerrei units (Carmignani et al., 1994). Comparing our results with the existing ones in the northern sector, a different exhumation path is recognizable (Fig. 10.2). In fact, the D_2 deformative event in the Internal Nappe Zone's northward sector is related to the orogen-parallel transpression linked to the Posada-Asinara shear zone (PASZ) activity and not to a syn-contractional exhumation driven by thrust-sense shear zones as the BT.

This is also clearly highlighted by the *P-T* path, characterized by a systematic increase in temperature during the retrograde path and not a generalized isothermal decompression, as discovered for the BU and MSU (Fig. 10.2). Also, inside the PASZ high-strain zone, the three previous investigated samples started from different *P-T* peak conditions during the D_1, but reached similar metamorphic conditions during the late stage of exhumation. The highest *P*-peak is recorded in the sample located within the border of the PASZ, whereas the closest one to the PASZ is associated with lower pressure.

Integrating metamorphic data with the existing kinematics of the flow estimations (Carosi et al., 2020; Graziani et al., 2020), the difference in the exhumation rate could be linked to the pure shear gradient recognizable along the PASZ. The boundary of the shear zones, where the sample reached the maximum pressure comes from, is the PASZ sector associated with the highest pure shear amount, whereas going towards the core, i.e., northward, the component of the simple shear increases (Fig. 10.2). Thus, the exhumation rate is strictly linked to the pure shear amount, as is well-observable in the PASZ, and classically observed in shear partitioned transpressive shear zone (Fossen & Cavalcante, 2017).

The D_2 event in the Monte Grighini dome (called D_p in Chapter 9) is still linked with the exhumation but driven by different forces than the BT. The D_2 deformation in this sector has been associated with the Monte Grighini shear zone (MGSZ) activity, the tectonic contact that marks the west-southwestern margin of the dome. An increase in strain and in the amount of kinematic indicators going toward the MGSZ has been recognized, where the strain is partitioned into tight and isoclinal folds (low-strain zone) and shear zone domains (high-strain zone) approaching the MGSZ. The Monte Grighini dome is characterized by a sub-vertical S_2 foliation, parallel to the boundaries of the shear zone, and F_2 fold axes, parallel to the sub-horizontal L_2 mineral lineation. The geometry and kinematics of the MGSZ, different respect to the previous interpretations (Musumeci, 1992; Cruciani et al., 2016), are compatible with a transpressive regime as a consequence of dextral shear deformation with a shortening component perpendicular to the shear zone boundaries, developed under medium- to high-temperature amphibolite-facies constrained at *T* ~625 ± 25 °C and a *P* ~0.4-0.6 GPa. *In-situ* U–(Th)–Pb geochronology on monazite highlights the contemporaneous folding and shearing event during the transpressive activity. The onset and the progressive evolution of the MGSZ with the associated syn-kinematic intrusions lasted from ~315 up to ~300 Ma, in a time span of ~15 My. A similar architecture obtained in the MGSZ has been described in the northern sector of the Sardinia island, where an amphibolite-facies transpressive shear zone, i.e., the PASZ (Carosi & Palmeri, 2002; Carosi

et al., 2012, 2020, 2022) crops out. The PASZ developed under decreasing temperature and pressure, starting at ~325 Ma and remaining active for ~25 My.

10.1.3. D_3 late collisional phase

The D_3 deformative event shows the same geometric features in the overall study area of the belt and is recognizable from the macro- to microscale. D_3 is associated with upright to slightly asymmetric folds with nearly-vertical axial planes (Fig. 10.1); therefore, no clear transport direction can be associated with this event.

Admitting that the shortening direction had to be perpendicular to the axial planes and to the trend of fold axes, the D_3 phase admits a similar shortening direction to the D_2. The presence of the BT mylonitic zone in the different sectors of the Barbagia Synform, with the same structural and kinematic features and the similar shortening direction between the D_2 and D_3 phase, confirms the post-nappe stacking folded structure. Also, the obtained RSCM data emphasize the strong influence of the regional-scale antiforms and synforms, in the present-day thermo-structural architecture of the belt. All these results are in agreement with the model of Carmignani et al. (1994) and Conti et al. (1999), which highlighted the presence of large-scale structures acquired in a contractional setting during the late deformation stage of crustal thickening and not during the late orogenic extension. The D_3 phase is characterized by pressure solution and no metamorphic mineral assemblage is recognizable in its axial plane foliation. Equivalent upright folds have also been documented in the metamorphic complexes of the hinterland zone (Carosi & Oggiano, 2002; Casini & Oggiano, 2008; Casini et al., 2010). Metamorphic conditions highlight a decrease in pressure from the D_1 to the D_2 (Chapter 8), while distinct evidence of cooling is seen from D_2 to D_3, from blastesis to dissolution (Montomoli et al., 2018; Chapters 5 and 6). This is consistent with the coupling of BU with MSU under greenschist-facies and their initial exhumation (D_1 and D_2) and a subsequent km-scale folding during the regional horizontal shortening under upper-crustal conditions (D_3).

Regarding the Monte Grighini dome, the observed geometry and kinematics of the D_3 event (called D_{p+1} in Chapter 9; Fig. 10.1) are similar to those identified in the BU and MSU. However, due to the different strain conditions involved in this sector with respect to the BT, the parallelism between the D_2 and D_3 fold axes suggests that the transpressive regime was probably active until the end of the D_3 deformation phase. Although two different events have been recognized, both deformative phases are linked to the same deformation regime and result from progressive deformation, suggesting that the basement continued to undergo

sub-horizontal shortening up to the final stages of collision. Thus, the D_3 in both investigated areas is associated with the same tectonic setting but with different tectonic styles.

10.1.4. D_4 post-collisional phase

Subsequent post-collision and post-nappe-stacking or transpression were characterized by the development of open folds with sub-horizontal axial plane and axes (D_4; Fig. 10.1).

This geometry suggests the gravitational collapse of the thickened orogen. Most of the Upper Carboniferous-Permian intrusions (except some syn-tectonic granite and the Monte Grighini Intrusive Complex) cross-cut the main structures in the metamorphic basement and the associated isotherms architecture, pointing out how the reconstructed thermal pattern was recorded during the collisional stage and before the emplacement of the intrusive granitic rocks. Therefore, the emplacement of the Sardo-Corso batholith, constrained at ~320-280 Ma (Del Moro et al., 1975; Casini et al., 2012, 2015) and cross-cutting the Variscan basement and its tectonic structures (i.e., the BT, the MGSZ and the PASZ) indicate the end of the orogenic shortening and the development of the post-collisional extensional phases (Cortesogno et al., 1998).

In summary, the hinterland-foreland transition zone in Sardinia records the complex *P*-*T*-D-*t* evolution of the orogenic wedge growth, characterized by (i) an early phase linked to burial and pre-nappe stacking event, associated with a systematic northward increase in the peak in pressure (D_1), (ii) a syn-collisional ductile deformation (D_2) linked to different tectonic exhumation, associated with thrust-sense or transpressive shear zones and (iii) a large-scale nappe refolding or the latest staged of transpression (D_3) acquired during the final stages of the contractional deformation. A late extensional stage (D_4), with the development of collapse folds with associated brittle/ductile to brittle structures, marks the end of the orogenic cycle.

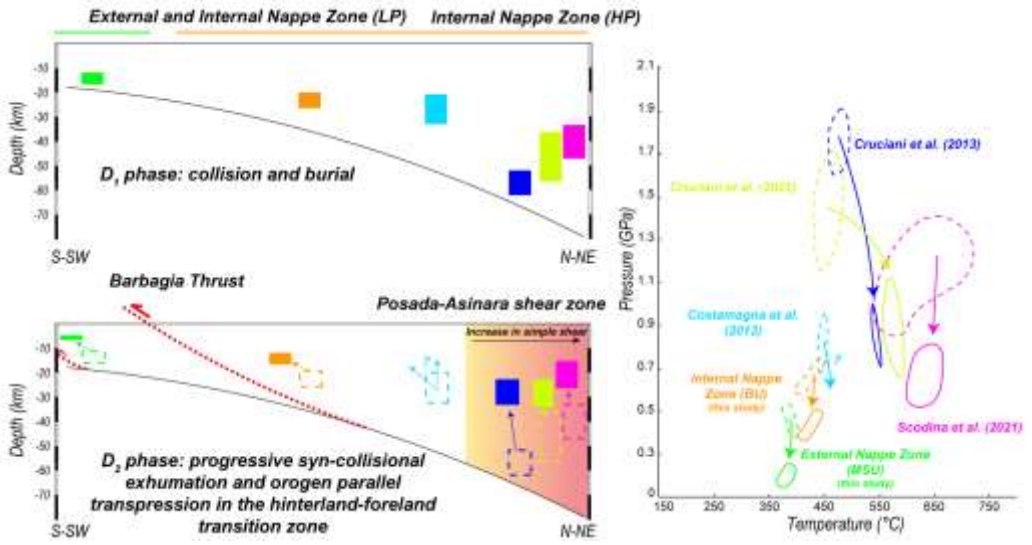

Figure 10.2: Tectono-metamorphic reconstruction during the progressive syn-collisional exhumation and orogen parallel transpression with associated P-T path from both this study and Costamagna et al. (2012); Cruciani et al. (2013, 2022) and Scodina et al. (2021).

10.2. From perpendicular collision to orogen parallel transpression

Understanding how the lithosphere accommodates convergence remains an important issue in tectonics for both recent and old orogenic belts (e.g., Conand et al., 2020; Torvela & Kurhila, 2020). Partitioning of convergence-related shortening into different components has been addressed in recent studies that focus on determining the geodynamics of plate boundary deformation (e.g., Van Hinsbergen et al., 2012, 2019), continental deformation (McQuarrie et al., 2014), and causative factors of lateral variation in the structure of the orogens (e.g., Macedo & Marshak, 1999; Robinson et al., 2006; Mitra et al., 2010; Long et al., 2011; Bhattacharya et al., 2015; Bhattacharyya & Ahmed, 2016; Long & Robinson, 2021). In an oblique collision, strain can be partitioned by combining lateral horizontal flow (i.e., escape), thrusting along the direction of shortening (Cagnard et al., 2006; Chardon et al., 2009; Bajolet et al., 2015) or with the coeval development of thrust, strike-slip, and mixed zones through orogens (Teyssier & Whitney, 2002; Iacopini et al., 2008; Nabavi et al., 2017, 2020). All tectonic regimes are significantly enhanced in the context of orocline formation (Bajolet et al., 2013; Johnston et al., 2013; Krýza et al., 2019; Parui et al., 2022). However, the convergence angle of the collision could progressively rotate and change the associated structures and exhumation style (e.g., Malavieille et al., 2019; Nania et al., 2021). It is widely accepted (e.g., Malavieille et al., 1984; Ellis & Watkinson, 1987; Dias & Ribeiro, 1994; Fossen, 2016) that lineations and foliations development is strictly related to the transport direction of geological structures.

Also, as discussed before, the hinterland-foreland transition zone in Sardinia is characterized by both transpression and syn-collisional exhumation. Thus the deformation has been partitioned between the PASZ, the BT and the MGSZ.

In the central Sardinian hinterland-foreland transition zone, the main trend of the extensional lineation linked to the BT activity is parallel to the transport direction of the Sardinian chain, i.e., S-SW, N-NE and nearly perpendicular to the syn-BT fold axes. This is in agreement with the kinematic indicators sense of shear and the fold-vergence associated with the syn-nappe stacking deformation. The contemporaneous pure and simple shearing recognized along the BT coupled with its orientation at the belt scale, i.e., approximately perpendicular to the belt's main sense of transport (Fig. 10.3), highlights the shear zone's potential growth during a slightly perpendicular collision. Finite strain data suggest a variation from general flattening to prolate ellipsoid, in agreement with an increase of simple shear in thrust-sense shear zones (Vitale & Mazzoli, 2008; Fossen, 2016). This implies that the core of the BT accommodated a higher amount of strain with respect to the shear zone peripheries (Fossen & Cavalcante, 2017) during a hybrid deformation involving both layer-parallel to layer-normal shortening coupled with heterogeneous simple shear.

The available geochronological constraints on the BT (Gemignani L. & Montomoli C. personal communication), fixed its activity at 330 Ma by Ar/Ar on white mica. This must be considered the first tectonic response during the perpendicular collision and the syn-nappe stacking exhumation.

However, both in the northern area (along the PASZ) and within the Monte Grighini dome (i.e., the MGSZ), the lineation is parallel to slightly inclined with respect to the main trend of the belt, i.e., NE-SW. The presence of a sub-vertical foliation parallel to the boundaries of both transpressive shear zones, and associated fold axes parallel to the sub-horizontal lineation, highlights the simultaneous development of shear and fold domains. The geometry and kinematics of the PASZ and the MGSZ are compatible with a transpressive regime due to dextral shear deformation with a shortening component perpendicular to the shear zone boundaries (Fig. 10.3). Kinematic vorticity estimations indicate a pure shear dominated transpression for the MGSZ, suggesting a general flattening. However, the PASZ is associated with a transition from pure to simple shear dominated transpression, approaching the high-strain zone (Fig. 10.3; Carosi et al., 2020). During the ongoing collisional stage, the Sardinian belt was affected by perpendicular to orogen parallel deformation during an oblique collision.

Transpression, involving both strike-slip and contractional deformation, has been conceptually introduced to explain structures within oblique convergent plate boundaries during the collision (e.g., Harland, 1971; Sanderson & Marchini, 1984; Tikoff & Fossen, 1993; Teyssier et al., 1995; Sullivan & Law, 2007; Nabavi et al., 2017, 2020) playing an important role during the exhumation of high-grade metamorphic rocks (e.g., Dasgupta et al., 2015). In this case, this is also widely confirmed by the proposed convergence angles estimated by the PASZ analysis, ranging between 50° to 60° (Carosi et al., 2020). The involvement of the metamorphic basement in dextral transpression due to the response of the orogen-perpendicular component of oblique convergence induced lateral extrusion. This is widely confirmed by the oblate plane strain condition recognized across the MGSZ and the PASZ and by the considerable amount of pure shear associated with them. The PASZ shear activity has been constrained at 325 Ma in a time span of 25 My. The obtained results from the MGSZ, indicated a shear activity at 315 Ma in a time span of 15 My (Fig. 10.3). This highlights a progressive rejunvement of the deformation from the hinterland to the foreland. In particular, the transpressive deformation onset of both PASZ and MGSZ is different. However, the timing of the end of the shearing is similar for both shear zones, indicating that the transpressive deformation developed under contractional regimes during the collisional stage and ended contemporaneously in different sectors of the Sardinian belt. The exhumation of the Sardinian orogenic wedge could be interpreted as an interplay of different forces during a strain partitioning at the belt scale in response from a perpendicular to an oblique collision. A possible scenario across time is reconstructible using the existing and newly obtained data.

The first deformation stage (D_1) initiates during pre-nappe stacking deformation, burial, and crustal thickening. It is characterized by the early accreted tectonic units of the wedge corresponding to the early deformation acquired during basal accretion of tectonic slices through subhorizontal forces. Continuous accretion evolved in a crustal exhumation driven by two different ways. The central part of the wedge, i.e., the investigated sector with BU and MSU, is defined by imbricated units and a thrust-sense shear zone (i.e., the BT) sub-perpendicular to the main vergence of the belt. The time constraints on the BT fixed the syn-collisional exhumation at 330 Ma. However, along the boundary between the Medium- and the High-Grade Metamorphic Complex (i.e., the boundary between the hinterland and the hinterland-foreland transition zone), the shifting from perpendicular to oblique collision induces ductile orogen-parallel transpression (i.e., the PASZ). Lateral and vertical extrusion combined with the erosion of uprising units allows the exhumation in this domain of the

orogenic wedge. Continuous compression during collision is marked by the progressive shifting of the deformation from the hinterland to the foreland.

The ongoing deformation far from the Inner Zone of the belt allows the development of an anticlinal stack of crustal units during the D_3. The erosion of the rapidly uplifted rocks constituting the antiformal stack favours a complex 3D behaviour that involves lateral and vertical extrusion of ductile crustal material. In the deeper parts of the antiform, the deformation results in shearing and not in folding, as in the MGSZ. The huge amount of pure shear and the lack of the increase of simple shear across the MGSZ with respect to the PASZ, could be ascribable to the paleo-position of the dome roughly perpendicular to the active forces due to the progressive rotation of the convergence angle. Thus, the development of a transpressive deformation within the Monte Grighini dome, a unicum in the Nappe Zone of the Variscan belt in Sardinia, could be associated both with the depth growth and the paleo-position of the dome during the oblique collision, allowing the exhumation of the deepest unit of the External Nappe Zone. The progressive renjuvement of the deformation and metamorphism toward the foreland is highlighted by the time constraints on the onset of the MGSZ activity.

Strain partitioning may occur at a wide range of scales (e.g., Bell & Hayward, 1991; Curtis, 1998; Bell et al., 2004; Bell, 2010; Curtis et al., 2010; Conand et al., 2020; Cochelin et al., 2021), and the progressive behaviour of the orogenic process may result in a continuous deformation or could be explained by different deformation events. In the investigated area, the combination of thrust-sense (i.e., the BT) and transpressive (i.e., PASZ, MGSZ) shear zones, orthogonal and oblique with respect to the displacement direction of the belt based on the spatial and chronological relationship forms a complex structural architecture. The degree of partitioning depends on the obliquity of the collisional process (Tikoff and Teyssier, 1994; Schulmann et al., 2003; Leever et al., 2011), which could change during the orogeny evolution.

Also, the existence of anisotropies, either pre- or syn-orogenic (e.g. juxtaposition of different complexes or the dipping/orientation of the previous structural elements, i.e., the PASZ and MGSZ), may induce localization of the strain along transpressive structures (e.g., Dias et al., 2022), enhanced during the progression of the orogenic process. The hinterland-foreland transition zone in Sardinia displays a spatial and temporal strain partitioning at the belt scale, involving diachronous and different-oriented contraction- and wrench-dominated structures developed from syn-collisional perpendicular collision to orogen parallel transpression, resulting in an oblique tectonic setting.

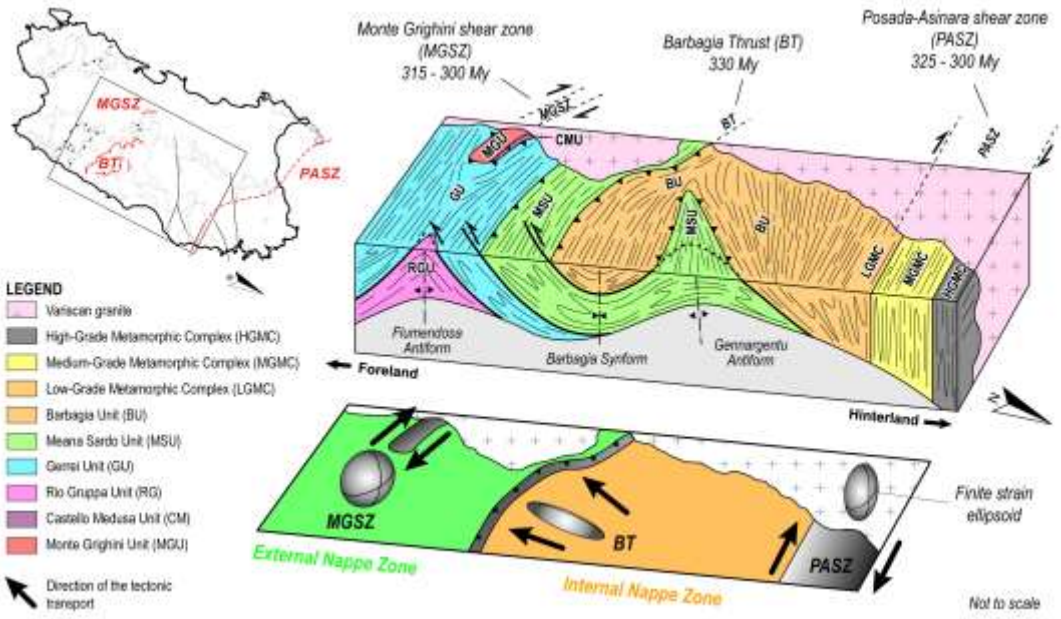

Figure 10.3: Schematic block diagram of the hinterland-foreland transition zone in Sardinia showing the present-day tectonic reconstruction highlighting the interplay among the Barbagia Thrust, the Monte Grighini shear zone and the Posada-Asinara shear zone.

References

Abrecht, J., & Hewitt, D.A. (1988). Experimental evidence on the substitution of Ti in biotite. *American Mineralogist*, *73*(11-12), 1275-1284.

Agard, P. (2021). Subduction of oceanic lithosphere in the Alps: selective and archetypal from (slow-spreading) oceans. *Earth-Science Reviews*, *214*, 103517. https://doi.org/10.1016/j.earscirev.2021.103517

Agard, P., Jolivet, L., & Goffe, B. (2001). Tectonometamorphic evolution of the Schistes Lustres Complex; implications for the exhumation of HP and UHP rocks in the Western Alps. *Bulletin de la Société géologique de France*, *172*(5), 617-636. https://doi.org/10.2113/172.5.617

Aguilar, C., Liesa, M., Štípská, P., Schulmann, K., Muñoz, J.A., & Casas, J.M. (2015). P–T–t–d evolution of orogenic middle crust of the Roc de Frausa Massif (Eastern Pyrenees): a result of horizontal crustal flow and Carboniferous doming?. *Journal of Metamorphic Geology*, *33*(3), 273-294. https://doi.org/10.1111/jmg.12120

Airaghi, L., Lanari, P., de Sigoyer, J., & Guillot, S. (2017). Microstructural vs compositional preservation and pseudomorphic replacement of muscovite in deformed metapelites from the Longmen Shan (Sichuan, China). *Lithos*, 282, 262-280. https://doi.org/10.1016/j.lithos.2017.03.013

Aleinikoff, J.N., Schenck, W.S., Plank, M.O., Srogi, L., Fanning, C.M., Kamo, S.L., & Bosbyshell, H. (2006). Deciphering igneous and metamorphic events in high-grade rocks of the Wilmington Complex, Delaware: Morphology, cathodoluminescence and backscattered electron zoning, and SHRIMP U-Pb geochronology of zircon and monazite. *Geological Society of America Bulletin*, *118*(1-2), 39-64. https://doi.org/10.1130/B25659.1

Alsop, G.I. (1992). Progressive deformation and the rotation of contemporary fold axes in the Ballybofey Nappe, north-west Ireland. *Geological Journal*, *27*(3), 271-283. https://doi.org/10.1002/gj.3350270305

Alsop, G.I., & Holdsworth, R.E. (2004). Shear zone folds: records of flow perturbation or structural inheritance?. *Geological Society, London, Special Publications*, *224*(1), 177-199. https://doi.org/10.1144/GSL.SP.2004.224.01.12

Aoya, M., Kouketsu, Y., Endo, S., Shimizu, H., Mizukami, T., Nakamura, D., & Wallis, S. (2010). Extending the applicability of the Raman carbonaceous-material geothermometer using data from contact metamorphic rocks. *Journal of Metamorphic Geology*, *28*(9), 895-914. https://doi.org/10.1111/j.1525-1314.2010.00896.x

Arima, M., & Edgar, A.D. (1981). Substitution mechanisms and solubility of titanium in phlogopites from rocks of probable mantle origin. *Contributions to Mineralogy and Petrology*, *77*(3), 288-295. https://doi.org/10.1007/BF00373544

Arthaud, F., & Matte, P. (1977). Late Paleozoic strike-slip faulting in southern Europe and northern Africa: Result of a right-lateral shear zone between the Appalachians and the Urals. *Geological Society of America Bulletin*, *88*(9), 1305-1320. https://doi.org/10.1130/0016-7606(1977)88%3C1305:LPSFIS%3E2.0.CO;2

Avouac, J.-P. (2003). Mountain Building, Erosion, and the Seismic Cycle in the Nepal Himalaya. *Advances in Geophysics*, *46*, 1-80. https://doi.org/10.1016/S0065-2687(03)46001-9

Avouac, J.P., & Burov, E.B. (1996). Erosion as a driving mechanism of intracontinental mountain growth. *Journal of Geophysical Research: Solid Earth*, *101*(B8), 17747-17769. https://doi.org/10.1029/96JB01344

Bailey, C.M., Polvi, L.E., & Forte, A.M. (2007). Pure shear dominated high-strain zones in basement terranes. *Memoirs-Geological Society of America*, *200*, 93. https://doi.org/10.1130/2007.1200(06)

Bajolet, F., Chardon, D., Martinod, J., Gapais, D., & Kermarrec, J.J. (2015). Synconvergence flow inside and at the margin of orogenic plateaus: Lithospheric-scale experimental approach. *Journal of Geophysical Research: Solid Earth*, *120*(9), 6634-6657. https://doi.org/10.1002/2015JB012110

Bajolet, F., Replumaz, A., & Lainé, R. (2013). Orocline and syntaxes formation during subduction and collision. *Tectonics*, *32*(5), 1529-1546. https://doi.org/10.1002/tect.20087

Balansa, J., Espurt, N., Hippolyte, J.C., Philip, J., & Caritg, S. (2022). Structural evolution of the superimposed Provençal and Subalpine fold-thrust belts (SE France). *Earth-Science Reviews*, *227*, 103972. https://doi.org/10.1016/j.earscirev.2022.103972

Balen, D., Massonne, H.J., & Lihter, I. (2018). Alpine metamorphism of low-grade schists from the Slavonian Mountains (Croatia): new PT and geochronological constraints. *International Geology Review*, *60*(3), 288-304. https://doi.org/10.1080/00206814.2017.1328710

Barca, S., & Jäger, H. (1989). New geological and biostratigraphical data on the Silurian in SE Sardinia. Close affinity with Thuringia. *Bollettino della Società Geologica Italiana*, *108*(4), 565-80.

Barca, S., Del Rio, M., & Pittau Demelia, P. (1988). New geological and stratigraphical data and discovery of lower Ordovician acritarchs in the San Vito sandstone of the genn'argiolas unit (Sarrabus, Southeastern Sardinia). *Rivista Italiana di Paleontologia e Stratigrafa*, 94(3), 339-360.

Barca, S., Forci, A., & Funedda, A. (2003). Nuovi dati stratigrafico-strutturali sul flysch ercinico dell'Unità del Gerrei (Sardegna SE). In V., Pascucci (Ed.). *GeoSed, Alghero 28-30 settembre 2003*, (pp. 291–298). Sassari: University of Sassari.

Bastida, F., Aller, J., Fernández, F.J., Lisle, R.J., Bobillo-Ares, N.C., & Menéndez, O. (2014). Recumbent folds: key structural elements in orogenic belts. *Earth-science reviews*, *135*, 162-183. https://doi.org/10.1016/j.earscirev.2014.05.002

Bastida, F., Aller, J., Pulgar, J.A., Toimil, N.C., Fernández, F.J., Bobillo-Ares, N.C., & Menéndez, C.O. (2010). Folding in orogens: a case study in the northern Iberian Variscan Belt. *Geological Journal*, *45*(5-6), 597-622. https://doi.org/10.1002/gj.1199

Behr, W.M., & Platt, J.P. (2014). Brittle faults are weak, yet the ductile middle crust is strong: Implications for lithospheric mechanics. *Geophysical Research Letters*, *41*(22), 8067-8075. https://doi.org/10.1002/2014GL061349

Bell, T.H. (1978). Progressive deformation and reorientation of fold axes in a ductile mylonite zone: the Woodroffe thrust. *Tectonophysics*, *44*(1-4), 285-320. https://doi.org/10.1016/0040-1951(78)90074-4

Bell, T.H. (2010). Deformation partitioning, foliation successions and their significance for orogenesis: hiding lengthy deformation histories in mylonites. *Geological Society, London, Special Publications, 335*(1), 275-292. https://doi.org/10.1144/SP335.13

Bell, T.H., & Hayward, N. (1991). Episodic metamorphic reactions during orogenesis: the control of deformation partitioning on reaction sites and reaction duration. *Journal of Metamorphic Geology, 9*(5), 619-640. https://doi.org/10.1111/j.1525-1314.1991.tb00552.x

Bell, T.H., Ham, A.P., & Kim, H.S. (2004). Partitioning of deformation along an orogen and its effects on porphyroblast growth during orogenesis. Journal of Structural Geology, 26(5), 825-845. https://doi.org/10.1016/j.jsg.2003.11.021

Bellanger, M., Augier, R., Bellahsen, N., Jolivet, L., Monié, P., Baudin, T., & Beyssac, O. (2015). Shortening of the European Dauphinois margin (Oisans Massif, Western Alps): New insights from RSCM maximum temperature estimates and 40Ar/39Ar in situ dating. *Journal of Geodynamics*, *83*, 37-64. https://doi.org/10.1016/j.jog.2014.09.004

Berger, A., Engi, M., Erne-Schmid, S., Glotzbach, C., Spiegel, C., de Goede, R., & Herwegh, M. (2020). The relation between peak metamorphic temperatures and subsequent cooling during continent–continent collision (western Central Alps, Switzerland). *Swiss journal of geosciences*, *113*(1), 1-18. https://doi.org/10.1186/s00015-020-00356-4

Berman, R.G. (1988). Internally-consistent thermodynamic data for minerals in the system Na_2O-K_2O-CaO-MgO-FeO-Fe_2O_3-Al_2O_3-SiO_2-TiO_2-H_2O-CO_2. *Journal of petrology*, *29*(2), 445-522. https://doi.org/10.1093/petrology/29.2.445

Berman, R.G. (1991). Thermobarometry using multi-equilibrium calculations; a new technique, with petrological applications. *The Canadian Mineralogist*, *29*(4), 833-855.

Beyssac, O., & Lazzeri, M. (2012). Application of Raman spectroscopy to the study of graphitic carbons in the Earth Sciences. *EMU Notes Mineral*, *12*(12), 415-454. http://dx.doi.org/10.1180/emu-notes.12.12

Beyssac, O., Bollinger, L., Avouac, J.P., & Goffé, B. (2004). Thermal metamorphism in the lesser Himalaya of Nepal determined from Raman spectroscopy of carbonaceous material. *Earth and Planetary Science Letters*, *225*(1-2), 233-241. https://doi.org/10.1016/j.epsl.2004.05.023

Beyssac, O., Goffé, B., Chopin, C., & Rouzaud, J.N. (2002). Raman spectra of carbonaceous material in metasediments: a new geothermometer. *Journal of metamorphic Geology*, *20*(9), 859-871. https://doi.org/10.1046/j.1525-1314.2002.00408.x

Beyssac, O., Goffé, B., Petitet, J.P., Froigneux, E., Moreau, M., & Rouzaud, J.N. (2003). On the characterization of disordered and heterogeneous carbonaceous materials by Raman spectroscopy. *Spectrochimica Acta Part A: Molecular and Biomolecular Spectroscopy*, *59*(10), 2267-2276. https://doi.org/10.1016/S1386-1425(03)00070-2

Beyssac, O., Pattison, D.R., & Bourdelle, F. (2019). Contrasting degrees of recrystallization of carbonaceous material in the Nelson aureole, British Columbia and Ballachulish aureole, Scotland, with implications for thermometry based on Raman spectroscopy of carbonaceous material. *Journal of Metamorphic Geology*, *37*(1), 71-95. https://doi.org/10.1111/jmg.12449

Beyssac, O., Simoes, M., Avouac, J.P., Farley, K.A., Chen, Y.G., Chan, Y.C., & Goffé, B. (2007). Late Cenozoic metamorphic evolution and exhumation of Taiwan. *Tectonics*, *26*(6). https://doi.org/10.1029/2006TC002064

Bhattacharyya, K., & Ahmed, F. (2016). Role of initial basin width in partitioning total shortening in the Lesser Himalayan fold-thrust belt: Insights from regional balanced cross-sections. *Journal of Asian Earth Sciences*, *116*, 122-131. https://doi.org/10.1016/j.jseaes.2015.11.012

Bhattacharyya, K., Mitra, G., & Kwon, S. (2015). Geometry and kinematics of the Darjeeling–Sikkim Himalaya, India: Implications for the evolution of the Himalayan fold-thrust belt. *Journal of Asian Earth Sciences*, *113*, 778-796. https://doi.org/10.1016/j.jseaes.2015.09.008

Bickle, M. J., & Powell, R. (1977). Calcite-dolomite geothermometry for iron-bearing carbonates. *Contributions to Mineralogy and Petrology*, *59*(3), 281-292. https://doi.org/10.1007/BF00374557

Boedo, F.L., Willner, A.P., Vujovich, G.I., & Massonne, H.J. (2016). High-pressure/low-temperature metamorphism in the collision zone between the Chilenia and Cuyania microcontinents (western Precordillera, Argentina). *Journal of South American Earth Sciences*, *72*, 227-240. https://doi.org/10.1016/j.jsames.2016.09.009

Bollinger, L., Avouac, J.P., Beyssac, O., Catlos, E.J., Harrison, T.M., Grove, M., Goffé, B., & Sapkota, S. (2004). Thermal structure and exhumation history of the Lesser Himalaya in central Nepal. *Tectonics*, *23*(5). https://doi.org/10.1029/2003TC001564

Bosellini, A., & Ogniben, G. (1968). Ricoprimenti ercinici nella Sardegna centrale. *Annali dell'Università di Ferrara*, *1*, 1-15.

Bourdelle, F. (2021). Low-Temperature chlorite geothermometry and related recent analytical advances: A review. *Minerals*, *11*(2), 130. https://doi.org/10.3390/min11020130

Bourdelle, F., & Cathelineau, M. (2015). Low-temperature chlorite geothermometry: a graphical representation based on a T–R2+–Si diagram. *European Journal of Mineralogy*, *27*(5), 617-626. https://doi.org/10.1127/ejm/2015/0027-2467

Bourdelle, F., Parra, T., Beyssac, O., Chopin, C., & Vidal, O. (2013). Clay minerals as geo-thermometer: A comparative study based on high spatial resolution analyses of illite and chlorite in Gulf Coast sandstones (Texas, USA). *American Mineralogist*, *98*(5-6), 914-926. https://doi.org/10.2138/am.2013.4238

Bousquet, R., Goffé, B., Vidal, O., Oberhänsli, R., & Patriat, M. (2002). The tectono-metamorphic history of the Valaisan domain from the Western to the Central Alps: New constraints on the evolution of the Alps. *Geological Society of America Bulletin*, *114*(2), 207-225. https://doi.org/10.1130/0016-7606(2002)114%3C0207:TTMHOT%3E2.0.CO;2

Bousquet, R., Oberhänsli, R., Goffé, B., Jolivet, L., & Vidal, O. (1998). High-pressure–low-temperature metamorphism and deformation in the Bündnerschiefer of the Engadine window: Implications for the regional evolution of the eastern Central Alps. *Journal of Metamorphic Geology*, *16*(5), 657-674. https://doi.org/10.1111/j.1525-1314.1998.00161.x

Broussolle, A., Štípská, P., Lehmann, J., Schulmann, K., Hacker, BR, Holder, R., Kylander-Clark, A.R.C., Hanžl, P., Racek, M., Hasalová, P., Lexa, O., Hrdličková, K. & Buriánek, D. (2015). P–T–t–D record of crustal-scale horizontal flow and magma-assisted doming in the SW Mongolian Altai, *Journal of Metamorphic Geology*, 33, 359-383. https://doi.org/10.1111/jmg.12124

Brown, M. (1993). P–T–t evolution of orogenic belts and the causes of regional metamorphism. *Journal of the Geological Society*, *150*(2), 227-241. https://doi.org/10.1144/gsjgs.150.2.0227

Brown, T.H., & Skinner, B.J. (1974). Theoretical prediction of equilibrium phase assemblages in multicomponent systems. *American Journal of Science*, *274*(9), 961-986. https://doi.org/10.2475/ajs.274.9.961

Brun, J.P., & Cobbold, P.R. (1980). Strain heating and thermal softening in continental shear zones: a review. *Journal of Structural Geology*, *2*(1-2), 149-158. https://doi.org/10.1016/0191-8141(80)90045-0

Buck, W. R. (1991). Modes of continental lithospheric extension. *Journal of Geophysical Research: Solid Earth*, *96*(B12), 20161-20178. https://doi.org/10.1029/91JB01485

Bühler, M., Zurbriggen, R., Berger, A., Herwegh, M., & Rubatto, D. (2022). Late Carboniferous Schlingen in the Gotthard nappe (Central Alps) and their relation to the Variscan evolution. *International Journal of Earth Sciences*, 1-26. https://doi.org/10.1007/s00531-022-02247-5

Burg, J.P., & Gerya, T.V. (2005). The role of viscous heating in Barrovian metamorphism of collisional orogens: thermomechanical models and application to the Lepontine Dome in the Central Alps. *Journal of Metamorphic Geology*, *23*(2), 75-95. https://doi.org/10.1111/j.1525-1314.2005.00563.x

Burg, J. P., & Schmalholz, S. M. (2008). Viscous heating allows thrusting to overcome crustal-scale buckling: Numerical investigation with application to the Himalayan syntaxes. *Earth and Planetary Science Letters*, *274*(1-2), 189-203. https://doi.org/10.1016/j.epsl.2008.07.022

Burg, J.P., Kaus, B.J., & Podladchikov, Y.Y. (2004). Dome structures in collision orogens: Mechanical investigation of the gravity/compression interplay. *Special papers-Geological society of America*, 47-66. https://doi.org/10.1130/0-8137-2380-9.47

Butler, R. W., Bond, C. E., Cooper, M. A., & Watkins, H. (2020). Fold–thrust structures–where have all the buckles gone?. *Geological Society, London, Special Publications*, *487*(1), 21-44. https://doi.org/10.1144/SP487.7

Caggianelli, A., Prosser, G., Festa, V., Langone, A., & Spiess, R. (2013). From the upper to the lower continental crust exposed in Calabria. *Geol. Field Trips*, *5*(1/2), 49. https://doi.org/10.3301/GFT.2013.02

Cagnard, F., Durrieu, N., Gapais, D., Brun, J. P., & Ehlers, C. (2006). Crustal thickening and lateral flow during compression of hot lithospheres, with particular reference to Precambrian times. *Terra Nova*, *18*(1), 72-78. https://doi.org/10.1111/j.1365-3121.2005.00665.x

Calvino, F. (1959). Lineamenti strutturali del Sarrabus- Gerrei (Sardegna sud-orientale). *Bollettino del Servizio Geologico d'Italia*, *81*, 489-556.

Camacho, A., McDougall, I., Armstrong, R., & Braun, J. (2001). Evidence for shear heating, Musgrave Block, central Australia. *Journal of Structural Geology*, *23*(6-7), 1007-1013. https://doi.org/10.1016/S0191-8141(00)00172-3

Cantarero, I., Alías, G., Cruset, D., Carola, E., Lanari, P., & Travé, A. (2018). Fluid composition changes in crystalline basement rocks from ductile to brittle regimes. *Global and planetary change*, *171*, 273-292. https://doi.org/10.1016/j.gloplacha.2018.03.002

Cantarero, I., Lanari, P., Vidal, O., Alías, G., Travé, A., & Baqués, V. (2014). Long-term fluid circulation in extensional faults in the central Catalan Coastal Ranges: P–T constraints from neoformed chlorite and K-white mica. *International Journal of Earth Sciences*, *103*(1), 165-188. https://doi.org/10.1007/s00531-013-0963-8

Cao, S., Zhan, L., & Tao, L. (2022). Exhumation processes of continental crustal metamorphic complexes. *Geosystems and Geoenvironment*, 100094. https://doi.org/10.1016/j.geogeo.2022.100094

Carlson, W.D., Pattison, D.R., & Caddick, M.J. (2015). Beyond the equilibrium paradigm: How consideration of kinetics enhances metamorphic interpretation. *American Mineralogist*, *100*(8-9), 1659-1667. https://doi.org/10.2138/am-2015-5097

Carmignani, L., & Pertusati, P. C. (1977). Analisi strutturale di un segmento della catena ercinica: il Gerrei (Sardegna sud-orientale). *Bollettino della Società Geologica Italiana*, *96*, 339-364.

Carmignani, L., Carosi, R., Di Pisa, A., Gattiglio, M., Musumeci, G., Oggiano, G., & Pertusati, P.C. (1994). The hercynian chain in Sardinia (Italy). *Geodinamica Acta*, *7*(1), 31–47. https://doi.org/10.1080/09853111.1994.11105257

Carmignani, L., Cherchi, G. P., Del, M., Franceschelli, M., Ghezzo, C., Musumeci, G., & Pertusati, P. C. (1987). The mylonitic granitoids and tectonic Units of the Monte Grighini Complex (West-Central Sardinia): a preliminary note. In *Paleozoic Stratgraphy, Tectonics and Magmatism in Italy* (pp. 25-26).

Carmignani, L., Conti, P., Funedda, A., Oggiano, G., & Pasci, S. (2012). La geologia della Sardegna-84 Congresso Nazionale della Società Geologica Italiana". In *Geology of Sardinia*–84 National Conference of the Italian Geological Society.

Carmignani, L., Minzoni, N., Pertusati, P.C., & Gattiglio, M. (1982). Lineamenti geologici principali del Sarcidano-Barbagia di Belvì. In L., Carmignani, T., Cocozza, C., Ghezzo, P.C., Pertusati & C.A. Ricci (Ed.). *Guida alla Geologia del Paleozoico Sardo* (pp. 119-125). Guide Geologiche Regionali, Società Geologica Italiana.

Carmignani, L., Oggiano, G., Barca, S., Conti, P., Eltrudis, A., Funedda, A., Pasci, S., & Salvadori, I. (2001). Geologia della Sardegna (Note illustrative della Carta Geologica della Sardegna in scala 1:200.000). Memorie descrittive della Carta Geologica d'Italia, Servizio Geologico Nazionale, Istituto Poligrafico e Zecca dello Stato, Roma.

Carmignani, L., Oggiano, G., Funedda, A., Conti, P., & Pasci, S. (2016). The geological map of Sardinia (Italy) at 1:250,000 scale. *Journal of Maps*, *12*(5), 826-835. https://doi.org/10.1080/17445647.2015.1084544

Carosi, R. (2004). Carta geologico-strutturale del Monte S. Vittoria (Sarcidano-Barbagia di Belvì, Sardegna centrale, Italia). Carosi R., Elter F.M. & Gattiglio M. (1997). Scala 1:25.000, Centrooffset, Siena, 1997. *Atti della Società Toscana di Scienze Naturali*, *serie A, 108* (2002-2003).

Carosi, R., & Malfatti, G. (1995). Analisi Strutturale dell'Unità di Meana Sardo e caratteri della deformazione duttile nel Sarcidano-Barbagia di Seulo (Sardegna centrale, Italia). *Atti della Società Toscana di Scienze Naturali*, *Serie A*, *102*, 121-136.

Carosi, R., & Oggiano, G. (2002). Transpressional deformation in northwestern Sardinia (Italy): insights on the tectonic evolution of the Variscan belt. *Comptes Rendus Geoscience*, *334*(4), 287-294. https://doi.org/10.1016/S1631-0713(02)01740-6

Carosi, R., & Palmeri, R. (2002). Orogen-parallel tectonic transport in the Variscan belt of northeastern Sardinia (Italy): implications for the exhumation of medium-pressure metamorphic rocks. *Geological Magazine*, *139*(5), 497-511. https://doi.org/10.1017/S0016756802006763

Carosi, R., & Pertusati, P.C. (1990). Evoluzione strutturale delle unità tettoniche erciniche nella Sardegna centro-meridionale. *Bollettino della Società Geologica Italiana*, *109*, 325-335.

Carosi, R., D'Addario, E., Mammoliti, E., Montomoli, C., & Simonetti, M. (2016). Geology of the northwestern portion of the ferriere-mollieres shear zone, Argentera massif, Italy. *Journal of Maps*, *12*, 466-475. https://doi.org/10.1080/17445647.2016.1243491

Carosi, R., Iacopini, D., & Montomoli, C. (2004). Asymmetric folds development in the Variscan Nappe of central Sardinia (Italy). *Comptes Rendus Geoscience*, *336*(10), 939-949. https://doi.org/10.1016/j.crte.2004.03.004

Carosi, R., Leoni, L., Montomoli, C., & Sartori, F. (2003). Very low-grade metamorphism in the Tuscan Nappe, Northern Apennines, Italy: relationships between deformation and metamorphic indicators in the La Spezia mega-fold. *Swiss Bulletin of Mineralogy and Petrology*, *83*(1), 15-32.

Carosi, R., Leoni, L., Paolucci, F., Pertusati, P.C., & Trumpy, E. (2010). Deformation and illite crystallinity in metapelitic rocks from the Mandas area, in the Nappe Zone of the Variscan belt of Sardinia. *Rendiconti Online Società Geologica Italiana*, *11*, 393-394.

Carosi, R., Montomoli, C., Iaccarino, S., Benetti, B., Petroccia, A., & Simonetti, M. (2022). Constraining the timing of evolution of shear zones in two collisional orogens: fusing structural geology and geochronology. *Geosciences*, *12*, 231. https://doi.org/10.3390/geosciences12060231

Carosi, R., Montomoli, C., & Iacopini, D. (2002). Le pieghe asimmetriche dell'Unità di Meana Sardo, Sardegna centrale (Italia): evoluzione e meccanismi di piegamento. *Atti della Società Toscana di Scienze Naturali*, *Serie A*, *108*, 51-58.

Carosi, R., Montomoli, C., Tiepolo, M., & Frassi, C. (2012). Geochronological constraints on post-collisional shear zones in the Variscides of Sardinia (Italy). *Terra Nova*, *24*(1), 42-51. https://doi.org/10.1111/j.1365-3121.2011.01035.x

Carosi, R., Musumeci, G., & Pertusati, P.C. (1991). Differences in the structural evolution of tectonic units in central-southern Sardinia. *Bollettino della Società Geologica Italiana*, *110*(3-4), 543-551.

Carosi, R., Petroccia, A., Iaccarino, S., Simonetti, M., Langone, A., & Montomoli, C. (2020). Kinematics and timing constraints in a transpressive tectonic regime: the example of the Posada-Asinara shear zone (NE Sardinia, Italy). *Geosciences*, *10*, 288. https://doi.org/10.3390/geosciences10080288

Carreras, J., & Druguet, E. (2014). Framing the tectonic regime of the NE Iberian Variscan segment. *Geological Society, London, Special Publications*, *405*(1), 249-264. https://doi.org/10.1144/SP405.7

Carreras, J., & Druguet, E. (2019). Complex fold patterns developed by progressive deformation. *Journal of Structural Geology*, *125*, 195-201. https://doi.org/10.1016/j.jsg.2018.07.015

Carreras, J., Druguet, E., & Griera, A. (2005). Shear zone-related folds. *Journal of Structural Geology*, *27*(7), 1229-1251. https://doi.org/10.1016/j.jsg.2004.08.004

Casini, L., & Oggiano, G. (2008). Late orogenic collapse and thermal doming in the northern Gondwana margin incorporated in the Variscan Chain: a case study from the Ozieri Metamorphic Complex, northern Sardinia, Italy. *Gondwana Research*, *13*(3), 396-406. https://doi.org/10.1016/j.gr.2007.11.004

Casini, L., Cuccuru, S., Maino, M., Oggiano, G., Puccini, A., & Rossi, P. (2015). Structural map of variscan northern Sardinia (Italy). *Journal of maps*, *11*(1), 75-84. https://doi.org/10.1080/17445647.2014.936914

Casini, L., Cuccuru, S., Maino, M, Oggiano, G., & Tiepolo, M. (2012). Emplacement of the Arzachena Pluton (Corsica-Sardinia Batholith) and the geodynamics of incoming Pangaea. *Tectonophysics*, *544-545*, 31-49. https://doi.org/10.1016/j.tecto.2012.03.028

Casini, L., Funedda, A., & Oggiano, G. (2010). A balanced foreland-hinterland deformation model for the Southern Variscan belt of Sardinia, Italy. *Geological Journal, 45*(5-6), 634-649. https://doi.org/10.1002/gj.1208

Casini, L., Maino, M., Langone, A., Oggiano, G., Corvò, S., Estrada, J. R., & Liesa, M. (2022). HTLP metamorphism and fluid-fluxed melting during multistage anatexis of continental crust (N Sardinia, Italy). *Journal of Metamorphic Geology*. https://doi.org/10.1111/jmg.12687

Caso, F., Nerone, S., Petroccia, A., & Bonasera, M. (2021). Geology of the southern Gran Paradiso Massif and Lower Piedmont Zone contact area (middle Ala valley, Western Alps, Italy). *Journal of Maps*, *17*(2), 237-246. https://doi.org/10.1080/17445647.2021.1911869

Cassinis, G., Cortesogno, L., Gaggero, L., Ronchi, A., Sarria, E., Serri, R., & Calzia, P. (2003). Reconstruction of igneous, tectonic and sedimentary events in the latest Carboniferous–Early Permian Seui basin (Sardinia, Italy), and evolutionary model. *Bollettino della Società Geologica Italiana*, *2*, 99-118.

Cathelineau, M. (1988). Cation site occupancy in chlorites and illites as a function of temperature. *Clay minerals*, *23*(4), 471-485. https://doi.org/10.1180/claymin.1988.023.4.13

Chang, E.Z. (2000). Geology and tectonics of the Songpan-Ganzi fold belt, southwestern China. *International Geology Review*, *42*(9), 813-831. https://doi.org/10.1080/00206810009465113

Chardon, D., Gapais, D., & Cagnard, F. (2009). Flow of ultra-hot orogens: a view from the Precambrian, clues for the Phanerozoic. *Tectonophysics*, *477*(3-4), 105-118. https://doi.org/10.1016/j.tecto.2009.03.008

Chen, C.T., Chan, Y.C., Lu, C.Y., Simoes, M., & Beyssac, O. (2011). Nappe structure revealed by thermal constraints in the Taiwan metamorphic belt. *Terra Nova*, *23*(2), 85-91. https://doi.org/10.1111/j.1365-3121.2011.00987.x

Chew, D.M., Petrus, J.A., & Kamber, B.S. (2014). U–Pb LA–ICPMS dating using accessory mineral standards with variable common Pb. *Chemical Geology*, *363*, 185-199. https://doi.org/10.1016/j.chemgeo.2013.11.006

Cocco, F., & Funedda, A. (2011). New data on the pre-Middle Ordovician deformation in SE Sardinia: a preliminary note. *Rendiconti online della Società Geologica Italiana*, *15*, 34-36.

Cocco, F., & Funedda, A. (2019). The Sardic phase: field evidence of Ordovician tectonics in SE Sardinia, Italy. *Geological Magazine*, *156*, 25-38. https://doi.org/10.1017/s0016756817000723

Cocco, F., Loi, A., Funedda, A., Casini, L., Ghienne, J. F., Pillola, G. L., Vidal, M., Meloni, M. A., & Oggiano, G. (2022). Ordovician tectonics of the South European Variscan Realm: new insights from Sardinia. *International Journal of Earth Sciences*, 1-24. https://doi.org/10.1007/s00531-022-02250-w

Cocco, F., Oggiano, G., Funedda, A., Loi, A., & Casini, L. (2018). Stratigraphic, magmatic and structural features of Ordovician tectonics in Sardinia (Italy): a review. *Journal of Iberian Geology*, *44*, 619–639. https://doi.org/10.1007/s41513-018-0075-1

Cochelin, B., Lemirre, B., Denèle, Y., & de Saint Blanquat, M. (2021). Strain partitioning within bending orogens, new insights from the Variscan belt (Chiroulet-Lesponne domes, Pyrenees). *Tectonics*, *40*(7), e2020TC006386. https://doi.org/10.1029/2020TC006386

Columbu, S., Cruciani, G., Fancello, D., Franceschelli, M., & Musumeci, G. (2015). Petrophysical properties of a granite-protomylonite-ultramylonite sequence: insight from the Monte Grighini shear zone, central Sardinia, Italy. *European Journal of Mineralogy*, *27*(4), 471-486. https://doi.org/10.1127/ejm/2015/0027-2447

Conand, C., Mouthereau, F., Ganne, J., Lin, A.T.S., Lahfid, A., Daudet, M., Mesalles, L., Giletycz, S., & Bonzani, M. (2020). Strain partitioning and exhumation in oblique Taiwan collision: Role of rift architecture and plate kinematics. *Tectonics*, *39*(4), e2019TC005798. https://doi.org/10.1029/2019TC005798

Condie, K.C., Hatcher, R.D., Carlson, M.P., & McBride, J.H. (2007). Accretionary orogens in space and time. *Memoirs-Geological Society of America*, *200*, 145. https://doi.org/10.1130/2007.1200(09)

Coney, P. J., & Harms, T. A. (1984). Cordilleran metamorphic core complexes: Cenozoic extensional relics of Mesozoic compression. *Geology*, *12*(9), 550-554. https://doi.org/10.1130/0091-7613(1984)12%3C550:CMCCCE%3E2.0.CO;2

Coney, P.J., Crittenden, M.D., & Davis, G.H. (1980). Cordilleran metamorphic core complexes: An overview. Cordilleran metamorphic core complexes: *Geological Society of America Memoir, 153,* 7-31.

Connolly, J. A. (2005). Computation of phase equilibria by linear programming: a tool for geodynamic modeling and its application to subduction zone decarbonation. *Earth and Planetary Science Letters*, *236*(1-2), 524-541. https://doi.org/10.1016/j.epsl.2005.04.033

Conti, P., & Patta, E.D. (1998). Large-scale Hercynian West-directed tectonics in southeastern Sardinia (Italy). *Geodinamica Acta*, *11*(5), 217-231. https://www.tandfonline.com/doi/abs/10.1080/09853111.1998.11105321

Conti, P., Carmignani, L., Cerbai, N., Eltrudis, A., Funedda, A., & Oggiano, G. (1999). From thickening to extension in the Variscan belt - kinematic evidence from Sardinia (Italy). *Terra Nova*, *11*(2/3), 93-99. https://doi.org/10.1046/j.1365-3121.1999.00231.x

Conti, P., Carmignani, L., & Funedda, A. (2001). Change of nappe transport direction during the Variscan collisional evolution of central-southern Sardinia (Italy). *Tectonophysics*, *332*(1-2), 255-273. https://doi.org/10.1016/S0040-1951(00)00260-2

Conti, P., Funedda, A., & Cerbai, N. (1998). Mylonite development in the Hercynian basement of Sardinia (Italy). *Journal of Structural Geology*, *20*(2/3), 121-133. https://doi.org/10.1016/S0191-8141(97)00091-6

Corradini, C., Ferretti, A., & Serpagli, E. (1998). The Silurian and Devonian sequence in SE Sardinia. ECOS VII [Special Issue]. *Giornale di Geologia*, *60*, 71-74.

Corsini, M., & Rolland, Y. (2009). Late evolution of the southern European Variscan belt: Exhumation of the lower crust in a context of oblique convergence. *Comptes Rendus Geoscience*, *341*(2-3), 214-223. https://doi.org/10.1016/j.crte.2008.12.002

Cortesogno, L., Cassinis, G., Dallagiovanna, G., Gaggero, L., Oggiano, G., Ronchi, A., Seno, S., & Vanossi, M. (1998). The Variscan post-collisional volcanism in late Carboniferous–Permian sequences of Ligurian Alps, southern Alps and Sardinia (Italy): A synthesis. *Lithos*, *45*(1-4), 305-328. https://doi.org/10.1016/S0024-4937(98)00037-1

Costamagna, L.G. (2019). The carbonates of the post-Variscan basins of Sardinia: the evolution from Carboniferous – Permian humid-persistent to Permian aridephemeral lakes in a morphotectonic framework. *Geological Magazine*, *156*(11), 1-23. https://doi.org/10.1017/S0016756819000232

Costamagna, L.G. (2022). Sedimentary evolution of the Pennsylvanian–Permian Mulargia–Escalaplano molassic basin (Sardinia, Italy): the most complete record in the Southern Variscan Realm. *Geological Magazine*, *159*(9), 1529-1568. https://doi.org/10.1017/S001675682200036X

Costamagna, L., & Barca, S. (2004). Stratigrafia, analisi di facies, paleogeografia e dinquadramento regionale della successione giurassica dell'area dei Tacchi (Sardegna Orientale). *Bollettino della Società Geologica Italiana*, *123*(3), 477-496.

Costamagna, L.G., Cruciani, G., Franceschelli, M., & Puxeddu, M. (2012). A volcano-sedimentary sequence with albitite layers in the Variscan basement of NE Sardinia: a petrographical and geochemical study. *Periodico di Mineralogia*, *81*(2).

Coward, M.P., & Kim, J.H. (1981). Strain within thrust sheets. *Geological Society, London, Special Publications*, *9*(1), 275-292. https://doi.org/10.1144/GSL.SP.1981.009.01.25

Cruciani, G., Fancello, D., Franceschelli, M., & Giovanni, M. (2017). The Paleozoic basement of Monte Grighini Unit, a deep view in the nappe structure of Variscan belt in Sardinia. Synthesis of geological data and field guide.

Cruciani, G, Franceschelli, M., Carosi, R., & Montomoli, C. (2022). P-T path from garnet zoning in pelitic schist from NE Sardinia, Italy: Further constraints on the metamorphic and tectonic evolution of the north Sardinia Variscan belt. *Lithos*, 428-429. https://doi.org/10.1016/j.lithos.2022.106836

Cruciani, G., Franceschelli, M., Massonne, H.-J., Musumeci, G., & Spano, M.E. (2016). Thermomechanical evolution of the highgrade core in the nappe zone of Variscan Sardinia, Italy: the role of shear deformation and granite emplacement. *Journal of Metamorphic Geology*, *34*, 321-342. https://doi.org/10.1111/jmg.12183

Cruciani, G., Franceschelli, M., Musumeci, G., Spano, M. E., & Tiepolo, M. (2013). U-Pb zircon dating and nature of metavolcanics and metarkoses from the Monte Grighini Unit: new insights on Late Ordovician magmatism in the Variscan belt in Sardinia, Italy. *International Journal of Earth Sciences*, *102*, 2077-2096. https://doi.org/10.1007/s00531-013-0919-z

Cruciani, G., Montomoli, C., Carosi, R., Franceschelli, M., & Puxeddu, M. (2015). Continental collision from two perspectives: a review of Variscan metamorphism and deformation in northern Sardinia. *Periodico di Mineralogia*, *84*, 657-699. https://doi.org/10.2451/2015PM0455

Curtis, M.L. (1998). Development of kinematic partitioning within a pure-shear dominated dextral transpression zone: the southern Ellsworth Mountains, Antarctica. *Geological Society, London, Special Publications*, *135*(1), 289-306. https://doi.org/10.1144/GSL.SP.1998.135.01.19

Curtis, M.L., Flowerdew, M.J., Riley, T.R., Whitehouse, M.J., & Daly, J.S. (2010). Andean sinistral transpression and kinematic partitioning in South Georgia. *Journal of Structural Geology*, *32*(4), 464-477. https://doi.org/10.1016/j.jsg.2010.02.002

Dasgupta, S., Mandal, N., & Bose, S. (2015). How far does a ductile shear zone permit transpression? In S., Mukherjee, K.F., Mulchrone (Ed.). *Ductile Shear Zones: From Micro to Macro-scale*s. (pp.14-29) Springer- https://doi.org/10.1002/9781118844953.ch2

Davis, G. H. (1983). Shear-zone model for the origin of metamorphic core complexes. *Geology*, *11*(6), 342-347. https://doi.org/10.1130/0091-7613(1983)11%3C342:SMFTOO%3E2.0.CO;2

De Capitani, C., & Brown, T.H. (1987). The computation of chemical equilibrium in complex systems containing non-ideal solutions. *Geochimica et Cosmochimica Acta*, *51*, 2639-2652. https://doi.org/10.1016/0016-7037(87)90145-1

De Capitani, C., & Petrakakis, K. (2010). The computation of equilibrium assemblage diagrams with Theriak/Domino software. *American Mineralogist, 95*, 1006-1016. https://doi.org/10.2138/am.2010.3354

Del Moro, A., Di Simplicio, P., Ghezzo, C., Guasparri, G., Rita, F., & Sabatini, G. (1975). Radiometric data and intrusive sequence in the Sardinian batholith. *Neues Jahrbuch für Mineralogie Monatshefte*, *126*, 28-44.

Del Moro, A., Laurenzi, M., Musumeci, G., & Pardini, G., (1991). Rb/Sr and Ar/Ar chronology of Hercynian Mt. Grighini intrusive and metamorphic rocks (central-western Sardinia). *Plinius*, *4*, 121-122.

Delchini, S., Lahfid, A., Plunder, A., & Michard, A. (2016). Applicability of the RSCM geothermometry approach in a complex tectono-metamorphic context: The Jebilet massif case study (Variscan Belt, Morocco). *Lithos, 256-257*, 1-12. https://doi.org/10.1016/j.lithos.2016.04.007

Denèle, Y., Olivier, P., Gleizes, G., & Barbey, P. (2007). The Hospitalet gneiss dome (Pyrenees) revisited: lateral flow during Variscan transpression in the middle crust. *Terra Nova*, *19*, 445-453. https://doi.org/10.1111/j.1365-3121.2007.00770.x

Denèle, Y., Olivier, Ph, Gleizes, G., & Barbey, P. (2009). Decoupling between the middle and upper crust during transpression- related lateral flow: Variscan evolution of the Aston gneiss dome (Pyrenees, France). *Tectonophysics*, *477*, 244-261. https://doi.org/10.1016/j.tecto.2009.04.033

Dessau, G., Duchi, G., Moretti, A., & Oggiano, G. (1982). Geologia della zona del Valico di Correboi (Sardegna centro-orientale). Rilevamento, tettonica e giacimenti minerari. *Bollettino della Società Geologica Italiana*, *101*, 223-231.

Di Milia, A., & Tongiorgi, M. (1993). Reworked palynomorphs in the Solanas Sandstones (Central Sardinia) and their significance for the basin analysis. In L., Carmignani, F.P., Sassi (Ed.). *Contributions to the Geology of Italy with special regards to Paleozoic basement: a volume dedicated to Tommaso Cocozza*. (pp. 461-463) IGPC Project no. 276, Newsletter, 5.

Di Pisa, A., Gattiglio, M., & Oggiano G. (1992). Pre-Hercynian basic magmatic activity in the Nappe Zone (Internal and External) of Sardinia: evidence of two within plate basaltic cycles. In L., Carmignani, F.P., Sassi (Ed.). *Contributions to the Geology of Italy*. (pp. 107-116), IOCP No 276, Newsletter 5, special issue.

Di Rosa, M., De Giorgi, A., Marroni, M., & Pandolfi, L. (2017). Geology of the area between Golo and Tavignano Valleys (Central Corsica): a snapshot of the continental metamorphic units of Alpine Corsica. *Journal of Maps*, *13*(2), 644-653. https://doi.org/10.1080/17445647.2017.1351900

Di Rosa, M., Frassi, C., Meneghini, F., Marroni, M., Pandolfi, L., & De Giorgi, A. (2019). Tectono-metamorphic evolution of the European continental margin involved in the Alpine subduction: New insights from Alpine Corsica, France. *Comptes Rendus Geoscience*, *351*(5), 384-394. https://doi.org/10.1016/j.crte.2018.12.002

Di Vincenzo, G., Carosi, R., & Palmeri, R. (2004). The relationship between tectono-metamorphic evolution and argon isotope records in white mica: Constraints from in situ 40Ar-39Ar laser analysis of the Variscan basement of Sardinia*. Journal of Petrology, 45*, 101-1043. https://doi.org/10.1093/petrology/egh002

Dias, R., & Ribeiro, A. (1994). Constriction in a transpressive regime: an example in the Iberian branch of the Ibero-Armorican arc. *Journal of Structural Geology*, *16*(11), 1543-1554. https://doi.org/10.1016/0191-8141(94)90032-9

Dias, R., Coke, C., & Ribeiro, A. (2022). Strain partitioning in the Variscan deformation of the Marão domain (Central Iberian zone; northern Portugal). *Journal of Structural Geology*, 104635. https://doi.org/10.1016/j.jsg.2022.104635

Dieni, I., & Massari, F. (2011). Discussion on «The Sardinia-Corsica microplate and its role in the Northern Apennine Geodynamics: new insights from the Tertiary intraplate strike-slip tectonics of Sardinia» by G. Oggiano, A. Funedda, L. Carmignani & S. Pasci (2009). *Italian journal of geosciences*, *130*(1), 136-138.

Dieni, I., Fischer, J.C., Massari, F., & Vozenin-Serra, C. (1983). La succession de Genna Selole (Baunei) dans le cadre de la paléogéographie mésojurassique de la Sardaigne orientale. *Memorie degli Istituti di Geologia e Mineralogia dell'Universita di Padova*, *36*, 117-148.

Domeier, M., & Torsvik, T.H. (2014). Plate tectonics in the late Paleozoic. *Geoscience Frontiers*, *5*(3), 303-350. https://doi.org/10.1016/j.gsf.2014.01.002

Douce, A.E.P. (1993). Titanium substitution in biotite: an empirical model with applications to thermometry, O_2 and H_2O barometries, and consequences for biotite stability. *Chemical Geology*, *108*(1-4), 133-162. https://doi.org/10.1016/0009-2541(93)90321-9

Druguet, E. (2001). Development of high thermal gradients by coeval transpression and magmatism during the Variscan orogen: insights from the Cap de Creus (Eastern Pyrenees). *Bulletin de la Société Géologique de France*, *174*, 585-594.

Dubacq, B., Vidal, O., & De Andrade, V. (2010). Dehydration of dioctahedral aluminous phyllosilicates: thermodynamic modelling and implications for thermobarometric estimates. *Contributions to Mineralogy and Petrology*, *159*(2), 159-174. https://doi.org/10.1007/s00410-009-0421-6

Duretz, T., Schmalholz, S.M., Podladchikov, Y.Y., & Yuen, D.A. (2014). Physics-controlled thickness of shear zones caused by viscous heating: Implications for crustal shear localization. *Geophysical Research Letters*, *41*(14), 4904-4911. https://doi.org/10.1002/2014GL060438

Ellis, M., & Watkinson, A.J. (1987). Orogen-parallel extension and oblique tectonics: The relation between stretching lineations and relative plate motions. *Geology*, *15*(11), 1022-1026. https://doi.org/10.1130/0091-7613(1987)15%3C1022:OEAOTT%3E2.0.CO;2

Elter, F.M., Musumeci, G., & Pertusati, P.C. (1990). Late Hercynian shear zones in Sardinia. *Tectonophysics*, *176*(3-4), 387-404. https://doi.org/10.1016/0040-1951(90)90080-R

Engi, M., Lanari, P., & Kohn, M. J. (2017). Significant ages—An introduction to petrochronology. *Reviews in Mineralogy and Geochemistry*, *83*(1), 1-12. https://doi.org/10.2138/rmg.2017.83.1

Fauconnier, J., Labrousse, L., Andersen, T.B., Beyssac, O., Duprat-Oualid, S., & Yamato, P. (2014). Thermal structure of a major crustal shear zone, the basal thrust in the Scandinavian Caledonides. *Earth and Planetary Science Letters*, *385*, 162-171. https://doi.org/10.1016/j.epsl.2013.10.038

Faure, M., Lardeaux, J.M., & Ledru, P. (2009). A review of the pre-Permian geology of the Variscan French Massif Central. *Comptes rendus géoscience*, *341*(2-3), 202-213. https://doi.org/10.1016/j.crte.2008.12.001

Ferreiro Mählmann, R., Bozkaya, Ö., Potel, S., Le Bayon, R., Šegvić, B., & Nieto, F. (2012). The pioneer work of Bernard Kübler and Martin Frey in very low-grade metamorphic terranes: paleo-geothermal potential of variation in Kübler-Index/organic matter reflectance correlations. A review. *Swiss Journal of Geosciences*, *105*(2), 121-152. https://doi.org/10.1007/s00015-012-0115-3

Flinn, D. (1962). On folding during three-dimensional progressive deformation. *Quarterly Journal of the Geological Society*, *118*(1-4), 385-428. https://doi.org/10.1144/gsjgs.118.1.0385

Forshaw, J.B., & Pattison, D.R. (2021). Ferrous/ferric (Fe^{2+}/Fe^{3+}) partitioning among silicates in metapelites. *Contributions to Mineralogy and Petrology*, *176*(9), 1-26. https://doi.org/10.1007/s00410-021-01814-4

Forshaw, J.B., & Pattison, D.R. (2023). Major-element geochemistry of pelites. *Geology*. https://doi.org/10.1130/G50542.1

Forte, A.M., & Bailey, C.M. (2007). Testing the utility of the porphyroclast hyperbolic distribution method of kinematic vorticity analysis. *Journal of Structural Geology*, *29*(6), 983-1001. https://doi.org/10.1016/j.jsg.2007.01.006

Fossen, H. (2016). *Structural geology*. Cambridge university press. https://doi.org/10.1017/9781107415096

Fossen, H. (2020). Writing papers with an emphasis on structural geology and tectonics: advices and warnings. *Brazilian Journal of Geology*, *49*. https://doi.org/10.1590/2317-4889201920190109

Fossen, H., & Cavalcante, G.C.G. (2017). Shear zones–A review. *Earth-Science Reviews*, *171*, 434-455. https://doi.org/10.1016/j.earscirev.2017.05.002

Fossen, H., & Tikoff, B. (1998). Extended models of transpression and transtension, and application to tectonic settings. *Geological Society, London, Special Publications*, *135*(1), 15-33. https://doi.org/10.1144/GSL.SP.1998.135.01.02

Fossen, H., Tikoff, B., & Teyssier, C. (1994). Strain modeling of transpressional and transtensional deformation. *Norsk geologisk tidsskrift*, *74*(3), 134-145.

Franceschelli, M., Battaglia, S., Cruciani, G., Pasci, S., & Puxeddu, M. (2017). Very low-temperature metamorphism in Ordovician metasedimentary rocks above and below the Sardic unconformity, SW Sardinia, Italy. *International Journal of Earth Sciences*, *106*(2), 531-548. https://doi.org/10.1007/s00531-016-1370-8

Franceschelli, M., Gattiglio, M., Pannuti, F., & Fadda, S. (1992). Illite crystallinity in pelitic rocks from the external and nappe zones of the Hercynian chain of Sardinia. In L., Carmignani, F.P., Sassi (Ed.). *Contributions to the Geology of Italy with special regard to the Paleozoic Basements*. (pp. 127–135) IGCP Project No. 276, Newsletter.

Franceschelli, M., Memmi, I., Pannuti, F., & Ricci, C.A. (1989). Diachronous metamorphic equilibria in the Hercynian basement of northern Sardinia, Italy. *Geological Society, London, Special Publications*, *43*(1), 371-375. https://doi.org/10.1144/GSL.SP.1989.043.01.33

Franceschelli, M., Puxeddu, M., & Cruciani, G. (2005). Variscan metamorphism in Sardinia, Italy: review and discussion. *Journal of the Virtual Explorer*, *19*, 2-36. https://dx.doi.org/10.3809%2Fjvirtex.2005.00121

Franke, W., Cocks, L. R. M., & Torsvik, T. H. (2017). The palaeozoic variscan oceans revisited. *Gondwana research*, *48*, 257-284. https://doi.org/10.1016/j.gr.2017.03.005

Fréville, K., Trap, P., Vanardois, J., Melleton, J., Faure, M., Bruguier, O., Poujol, M., & Lach, P. (2022). Carboniferous-Permian tectono-metamorphic evolution of the Pelvoux Massif (External Crystalline Massif, Western Alps), with discussion on flow kinematics of the Eastern-Variscan Shear Zone. *BSGF-Earth Sciences Bulletin*, *193*, 13. https://doi.org/10.1051/bsgf/2022008

Frey, M. (1987). Very low grade metamorphism of clastic sedimentary rock. In M., Frey (Ed.). *Low temperature metamorphism*. New York: Chapman and Hall.

Frey, M., & Robinson, D. (1999). Low-grade metamorphism. Blackwell Science, Oxford. https://doi.org/10.1002/9781444313345

Fry, N. (1979). Random point distribution and strain measurement in rocks. *Tectonophysics*, *60*, 89-105. https://doi.org/10.1016/0040-1951(79)90135-5

Fu, J., Li, G., Wang, G., Zhang, L., Liang, W., Zhang, X., Jiao, Y., & Dong, S. (2022). Structural and kinematic analysis of the Cuonadong dome, southern Tibet, China: Implications for middle-crust deformation. *Journal of Asian Earth Sciences: X*, *8*, 100112. https://doi.org/10.1016/j.jaesx.2022.100112

Funedda, A. (2009). Foreland- and hinterland-verging structures in fold-and-thrust belt: an example from the Variscan foreland of Sardinia. *International Journal of Earth Sciences*, *98*, 1625-1642. https://doi.org/10.1007/s00531-008-0327-y

Funedda, A., Meloni, M.A., & Loi, A. (2015). Geology of the Variscan basement of the Laconi-Asuni area (central Sardinia, Italy): the core of a regional antiform refolding a tectonic nappe stack. *Journal of Maps*, *11*(1), 146-156. https://doi.org/10.1080/17445647.2014.942396

Funedda, A., Naitza, S., Conti, P., Dini, A., Buttau, C., & Tocco, S. (2011). The geological and metallogenic map of the Baccu Locci mine area (Sardinia, Italy). *Journal of Maps*, *7*(1), 103-114. https://doi.org/10.4113/jom.2011.1134

Furuichi, H., Ujiie, K., Kouketsu, Y., Saito, T., Tsutsumi, A., & Wallis, S. (2015). Vitrinite reflectance and Raman spectra of carbonaceous material as indicators of frictional heating on faults: Constraints from friction experiments. Earth and Planetary Science Letters, *424*, 191-200. https://doi.org/10.1016/j.epsl.2015.05.037

Gaggero, L., Oggiano, G., Funedda, A., & Buzzi, L. (2012). Rifting and arc-related early Paleozoic volcanism along the north Gondwana margin: geochemical and geological evidence from Sardinia (Italy). *The Journal of Geology*, *120*(3), 273-292. https://doi.org/10.1086/664776

Galy, V., Beyssac, O., France-Lanord, C., & Eglinton, T. (2008). Recycling of graphite during Himalayan erosion: A geological stabilization of carbon in the crust. *Science*, *322*(5903), 943-945. http://dx.doi.org/10.1126/science.1161408

Ganne, J., De Andrade, V., Weinberg, R.F., Vidal, O., Dubacq, B., Kagambega, N., Naba, S., Jessell, M., Allibon, J. (2012). Modern-style plate subduction preserved in the Palaeoproterozoic West African craton. *Nature Geoscience*, *5*(1), 60-65. https://doi.org/10.1038/ngeo1321

Gapais, D., Brun, J.P., & Cobbold, P. R. (Eds.). (2005). Deformation mechanisms, rheology and tectonics: from minerals to the lithosphere. Geological Society of London.

Gapais, D., Brun, J.P., Gumiaux, C., Cagnard, F., Ruffet, G., & Le Carlier De Veslud, C. (2015). Extensional tectonics in the Hercynian Armorican belt (France). An overview. *Bulletin de la Société Géologique de France*, *186*(2-3), 117-129. https://doi.org/10.2113/gssgfbull.186.2-3.117

Gattiglio, M., & Oggiano, G. (1990). L'unità tettonica di Bruncu Nieddu ei suoi rapporti con le unità della Sardegna sud-orientale. *Bollettino della Società geologica italiana*, *109*(3), 547-555.

Gébelin, A., Roger, F., & Brunel, M. (2009). Syntectonic crustal melting and high-grade metamorphism in a transpressional regime, Variscan Massif Central, France. *Tectonophysics*, *477*(3-4), 229-243. https://doi.org/10.1016/j.tecto.2009.03.022

Ghosh, P., Bhattacharyya, K., & Parui, C. (2020). Tracking progressive deformation of an orogenic wedge through two successive internal thrusts: Insights from structure, deformation profile, strain, and vorticity of the Main Central thrust (MCT) and the Pelling-Munsiari thrust (PT), Sikkim Himalayan fold thrust belt. *Journal of Structural Geology*, *140*, 104120. https://doi.org/10.1016/j.jsg.2020.104120

Gillam, B.G., Little, T.A., Smith, E., & Toy, V.G. (2013). Extensional shear band development on the outer margin of the Alpine mylonite zone, Tatare Stream, Southern Alps, New Zealand. *Journal of Structural Geology*, *54*, 1-20. https://doi.org/10.1016/j.jsg.2013.06.010

Girault, J.B., Bellahsen, N., Boutoux, A., Rosenberg, C.L., Nanni, U., Verlaguet, A., & Beyssac, O. (2020). The 3-D thermal structure of the Helvetic nappes of the European Alps: Implications for collisional processes. *Tectonics*, *39*(3), e2018TC005334. https://doi.org/10.1029/2018TC005334

Giuntoli, F., Lanari, P., Burn, M., Kunz, B.E., & Engi, M. (2018). Deeply subducted continental fragments–Part 2: Insight from petrochronology in the central Sesia Zone (western Italian Alps). *Solid Earth*, *9*(1), 191-222. https://doi.org/10.5194/se-9-191-2018

Gnoli, M. (1992). Occurrence of Middle-Late Silurian Nautiloids from S. Basilio area (Gerrei, SE Sardinia). Museo Regionale di Scienze Naturali.

Gnoli, M., & Pillola, G. L. (2002). The oldest nautiloid cephalopod of Sardinia: Cameroceras cf. vertebrate (Eichwald, 1860) from the Arenig (Early Ordovician) of Tacconis (South East Sardinia) and remarks on the associated biota. *Neues Jahrbuch für Geologie und Paläontologie-Monatshefte*, 19-26.

Gonçalves, G.O., Lana, C., Scholz, R., Buick, I.S., Gerdes, A., Kamo, S.L., Corfu, F., Marinho, M.M., Chaves, A.O., Valeriano, C., & Nalini, H.A. (2016). An assessment of monazite from the Itamb´e pegmatite district for use as U-Pb isotope reference material for microanalysis and implications for the origin of the “Moacyr” monazite. *Chemical Geology 424*, 30–50. https://doi.org/10.1016/j.chemgeo.2015.12.019

Gordon, T. M. (1992). Generalized thermobarometry: solution of the inverse chemical equilibrium problem using data for individual species. *Geochimica et Cosmochimica Acta*, *56*(5), 1793-1800. https://doi.org/10.1016/0016-7037(92)90310-F

Grasemann, B., Fritz, H., & Vannay, J.C. (1999). Quantitative kinematic flow analysis from the Main Central Thrust Zone (NW-Himalaya, India): implications for a decelerating strain path and the extrusion of orogenic wedges. *Journal of Structural Geology*, *21*(7), 837-853. https://doi.org/10.1016/s0191-8141(99)00077-2

Graveleau, F., Malavieille, J., & Dominguez, S. (2012). Experimental modelling of orogenic wedges: A review. *Tectonophysics*, *538*, 1-66. https://doi.org/10.1016/j.tecto.2012.01.027

Graziani, R., Montomoli, C., Iaccarino, S., Menegon, L., Nania, L. & Carosi, R. (2020). Structural setting of a transpressive shear zone: Insights from geological mapping, quartz petrofabric and kinematic vorticity analysis in NE Sardinia (Italy). *Geological Magazine,* 1–19, https://doi.org/10.1017//S0016756820000138

Grosch, E. G., Vidal, O., Abu-Alam, T., & McLoughlin, N. (2012). P–T constraints on the metamorphic evolution of the Paleoarchean Kromberg type-section, Barberton Greenstone Belt, South Africa. *Journal of Petrology*, *53*(3), 513-545. https://doi.org/10.1093/petrology/egr070

Grujic, D., Ashley, K.T., Coble, M.A., Coutand, I., Kellett, D.A., Larson, K.P., Whipp, D.M. Jr., Gao, M., & Whynot, N. (2020). Deformational temperatures across the Lesser Himalayan Sequence in eastern Bhutan and their implications for the deformation history of the Main Central Thrust. *Tectonics, 39*, e2019TC005914. https://doi.org/10.1029/2019TC005914

Guidotti, C.V. (1984). Micas in metamorphic rocks. *Reviews in Mineralogy and Geochemistry*, *13*(1), 357-467. https://doi.org/10.1515/9781501508820-014

Guidotti, C.V. &, Sassi, F.P. (1998) Miscellaneous isomorphous substitutions in Na-K white micas: a review, with special emphasis to metamorphic micas. *Rendiconti Lincei*, 53, 1689–1699. https://doi.org/10.1017/CBO9781107415324.004

Guidotti, C.V., Yates, M.G., Dyar, M.D., & Taylor, M.E. (1994). Petrogenetic implications of the Fe3+ content of muscovite in pelitic schists. *American Mineralogist, 79*(7-8), 793-795.

Hammerstein, J.A., Di Cuia, R., Cottam, M.A., Zamora, G., & Butler, R.W. (2020). Fold and thrust belts: structural style, evolution and exploration–an introduction. *Geological Society, London, Special Publications*, *490*(1), 1-8. https://doi.org/10.1144/SP490-2020-81

Hansberry, R.L., King, R., Collins, A.S., & Morley, C.K. (2014). Complex structure of an upper-level shale detachment zone: Khao Khwang fold and thrust belt, Central Thailand. *Journal of Structural Geology*, *67*, 140-153. https://doi.org/10.1016/j.jsg.2014.07.016

Harland, W.B. (1971). Tectonic transpression in Caledonian Spitzbergen. *Geological Magazine*, *108*, 27-42. https://doi.org/10.1017/S0016756800050937

Henk, A. (1997). Gravitational orogenic collapse vs plate-boundary stresses: a numerical modelling approach to the Permo-Carboniferous evolution of Central Europe. *Geologische Rundschau*, *86*(1), 39-55. https://doi.org/10.1007/s005310050120

Henry, D.J., Guidotti, C.V., & Thomson, J.A. (2005). The Ti-saturation surface for low-to-medium pressure metapelitic biotites: Implications for geothermometry and Ti-substitution mechanisms. *American Mineralogist*, *90*(2-3), 316-328. https://doi.org/10.2138/am.2005.1498

Henry, D.G., Jarvis, I., Gillmore, G., & Stephenson, M. (2019). Raman spectroscopy as a tool to determine the thermal maturity of organic matter: Application to sedimentary, metamorphic and structural geology. *Earth-Science Reviews*, *198*, 102936. https://doi.org/10.1016/j.earscirev.2019.102936

Herviou, C., Agard, P., Plunder, A., Mendes, K., Verlaguet, A., Deldicque, D., & Cubas, N. (2022). Subducted fragments of the Liguro-Piemont ocean, Western Alps: Spatial correlations and offscraping mechanisms during subduction. *Tectonophysics*, *827*, 229267. https://doi.org/10.1016/j.tecto.2022.229267

Hirth, G., Teyssier, C., & Dunlap, J.W. (2001). An evaluation of quartzite flow laws based on comparisons between experimentally and naturally deformed rocks. *International Journal of Earth Sciences*, *90*(1), 77-87. https://doi.org/10.1007/s005310000152

Holland, T.J.B., & Powell, R. (1998). An internally consistent thermodynamic data set for phases of petrological interest. *Journal of metamorphic Geology*, *16*(3), 309-343. https://doi.org/10.1111/j.1525-1314.1998.00140.x

Holland, T.J.B., & Powell, R. (2010). Using equilibrium thermodynamics to understand metamorphism and metamorphic rocks. *Elements*, 6(5), 309-314. https://doi.org/10.2113/gselements.6.5.309

Holland, T.J.B., & Powell, R. (2011). An improved and extended internally consistent thermodynamic dataset for phases of petrological interest, involving a new equation of state for solids. *Journal of metamorphic Geology*, *29*(3), 333-383. https://doi.org/10.1111/j.1525-1314.2010.00923.x

Holland, T.J.B., Green, E.C.R., & Powell, R. (2021). A thermodynamic model for feldspars in $KAlSi_3O_8$− $NaAlSi_3O_8$− $CaAl_2Si_2O_8$ for mineral equilibrium calculations. *Journal of Metamorphic Geology*, *40*(4), 587-600. https://doi.org/10.1111/jmg.12639

Horstwood, M.S.A., Foster, G.L., Parrish, R.R., Noble, S.R., & Nowell, G.M. (2003). Common-Pb corrected in situ U-Pb accessory mineral geochronology by LA-MC-ICP-MS. Journal of Analytical Atomic Spectrometry, 18:837–846. https://doi.org/10.1039/b304365g

Hudleston, P.J. (1977). Similar folds, recumbent folds, and gravity tectonics in ice and rocks. *The Journal of Geology*, *85*(1), 113-122. https://doi.org/10.1086/628272

Iaccarino, S., Montomoli, C., Montemagni, C., Massonne, H. –J., Langone, A., Jain, A.K., Visona, D., & Carosi, R. (2020). The main central thrust zone along the Alaknanda and Dhauli Ganga valleys (Garhwal Himalaya, NW India): Insights into an inverted metamorphic sequence. *Lithos, 372-373*, 105669. https://doi.org/10.1016/j.lithos.2020.105669

Iacopini, D., Carosi, R., Montomoli, C., & Passchier, C.W. (2008). Strain analysis and vorticity of flow in the Northern Sardinian Variscan Belt: recognition of a partitioned oblique deformation event. *Tectonophysics*, *446*(1-4), 77-96. https://doi.org/10.1016/j.tecto.2007.10.002

Iacopini, D., Frassi, C., Carosi, R., & Montomoli, C. (2011). Biases in three-dimensional vorticity analysis using porphyroclast system: limits and application to natural examples. *Geological Society, London, Special Publications*, *360*(1), 301-318. https://doi.org/10.1144/SP360.17

Jaboyedoff, M., Bussy, F., Kübler, B., & Thelin, P. (2001). Illite “crystallinity” revisited. *Clays and clay minerals*, *49*(2), 156-167. https://doi.org/10.1346/CCMN.2001.0490205

Jacob, J.B., Guillot, S., Rubatto, D., Janots, E., Melleton, J., & Faure, M. (2021). Carboniferous high-P metamorphism and deformation in the Belledonne Massif (Western Alps). *Journal of metamorphic geology*, *39*(8), 1009-1044. https://doi.org/10.1111/jmg.12600

Jamieson, R.A., & Beaumont, C. (2013). On the origin of orogens. *GSA Bullettin*, *125*, 1671-1702. https://doi.org/10.1130/B30855.1

Jamieson, R.A., Beaumont, C., Fullsack, P., & Lee, B. (1998). Barrovian regional metamorphism: where’s the heat?. *Geological Society, London, Special Publications*, *138*(1), 23-51. https://doi.org/10.1144/GSL.SP.1996.138.01.03

Jamieson, R.A., Beaumont, C., Fullsack, P., Treloar, P.J., & O'Brien, P. (1998). What controls regional metamorphism in orogens? Insights from thermal and mechanical models. *Electronic Geosciences*.

Jamieson, R.A., Beaumont, C., Hamilton, J., & Fullsack, P. (1996). Tectonic assembly of inverted metamorphic sequences. *Geology*, *24*(9), 839-842. https://doi.org/10.1130/0091-7613(1996)024%3C0839:TAOIMS%3E2.3.CO;2

Jamieson, R.A., Beaumont, C., Nguyen, M.H., & Lee, B. (2002). Interaction of metamorphism, deformation and exhumation in large convergent orogens. *Journal of Metamorphic Geology*, *20*(1), 9-24. https://doi.org/10.1046/j.0263-4929.2001.00357.x

Jaquet, Y., Duretz, T., Grujic, D., Masson, H., & Schmalholz, S.M. (2018). Formation of orogenic wedges and crustal shear zones by thermal softening, associated topographic evolution and application to natural orogens. *Tectonophysics*, *746*, 512-529. https://doi.org/10.1016/j.tecto.2017.07.021

Jessup, M.J., Law, R.J., & Frassi, C. (2007). The Rigid Grain Net (RGN): An alternative method for estimating mean kinematic vorticity number (Wm). *Journal of Structural Geology*, *29*, 411–421. https://doi.org/10.1016/j.jsg.2006.11.003

Johnston, S.T., Weil, A.B., & Gutiérrez-Alonso, G. (2013). Oroclines: Thick and thin. *Bulletin*, *125*(5-6), 643-663. https://doi.org/10.1130/B30765.1

Kaneki, S., Hirono, T., Mukoyoshi, H., Sampei, Y., & Ikehara, M. (2016). Organochemical characteristics of carbonaceous materials as indicators of heat recorded on an ancient plate-subduction fault. *Geochemistry, Geophysics, Geosystems*, *17*(7), 2855-2868. https://doi.org/10.1002/2016GC006368

Kedar, L., Bond, C., & Muirhead, D. (2020). Carbon ordering in an aseismic shear zone: implications for crustal weakening and Raman spectroscopy. In *EGU General Assembly Conference Abstracts* (pp. 9155). https://doi.org/10.5194/egusphere-egu2020-9155

Keller, L.M., De Capitani, C., & Abart, R. (2005). A quaternary solution model for white micas based on natural coexisting phengite–paragonite pairs. *Journal of Petrology*, *46*(10), 2129-2144. https://doi.org/10.1093/petrology/egi050

Kitamura, M., Mukoyoshi, H., Fulton, P.M., & Hirose, T. (2012). Coal maturation by frictional heat during rapid fault slip. *Geophysical research letters*, *39*(16). https://doi.org/10.1029/2012gl052316

Kohn, M.J., & Spear, F.S. (1991). Error propagation for barometers: 2. Application to rocks. *American Mineralogist*, *76*(1-2), 138-147.

Kohn, M.J. (2014). "Thermoba-Raman-try": Calibration of spectroscopic barometers and thermometers for mineral inclusions. *Earth and Planetary Science Letters*, *388*, 187-196. https://doi.org/10.1016/j.epsl.2013.11.054

Kohn, M.J., Engi, M., Lanari, P. (2017). *Petrochronology: Methods and Applications*. De Gruyter: Berlin, Germany, 2017; Volume 83. https://doi.org/10.1515/9783110561890

Konstantinovskaya, E.A., & Malavieille, J. (2005). Accretionary Orogens: Erosion and Exhumation. *Geotectonics*, *39*, 69-86.

Konstantinovskaya, E.A., & Malavieille, J. (2011). Thrust wedges with décollement levels and syntectonic erosion: A view from analog models. *Tectonophysics*, 502(3-4), 336-350. https://doi.org/10.1016/j.tecto.2011.01.020

Kouketsu, Y., Miyake, A., Igami, Y., Taguchi, T., Kagi, H., & Enami, M. (2019). Drastic effect of shearing on graphite microtexture: attention and application to Earth science. Prog. *Earth and Planetary Science Letters*, *6*, 23. https://doi.org/10.1186/s40645-019-0271-4

Kouketsu, Y., Mizukami, T., Mori, H., Endo, S., Aoya, M., Hara, H., Nakamura, D., & Wallis, S. (2014). Raman CM geothermometer using FWHM. *Island Arc, 23*, 33-50. https://doi.org/10.1111/iar.12057

Kříbek, B., Sýkorová, I., Machovič, V., & Laufek, F. (2008). Graphitization of organic matter and fluid-deposited graphite in Palaeoproterozoic (Birimian) black shales of the Kaya-Goren greenstone belt (Burkina Faso, West Africa). *Journal of Metamorphic Geology*, *26*, 937-958. https://doi.org/10.1111/j.1525-1314.2008.00796.x

Krýza, O., Závada, P., & Lexa, O. (2019). Advanced strain and mass transfer analysis in crustal-scale oroclinal buckling and detachment folding analogue models. *Tectonophysics*, *764*, 88-109. https://doi.org/10.1016/j.tecto.2019.05.001

Kuo, L.W., Huang, J.R., Fang, J.N., Si, J., Song, S.R., Li, H., & Yeh, E.C. (2018). Carbonaceous materials in the fault zone of the longmenshan fault belt: 2. Characterization of fault gouge from deep drilling and implications for fault maturity. *Minerals*, *8*(9), 393. https://doi.org/10.3390/min8100457

Kuo, L.-W., Di Felice, F., Spagnuolo, E., Di Toro, G., Song, S.-R., Aretusini, S., Li, H., Suppe, J., Si, J., & Wen, C.-Y. (2017). Fault gouge graphitization as evidence of past seismic slip. *Geology*, *45*(11), 979-982. https://doi.org/10.1130/G39295.1

Kurz, G.A., & Northrup, C.J. (2008). Structural analysis of mylonitic rocks in the Cougar Creek Complex, Oregon–Idaho using the porphyroclast hyperbolic distribution method, and potential use of SC′-type extensional shear bands as quantitative vorticity indicators. *Journal of Structural Geology*, *30*(8), 1005-1012. https://doi.org/10.1016/j.jsg.2008.04.003

Lahfid, A., Baidder, L., Ouanaimi, H., Soulaimani, A., Hoepffner, C., Farah, A., Omar, S., & Michard, A. (2019). From extension to compression: high geothermal gradient during the earliest Variscan phase of the Moroccan Meseta; a first structural and RSCM thermometric study. *European Journal of Mineralogy*, *31*(4), 695-713. https://doi.org/10.1127/ejm/2019/0031-2882

Lahfid, A., Beyssac, O., Deville, E., Negro, F., Chopin, C., & Goffé, B. (2010). Evolution of the Raman spectrum of carbonaceous material in low-grade metasediments of the Glarus Alps (Switzerland). *Terra nova*, *22*(5), 354-360. https://doi.org/10.1111/j.1365-3121.2010.00956.x

Lanari, P. (2012). *Micro-cartographie PT-» dans les roches métamorphiques. Applications aux Alpes et à l'Himalaya* (Doctoral dissertation, Université de Grenoble),534 pp.

Lanari, P., & Duesterhoeft, E. (2019). Modeling metamorphic rocks using equilibrium thermodynamics and internally consistent databases: Past achievements, problems and perspectives. *Journal of Petrology*, *60*(1), 19-56. https://doi.org/10.1093/petrology/egy105

Lanari, P., & Engi, M. (2017). Local bulk composition effects on metamorphic mineral assemblages. *Reviews in Mineralogy and Geochemistry*, *83*(1), 55-102. https://doi.org/10.2138/rmg.2017.83.3

Lanari, P., & Hermann, J. (2021). Iterative thermodynamic modelling—Part 2: Tracing equilibrium relationships between minerals in metamorphic rocks. *Journal of metamorphic geology*, *39*(6), 651-674. https://doi.org/10.1111/jmg.12575

Lanari, P., Giuntoli, F., Loury, C., Burn, M., & Engi, M. (2017). An inverse modeling approach to obtain P–T conditions of metamorphic stages involving garnet growth and resorption. *European Journal of Mineralogy*, *29*(2), 181-199. https://doi.org/10.1127/ejm/2017/0029-2597

Larson, K.P., Godin, L., Davis, W.J., & Davis, D.W. (2010). Relationships between displacement and distortion in orogens: linking the Himalayan foreland and hinterland in central Nepal.*GSA Bulletin*, *122*, 1116-1134. https://doi.org/10.1130/b30073.1

Lanari, P., Guillot, S., Schwartz, S., Vidal, O., Tricart, P., Riel, N., & Beyssac, O. (2012). Diachronous evolution of the alpine continental subduction wedge: evidence from P–T estimates in the Briançonnais Zone houillère (France–Western Alps). *Journal of Geodynamics*, *56*, 39-54. https://doi.org/10.1016/j.jog.2011.09.006

Lanari, P., Riel, N., Guillot, S., Vidal, O., Schwartz, S., Pêcher, A., & Hattori, K.H. (2013). Deciphering high-pressure metamorphism in collisional context using microprobe mapping methods: Application to the Stak eclogitic massif (northwest Himalaya). *Geology*, *41*(2), 111-114. https://doi.org/10.1130/G33523.1

Lanari, P., Vidal, O., De Andrade, V., Dubacq, B., Lewin, E., Grosch, E.G., & Schwartz, S. (2014). XMapTools: A MATLAB©-based program for electron microprobe X-ray image processing and geothermobarometry. *Computers & Geosciences*, *62*, 227-240. https://doi.org/10.1016/j.cageo.2013.08.010

Law, R.D. (2014). Deformation thermometry based on quartz c-axis fabrics and recrystallization microstructures: A review. *Journal of Structural Geology*, *66*, 129-161. https://doi.org/10.1016/j.jsg.2014.05.023

Law, R.D., Searle, M.P., & Simpson, R.L. (2004). Strain, deformation temperatures and vorticity of flow at the top of the Greater Himalayan Slab, Everest Massif, Tibet. *Journal of the Geological Society, 161*, 305-320. https://doi.org/10.1144/0016-764903-047

Law, R.D., Thigpen, J.R., Mazza, S.E., Mako, C.A., Krabbendam, M., Spencer, B.M., Ashley, K.T., Strachan, R.A., & Davis, E.F. (2021). Tectonic Transport Directions, Shear Senses and Deformation Temperatures Indicated by Quartz c-Axis Fabrics and Microstructures in a NW-SE Transect across the Moine and Sgurr Beag Thrust Sheets, Caledonian Orogen of Northern Scotland. *Geosciences*, *11*, 411. https://doi.org/10.3390/geosciences11100411

Leever, K.A., Gabrielsen, R.H., Sokoutis, D., & Willingshofer, E. (2011). The effect of convergence angle on the kinematic evolution of strain partitioning in transpressional brittle wedges: Insight from analog modeling and high-resolution digital image analysis. *Tectonics*, *30*(2). https://doi.org/10.1029/2010TC002823

Lister, G.S., & Davis, G.A. (1989). The origin of metamorphic core complexes and detachment faults formed during Tertiary continental extension in the northern Colorado River region, USA. *Journal of Structural Geology*, *11*(1-2), 65-94. https://doi.org/10.1016/0191-8141(89)90036-9

Lister, G.S., Forster, M.A., & Rawling, T.J. (2001). Episodicity during orogenesis. *Geological Society, London, Special Publications*, *184*(1), 89-113. https://doi.org/10.1144/GSL.SP.2001.184.01.06

Loi, A. (1993). Sedimentological-petrographical study and paleogeographical approach of the Upper Ordovician of the central southern Sardinia. *Plinius*, *9*, 81-86.

Loi, A., & Dabard, M.P. (1997). Zircon typology and geochemistry in the palaeogeographic reconstruction of the Late Ordovician of Sardinia (Italy). *Sedimentary Geology*, *112*, 3-4, 263-279. https://doi.org/10.1016/S0037-0738(97)00038-9

Loi, A., Barca, S., Chauvell, J.J., Dabard, M.P., & Leone, F. (1992). The Punta Sepeddì Formation near Dolianova (Sarrabus—SE Sardinia) recent petrographical and geochemical data. In L., Carmignani, F.P., Sassi (Ed.). *Contribution to the Geology of Italy with special regard to the Paleozoic basement*. *A volume dedicated to Tommaso Cocozza* (Vol. 5, pp. 163–166, Newsletter). Siena: IGCP Project No. 276.

Loi, A., Cocco, F., Oggiano, G., Funedda, A., Vidal, M., Ferretti, A., Leone, F., Barca, S., Naitza, S., Ghienne, J.-F., & Pillola, G.L. (2023). The Ordovician of Sardinia (Italy): from the "Sardic Phase" to the end-Ordovician glaciation, palaeogeography and geodynamic context. *Geological Society, London, Special Publications*, *532*(1), SP532-2022. https://doi.org/10.1144/SP532-2022-121

Long, S.P., & Robinson, D.M. (2021). Construction of the Lesser Himalayan–Subhimalayan thrust belt: The primary driver of thickening, exhumation, and high elevations in the Himalayan orogen since the middle Miocene. *Geology*, *49*(11), 1283-1288. https://doi.org/10.1130/G48967.1

Long, S.P., Gordon, S.M., Young, J.P., & Soignard, E. (2016). Temperature and strain gradients through Lesser Himalayan rocks and across the Main Central thrust, south central Bhutan: Implications for transport-parallel stretching and inverted metamorphism. *Tectonics*, *35*, 1863-1891. https://doi.org/10.1002/2016TC004242

Long, S.P., McQuarrie, N., Tobgay, T., & Grujic, D. (2011). Geometry and crustal shortening of the Himalayan fold-thrust belt, eastern and central Bhutan. *Bulletin*, *123*(7-8), 1427-1447. https://doi.org/10.1130/B30203.1

Ludwig, K.R. (2003). Isoplot/Ex Version 3.00: A Geochronological Toolkit for Microsoft Excel; Berkeley Geochronology Center: Berkeley, CA, USA, 2003.

Lünsdorf, N.K., Dunkl, I., Schmidt, B.C., Rantitsch, G., & Von Eynatten, H. (2014). Towards a higher comparability of geothermometric data obtained by Raman spectroscopy of carbonaceous material. Part I: evaluation of biasing factors. *Geostandards and Geoanalytical Research*, *38*, 73-94. https://doi.org/10.1111/j.1751-908X.2013.12011.x

Lünsdorf, N.K., Dunkl, I., Schmidt, B.C., Rantitsch, G., & Von Eynatten, H. (2017). Towards a higher comparability of geothermometric data obtained by Raman spectroscopy of carbonaceous material. Part 2: A revised geothermometer. *Geostandards and Geoanalytical Research, 41*(4), 593-612. https://doi.org/10.1111/ggr.12178

Lyu, M., Cao, S., Neubauer, F., Li, J., & Cheng, X. (2020). Deformation fabrics and strain localization mechanisms in graphitic carbon-bearing rocks from the Ailaoshan-Red River strike-slip fault zone. *Journal of Structural Geology*, *140*, 104150. https://doi.org/10.1016/j.jsg.2020.104150

Macedo, J., & Marshak, S. (1999). Controls on the geometry of fold-thrust belt salients. *Geological Society of America Bulletin*, *111*(12), 1808-1822. https://doi.org/10.1130/0016-7606(1999)111%3C1808:COTGOF%3E2.3.CO;2

Maino, M., Casini, L., Ceriani, A., Decarlis, A., Di Giulio, A., Seno, S., Setti, M., & Stuart, F. (2015). Dating shallow thrusts with zircon (U-Th)/ He thermochronometry - The shear heating connection. *Geology*, *43*(6), 495-498. https://doi.org/10.1130/G36492.1

Mako, C.A., Caddick, M.J. (2018). Quantifying magnitudes of shear heating in metamorphic systems. *Tectonophysics*, *744*, 499-517. https://doi.org/10.1016/j.tecto.2018.07.003

Malavieille, J., Dominguez, S., Lu, C.-Y., Chen, C.-T., & Konstantinovskaya, E. (2019). Deformation partitioning in mountain belts: insights from analogue modelling experiments and the Taiwan collisional orogen. *Geological Magazine*, *158*(1), 1-20. https://doi.org/10.1017/S0016756819000645

Malavieille, J., Lacassin, R., & Mattauer, M. (1984). Signification tectonique des linéations d'allongement dans les Alpes occidentales. *Bull. Soc. Geol. Fr*, *26*, 895-906.

Massonne, H.J. (1992). Evidence for low-temperature ultrapotassic siliceous fluids in subduction zone environments from experiments in the system K_2O-MgO-Al_2O_3-SiO_2-H_2O (KMASH). *Lithos*, *28*(3-6), 421-434. https://doi.org/10.1016/0024-4937(92)90017-S

Massonne, H.J., & Schreyer, W. (1987). Phengite geobarometry based on the limiting assemblage with K-feldspar, phlogopite, and quartz. *Contributions to mineralogy and petrology*, *96*(2), 212-224. https://doi.org/10.1007/BF00375235

Massonne, H.J., & Schreyer, W. (1989). Stability field of the high-pressure assemblage, talc+ phengite and two new phengite barometers. *European Journal of Mineralogy*, *1*(3), 391-410. https://doi.org/10.1127/ejm/1/3/0391

Matte, P. (1998). Continental subduction and exhumation of HP rocks in Paleozoic orogenic belts: Uralides and Variscides. *GFF*, *120*(2), 209–222. https://doi.org/10.1080/11035899801202209

Matte, P. (2001). The Variscan collage and orogeny (480–290 ma) and the tectonic definition of the Armorica microplate: a review. *Terra Nova*, *13*, 117–121. https://doi.org/10.1046/j.1365-3121.2001.00327.x

McQuarrie, N., Tobgay, T., Long, S.P., Reiners, P.W., & Cosca, M.A. (2014). Variable exhumation rates and variable displacement rates: Documenting recent slowing of Himalayan shortening in western Bhutan. *Earth and Planetary Science Letters*, *386*, 161-174. https://doi.org/10.1016/j.epsl.2013.10.045

Meloni, M.A., Oggiano, G., Funedda, A., Pistis, M., & Linnemann, U. (2017). Tectonics, ore bodies, and gamma-ray logging of the Variscan basement, southern Gennargentu massif (central Sardinia, Italy). *Journal of Maps*, *13*(2), 196-206. https://doi.org/10.1080/17445647.2017.1287601

Merriman, R., & Frey, M. (1999). Patterns of very low-grade metamorphism in metapelitic rocks. In D., Robinson, M., Frey (Ed.). *Low-grade metamorphism*. Blackwell Science, Oxford.

Merriman, R., & Peacor, D.R. (1999). Very low-grade metapelites: mineralogy, microfabrics and measuring reaction progress. In D., Robinson, M., Frey (Ed.). *Low-grade metamorphism*. Blackwell Science, Oxford.

Merriman, R. J., Roberts, B., Peacor, D. R., & Hirons, S. R. (1995). Strain-related differences in the crystal growth of white mica and chlorite: a TEM and XRD study of the development of metapelitic microfabrics in the Southern Uplands thrust terrane, Scotland. *Journal of Metamorphic Geology*, *13*(5), 559-576. https://doi.org/10.1111/j.1525-1314.1995.tb00243.x

Minzoni, N. (1975). La serie delle successioni paleozoiche a sud del Gennargentu. *Bollettino della Società Geologica Italiana*, *94*, 347-392.

Mitra, G. (1994). Strain variation in thrust sheets across the Sevier fold-and-thrust belt (Idaho-Utah-Wyoming): Implications for section restoration and wedge taper evolution. *Journal of Structural Geology*, *16*(4), 585-602. https://doi.org/10.1016/0191-8141(94)90099-X

Mitra, G., Bhattacharyya, K., & Mukul, M. (2010). The lesser Himalayan duplex in Sikkim: implications for variations in Himalayan shortening. *Journal of the Geological Society of India*, *75*(1), 289-301. https://doi.org/10.1007/s12594-010-0016-x

Molli, G., Vitale Brovarone, A., Beyssac, O., & Cinquini, I. (2018). RSCM thermometry in the Alpi Apuane (NW Tuscany, Italy): New constraints for the metamorphic and tectonic history of the inner northern Apennines. *Journal of Structural Geology, 113*, 200-216. https://doi.org/10.1016/j.jsg.2018.05.020

Molnar, P., & England, P. (1990). Temperatures, heat flux, and frictional stress near major thrust faults. *Journal of Geophysical Research: Solid Earth*, *95*(B4), 4833-4856. https://doi.org/10.1029/JB095iB04p04833

Montel, J.M., Razafimahatratra, D., de Parseval, P., Poitrasson, F., Moine, B., Seydoux-Guillaume, A.M., Pik, R., Arnaud, N., & Gibert, F. (2018). The giant monazite crystals from Manangotry (Madagascar). *Chemical Geology*, *484*, 36-50. https://doi.org/10.1016/j.chemgeo.2017.10.034

Montési, L.G. (2013). Fabric development as the key for forming ductile shear zones and enabling plate tectonics. *Journal of Structural Geology*, *50*, 254-266. https://doi.org/10.1016/j.jsg.2012.12.011

Montmartin, C., Faure, M., & Raimbourg, H. (2021). Paleotemperature investigation of the Variscan southern external domain: the case of the Montagne Noire (France). *BSGF-Earth Sciences Bulletin*, *192*(1), 3. http://dx.doi.org/10.1051/bsgf/2020043

Montomoli, C. (2003). Zone di taglio fragili-duttili nel basamento varisico metamorfico di basso grado della Nurra meridionale (Sardegna nord-occidentale). *Atti della Società Toscana di Scienze Naturali, Serie A*, *108*, 23-29.

Montomoli, C., Iaccarino, S., Simonetti, M., Lezzerini, M., & Carosi, R. (2018). Structural setting, kinematics and metamorphism in a km-scale shear zone in the inner nappes of Sardinia (Italy). *Italian Journal of Geoscience*, *137*, 294-310. https://doi.org/10.3301/IJG.2018.16

Mori, H., Mori, N., Wallis, S., Westaway, R., & Annen, C. (2017). The importance of heating duration for Raman CM thermometry: evidence from contact metamorphism around the Great Whin Sill intrusion, UK. *Journal of Metamorphic Geology*, *35*(2), 165-180. https://doi.org/10.1111/jmg.12225

Moris-Muttoni, B., Raimbourg, H., Augier, R., Champallier, R., & Le Trong, E. (2022). The impact of melt versus mechanical wear on the formation of pseudotachylyte veins in accretionary complexes. *Scientific reports*, *12*(1), 1-12. https://doi.org/10.1038/s41598-022-05379-5

Muirhead, D.K., Kedar, L., Schito, A., Corrado, S., Bond, C.E., & Romano, C. (2021). Raman spectral shifts in naturally faulted rocks. *Geochemistry, Geophysics, Geosystems*, *22*(10), e2021GC009923. https://doi.org/10.1029/2021GC009923

Musumeci, G. (1992). Ductile wrench tectonics and exhumation of hercynian metamorphic basement in Sardinia: Monte Grighini Complex. *Geodinamica Acta*, *5*(1-2), 119-133. https://doi.org/10.1080/09853111.1992.11105223

Musumeci, G., Spano, M. E., Cherchi, G. P., Franceschelli, M., Pertusati, P. C., & Cruciani, G. (2015). Geological map of the Monte Grighini Variscan Complex (Sardinia, Italy). *Journal of Maps*, *11*(2), 287-298. https://doi.org/10.1080/17445647.2014.924441

Miyashiro, A. (1961). Evolution of metamorphic belts. *Journal of petrology*, *2*(3), 277-311. https://doi.org/10.1093/petrology/2.3.277

Nabavi, S.T., Alavi, S.A., Díaz-Azpiroz, M., Mohammadi, S., Ghassemi, M.R., Fernàndez, C., Barcos, L., & Frehner, M. (2020). Deformation Mechanics in Inclined, Brittle-Ductile Transpression Zones: Insights from 3D Finite Element Modelling. *Journal of Structural Geology*, *137*, 104082. https://doi.org/10.1016/j.jsg.2020.104082

Nabavi, S.T., Alavi, S.A., Mohammadi, S., Ghassemi, M.R., & Frehner, M. (2017). Analysis of transpression within contractional fault steps using finite-element method. *Journal of Structural Geology*, *96*, 1-20. https://doi.org/10.1016/j.jsg.2017.01.004

Nakamura, Y., Oohashi, K., Toyoshima, T., Satish-Kumar, M., & Akai, J. (2015). Strain-induced amorphization of graphite in fault zones of the Hidaka metamorphic belt, Hokkaido, Japan. *Journal of Structural Geology*, *72*, 142-161. https://doi.org/10.1016/j.jsg.2014.10.012

Nakamura, Y., Yoshino, T., & Satish-Kumar, M. (2017). An experimental kinetic study on the structural evolution of natural carbonaceous material to graphite. *American Mineralogist*, *102*, 135–148. https://doi.org/10.2138/am-2017-5733

Nakamura, Y., Yoshino, T., & Satish-Kumar, M. (2020). Pressure dependence of graphitization: implications for rapid recrystallization of carbonaceous material in a subduction zone. *Contributions to Mineralogy and Petrology*, *175*(4), 1-14. https://doi.org/10.1007/s00410-020-1667-2

Nania, L., Montomoli, C., Iaccarino, S., Di Vincenzo, G., & Carosi, R. (2022). A thermal event in the Dolpo region (Nepal): a consequence of the shift from orogen perpendicular to orogen parallel extension in central Himalaya?. *Journal of the Geological Society*, *179*(1). https://doi.org/10.1144/jgs2020-261

Naud, G. (1979). Les shales de Rio Canoni, formation-repère fossilifère dans l'Ordovicien supérieur de Sardaigne orientale. Conséquences stratigraphiques et structurales. *Bulletin de la Société Géologique de France*, *21*(2), 155-159.

Nibourel, L., Berger, A., Egli, D., Heuberger, S., & Herwegh, M. (2021). Structural and thermal evolution of the eastern Aar Massif: insights from structural field work and Raman thermometry. *Swiss journal of geosciences*, *114*(1), 1-43. https://doi.org/10.1186/s00015-020-00381-3

Oggiano, G. (1994). Lineamenti stratigrafico-strutturali del basamento del Goceano (Sardegna centro-settentrionale). *Bollettino della Società Geologica Italiana*, *113*(1), 105-115.

Oggiano, G., Funedda, A., Carmignani, L., & Pasci, S. (2009). The Sardinia-Corsica microplate and its role in the Northern Apennine Geodynamics: new insights from the Tertiary intraplate strike-slip tectonics of Sardinia. *Italian Journal of Geosciences*, *128*(2), 527-539. https://doi.org/10.3301/IJG.2009.128.2.527

Oggiano, G., Funedda, A., Carmignani, L., & Pasci, S. (2011). Reply to: Discussion on «The Sardinia-Corsica microplate and its role in the Northern Apennine Geodynamics: new insights from the Tertiary intraplate strike-slip tectonics of Sardinia» by Igino Dieni & Francesco Massari. *Italian Journal of Geosciences*, *130*(1), 139-143. https://doi.org/10.3301/IJG.2010.26

Oggiano, G., Gaggero, L., Funedda, A., Buzzi, L., & Tiepolo, M. (2010). Multiple early Paleozoic volcanic events at the northern Gondwana margin: U–Pb age evidence from the Southern Variscan branch (Sardinia, Italy), *Gondwana Research*, *17*, 44-58. https://doi.org/10.1016/j.gr.2009.06.001

Oriolo, S., Schulz, B., Hueck, M., Oyhantçabal, P., Heidelbach, F., Sosa, G., van der Kerkhof, A., Wemmer, K., Fossen, H., Druget, E., Walter, J., Cavalcante, C., & Siegesmund, S. (2022). The petrologic and petrochronologic record of progressive vs polyphase deformation: Opening the analytical toolbox. *Earth-Science Reviews*, 104235. https://doi.org/10.1016/j.earscirev.2022.104235

Padovano, M., Dörr, W., Elter, F.M., & Gerdes, A. (2014). The east Variscan shear zone: geochronological constraints from the Capo Ferro area (NE Sardinia, Italy). *Lithos*, *196*, 27-41. https://doi.org/10.1016/j.lithos.2014.01.015.

Padovano, M., Elter, F. M., Pandeli, E., & Franceschelli, M. (2012). The East Variscan Shear Zone: new insights into its role in the Late Carboniferous collision in southern Europe. *International Geology Review*, *54*(8), 957-970. https://doi.org/10.1080/00206814.2011.626120.

Palin, R.M., Weller, O.M., Waters, D.J., & Dyck, B. (2016). Quantifying geological uncertainty in metamorphic phase equilibria modelling; a Monte Carlo assessment and implications for tectonic interpretations. *Geoscience Frontiers*, *7*(4), 591-607. https://doi.org/10.1016/j.gsf.2015.08.005

Pan, R., Macris, C.A., & Menold, C.A. (2020). Thermodynamic modeling of high-grade metabasites: a case study using the Tso Morari UHP eclogite. *Contributions to Mineralogy and Petrology, 175*(8), 1-28. https://doi.org/10.1007/s00410-020-01717-w

Papeschi, S., Iaccarino, S., & Montomoli, C. (2020). Underthrusting and exhumation of continent-derived units within orogenic wedge: An example from the Northern Apennines (Italy). *Journal of Maps*, *16*(2), 638-650. https://doi.org/10.1080/17445647.2020.1795736

Parra, T., Vidal, O., & Jolivet, L. (2002). Relation between the intensity of deformation and retrogression in blueschist metapelites of Tinos Island (Greece) evidenced by chlorite–mica local equilibria. *Lithos*, *63*(1-2), 41-66. https://doi.org/10.1016/S0024-4937(02)00115-9

Parra, T., Vidal, O., & Theye, T. (2005). Experimental data on the Tschermak substitution in Fe-chlorite. *American Mineralogist*, *90*(2-3), 359-370. https://doi.org/10.2138/am.2005.1556

Parrish, R.R. (1990). U–Pb dating of monazite and its application to geological problems. *Canadian Journal of Earth Sciences*, *27*(11), 1431-1450. https://doi.org/10.1139/e90-152

Parui, C., Bhattacharyya, K., & Ghosh, P. (2022). Penetrative strain and partitioning of convergence-related shallow crustal shortening, across scales, in the Lesser-and Sub-Himalayan thrusts: Insights from the eastern Himalaya, Sikkim. *Tectonics*, e2022TC007210. https://doi.org/10.1029/2022TC007210

Passchier, C. W. (1987). Stable positions of rigid objects in non-coaxial flow—a study in vorticity analysis. *Journal of Structural Geology*, *9*(5-6), 679-690. https://doi.org/10.1016/0191-8141(87)90152-0

Passchier, C.W., & Williams, P.R. (1996). Conflicting shear sense indicators in shear zones; the problem of non-ideal sections. *Journal of Structural Geology*, *18*(10), 1281-1284. https://doi.org/10.1016/S0191-8141(96)00051-X

Passchier, C.W., & Trouw, R.A.J. (2005). Microtectonics. Springer, Berlin, Heidelberg, pp. 366. https://doi.org/10.1007/3-540-29359-0

Paton, C., Hellstrom, J., Paul, B., Woodhead, J., & Hergt, J. (2011). Iolite: Freeware for the visualisation and processing of mass spectrometric data. *Journal of Analytical Atomic Spectrometry*, *26*(12), 2508-2518. https://doi.org/10.1039/c1ja10172b

Pattison, D.R., & DeBuhr, C.L. (2015). Petrology of metapelites in the Bugaboo aureole, British Columbia, Canada. *Journal of Metamorphic Geology*, *33*(5), 437-462. https://doi.org/10.1111/jmg.12128

Pattison, D.R., & Spear, F. S. (2018). Kinetic control of staurolite–Al_2SiO_5 mineral assemblages: implications for Barrovian and Buchan metamorphism. *Journal of Metamorphic Geology*, *36*(6), 667-690. https://doi.org/10.1111/jmg.12302

Pavanetto, P., Funedda, A., Northrup, C.J., Schimtz, M., Crowley, J., & Loi, A. (2012). Structure and U–Pb zircon geochronology in the Variscan foreland of SW Sardinia, Italy. *Geological Journal*, *47*(4), 426–445. https://doi.org/10.1002/gj.1350

Peacock, S. M. (1992). Blueschist-facies metamorphism, shear heating, and P-T-t paths in subduction shear zones. *Journal of Geophysical Research: Solid Earth*, *97*(B12), 17693-17707. https://doi.org/10.1029/92JB01768

Pérez-Cáceres, I., Martínez Poyatos, D. J., Vidal, O., Beyssac, O., Nieto, F., Simancas, J. F., Azor, A., & Bourdelle, F. (2020). Deciphering the metamorphic evolution of the Pulo do Lobo metasedimentary domain (SW Iberian Variscides). *Solid Earth*, *11*(2), 469-488. https://doi.org/10.5194/se-11-469-2020

Pertusati, P., Sarria, E., Cherchi, G.P., Carmignani, L., Barca, S., Benedetti, M., Chighine, G., Cincotti, F., Oggiano, G., Ulzega, A., Orrù, P., & Pintus, C. (2002). Note illustrative della Carta Geologica d'Italia alla scala 1:50.000 - foglio 541 Jerzu, pp. 143, *Servizio Geologico Nazionale – Regione Autonoma Sardegna, 168.*

Petroccia, A., Carosi, R., Montomoli, C., Iaccarino, S., & Vitale Brovarone, A. (2022a). Deformation and temperature variation along thrust-sense shear zones in the hinterland-foreland transition zone of collisional settings: a case study from the Barbagia Thrust (Sardinia, Italy). Journal of Structural Geology, *161*, https://doi.org/10.1016/j.jsg.2022.104640

Petroccia, A., Montomoli, C., Iaccarino, S., & Carosi, R. (2022b). Geology of the contact area between the Internal and External Nappe Zone of the Sardinian Variscan Belt (Italy): new insights on the complex polyphase deformation occurring in the hinterland-foreland transition zone of collisional belts. *Journal of Maps*, https://doi.org/10.1080/17445647.2022.2093660

Petroccia, A., Carosi, R., Montomoli, C., Iaccarino, S., & Vitale Brovarone, A. (2022c). Thermal variation across collisional orogens: insights from the hinterland-foreland transition zone of the Sardinian Variscan belt. *Terra Nova*, https://doi.org/10.1111/ter.12635

Piazolo, S., & Passchier, C.W. (2002). Controls on lineation development in low to medium-grade shear zones: A study from the Cap de Creus peninsula, NE Spain. *Journal of Structural Geology*, *24*, 25-44. https://doi.org/10.1016/s0191-8141(01)00045-1

Piccolo, A., Faccenda, M., Carosi, R., Montomoli, C., & Visonà, D. (2018). Crustal strength control on structures and metamorphism in collisional orogens. *Tectonophysics*, *746*, 470-492. https://doi.org/10.1016/j.tecto.2017.09.018

Pili, P., & Saba, O. (1975). Presenza di Devoniano a Conodonti nelle rocce carbonatiche di Correboi (Sardegna centro-orientale). *Bollettino della SocietaSarda di Scienze Naturali, Cagliari*, *15*.

Platt, J.P. (1983). Progressive refolding in ductile shear zones. *Journal of Structural Geology*, *5*(6), 619-622. https://doi.org/10.1016/0191-8141(83)90074-3

Platt, J. P. (1993). Exhumation of high-pressure rocks: A review of concepts and processes. *Terra nova*, *5*(2), 119-133. https://doi.org/10.1111/j.1365-3121.1993.tb00237.x

Platt, J.P. (2015). Rheology of two-phase systems: A microphysical and observational approach. *Journal of Structural Geology*, *77*, 213-227. https://doi.org/10.1016/j.jsg.2015.05.003

Platt, J. P. (2018). Corrigendum to" Influence of shear heating on microstructurally defined plate boundary shear zones"[J. Struct. Geol. 79 (2015), 80-89]. *Journal of Structural Geology*, *113*, 242-243. https://doi.org/10.1016/j.jsg.2017.08.005

Platt, J.P., & Vissers, R.L.M. (1980). Extensional structures in anisotropic rocks. *Journal of Structural Geology*, *2*(4), 397-410. https://doi.org/10.1016/0191-8141(80)90002-4

Platt, J.P., Behr, W.M., & Cooper, F.J. (2015). Metamorphic core complexes: Windows into the mechanics and rheology of the crust. *Journal of the Geological Society*, *172*(1), 9-27. https://doi.org/10.1144/jgs2014-036

Pò, D.L., Braga, R., & Massonne, H.J. (2016). Petrographic, mineral and pressure-temperature constraints on phyllites from the Variscan basement at Punta Bianca, Northern Apennines, Italy. *Italian Journal of Geosciences*, *135*(3), 489-502. https://doi.org/10.3301/IJG.2015.29

Pourteau, A., Bousquet, R., Vidal, O., Plunder, A., Duesterhoeft, E., Candan, O., & Oberhänsli, R. (2014). Multistage growth of Fe–Mg–carpholite and Fe–Mg–chloritoid, from field evidence to thermodynamic modelling. *Contributions to Mineralogy and Petrology*, *168*(6), 1-25. https://doi.org/10.1007/s00410-014-1090-7

Pourteau, A., Sudo, M., Candan, O., Lanari, P., Vidal, O., & Oberhänsli, R. (2013). Neotethys closure history of Anatolia: insights from 40Ar–39Ar geochronology and P–T estimation in high-pressure metasedimentary rocks. *Journal of Metamorphic Geology*, *31*(6), 585-606. https://doi.org/10.1111/jmg.12034

Powell, R., & Holland, T.J.B. (1988). An internally consistent dataset with uncertainties and correlations: 3. Applications to geobarometry, worked examples and a computer program. *Journal of metamorphic Geology*, *6*(2), 173-204. https://doi.org/10.1111/j.1525-1314.1988.tb00415.x

Powell, R., & Holland, T.J.B. (1990). Calculated mineral equilibria in the pelite system, KFMASH (K_2O-FeO-MgO-Al_2O_3-SiO_2-H_2O). *American Mineralogist*, *75*(3-4), 367-380.

Powell, R., & Holland, T.J.B. (1994). Optimal geothermometry and geobarometry. *American Mineralogist*, *79*(1-2), 120-133.

Powell, R., Holland, T.J.B., & Worley, B. (1998). Calculating phase diagrams involving solid solutions via non-linear equations, with examples using THERMOCALC. *Journal of metamorphic Geology*, *16*(4), 577-588. https://doi.org/10.1111/j.1525-1314.1998.00157.x

Powell, R., & Holland, T.J.B. (2008). On thermobarometry. *Journal of Metamorphic Geology*, *26*(2), 155-179. https://doi.org/10.1111/j.1525-1314.2007.00756.x

Powell, R., & Holland, T.J.B. (2010). Using equilibrium thermodynamics to understand metamorphism and metamorphic rocks. *Elements*, *6*(5), 309-314. https://doi.org/10.2113/gselements.6.5.309

Pryer, L.L. (1993). Microstructures in feldspars from a major crustal thrust zone: the Grenville Front, Ontario, Canada. *Journal of structural Geology*, *15*(1), 21-36. https://doi.org/10.1016/0191-8141(93)90076-M

Rahl, J.M., Anderson, K.M., Brandon, M.T., & Fassoulas, C. (2005). Raman spectroscopic carbonaceous material thermometry of low-grade metamorphic rocks: Calibration and application to tectonic exhumation in Crete, Greece. *Earth and Planetary Science Letters*, *240*(2), 339-354. https://doi.org/10.1016/j.epsl.2005.09.055

Ramsay, J.G. (1967). Folding and fracturing of rocks, Mcgraw-Hill.

Ramsay, J.G., Casey, M., & Kligfield, R. (1983). Role of shear in development of the Helvetic fold-thrust belt of Switzerland. *Geology*, *11*(8), 439-442. https://doi.org/10.1130/0091-7613(1983)11%3C439:ROSIDO%3E2.0.CO;2

Regenauer-Lieb, K., Rosenbaum, G., Lyakhovsky, V., Liu, J., Weinberg, R., Segev, A., & Weinstein, Y. (2015). Melt instabilities in an intraplate lithosphere and implications for volcanism in the Harrat Ash-Shaam volcanic field (NW Arabia). *Journal of Geophysical Research: Solid Earth*, *120*(3), 1543-1558. https://doi.org/10.1002/2014JB011403

Ring, U., & Brandon, M.T. (1999). Ductile deformation and mass loss in the Franciscan subduction complex: implications for exhumation processes in accretionary wedges. *Geological Society, London, Special Publications*, *154*(1), 55-86. https://doi.org/10.1144/gsl.sp.1999.154.01.03

Ring, U., & Kumerics, C. (2008). Vertical ductile thinning and its contribution to the exhumation of high-pressure rocks: the Cycladic blueschist unit in the Aegean. *Journal of the Geological Society*, *165*(6), 1019-1030. https://doi.org/10.1144/0016-76492008-010

Ring, U., Bernet, M., & Tulloch, A. (2015). Kinematic, finite strain and vorticity analysis of the Sisters shear zone, Stewart Island, New Zealand. *Journal of Structural Geology*, *73*, 114-129. https://doi.org/10.1016/j.jsg.2015.02.004

Ring, U., Brandon, M.T., & Ramthun, A. (2001). Solution-mass-transfer deformation adjacent to the Glarus Thrust, with implications for the tectonic evolution of the Alpine wedge in eastern Switzerland. *Journal of Structural Geology*, *23*(10), 1491-1505. https://doi.org/10.1016/S0191-8141(01)00015-3

Robert, J.L. (1976). Titanium solubility in synthetic phlogopite solid solutions. *Chemical Geology*, *17*, 213-227. https://doi.org/10.1016/0009-2541(76)90036-X

Robinson, D.M., & Pearson, O.N. (2006). Exhumation of Greater Himalayan rock along the Main Central Thrust in Nepal: implications for channel flow. *Geological Society, London, Special Publications*, *268*(1), 255-267. https://doi.org/10.1144/GSL.SP.2006.268.01.12

Rogers, J.J., & Santosh, M. (2004). *Continents and supercontinents*. Oxford University Press. https://doi.org/10.1016/S1342-937X(05)70827-3

Rosenberg, C.L., & Handy, M.R. (2005). Experimental deformation of partially melted granite revisited: implications for the continental crust. *Journal of metamorphic Geology*, *23*(1), 19-28. https://doi.org/10.1111/j.1525-1314.2005.00555.x

Saliot, P., & Velde, B. (1982). Phengite compositions and post-nappe high-pressure metamorphism in the Pennine zone of the French Alps. *Earth and Planetary Science Letters*, *57*(1), 133-138. https://doi.org/10.1016/0012-821X(82)90179-0

Sanderson, D.J. (1982). Models of strain variation in nappes and thrust sheets: a review. *Tectonophysics*, *88*(3-4), 201-233. https://doi.org/10.1016/0040-1951(82)90237-2

Sanderson, D.J., & Marchini, W.R.D. (1984). Transpression. *Journal of structural Geology*, *6*(5), 449-458. https://doi.org/10.1016/0191-8141(84)90058-0

Sanità, E., Di Rosa, M., Lardeaux, J. M., Marroni, M., & Pandolfi, L. (2022). Metamorphic peak estimates of the Marguareis Unit (Briançonnais Domain): New constrains for the tectonic evolution of the south-western Alps. *Terra Nova*. https://doi.org/10.1111/ter.12592

Sarkarinejad, K., & Ghanbarian, M.A. (2014). The Zagros hinterland fold-and-thrust belt in-sequence thrusting, Iran. *Journal of Asian Earth Sciences, 85*, 66-79. https://doi.org/10.1016/j.jseaes.2014.01.017

Scharf, A., Handy, M.R., Ziemann, M.A., & Schmid, S.M. (2013). Peak-temperature patterns of polyphase metamorphism resulting from accretion, subduction and collision (eastern Tauern Window, E uropean Alps)–a study with R aman microspectroscopy on carbonaceous material (RSCM). *Journal of metamorphic Geology*, *31*(8), 863-880. https://doi.org/10.1111/jmg.12048

Schavemaker, Y.A., De Bresser, J.H., Van Baelen, H., & Sintubin, M. (2012). Geometry and kinematics of the "Herbeumont shear zone" in the High-Ardenne slate belt (Belgium). *Geologica belgica*, *15*(3), 126-136.

Scheffer, C., Vanderhaeghe, O., Lanari, P., Tarantola, A., Ponthus, L., Photiades, A., & France, L. (2016). Syn-to post-orogenic exhumation of metamorphic nappes: Structure and thermobarometry of the western Attic-Cycladic metamorphic complex (Lavrion, Greece). *Journal of Geodynamics*, *96*, 174-193. https://doi.org/10.1016/j.jog.2015.08.005

Schmalholz, S. M., & Duretz, T. (2015). Shear zone and nappe formation by thermal softening, related stress and temperature evolution, and application to the Alps. *Journal of Metamorphic Geology*, *33*(8), 887-908. https://doi.org/10.1111/jmg.12137

Schneider, J., Corsini, M., Peila, A., & Lardeaux, J. (2014). Thermal and mechanical evolution of an orogenic wedge during Variscan collision: an example in the Maures-Tanneron Massif (SE France). *Geological Society, London, Special Publications*, *405*, 313–331. https://doi.org/10.1144/SP405.4

Schott, B., Yuen, D.A., & Schmeling, H. (2000). The significance of shear heating in continental delamination. *Physics of the Earth and Planetary Interiors*, *118*(3-4), 273-290. https://doi.org/10.1016/S0031-9201(99)00159-4

Schulmann, K., Thompson, A.B., Lexa, O., & Ježek, J. (2003). Strain distribution and fabric development modeled in active and ancient transpressive zones. *Journal of Geophysical Research: Solid Earth*, *108*(B1), ETG-6. https://doi.org/10.1029/2001JB000632

Scodina, M., Cruciani, G., & Franceschelli, M. (2021). Metamorphic evolution and P–T path of the Posada Valley amphibolites: new insights on the Variscan high pressure metamorphism in NE Sardinia, Italy. *Comptes Rendus. Géoscience*, *353*(1), 227-246. https://doi.org/10.5802/crgeos.65

Seno, S., Dallagiovanna, G., & Vanossi, M. (1998). From finite strain data to strain history: a model for a sector of the Ligurian Alps, Italy. *Journal of Structural Geology*, *20*(5), 573-585. https://doi.org/10.1016/S0191-8141(97)00104-1

Sharib, A.A., Reinhardt, J., & McCourt, S. (2021). Structural diversity within a thrust complex reflecting progressive overprinting during a protracted orogenic process of terrane accretion, Natal belt, South Africa. *Journal of Structural Geology*, *142*, 104231. https://doi.org/10.1016/j.jsg.2020.104231

Simonetti, M. (2021). The East Variscan Shear Zone: a structural and geochronological review for improving paleogeographic reconstruction of the southern Variscides. *Rendiconti Online della Società Geologica Italiana, 55*, 36–52. https://doi.org/10.3301/ROL.2021.13

Simonetti, M., Carosi, R., Montomoli, C., Corsini, M., Petroccia, A., Cottle, J. M., & Iaccarino, S. (2020b). Timing and kinematics of flow in a transpressive dextral shear zone, Maures Massif (Southern France). *International Journal of Earth Sciences*, *109*(7), 2261-2285. https://doi.org/10.1007/s00531-020-01898-6

Simonetti, M., Carosi, R., Montomoli, C., Cottle, J. M., & Law, R. D. (2020a). Transpressive deformation in the southern european variscan belt: new insights from the aiguilles rouges massif (Western Alps). *Tectonics*, *39*(6), e2020TC006153. https://doi.org/10.1029/2020TC006153

Simonetti, M., Carosi, R., Montomoli, C., Langone, A., D'Addario, E., & Mammoliti, E. (2018). Kinematic and geochronological constraints on shear deformation in the Ferriere-Mollières shear zone (Argentera-Mercantour Massif, Western Alps): Implications for the evolution of the Southern European Variscan Belt. *International Journal of Earth Sciences*, *107*(6), 2163-2189. https://doi.org/10.1007/s00531-018-1593-y

Simonetti, M., Carosi, R., Montomoli, C., Law, R. D., & Cottle, J. M. (2021). Unravelling the development of regional-scale shear zones by a multidisciplinary approach: The case study of the Ferriere-Mollières Shear Zone (Argentera Massif, Western Alps). *Journal of Structural Geology*, *149*, 104399. https://doi.org/10.1016/j.jsg.2021.104399

Simpson, C., & De Paor, D.G. (1993). Strain and kinematic analysis in general shear zones. *Journal of Structural Geology*, *15*(1), 1-20. https://doi.org/10.1016/0191-8141(93)90075-l

Skrzypek, E. (2021). First-and second-order Raman spectra of carbonaceous material through successive contact and regional metamorphic events (Ryoke belt, SW Japan). *Lithos*, *388*, 106029. https://doi.org/10.1016/j.lithos.2021.106029.

Spear, F.S. (1988). The Gibbs method and Duhem's theorem: The quantitative relationships among P, T, chemical potential, phase composition and reaction progress in igneous and metamorphic systems. *Contributions to Mineralogy and Petrology*, *99*(2), 249-256. https://doi.org/10.1007/BF00371465

Spear, F.S., & Menard, T. (1989). Program GIBBS; a generalized Gibbs method algorithm. *American Mineralogist*, *74*(7-8), 942-943.

Spear, F.S., & Pyle, J.M. (2010). Theoretical modeling of monazite growth in a low-Ca metapelite. *Chemical Geology, 273*(1-2), 111-119. https://doi.org/10.1016/j.chemgeo.2010.02.016

Spear, F.S., Pattison, D.R.M., & Cheney, J.T. (2016). The web of geological sciences: Advances, impacts, and interactions II Geological Society of America. *Geological Society of America, Special Papers*, *523*, 31-73.

Stipp, M., Stünitz, H., Heilbron, M., & Schmid, D.W. (2002). The eastern tonale fault zone: A natural laboratory for crystal plastic deformation of quartz over a temperature range from 250 to 700 °C. *Journal of Structural Geology*, *24*, 1861-1884. https://doi.org/10.1016/S0191-8141(02)00035-4

Stüwe, K., & Powell, R. (1995). PT paths from modal proportions: application to the Koralm Complex, Eastern Alps. *Contributions to Mineralogy and Petrology*, *119*(1), 83-93. https://doi.org/10.1007/BF00310719

Sullivan, W. A., & Law, R. D. (2007). Deformation path partitioning within the transpressional White Mountain shear zone, California and Nevada. *Journal of Structural Geology*, *29*(4), 583-599. https://doi.org/10.1016/j.jsg.2006.11.001

Symmes, G. H., & Ferry, J. M. (1992). The effect of whole-rock MnO content on the stability of garnet in pelitic schists during metamorphism. *Journal of Metamorphic Geology, 10*(2), 221-237. https://doi.org/10.1111/j.1525-1314.1992.tb00080.x

Takeuchi, C. S., & Fialko, Y. (2012). Dynamic models of interseismic deformation and stress transfer from plate motion to continental transform faults. *Journal of Geophysical Research: Solid Earth, 117*(B5). https://doi.org/10.1029/2011JB009056

Tarquini, S., Isola, I., Favalli, M., Mazzarini, F., Bisson, M., Pareschi, M.T., & Boschi, E. (2007). TINITALY/01: A new Triangular Irregular Network of Italy. *Annals of Geophysics, 50*, 407–425. https://doi.org/10.4401/ag-4424

Teyssier, C., & Whitney, D.L. (2002). Gneiss domes and orogeny. *Geology*, *30*(12), 1139-1142. https://doi.org/10.1130/0091-7613(2002)030%3C1139:GDAO%3E2.0.CO;2

Teyssier, C., Tikoff, B., & Markley, M. (1995). Oblique plate motion and continental tectonics. *Geology, 23*(5), 447-450. https://doi.org/10.1130/0091-7613(1995)023%3C0447:OPMACT%3E2.3.CO;2

Thielmann, M., & Kaus, B. J. (2012). Shear heating induced lithospheric-scale localization: Does it result in subduction?. *Earth and Planetary Science Letters, 359*, 1-13. https://doi.org/10.1016/j.epsl.2012.10.002

Thigpen, J.R., Ashley, K.T., & Law, R.D. (2017). Evaluating kinematic displacement rate effects on transient thermal processes in thrust belts using coupled thermomechanical finite-element models. In R.D., Law, J.R., Thigpen, A.J., Merschat, H.H. Stowell, (Ed*.). Linkage and Feedbacks in Orogenic Systems*. (213, pp. 1-23). Geological Society of America Memoir. https://doi.org/10.1130/2017.1213(01)

Thigpen, J.R., Ashley, K.T., Mako, C., Law, R.D., & Spencer, B. (2021). Interplay between crustal-scale thrusting, high metamorphic heating rates, and the development of inverted thermal-metamorphic gradients: numerical models and examples from the Caledonides of northern Scotland. *Tectonics*, 40, e2021TC006716. https://doi.org/10.1029/2021TC006716

Thigpen, J.R., Law, R.D., Lloyd, G.E., Brown, S.J., & Cook, B. (2010). Deformation Temperatures, Vorticity of Flow and Strain Symmetry in the Loch Eriboll Mylonites, NW Scotland: Implications for the Kinematic and Structural Evolution of the Northernmost Moine Thrust Zone. *Geological Society of London, Special Publications*, *335*, 623-662. https://doi.org/10.1144/sp335.26

Thigpen, J.R., Law, R.D., Loehn, C., Strachan, R.A., Tracy, R., Lloyd, G., Roth, B., & Brown, S. (2013). Thermal structure and tectonic evolution of the Scandian orogenic wedge, Scottish Caledonides: Integrating geothermometry, deformation temperatures, and kinematic-thermal modeling. *Journal of Metamorphic Geology, 31*, 813–842. https://doi.org/10.1111/jmg.12046

Tinkham, D.K., & Ghent, E.D. (2005). Estimating PT conditions of garnet growth with isochemical phase-diagram sections and the problem of effective bulk-composition. *The Canadian Mineralogist*, *43*(1), 35-50. https://doi.org/10.2113/gscanmin.43.1.35

Tomkins, H.S., Powell, R., & Ellis, D.J. (2007). The pressure dependence of the zirconium-in-rutile thermometer. *Journal of metamorphic Geology*, *25*(6), 703-713. https://doi.org/10.1111/j.1525-1314.2007.00724.x

Thompson Jr, J.B. (1957). The graphical analysis of mineral assemblages in pelitic schists. *American Mineralogist: Journal of Earth and Planetary Materials*, *42*(11-12), 842-858. https://pubs.geoscienceworld.org/msa/ammin/article-abstract/42/11-12/842/539812/The-Graphical-Analysis-of-Mineral-Assemblages-in

Tikoff, B., & Fossen, H. (1993). Simultaneous pure and simple shear: the unifying deformation matrix. *Tectonophysics, 217*(3-4), 267-283. https://doi.org/10.1016/0040-1951(93)90010-H

Tikoff, B., & Fossen, H. (1995). The limitations of three-dimensional kinematic vorticity analysis. Journal of *Structural Geology, 17*(12), 1771-1784. https://doi.org/10.1016/0191-8141(95)00069-P

Tikoff, B., & Teyssier, C. (1994). Strain modeling of displacement-field partitioning in transpressional orogens. *Journal of Structural Geology, 16*(11), 1575-1588. https://doi.org/10.1016/0191-8141(94)90034-5

Tischendorf, G., Rieder, M., Förster, H.J., Gottesmann, B., & Guidotti, C. V. (2004). A new graphical presentation and subdivision of potassium micas. *Mineralogical Magazine*, *68*(4), 649-667. https://doi.org/10.1180/0026461046840210

Torvela, T., & Kurhila, M. (2020). How does orogenic crust deform? Evidence of crustal-scale competent behaviour within the partially molten middle crust during orogenic compression. *Precambrian Research*, *342*, 105670. https://doi.org/10.1016/j.precamres.2020.105670

Tracy, R.J. (1982). Compositional zoning and inclusions in metamorphic minerals. In: Ferry, J. M. (ed.) Characterization of Metamorphism Through Mineral Equilibria.

Trincal, V., & Lanari, P. (2016). Al-free di-trioctahedral substitution in chlorite and a ferri-sudoite end-member. *Clay Minerals*, *51*(4), 675-689. https://doi.org/10.1180/claymin.2016.051.4.09

Vai, G.B., & Cocozza, T. (1974). Il “postgotlandiano” sardo, unità sinorogenica ercinica. *Bollettino della Società Geologica Italiana, 93*, 61–72.

Van der Pluijm, B. A., & Marshak, S. (2003). Earth structure. *New York*.

Van Hinsbergen, D.J., Lippert, P.C., Dupont-Nivet, G., McQuarrie, N., Doubrovine, P.V., Spakman, W., & Torsvik, T.H. (2012). Greater India Basin hypothesis and a two-stage Cenozoic collision between India and Asia. *Proceedings of the National Academy of Sciences*, *109*(20), 7659-7664. https://doi.org/10.1073/pnas.1117262109

Van Hinsbergen, D.J., Lippert, P.C., Li, S., Huang, W., Advokaat, E.L., & Spakman, W. (2019). Reconstructing Greater India: Paleogeographic, kinematic, and geodynamic perspectives. *Tectonophysics*, *760*, 69-94. https://doi.org/10.1016/j.tecto.2018.04.006

Vanardois, J., Roger, F., Trap, P., Goncalves, P., Lanari, P., Paquette, J.L., Marquer, D., Cagnard, F., Le Bayon, B., & Barou, F. (2022). Exhumation of deep continental crust in a transpressive regime: The example of Variscan eclogites from the Aiguilles-Rouges massif (Western Alps). *Journal of Metamorphic Geology*. https://doi.org/10.1111/jmg.12659

Vanardois, J., Trap, P., Roger, F., Melleton, J., Marquer, D., Paquette, J. L., Gonclaves, P., Cagnard, F., & Le Bayon, B. (2022). Deformation, crustal melting and magmatism in the crustal-scale East-Variscan Shear Zone (Aiguilles-Rouges and Mont-Blanc massifs, Western Alps). *Journal of Structural Geology*, *163*, 104724. https://doi.org/10.1016/j.jsg.2022.104724

Vanderhaeghe, O., & Teyssier, C. (2001). Partial melting and flow of orogens. *Tectonophysics, 342,* 451–472. https://doi.org/10.1016/S0040-1951(01)00175-5

Vanderhaeghe, O., Oscar, L., Gardien, V., Moyen, J.F., Gébelin, A., Chelle-Michou, C., Couzinié, S., Villaros, A., & Bellanger, M. (2020). Flow of partially molten crust controlling construction, growth and collapse of the Variscan orogenic belt: The geologic record of the French Massif Central. *Bulletin de la Société Géologique de France, 191,* 25. https://doi.org/10.1051/bsgf/2020013

Vásquez-Serrano, A., Nieto-Samaniego, Á.F., Rangel-Granados, E., Alaníz-Álvarez, S., & Olmos-Moya, M.D.J.P. (2021). Architecture of an upper-level weak detachment zone: Mexican Fold and Thrust Belt, central Mexico. *Journal of Structural Geology*, *148*, 104361. https://doi.org/10.1016/j.jsg.2021.104361

Verdecchia, S. O., Collo, G., Zandomeni, P. S., Wunderlin, C., & Fehrmann, M. (2019). Crystallochemical indexes and geothermobarometric calculations as a multiproxy approach to PT condition of the low-grade metamorphism: The case of the San Luis Formation, Eastern Sierras Pampeanas of Argentina. *Lithos, 324,* 385-401. https://doi.org/10.1016/j.lithos.2018.11.021

Vidal, O., & Parra, T. (2000). Exhumation paths of high-pressure metapelites obtained from local equilibria for chlorite–phengite assemblages. *Geological Journal*, *35*(3-4), 139-161. https://doi.org/10.1002/gj.856

Vidal, O., De Andrade, V., Lewin, E., Munoz, M., Parra, T., & Pascarelli, S. (2006). P–T-deformation-Fe^{3+}/Fe^{2+} mapping at the thin section scale and comparison with XANES mapping: application to a garnet-bearing metapelite from the Sambagawa metamorphic belt (Japan). *Journal of Metamorphic Geology*, *24*(7), 669-683. https://doi.org/10.1111/j.1525-1314.2006.00661.x

Vidal, O., Lanari, P., Munoz, M., Bourdelle, F., & De Andrade, V. (2016). Deciphering temperature, pressure and oxygen-activity conditions of chlorite formation. *Clay Minerals*, *51*(4), 615-633. https://doi.org/10.1180/claymin.2016.051.4.06

Vidal, O., Parra, T., & Trotet, F. (2001). A thermodynamic model for Fe-Mg aluminous chlorite using data from phase equilibrium experiments and natural pelitic assemblages in the 100 to 600 C, 1 to 25 kb range. *American journal of Science*, *301*(6), 557-592. https://doi.org/10.2475/ajs.301.6.557

Vidal, O., Parra, T., & Vieillard, P. (2005). Thermodynamic properties of the Tschermak solid solution in Fe-chlorite: Application to natural examples and possible role of oxidation. *American Mineralogist*, *90*(2-3), 347-358. https://doi.org/10.2138/am.2005.1554

Vitale Brovarone, A., Beyssac, O., Malavieille, J., Molli, G., Beltrando, M., Compagnoni, R. (2013). Stacking and metamorphism of continuous segments of subducted lithosphere in a high-pressure wedge: The example of Alpine Corsica (France). *Earth-Science Reviews, 116,* 35-56. https://doi.org/10.1016/j.earscirev.2012.10.003

Vitale Brovarone, A., Tumiati, S., Piccoli, F., Ague, J. J., Connolly, J. A. D., Beyssac, O. (2020). Fluid-mediated selective dissolution of subducting carbonaceous material: Implications for carbon recycling and fluid fluxes at forearc depths, *Chemical Geology 549,* 119682, https://doi.org/10.1016/j.chemgeo.2020.119682

Vitale, S., & Mazzoli, S. (2008). Heterogeneous shear zone evolution: the role of shear strain hardening/softening. *Journal of Structural Geology, 30*(11), 1383-1395. https://doi.org/10.1016/j.jsg.2008.07.006

Vollmer, FW. (2015). EllipseFit 3.2. https://www.frederickvollmer.com/ellipsefit/

Wallis, S.R., Platt, J.P., Knott, S.D. (1993). Recognition of synconvergence extension in accretionary wedges with examples from the Caiabrian Arc and the Eastern Alps. *American Journal of Science, 293,* 463–495. https://doi.org/10.2475/ajs.293.5.463

Wang, L., Cao, D.Y., Peng, Y.W., Ding, Z.Y., Li, Y. (2019). Strain-induced graphitization mechanism of coal-based graphite from Lutang, Hunan Province, *China. Minerals, 9*(10), 617. https://doi.org/10.3390/min9100617

Warr. (2021). IMA–CNMNC approved mineral symbols. *Mineralogical Magazine, 85,* 291–320 doi:10.1180/mgm.2021.43

Waters, D.J. (2019). Metamorphic constraints on the tectonic evolution of the High Himalaya in Nepal: the art of the possible. *Geological Society, London, Special Publications, 483*(1), 325-375. https://doi.org/10.1144/SP483-2018-187

Waters, D.J., & Lovegrove, D.P. (2002). Assessing the extent of disequilibrium and overstepping of prograde metamorphic reactions in metapelites from the Bushveld Complex aureole, South Africa. *Journal of Metamorphic Geology*, *20*(1), 135-149. https://doi.org/10.1046/j.0263-4929.2001.00350.x

Waters, D.J., Law, R.D., Searle, M.P., & Jessup, M.J. (2019). Structural and thermal evolution of the South Tibetan Detachment shear zone in the Mt Everest region, from the 1933 sample collection of LR Wager. *Geological Society, London, Special Publications, 478*(1), 335-372. https://doi.org/10.1144/SP478.17

White, R.W., Powell, R., Holland, T.J.B., Johnson, T.E., & Green, E.C.R. (2014). New mineral activity–composition relations for thermodynamic calculations in metapelitic systems. *Journal of Metamorphic Geology*, *32*(3), 261-286. https://doi.org/10.1111/jmg.12071

Whitney, D., & Evans, B. (2010). Abbreviations for names of rock-forming minerals. *American Mineralogist, 95,* 185–187. https://doi.org/10.2138/am.2010.3371

Whitney, D. L., Teyssier, C., Rey, P., & Buck, W. R. (2013). Continental and oceanic core complexes. *GSA Bulletin, 125*(3-4), 273-298. https://doi.org/10.1130/B30754.1

Whitney, D. L., Teyssier, C., & Vanderhaeghe, O. (2004). Gneiss domes and crustalflow. Gneiss domes in orogeny,*Geological Society of America, Special Papers, 380*, 15–33.

Williams, M.L., Jercinovic, M.J., & Hetherington, C.J. (2007). Microprobe monazite geochronology: understanding geologic processes by integrating composition and chronology. *Annual Review of Earth and Planetary Sciences, 35,* 137-175. https://doi.org/10.1146/annurev.earth.35.031306.140228

Willis, K., Houseman, G. A., Evans, L., Wright, T., Hooper, A. (2019). Strain localization by shear heating and the development of lithospheric shear zones, *Tectonophysics 764,* 62–76. https://doi.org/10.1016/j.tecto.2019.05.010

Willner, A. P. (2020). Very-low-grade Metamorphism.

Willner, A. P., Barr, S.M., Gerdes, A., Massonne, H.J., & White, C.E. (2013). Origin and evolution of Avalonia: evidence from U–Pb and Lu–Hf isotopes in zircon from the Mira terrane, Canada, and the Stavelot–Venn Massif, Belgium. *Journal of the Geological Society*, *170*(5), 769-784. https://doi.org/10.1144/jgs2012-152

Willner, A.P., Barr, S.M., Glodny, J., Massonne, H.J., Sudo, M., Thomson, S.N., Van Staal, C.R., & White, C.E. (2015). Effects of fluid flow, cooling and deformation as recorded by 40Ar/39Ar, Rb–Sr and zircon fission track ages in very low-to low-grade metamorphic rocks in Avalonian SE Cape Breton Island (Nova Scotia, Canada). *Geological Magazine*, *152*(5), 767-787. https://doi.org/10.1017/S0016756814000508

Wopenka, B., & Pasteris, J.D. (1993). Structural characterization of kerogens to granulite-facies graphite: applicability of Raman microprobe spectroscopy. *American mineralogist, 78*(5-6), 533-557.

Xypolias, P. (2010). Vorticity analysis in shear zones: A review of methods and applications. *Journal of Structural Geology, 32,* 2072–2092. https://doi.org/10.1016/j.jsg.2010.08.009

Yakymchuk, C., Clark, C., & White, R.W. (2017). Phase relations, reaction sequences and petrochronology. *Reviews in Mineralogy and Geochemistry*, *83*(1), 13-53. https://doi.org/10.1515/9783110561890

Yamaoka, K., Wallis, S.R., Miyake, A., Kouketsu, Y. (2022). Recognition of Detrital Carbonaceous Material in the Ryoke Metamorphic Belt by Using Raman Thermometry: Implications for Thermal Structure and Detrital Origin. *Lithosphere*, https://doi.org/10.2113/2022/3899340

Yonkee, A. (2005). Strain patterns within part of the Willard thrust sheet, Idaho-Wyoming-Utah thrust belt. *Journal of Structural Geology, 27,* 1315-1343. https://doi.org/10.1016/j.jsg.2004.06.014

Zhang, B., Chai, Z., Yin, C. Y., Huang, W. T., Wang, Y., Zhang, J. J., Wang, X.X, & Cao, K. (2017). Intra-continental transpression and gneiss doming in an obliquely convergent regime in SE Asia. *Journal of Structural Geology*, *97*, 48-70. https://doi.org/10.1016/j.jsg.2017.02.010